Characterization of the cardiac ISGylome and its influence on protein function during Coxsackievirus B3 infection

Inaugural-Dissertation

to obtain the academic degree

Doctor rerum naturalium (Dr. rer. nat.)

submitted to the Department of Biology, Chemistry, Pharmacy

of Freie Universität Berlin

by

CLARA BREDOW

2022

June 1st, 2017 – March 31st, 2022

under supervision of Prof. Dr. med. Antje Beling

Charité – Universitätsmedizin Berlin

Institute of Biochemistry

1st reviewer: Prof. Dr. med. Antje Beling

2nd reviewer: Prof. Dr. Haike Antelmann

Date of defense: June 30th, 2022

Acknowledgements

I would like to take this opportunity to thank all those people without whom this project would never have been realized.

First and foremost, I would like to express my gratitude towards my supervisor Prof. Antje Beling. My research and this dissertation would have been impossible without your advice, expertise, and encouragement. I was always able to come to you for guidance, constructive discussions, and creative input. Thank you for your trust and continuous support.

I would like to express my appreciation for all collaboration partners as well. Special thanks go to Fabien and Eva, who not only gave invaluable technical support, but contributed their precious time and unconditional help whenever and wherever it was needed. I also thank Francis Impens, Klaus-Peter Knobeloch, Lilliana Radoshevic, Karin Klingel, Niclas Gimber, and Jan Schmoranzer.

A huge amount of gratitude goes out to the members of the Beling lab for creating a warm and joyous working environment. You have become friends, rather than colleagues. Especially my lab-wife Meike, who was always ready with unwavering support and cookies. Karo, Sandra, Zickler, Martin, Prisca, Nicolas, Sophia, Hannah, and Anja: I could not have asked for better company, guidance, and assistance. You even made stressful times bearable and helped me to overcome.

I would be remiss not mentioning the ZIBI Graduate School, which provided financial support and opportunities for countless workshops and conferences. This unique scientific environment really enabled me to thrive and to become the scientist I am today.

Last but not least, my heart goes out to my family and friends! Thank you for bearing with me, listening to never-ending rants, and picking up the pieces when I could not hold them together. Katrin and Hartmut, without you, I would not exist. This is as much your win as it is mine. Jorrit, the best little brother I could have asked for. Opa, for cheering me on and taking over for Oma when she was not here anymore. Philip, who has been by my side the entire time.

Thank you.

Selbstständigkeitserklärung

Hierdurch versichere ich, dass ich meine Dissertation selbstständig verfasst und keine anderen als die von mir angegebenen Quellen und Hilfsmittel verwendet habe.

Table of contents

1. Summary

Infection with cardiotropic Coxsackievirus B3 (CVB3) leads to activation of the innate immune system and production of type I Interferons (IFNs). Upon detection of IFNs, cells upregulate the expression of hundreds of downstream effector proteins called Interferon Stimulated Genes (ISGs) to establish the host cellular antiviral state. Among the ISGs, the small ubiquitin-like modifier ISG15 has pleiotropic antiviral function acting in its free form or covalently conjugated to other proteins. This so-called ISGylation is mediated by an E1/E2/E3 enzyme cascade, peaking around day 3 of infection in cardiac tissue. Subsequent infiltration of innate and adaptive immune cells into the myocardium results in both, viral elimination as well as inflammation-induced cell death and thus causes acute viral myocarditis. Inefficient virus clearance and persistence of viral RNA in cardiac cells can then cause chronic cardiac inflammation. Previous work showed that ISGylation suppresses CVB3-mediated pathology, and enrichment of ISGylation by deactivating the deconjugating activity of the Ubiquitin-specific protease 18 (USP18) further enhances the antiviral host response. However, the manner in which ISGylation orchestrates resistance against CVB3 remains unclear.

To investigate this, the cardiac proteome and ISGylome of infected wildtype, ISG15$^{-/-}$, and USP18$^{C61A/C61A}$ mice was analyzed by LC-MS/MS. On the one hand, proteome analysis showed an infection-induced upregulation of the host-cellular immune response to establish a cardiac antiviral state. Additionally, IFIT1 and IFIT3, proteins with known antiviral effect against CVB3, were identified as ISG15-target proteins and ISGylation positively influenced their expression levels. On the other hand, infection led to a downregulation of proteins associated with metabolic pathways. Nonetheless, the cardiac mitochondrial energy production was upregulated in an ISGylation-dependent manner, indicating infection-induced increased energy demand. Concordantly, analysis of the cardiac ISGylome identified a variety of metabolic enzymes to be covalently modified by ISG15. Upregulation of glycolytic levels in primary cardiomyocytes was restricted by ISG15, which might be at least partly due to an attenuated activity of ISGylated hexokinase-2 and phosphofructokinase. Taken together, this study highlights the regulation of two key response pathways in viral infection by the ISG15 system. While the direct antiviral response might be supported by ISGylation-mediated stabilization of IFIT1/3, ISG15/ISGylation further ensures the efficient regulation of metabolic energy production during infection.

Zusammenfassung

Eine Infektion mit Coxsackievirus B3 (CVB3) führt zur Aktivierung des angeborenen Immunsystems und zur Produktion von Typ I Interferonen. Binden Interferone an ihre Rezeptoren, wird die Expression von hunderten Effektorproteinen induziert, den Interferon Stimulierten Genen (ISG). Dies versetzt die Zelle in einen antiviralen Zustand. Das ubiquitinähnliche Protein ISG15 ist ein hoch abundantes ISG. Es hat pleiotrope antivirale Funktion, die es in seiner freien Form oder kovalent an andere Proteine konjugiert ausübt. Diese sogenannte ISGylierung wird durch eine E1/E2/E3-Enzymkaskade umgesetzt und erreicht ihr Maximum im Herzen am dritten Tag der CVB3 Infektion. Die Infiltration von angeborenen und adaptiven Immunzellen in das Myokard führt sowohl zur Viruseliminierung als auch zum entzündungsbedingten Zelltod und somit zu akuter viraler Myokarditis. Ineffiziente Eliminierung und die Persistenz der viralen RNA in Herzzellen können dann eine chronische Entzündung des Herzens verursachen. Frühere Arbeiten haben gezeigt, dass ISGylierung die CVB3-vermittelte Pathologie unterdrückt. Zusätzlich wird die antivirale Antwort durch Anreicherung von ISGylierung verbessert. Dies wird durch die Deaktivierung der ISG15-dekonjugierenden Aktivität der Ubiquitin-spezifischen Protease 18 (USP18) realisiert. Unklar ist jedoch, über welche Zielproteine und Mechanismen die ISGylierung die Resistenz gegen CVB3 steuert.

Um dies zu untersuchen, wurde das kardiale Proteom und ISGylom von infizierten Wildtyp-, $ISG15^{-/-}$- und $USP18^{C61A/C61A}$- Mäusen mittels LC-MS/MS analysiert. In der Infektion zeigte die Proteomanalyse eine Hochregulierung der zellulären Immunantwort. IFIT1 und IFIT3 (Proteine mit bekannter antiviraler Wirkung gegen CVB3) wurden als ISG15-Zielproteine identifiziert und ISGylierung hatte positiven Einfluss auf IFIT1/3-Proteinexpression. Zusätzlich führte die Infektion zu einer Herabregulierung von Proteinen, die mit Stoffwechselwegen in Verbindung stehen. Trotzdem wurde die kardiale mitochondriale Energieproduktion in Abhängigkeit der ISGylierung hochreguliert. Dies deutet auf einen infektionsbedingten erhöhten Energiebedarf hin. Das kardiale ISGylom wies zudem eine Vielzahl von Stoffwechselenzymen aus der Glykolyse auf. Analyse der glykolytischen Rate in primären Kardiomyozyten zeigte, dass sie durch ISG15 eingeschränkt wird. Diese Einschränkung könnte zum Teil durch eine reduzierte Aktivität der ISGylierten Enzyme Hexokinase-2 und Phosphofructokinase zustande kommen.

Zusammenfassend unterstreicht diese Studie die Regulierung von zwei wichtigen Reaktionswegen bei Virusinfektionen durch das ISG15-System. Während die direkte antivirale Antwort durch die ISGylierung-vermittelte Stabilisierung von IFIT1/3 unterstützt werden könnte, sorgt ISG15/ISGylierung zusätzlich für die effiziente Regulierung der metabolischen Energieproduktion während der Infektion.

2. Introduction

2.1 Innate Immune System

The innate immune response represents the first line of defense against infection. Initially, pattern recognition receptors (PRRs) detect invading pathogens by their highly conserved microbial components, so-called pathogen-associated molecular patterns (PAMPs), as well as damage-associated molecular patterns (DAMPs). PAMPs include bacterial lipopolysaccharide (LPS), flagellin, viral fusion glycoproteins, as well as unique nucleic acid structures, such as viral genomes. The latter comprise single stranded (ss) or double stranded (ds) DNA or RNA, the latter of which can be positively oriented and coding (+ strand) or negatively oriented (- strand), meaning their complements encode viral proteins (O'Carroll and Rein 2016). DAMPS on the other hand are indicators of host-cell damage, i.e., molecules released upon tissue injury, which initiate an inflammatory response (Murphy 2018). Some PRRs are able to detect PAMPs as well as DAMPs, such as the nucleic acid sensor cyclic GMP-AMP synthase (cGAS), which detects both, viral and host DNA within the cytoplasm (Sun et al. 2013).

Across species, the so-called Toll-like receptors (TLRs) are a highly conserved class of PRRs. These transmembrane receptors are expressed in several immunity-related cell types, such as dendritic cells (DCs), macrophages, and B-cells (Iwasaki and Medzhitov 2004). While TLR1/2/4/5/6 are located at the cell membrane, TLR3/7/8/9 are found within the endosomal membranes where they detect ss and ds DNA as well as RNA (Barbalat et al. 2011). Upon ligand detection, TLRs dimerize and activate either the TIR domain-containing adaptor–inducing interferon β (TRIF) -dependent or the Myeloid differentiation primary response 88 (MyD88) -dependent signaling cascades. Ultimately, this cascade activates key transcription factors, such as nuclear factor κB (NF-κB), activator protein (AP) 1, and the interferon regulatory factor (IRF) 3 (Kawai and Akira 2008).

Another class of PRRs are the retinoic acid inducible gene (RIG) -I like receptors (RLRs) consisting of RIG-I, melanoma differentiation-associated 5 (MDA5), and laboratory of genetics and physiology 2 (LGP2). RLRs detect cytosolic foreign RNA, differentiating between host mRNA and pathogenic RNA by recognizing non-self cap-structures (Kawai and Akira 2006). While the 5'-end of mRNA in higher eukaryotes is capped by cap-1 or cap-2 structures to prevent premature degradation and efficient translation, viral RNAs often lack cap structures or present with modified versions, i.e., cap-0 RNA, 5'-triphosphate (5'-PPP) RNA or viral protein genome-linked (VPg)-capped RNA (Decroly et al. 2011; Werner et al. 2011). Upon detection of these PAMPs, RIG-I and MDA5 activate the transcription factors IRF3 or IRF7 via the mitochondrial antiviral signaling protein (MAVS) (Wilkins and Gale 2010).

The third family member, LGP2, is a regulator of the RIG-I signaling pathway and has been reported as both, negative regulator (Rothenfusser et al. 2005) and enhancing factor (Satoh et al. 2010) of the antiviral response. Thus, it was proposed to function as a regulatory switch, enhancing or inhibiting antiviral RIG-I and MDA5 mediated signaling in a concentration dependent manner (Rodriguez et al. 2014).

Together, PRRs induce a robust inflammatory response immediately after pathogen recognition, triggering protective chemokine and cytokine production (Fig. 1), which attract innate immune cells to the site of infection.

2.1.1 Interferons

An important class of cytokines, particularly in viral infection, are interferons (IFNs) which are classified as type I and type II, distinguished by their function, sequence homology, and receptors (Durbin et al. 2000). Type I IFNs comprise IFNα, β, κ, ε, and ω, the first two being the best characterized IFNs (Capobianchi et al. 2015; Kretschmer and Lee-Kirsch 2017).

Upon release from the cell, IFNα/β bind to the IFN activated receptor (IFNAR) 1 and 2 (Fig. 1). As most cells are capable of type I IFN production, their receptors are also ubiquitously expressed. Ligand binding induces IFNAR-1 and -2 dimerization which activates Janus kinase 1 (JAK1) and tyrosine kinase 2 (TYK2) to phosphorylate tyrosine residues within the cytoplasmic receptor domains. The phosphotyrosines then recruit Src Homology 2 (SH2) containing signal transducer and activator of transcription (STAT) 1 and 2, which are themselves phosphorylated and subsequently dimerize (Murphy 2018). Association of STAT1/2 with IRF9 forms the IFN-stimulated gene factor 3 (ISGF3) complex, which translocates into the nucleus and binds to the IFN-stimulated response elements (ISREs) in the genome, thus inducing transcription of IFN-stimulated genes (ISGs) (Fig. 1, (Ivashkiv and Donlin 2014)). In contrast, type II IFNs bind to IFNγ-receptor (IFNGR) and induce the formation of a STAT1-homodimer, which binds to the gamma-activated sequence (GAS) elements in promoter regions (Murphy 2018).

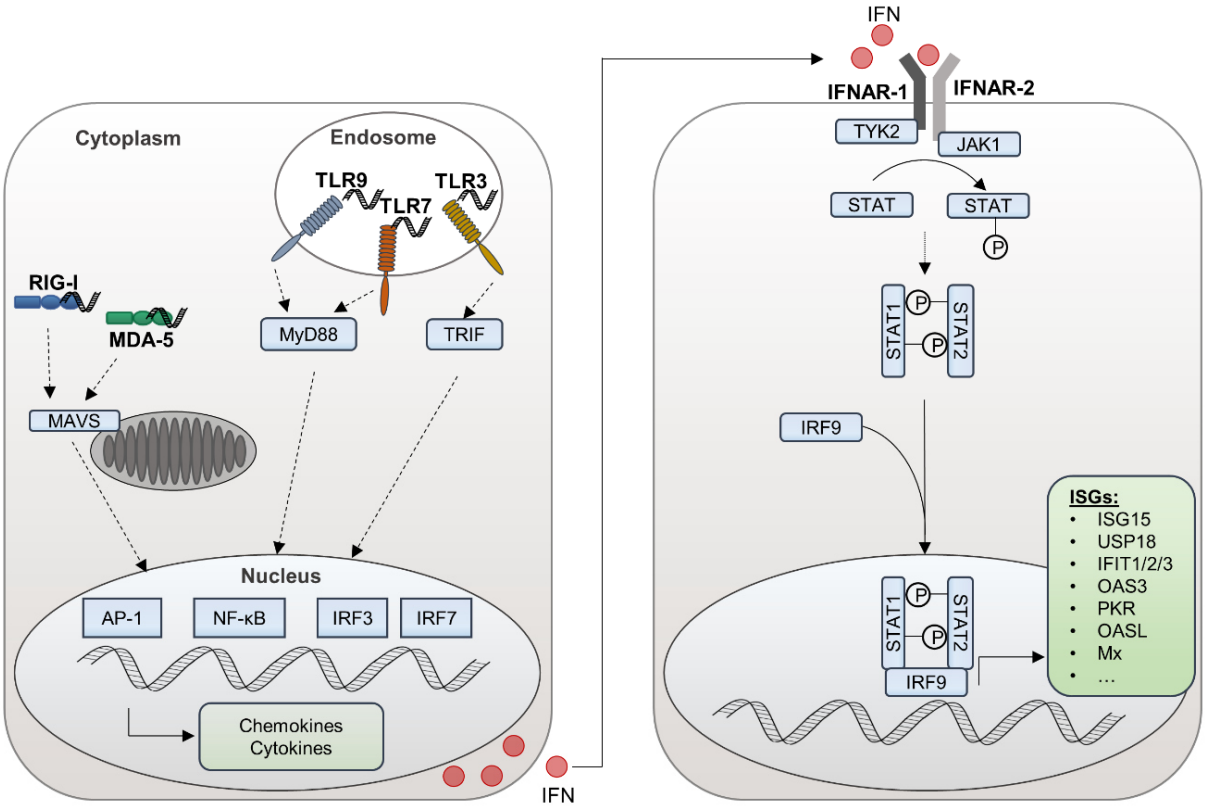

Figure 1: Type I IFN production and signaling.
Pattern recognition receptors (PRRs) and RNA sensors detect viral nucleic acids in the endosome (TLR3, 7, and 9) and in the cytoplasm (RIG-I, MDA-5), respectively. Activation of PRRs leads to association with adaptor proteins such as mitochondrial antiviral signaling (MAVS), myeloid differentiation primary response 88 (MyD88) or TIR domain-containing adaptor-inducing interferon β (TRIF) which induces a signaling cascade to activate transcription factors. Activator protein 1 (AP-1) and NF-κB regulate the expression of a broad range of cytokines, chemokines, immune receptors and more, while interferon regulatory factors (IRF) 3 and 7 induce expression of IFNα and IFNβ. IFNα/β bind to their receptors interferon α/β receptor (IFNAR) 1 and 2. Upon ligand binding, the IFNAR receptor complex activates Tyrosine kinase 2 (TYK2) and Janus kinase 1 (JAK1) which phosphorylate signal transducer and activator of transcription (STAT) 1 and 2. STAT1 and STAT2 dimerize, associate with IRF9 and translocate into the nucleus where the complex induces transcription of interferon stimulated genes (ISGs) (Murphy 2018).

2.1.2 IFN signaling regulation

Some proteins of the IFN signaling pathway are ISGs themselves, such as STAT1 and IRF9. For STAT1, very low levels of IFNs are necessary to induce its production, ensuring macrophage responsiveness in the early stages of infection (Ivashkiv and Donlin 2014). High levels of STAT1 and IRF9 increase IFNAR1/2 signaling, leading to prolonged expression of ISGs and thus the maintenance of the antiviral state. However, unregulated IFN signaling can contribute to autoimmune diseases, so-called interferonopathies, which include Aicardi-Goutières syndrome (AGS) and Pseudo-TORCH syndrome (Lee-Kirsch 2017). Thus, efficient downregulation of IFN signaling is a vital factor for the innate immune system and can be realized at different stages of the signaling cascade. For instance, protein kinase D2 (PKD2) phosphorylates a serine residue on IFNAR1, resulting in its ubiquitination, endocytosis, and subsequent lysosomal degradation (Zheng et al. 2011a;

Zheng et al. 2011b). Similarly, p38 protein kinase mediates ubiquitination and degradation of IFNAR1 (Bhattacharya et al. 2011). Downstream receptor signaling can be interrupted by STAT2-mediated (Arimoto et al. 2017) binding of ubiquitin specific protease (USP) 18 to IFNAR2, effectively blocking the JAK1 binding site and destabilizing the IFNAR complex (Malakhov et al. 2002). Through its function as a deISGylating enzyme (section 2.3.3), USP18 also enables peptidylpropyl isomerase 1 (Pin1) -mediated ubiquitination of IRF3, downregulating IFNβ production (Saitoh et al. 2006). Additionally, JAK1 and TYK2 kinase ability is inhibited by suppressor of cytokine signaling (SOCS), preventing phosphorylation of STAT1/2 and thus their dimerization (Yasukawa et al. 1999; Piganis et al. 2011). Within the nucleus, the E3 ligase ring finger protein (RNF) 2 is able to ubiquitinate a residue within the DNA binding domain of STAT1, which results in the dissociation of the STAT1/2 complex from the DNA, thereby suppressing transcription of ISGs (Liu et al. 2018).

Several viruses have adapted the downregulation of IFN signaling as an immune evasion technique (Fuchs 2013; Xia et al. 2018). For instance, hepatitis C Virus protein NS3 mediates IFNAR internalization and degradation by activating PKD2 (Lu et al. 2008), as does Enterovirus 71 (EV71) protease 2A, albeit in a yet to be determined manner (Lu et al. 2012). Other viral proteins inhibit phosphorylation of JAK1 and TYK2, such as Sendai Virus protein C (Kitagawa et al. 2020) or Japanese Encephalitis Virus (JEV) protein NS5 (Lin et al. 2006). Phosphorylation of STAT1 is inhibited by Measles Virus (MeV) V protein (Sanchez-Aparicio et al. 2018), NS4B protein of Dengue Virus (Munoz-Jordan et al. 2005), as well as NS5 of Hepatitis C Virus (HCV) (Kumthip et al. 2012), while E7 of Human Papilloma Virus (HPV) 16 prevents formation of the ISGF3 complex (Antonsson et al. 2006). In this manner, viruses are able to interfere with the expression of a plethora of antiviral ISGs.

2.2 Interferon Stimulated Genes

The expression of over 100 ISGs with an extensive range of anti-pathogenic function is crucial to fight invading pathogens. As part of the IFN signaling cascade, STAT1 is directly involved in the production of other ISGs, such as stimulator of interferon genes (STING) (Sato et al. 1998), MDA5 (Kang et al. 2004), and IRF7 (Sato et al. 1998), which in turn further induce type I IFN production. Aside from the promotion of the innate immune system, ISGs can also have direct antimicrobial actions. For instance, the ISG Cholesterol-25-hydroxylase (CH25H) converts cholesterol to 25-hydroxycholesterol (25HC), a soluble molecule which was shown to directly interfere with enveloped virus entry, i.e., Vesicular Stomatitis Virus (VSV), Herpes Simplex Virus (HSV), and Human Immunodeficiency Virus (HIV), by blocking membrane fusion between virus and cell (Liu et al. 2013). Another family of ISGs are myxovirus-resistance proteins (Mx), large GTPases that play a central role in

the innate immune system. MxA binds and sequesters La Crosse Virus (LACV) nucleocapsid protein, inhibiting viral replication (Kochs et al. 2002). Moreover, MxA has been shown to confer resistance against Influenza A Virus, as well as VSV (Pavlovic et al. 1990), and MeV (Schneider-Schaulies et al. 1994). Other ISGs, such as the plasminogen activator inhibitor-1 (SERPIN E1), virus inhibitory protein, endoplasmic reticulum-associated, IFN-inducible (viperin), as well as tetherin prevent viral particle maturation or their release (Wang et al. 2007; Neil et al. 2008; Dittmann et al. 2015). Additionally, virus protein translation is directly targeted by the protein kinase R (PKR) (Dauber and Wolff 2009) and Interferon Induced Proteins with Tetratricopeptide Repeats (IFITs).

2.2.1 Interferon Induced Proteins with Tetratricopeptide Repeats

The IFIT family encompasses four members in humans (IFIT1/2/3/5) and three in mice (IFIT1/2/3) (Ablasser and Hornung 2011). Between species, IFIT proteins have low sequence identity, thus functions of one orthologue do not necessarily apply to the other (Fensterl and Sen 2015). The IFIT family exerts antiviral function against a range of different pathogens, such as Dengue Virus (Hsu et al. 2013), vesicular stomatitis virus (VSV) (Jiang et al. 2016), Sendai Virus (Li et al. 2009), Hepatitis B (Pei et al. 2014) (HBV) and C (Raychoudhuri et al. 2011) Virus, as well as Coxsackievirus B3 (CVB3) (Kimura et al. 2019). IFIT1 was first identified as strongly upregulated in response to IFN treatment of cells (Wathelet et al. 1986) and is characterized best. In addition to IFN stimulation, its expression was found to be induced directly upon infection with VSV, encephalomyocarditis virus and Sendai Virus (Guo et al. 2000). IFIT1 detects foreign RNA in the cytosol, such as cap-0 RNA and 5'-PPP RNA (Habjan et al. 2013; Kimura et al. 2013). By binding to viral cap-0 RNA, IFIT1 prevents the binding of eukaryotic translation initiation factor 4E (eIF4E) thus inhibiting viral translation (Fig. 2, (Kumar et al. 2014)). Furthermore, IFIT1 binds directly to 5'-PPP RNA, sequestering it and thus inhibiting replication of several viruses (Fig. 2 A, (Pichlmair et al. 2011; Abbas et al. 2013; Habjan et al. 2013)). Interestingly, IFIT1 is reported to have an approximately 10-fold higher affinity to cap-0 RNA than to 5'-PPP RNA, resulting in lower reactivity towards Influenza A Virus, LACV, and Ebola Virus, which present with a 5'-PPP RNA genome (Pinto et al. 2015). Further insight into its mechanism of action was given by structural determination of IFIT1, revealing a positively charged binding tunnel with several hydrophobic extensions, which allows IFIT1 to distinguish between methylated self RNA and unmethylated non-self RNA (Abbas et al. 2017). However, other structural features of mRNAs likely factor into IFIT1-mediated blocking of viral replication, as Parainfluenza virus 5M is still sensitive to IFIT1 despite its 2'O-methylation (Young et al. 2016). IFIT1 is stabilized by interaction with either IFIT2 or IFIT3 (Fig. 2 B), thus enhancing its antiviral properties (Pichlmair et al. 2011; Kumar et al. 2014). Even a heterotrimeric

complex consisting of IFIT1/2/3 has been described (Fleith et al. 2018). Both, IFIT1 and IFIT2 were shown to directly interact with subunit e of eIF3, interfering with translation and protein synthesis (Fig. 2 C, (Terenzi et al. 2006)). Similar to IFIT1, IFIT3 is strongly induced upon RNA virus infection (Liu et al. 2011). In addition to its function of stabilizing IFIT1, IFIT3 ensures type I IFN production by bridging MAVS and TANK Binding Kinase 1 (TBK1), thus promoting TBK1 activation which in turn activates the downstream transcription factor IRF3 (Fig. 2 D, (Liu et al. 2011)).

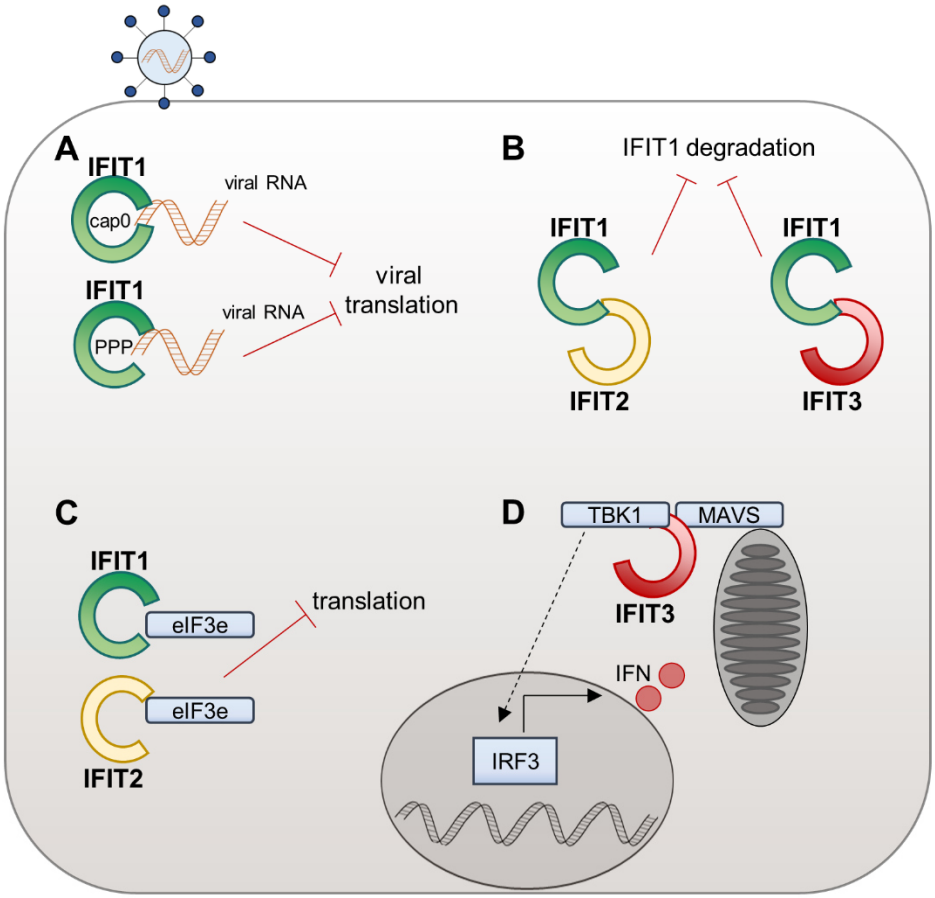

Figure 2: Antiviral activity of IFIT1/3.
IFNα/β signaling induces IFIT expression. **(A)** IFIT1 recognizes and binds viral RNA by its capO or uncapped 5' end, thus blocking viral translation. **(B)** IFIT1 protein levels are stabilized by IFIT2 and IFIT3, thus inhibiting IFIT1 degradation and contributing to its antiviral properties. **(C)** IFIT1 and IFIT2 interact with translation initiation complex subunit eIF3e, thereby inhibiting protein translation. **(D)** IFIT3 bridges TBK1 and MAVS at the mitochondria, facilitating TBK1 activation, leading to IRF3-mediated expression of type I IFNs (Fensterl and Sen 2015).

The importance of IFIT family antiviral action is underlined by specific viral evasion strategies. Herpes Simplex Virus 1 (HSV-1) tegument protein UL41, an endoribonuclease, was shown to degrade IFIT3 mRNA (Jiang et al. 2016), while Hepatitis E Virus (HEV) RNA-dependent RNA polymerase binds and sequesters IFIT1 protein to ensure successful replication (Pingale et al. 2019). Other viruses, such as West Nile Virus, avoid detection by IFIT1 through a virally encoded 2'O-methylation transferase (Szretter et al. 2012).

2.2.2 Oligoadenylate synthases

Another group of interferon-induced antiviral proteins is the oligoadenylate synthase (OAS) enzyme family. In humans, there are 8 – 10 isoforms encoded by three genes (*OAS1*, *OAS2*, *OAS3*) and one *OASL* gene (Chebath et al. 1987). In mice there are 8 *oas1,* one *oas2* and *oas3*, and two *oasl* genes (Silverman 2007). OAS1-3, named according to their number of domains, act as cytosolic dsRNA sensors, differing in the number of catalytic domains (Justesen et al. 2000). Even though most insights into OAS action have been gained by study of OAS1, the mechanistic details of activation appear to be conserved for OAS2 and 3 (Kristiansen et al. 2011). After binding of dsRNA, OAS1/2/3 recruit two Mg^{2+} ions as cofactors and two ATP molecules for production of 2'-5'oligoadenylates (2-5A) (Fig. 3). One ATP molecule acts as donor, the other as acceptor of an AMP moiety for synthesis of 2-5A (Sarkar et al. 1999). 2-5A in turn bind to ribonuclease (RNase) L, triggering its dimerization and a conformational change, ultimately leading to its activation (Kristiansen et al. 2011). RNaseL then cleaves RNA within single stranded regions, i.e., viral ssRNA genomes or viral mRNAs (Wreschner et al. 1981; Silverman et al. 1983; Sadler and Williams 2008). Thus, OAS-mediated RNAseL activation does not only inhibit viral replication, directly targeting viral RNA, but also produces RNA degradation products acting as PAMPs, activating RLR-mediated IFNβ production (Malathi et al. 2007). However, RNaseL cleavage is not limited to viral RNA but targets host mRNA and ribosomal RNA (rRNA) as well (Fig. 3, (Gusho et al. 2020)). In this manner, RNaseL is involved in the induction of autophagy, reducing viral titers in the early stages of Encephalomyocarditis Virus (EMCV) infection (Siddiqui and Malathi 2012).

The largest OAS family member, OAS3, has been shown to have antiviral activity against West Nile virus, Sindbis virus, Influenza virus, or Vaccinia virus (VACV) (Li et al. 2016), Chikungunya virus (Brehin et al. 2009), and Dengue virus (Lin et al. 2009). Moreover, several viruses have developed specific evasion strategies against OAS family members. For instance, Poliovirus contains a distinct RNA structure in the coding sequence of $3C^{Pro}$ which inhibits cleavage by RNaseL (Han et al. 2007). This structure appears to be conserved in other enteroviruses, such several coxsackievirus A types, but not in CVB3 which remains sensitive to RNaseL-mediated degradation, as does hepatitis C virus (Han et al. 2007).

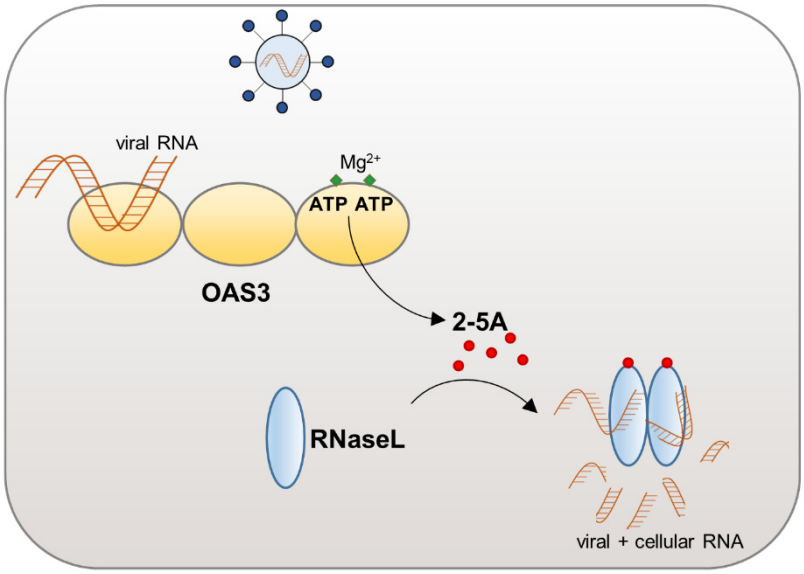

Figure 3: Antiviral activity of OAS3.
IFNα/β signaling induces OAS3 expression. OAS3 consists of three domains. Domain 1 recognizes double-stranded RNA within the cytosol, i.e., viral dsRNA and dsRNA-intermediates. Upon activation, domain 3 recruits ATP to synthesize 2'-5' oligoadenylates (2-5A) while two Mg^{2+} ions serve as cofactors. 2-5A production in turn activates RNase L, which subsequently dimerizes and degrades all cytosolic RNA, thus interfering with viral replication. (Silverman 2007)

2.3 The Interferon Stimulated Gene of 15 kDa (ISG15)

Among the most upregulated ISGs in infection is the Interferon Stimulated Gene of 15 kDa (ISG15) (D'Cunha et al. 1996; Lenschow et al. 2007), its pleiotropic functions ranging from direct influence on virus replication to the regulation of immune cell function and IFN signaling. Its expression is mainly induced by IFN signaling-mediated ISGF3 binding to the ISRE within the ISG15 promoter (Reich et al. 1987), yet can be directly stimulated by PAMP detection (Farrell et al. 1979; Memet et al. 1991), i.e., by bacterial DNA, which leads to ISG15 production in an IRF3-dependent manner (Radoshevich et al. 2015). Moreover, the transcription factor p53 can bind to p53-response elements in the ISG15 promoter, inducing its transcription in response to DNA damage (Park et al. 2016). In humans, mice, and most other mammalian species, the *Isg15* gene spans two exons, the first of which consists only of the ATG start codon. Its transcript is approximately 700 base pairs (bp) in size and translated as an inactive precursor protein of 165 amino acids (aa) in length. C-terminal proteolytic processing by an as of yet unidentified protease reveals a C-terminal LRGG motif by which the active form of ISG15 (156 aa long, 15 kDa in size) can be covalently attached to other proteins (section 2.3.2, (Knight et al. 1988; Potter et al. 1999; Lenschow et al. 2005)). Mature ISG15 consists of two domains connected by a short hinge. Each domain contains four β-sheets and one α-helix and is related to ubiquitin sharing ~30% sequence homology (Haas et al. 1987; Narasimhan et al. 2005). Together with the C-terminal LRGG motif, this homology classifies ISG15 as a ubiquitin-like modifier (UBL) (Haas et al. 1987;

Narasimhan et al. 2005). ISG15 can act in its free form (section 2.3.1) as well as covalently conjugated to proteins of host cellular (section 2.3.2) or pathogenic origins (section 2.3.4 and 2.3.5).

2.3.1 Unconjugated ISG15

A central function of free ISG15 is the regulation of the type I IFN response. ISG15 is able to interact with proteins in a non-covalent manner, altering their stability or function. For instance, by associating with RIG-I, ISG15 enables RIG-I autophagic degradation by Leucine Rich Repeat Containing protein 25 (LRRC25) (Du et al. 2018). In this manner, ISG15 performs negative feedback on the activation of type I IFN production. Moreover, free ISG15 influences the IFN signaling cascade by abrogating the complex-formation of USP18 with S-phase kinase associated protein 2 (SKP2) (Vuillier et al. 2019), thus protecting USP18 from SKP2-mediated ubiquitination and proteasomal degradation (Tokarz et al. 2004). In doing so, ISG15 downregulates ISG expression and prevents type I IFN-induced autoinflammation, as USP18 is a negative regulator of type I IFN signaling (section 2.1.2, (Zhang et al. 2015; Vuillier et al. 2019)). Hence, humans with a hereditary ISG15-deficiency display hyper-responsiveness to type I IFNs resulting in an interferonopathy combined with intracranial calcifications (Zhang et al. 2015; Speer et al. 2016). Of note, this stabilization of USP18 is restricted to human ISG15 and was not observed in mice (Zhang et al. 2015; Speer et al. 2016).

Despite not possessing a distinct secretion sequence, ISG15 was detected extracellularly in the supernatant of type I IFN treated leukocytes (Knight and Cordova 1991) as well as in the serum of patients (D'Cunha et al. 1996). While damaged cells might be leaking ISG15 into the extracellular space, another explanation could be its release through exosomes and microvesicles from macrophages (Hare et al. 2015; Sun et al. 2016b). Correspondingly, ISG15 was found within granulocyte secretory granules, although the mechanism by which ISG15 is located to the granules remains to be elucidated (Bogunovic et al. 2012). Additionally, epithelial cells and lymphocytes were observed to secrete ISG15 (Swaim et al. 2020). Extracellular ISG15 binds to the lymphocyte function-associated antigen-1 (LFA-1) receptor, which is mainly expressed by leucocytes (Swaim et al. 2017). In natural killer (NK) cells that were stimulated by interleukin (IL) -12, binding of ISG15 to LFA-1 resulted in increased secretion of IFNγ (Swaim et al. 2017). Accordingly, ISG15-deficient patients present with lower lymphocytic IFNγ production levels and higher susceptibility to mycobacterial disease (Bogunovic et al. 2012). Furthermore, IL-10 production was induced by stimulation of monocytes with recombinant ISG15 (Dos Santos et al. 2018). However, the effects of ISG15 pro-inflammatory cytokine production, i.e., IL-6, remain contradictory. Intrinsic ISG15 decreased their mRNA expression and secretion in macrophages (Baldanta

et al. 2017; Kespohl et al. 2020) while exposure of macrophages to vesicles containing ISG15 had the opposite effect (Hare et al. 2015). Further studies are needed to elucidate specific effects of ISG15 on macrophages as well as other immune cells.
Aside from its immune-modulatory function, free ISG15 shows antiviral activity as detailed in section 2.3.4.

2.3.2 Conjugated ISG15

In addition to non-covalent association, ISG15 can be covalently attached to lysine residues of proteins in a ubiquitin-like manner (Loeb and Haas 1992). This so-called ISGylation of target proteins is achieved in an E1/E2/E3 enzyme cycle via ISG15's C-terminal LRGG motif. Unlike ubiquitination, in which many different enzymes have been identified, only one E1, two E2, and three E3 enzymes are known to be involved in ISGylation. Ubiquitin-activating enzyme (Ube) 1L, also known as UBA7 (Ubiquitin-like modifier-activating enzyme 7) in humans, activates ISG15 by forming an ATP-dependent thioester bond (Yuan and Krug 2001) (Fig. 4 A, 2.). Subsequently, activated ISG15 is transported to the Ubiquitin/ISG15-conjugating enzyme E2 L6 (Ube2L6) (Kim et al. 2004; Zhao et al. 2004) or UbE2E1 (Takeuchi et al. 2005) (Fig.4 A, 3.), which finally transfers it to the E3 ligase.
While estrogen-responsive finger protein (EFP) (Nakasato et al. 2006; Zou and Zhang 2006) and human homolog of Drosophila ariadne (HHARI) (Okumura et al. 2007) are also known to catalyze ISGylation, they only do so for specific substrates of ISG15, i.e., 14-3-3σ and eIF4E-homologous protein (4EHP). Generally, EFP and HHARI both function as E3 ligases for ubiquitin (Zou and Zhang 2006). Instead, Herc5 and Herc6 are the predominant E3 ligase in humans (Dastur et al. 2006; Takeuchi et al. 2006; Wong et al. 2006) and mice (Versteeg et al. 2010; Ketscher et al. 2012), respectively (Fig.4A, 4.).
Since Herc5 is associated with polyribosomes, ISG15 is mainly thought to modify newly synthesized proteins (Durfee et al. 2010). ISGylation-target proteins can be modified once (mono-ISGylation) or on several lysine residues (multi-ISGylation) (Fig. 4 B). Furthermore, ubiquitin has been found to be ISGylated, resulting in mixed chains (Fig. 4B) and indicating a cross-talk of the ubiquitin and ISG15 systems (Fan et al. 2015). This is supported by the modification of UbcH6, an E2 enzyme involved in ubiquitination. ISGylation of a lysine residue in close spatial proximity to the active center of UbcH6 negatively regulates the conjugating activity of the enzyme (Takeuchi et al. 2005). Yet nothing is known about modifications of ISG15 itself. In contrast to ubiquitination, no poly-ISGylation has been observed (van der Veen and Ploegh 2012; Perng and Lenschow 2018; Dzimianski et al. 2019a), even though a recent study identified modification remnants on ISG15 in a proteomic approach (Zhang et al. 2019). However, the experimental setup did not allow conclusions about whether these remnants stem from ISG15, ubiquitin, or other UBLs.

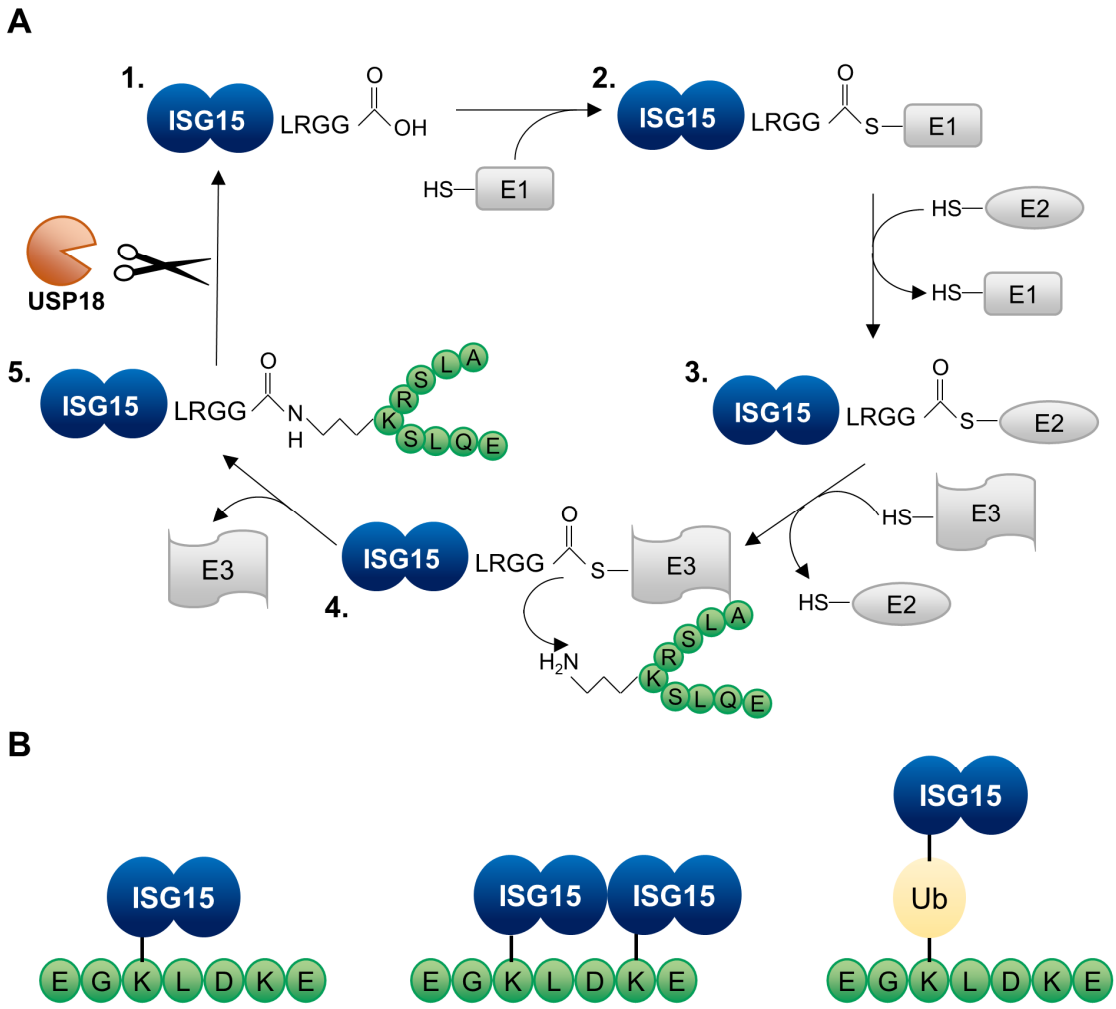

Figure 4: ISGylation cycle.
(A) By its C-terminal LRGG motif, ISG15 is conjugated to K residues of target proteins in an E1/E2/E3 enzyme cycle (1.). E1 (Ube1L) forms a thioester bond with ISG15's C-terminal carboxyl group using ATP (2.). 3. ISG15 is then transferred first to the E2 enzyme (Ube2L6 or UbE2E1), then to the E3 ligase (Herc5, HHARI, EFP) (3.). The E3 ligase transfers ISG15 to the designated K residue on the target protein (4.). ISGylation can be reversed by the deISGylase USP18 (5.) (Dao and Zhang 2005). **(B)** A target protein can be modified once (mono-ISGylation) or on several K residues (multi-ISGylation). Furthermore, a K residue can be modified by a mixed chain consisting of ubiquitin and ISG15 (van der Veen and Ploegh 2012; Fan et al. 2015).

Several studies have identified hundreds of ISG15 target proteins using immunoaffinity chromatography, co-immunoprecipitation, and mass spectrometry analyses of IFN-stimulated cells, as well as human and murine tissue (Giannakopoulos et al. 2005; Zhao et al. 2005; Takeuchi et al. 2006; Wong et al. 2006; Durfee et al. 2010; Radoshevich et al. 2015; Zhang et al. 2019; Yan et al. 2021). Across these studies, no ISGylation motif has become apparent, making it impossible to predict which lysine residue will be covalently modified (Radoshevich et al. 2015; Zhang et al. 2019). Among the identified ISGylation targets are several innate immune proteins and other ISGs, such as IFIT1/2/3, PKR, and RIG-I (Zhao et al. 2005; Wong et al. 2006; Kim et al. 2008; Okumura et al. 2013). Correspondingly, ISGylation plays an important role in the antimicrobial response (Perng

and Lenschow 2018). For instance, ISG15-modification of IRF3 inhibits its polyubiquitination and subsequent degradation, thus stabilizing IRF3-mediated expression of type I IFNs (Shi et al. 2010). The importance of this ISGylation-mediated stabilization is underlined by the severe acute respiratory syndrome (SARS) – coronavirus (CoV) 2 papain-like protease (PLpro), which cleaves ISG15 from IRF3 to downregulate the type I IFN response and promote viral spread (Shin et al. 2020). Nevertheless, ISGylation also negatively regulates the expression of pro-inflammatory cytokines. By modifying tumor necrosis factor (TNF) receptor associated factor 6 (TRAF6), ISG15 inhibits its polyubiquitination and downstream signaling, decreasing NF-kB mediated transcription of pro-inflammatory cytokines (Minakawa et al. 2008). Moreover, ISGylation of RIG-I leads to decreased RIG-I abundance, thus downregulating the type I IFN production (Fig. 5, (Kim et al. 2008)). While the modification of JAK1 and STAT1 has been proposed to increase type I IFN signaling, the exact functional influence of ISG15-conjugation to either protein remains poorly understood (Malakhov et al. 2003; Malakhova et al. 2003).

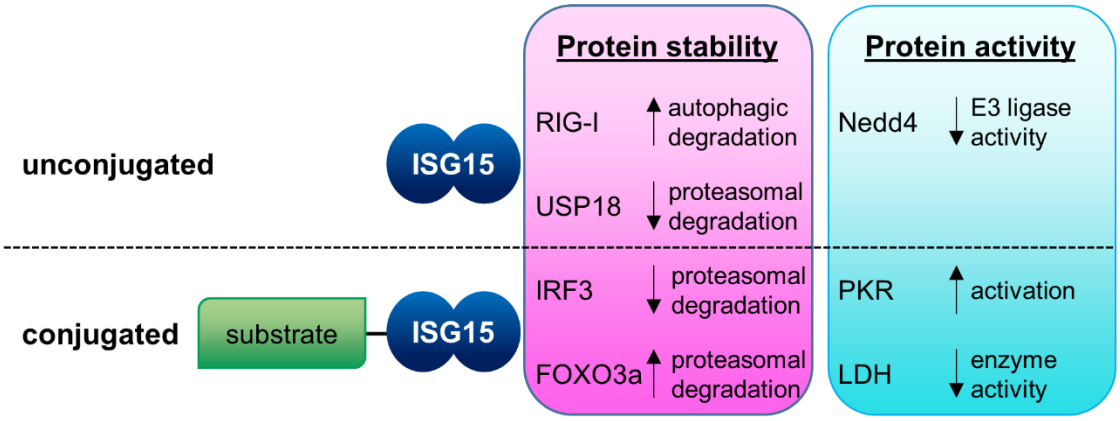

Figure 5: Functional implications of ISG15.
Free and conjugated ISG15 influences the stability and activity of other proteins in various ways. Association with free ISG15 leads to an increased autophagic degradation of RIG-I (Du et al. 2018), while USP18 is protected from proteasomal degradation (Vuillier et al. 2019). Similarly, ISGylation protects IRF3 (Shi et al. 2010) from, yet upregulates FOXO3a's proteasomal degradation (Wang et al. 2019). Free ISG15 negatively regulates Nedd4 E3 ligase activity (Okumura et al. 2008). PKR is activated by ISGylation (Okumura et al. 2013) while LDH activity is impaired upon ISGylation (Yan et al. 2021).

While ISGylation plays a role in autophagy, differing effects have been published. Covalent modification with ISG15 has been reported to block ubiquitination of beclin-1 (BECN1), resulting in the decreased activation of Phosphatidylinositol 3-Kinase Catalytic Subunit Type 3 (PIK3C3) complex and suppressing autophagy (Xu et al. 2015). Additionally, the stability of transcription factor Forkhead Box (FOX) protein of the subgroup O (FOXO3a) was reported to be downregulated by ISGylation, directing FOXO3a for proteasomal degradation FOXO3a (Fig.5, (Wang et al. 2019)). As FOXO3a is involved in the transcription of pro-autophagy genes (Warr et al. 2013), ISG15 might impact the cellular capability to

induce autophagy in this manner. On the other hand, ISGylation of Histone deacetylase 6 (HDAC6), which is involved in autophagic clearance of ubiquitinated proteins, led to increased levels of autophagy (Nakashima et al. 2015). This was further supported by the upregulated autophagic degradation of autophagy adaptor p62/SQSTM in deISGylation-deficient mouse embryonic fibroblasts (MEFs) (Zhang et al. 2019). In a recent study, the *in vivo* ISGylome analysis revealed other autophagic modulators as ISG15 target proteins, such as mammalian target of rapamycin (mTOR), WD repeat domain phosphoinositide-interacting protein 2 (WIPI2), and Ras-related protein RAB7. Here, mTOR ISGylation within the Rapamycin-binding domain was proposed to act as a switch, downregulating its role in metabolism and cellular growth while promoting its autophagic function (Zhang et al. 2019). However, more in-depth studies are needed to elucidate the effect of ISG15 on autophagy.

In the above-mentioned study, several putative ISGylation sites were found within catalytic domains or interfaces for dimerization which could indicate functional implications (Zhang et al. 2019). In fact, the influence of ISGylation on protein activity has been well documented (Fig. 5). For instance, ISGylation of PKR promotes its autophosphorylation and -activation (Okumura et al. 2013). Upon activation, the IFN-induced PKR phosphorylates the α-subunit of eukaryotic initiation factor 2 (eIF2α), downregulating cap-dependent protein translation to restrict viral replication (Meurs et al. 1992). ISGylation-mediated activation of PKR is independent of dsRNA, suggesting that ISG15 mediates protein translation shutdown irrespective of virus infection (Okumura et al. 2013). Another example of ISGylation-induced alteration of protein function is the glycolytic enzyme lactate dehydrogenase (LDH). During obesity-induced inflammation, ISG15 has been shown to downregulate LDH activity, reducing glycolytic levels and suppressing adipocyte thermogenicity (Yan et al. 2021). In this manner, ISGylation promotes diet-induced obesity and glucose intolerance (section 2.3.6).
Taken together, ISGylation is a post-translational modification with multifaceted downstream functions, ranging from activation of proteins to their stabilization, i.e., by protection from or induction of degradation.

2.3.3 The deISGylating enzyme USP18

Even though several deubiquitinases appear to exhibit reactivity towards ISG15, only USP18 is specifically removing ISG15 from proteins in a process called deISGylation (Fig. 4 A, 5., Fig. 6, (Malakhov et al. 2002; Catic et al. 2007; Ye et al. 2011; Basters et al. 2017)). This specificity is conveyed by two ISG15-binding boxes (IBB) within USP18, as revealed by structural analysis (Basters et al. 2017). Accordingly, loss of USP18 or its

deISGylating activity leads to a significant increase in ISGylation *in vivo* (Malakhov et al. 2002; Ketscher et al. 2015).

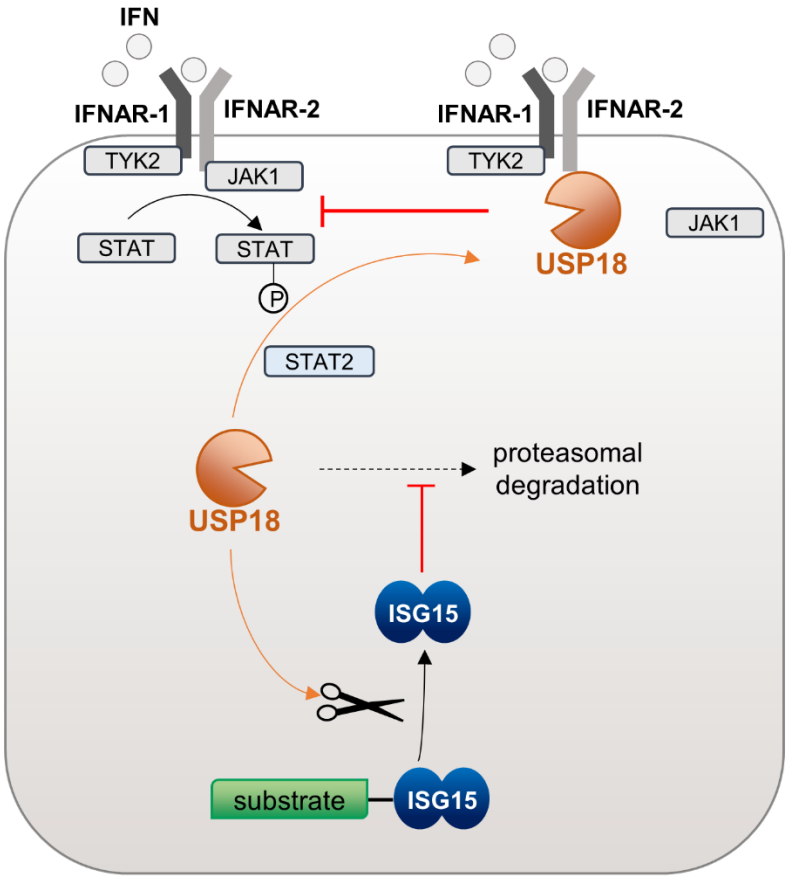

Figure 6: Role of USP18 in IFN signaling and ISGylation.
USP18 expression is induced by type I IFN signaling (Kang et al. 2001). It is recruited by STAT2 (Arimoto et al. 2017)and binds to IFNAR-2 and blocks JAK1 from associating with the IFN receptor complex, thus preventing downstream signaling (Malakhova et al. 2006). Free ISG15 supports this negative regulatory function by inhibiting proteasomal degradation of USP18. Furthermore, USP18 functions as a deISGylase, cleaving the isopeptide bond between an ISGylated substrate and ISG15 (Catic et al. 2007).

However, it is important to consider other cellular functions of USP18 when investigating the effects of impaired deISGylation. Humans with USP18 gene mutations suffer from symptoms such as perinatal onset of intracranial hemmorrhage, calcifications, brain malformations, and liver dysfunction, resulting in death in early infancy at the latest (Meuwissen et al. 2016). While detrimental effects of a lack of USP18 (Ritchie et al. 2002) were initially attributed to a lack of deISGylation (Kim and Zhang 2003), this assumption was revoked when no phenotypic changes in ISG15$^{-/-}$ mice were detected (Osiak et al. 2005) and USP18$^{-/-}$ mice were not rescued by an absence of ISG15 (Knobeloch et al. 2005). Instead, USP18 plays an important role in the negative feedback for IFN signaling (Malakhova et al. 2006). It is recruited to the IFNAR2 subunit by STAT2 (Arimoto et al. 2017) where it competes with JAK1 for binding, thus preventing JAK1 phosphorylation and downstream signaling (Fig. 6, (Malakhova et al. 2006)). Consequently, when USP18 is lost,

IFN signaling and ISG expression become unregulated (section 2.1.2). This negative regulation of the IFN signaling cascade is independent of its deISGylating protease activity, as knock-in mice expressing the catalytically inactive form USP18$^{C61A/C61A}$ showed enhanced ISGylation and concomitantly enhanced antiviral resistance (Ketscher et al. 2015; Kespohl et al. 2020) without the detrimental effects of USP18-deficiency (Ritchie et al. 2002).

2.3.4 ISG15 in viral infection

As detailed in section 2.1, viral infection triggers the innate immune response through RIG-I- and TLR-mediated detection of viral PAMPs. In some instances, ISG expression can be induced in an IFN independent manner via IRF3 (Grandvaux et al. 2002), i.e., during Cytomegalovirus (CMV) infection (Ashley et al. 2019). In viral infection, ISG15 can act in its free or conjugated form (Fig. 7). Extracellular ISG15 has been described to have immune modulatory function in human rhinovirus (HRV) 16 infection (Zaheer et al. 2014). Similarly, in Chikungunya virus infection only ISG15$^{-/-}$ but not Ube1L$^{-/-}$ mice exhibited increased lethality and cytokine production, indicating an inflammation-control mechanism of unconjugated ISG15 (Werneke et al. 2011). In Ebola Virus infection, free intracellular ISG15 inhibits ubiquitination of Ebola virus protein VP40 by interacting with the E3 ligase Neural precursor cell expressed, developmentally down-regulated (Nedd) 4, thus inhibiting the virus budding process (Fig. 5, (Malakhova and Zhang 2008; Okumura et al. 2008)). Concordantly, free ISG15 inhibits human immunodeficiency virus (HIV) -1 virion release by inhibition of Gag protein ubiquitination, which is important for virus assembly and association with Tsg101, a protein of the endosomal sorting complex (ESCRT) -I (Okumura et al. 2006).

In addition to free ISG15, covalent modification with ISG15 also play an important role in the antiviral immune response (Fig. 7). In human CMV infection, ISG15 expression restricted virus growth in an IFN-signaling independent manner (Bianco and Mohr 2017). Instead, ISG15 and ISGylation were induced by cGAS- and STING-mediated dsDNA sensing (Bianco and Mohr 2017). In Sindbis virus infection, the detrimental effect of abolished type I IFN signaling could be compensated by reconstitution of ISG15 (Giannakopoulos et al. 2009). The fact that Ube1L$^{-/-}$ mice also exhibited increased susceptibility to Sindbis virus infection underlines the importance of ISGylation in the antiviral response. This was further substantiated in Influenza A and Sendai Virus infection, where ISG15 did not affect viral replication, but appears to exert its protective role in a conjugation-dependent manner (Morales et al. 2015). Moreover, ISG15$^{-/-}$ mice are more susceptible to Influenza A/WSN/33, Influenza B/Lee/40, and HSV-1 infection (Lenschow et al. 2007). Furthermore, by modification of the ESCRT proteins, ISG15 weakens binding of

the coactivator protein LIP5 and thus interferes with VPS4-mediated HIV-1 retroviral budding from the cell membranes (Pincetic et al. 2010; Kuang et al. 2011). Susceptibility to Sindbis virus infection was counteracted by reconstitution of ISG15, but not by an inconjugable ISG15-LRAA mutant, highlighting the importance of ISGylation in antiviral immunity (Lenschow et al. 2007). In CVB3 infection, ISGylation plays a profound antiviral role as shown by increased viral titers of ISG15$^{-/-}$ and Ube1L$^{-/-}$ mice that also develop a more severe virus-induced myocarditis (Rahnefeld et al. 2014; Kespohl et al. 2020). The ISGylation-mediated inhibition of the CVB3 burden can be further enhanced by accumulating ISGylated proteins through catalytic inactivation of USP18 (Kespohl et al. 2020). These studies highlight ISG15 as an essential antiviral host effector protein in its free as well as conjugated form.

Moreover, ISG15 also interacts directly with virus proteins. In CVB3 infection, covalent modification of the viral 2A protease with ISG15 interferes with cleavage of translation initiation factor eIF4G, preventing the virus from hijacking the host translational machinery for its own reproduction (Rahnefeld et al. 2014). Furthermore, Influenza virus non-structural protein 1 (NS1) (Tang et al. 2010) and nucleoproteins (NP) (Zhao et al. 2016), as well as the capsid protein L1 of Human Papillomavirus (HPV) (Durfee et al. 2010) and human CMV tegument protein pUL26 (Kim et al. 2016) were reported to be ISGylated.

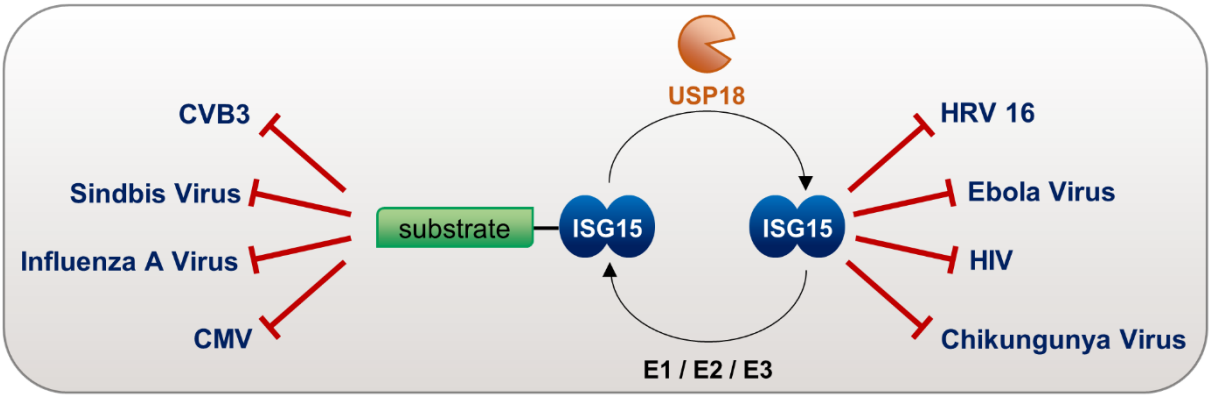

Figure 7: Antiviral activity of free and conjugated ISG15.
ISG15 inhibits viral replication in its free and conjugated form. Free ISG15 displays immune modulatory function against HRV (Zaheer et al. 2014) and Chikungunya Virus (Werneke et al. 2011), while it blocks Ebola and HI Virus budding and assembly by interfering with ubiquitination of viral proteins (Okumura et al. 2006; Malakhova and Zhang 2008; Okumura et al. 2008). ISGylation of both, host and viral proteins is crucial against antiviral activity against Sindbis Virus (Giannakopoulos et al. 2009), Influenza A Virus (Morales et al. 2015), CMV (Bianco and Mohr 2017), as well as CVB3 (Rahnefeld et al. 2014; Kespohl et al. 2020).

As a consequence, several viruses have developed evasion strategies. For instance, NS1 of Influenza B can bind directly to E1 protein UBE1L to inhibit the first step of ISGylation (Yuan and Krug 2001). Furthermore, binding of NS1 to ISG15 results in sequestration of ISGylated proteins, thus facilitating Influenza B evasion of ISGylation-mediated effects

(Zhao et al. 2016). VACV is able to suppress ISGylation through its protein E3, which binds and antagonizes ISG15 (Eduardo-Correia et al. 2014). Proteases with Ovarian Tumor Domains (OTU) have been described to evade the ISGylation mediated antiviral response of their hosts through deISGylating function, such as several proteases of the *Nairoviridae* family (Dzimianski et al. 2019b), Lb^{pro} of Foot and Mouth Disease Virus (FMDV) (Swatek et al. 2018) and most recently also SARS-CoV2 PLpro (Shin et al. 2020). Even though deubiquitination (DUB) and deISGylation activities have been described for SARS-CoV1 (Lindner et al. 2005), as well as middle eastern respiratory syndrome (MERS) -CoV (Mielech et al. 2014), the preferences of their papain-like proteases towards ubiquitin and ISG15 vary. Despite sharing ~83% sequence identity, SARS-CoV1 PLpro predominantly targets ubiquitin chains, while SARS-CoV2 PLpro prefers cleavage of ISG15 (Rut et al. 2020; Shin et al. 2020). Both present effective ways to evade the immune system. For instance, deubiquitination of STING by SARS-CoV1 PLpro interferes with its ability to activate TBK1 and thus downregulates IRF3 transcriptional activity (Sun et al. 2012; Ni et al. 2017). While SARS-CoV2 PLpro downregulates transcription of antiviral gene transcription as well, it does so by deISGylating and thus destabilizing IRF3 (section 2.3.2, (Shin et al. 2020). Moreover, SARS-CoV2 PLpro removes ISG15 from MDA5, thus antagonizing MDA5 activation and its downstream induction of the antiviral response (Liu et al. 2021).

2.3.5 ISG15 function in non-viral infectious disease

In addition to its activation during viral infections, ISG15 is also expressed in a response to non-viral pathogens, i.e. in fungal (Dong et al. 2017), parasitic (Napolitano et al. 2018), as well as bacterial infections (Radoshevich et al. 2015; Kimmey et al. 2017). Depending on the specific pathogen, different ISG15 effector functions have been reported. Extracellular ISG15 triggered by *Toxoplasma gondii* infection enhanced interleukin (IL) -1β production by $CD8^+$ DCs (Napolitano et al. 2018), demonstrating its proinflammatory function. Patients with inherited ISG15 deficiency are highly susceptible to mycobacterial disease (Bogunovic et al. 2012), as a lack of leukocyte mediated ISG15 secretion resulted in decreased IFNγ production (Swaim et al. 2017). Additionally, bacterium *Lysteria monocytogenes* infection is counteracted by ISG15, more precisely by ISGylation, induction of which appears to be independent of type I IFN signaling, but rather mediated by STING, TBK1, IRF3, and IRF7, activated by bacterial DNA (Radoshevich et al. 2015). By modification of Endoplasmatic Reticulum (ER) and Golgi proteins, ISG15 might facilitate the release of cytokines important to counteract the infection (Radoshevich et al. 2015). Conflicting reports implicate ISG15 in *Salmonella typhimurium* infection. On the one hand, deISGylating deficient $USP18^{-/-}$ mice showed increased antibacterial activity against *S. typhimurium* (Kim et al. 2005). On the

other hand, a loss-of-function mutation within the *Usp18* gene was described to result in increased susceptibility to *S. typhimurium* (Dauphinee et al. 2014), which was attributed to an ISG15-independent hypersensitivity to IFN (Knobeloch et al. 2005).
Taken together, ISG15 and SGylation represent an integral part of the host immune response, regulating protein stability, activity, and localization as well as directly interacting with pathogenic proteins.

2.4 Coxsackievirus B3 life cycle and pathogenesis

Coxsackievirus B3 (CVB3), of the genus *Enterovirus* and family *Picornaviridae*, is a non-enveloped virus with an icosahedral capsid structure ~30 nm in diameter. Its positive single strand RNA (+ssRNA) genome is approximately 7.5 kb in size and encodes for 11 proteins in one open reading frame (ORF). CVB3 structural proteins consist of VP1 - 4, with VP1 - 3 oriented towards the outside and VP4 towards the inside of the viral capsid. Additionally, CVB3 encodes for two proteases, 2A and 3C, an RNA-dependent RNA polymerase (3D), and three proteins capable of i.e. membrane alteration and virion release: 2B, 2C, and 3A. 2B and 3A assist in the formation of so-called replication organelles by reorganizing the cellular secretory pathway (Hsu et al. 2010). 3B or Vpg functions as a primer for initiation of RNA synthesis by the 3D polymerase. As detailed in section 2.1, it is also used as a 5' UTR cap to protect the genome from degradation (Flanegan et al. 1977). To enter the cells, CVB3 binds to the coxsackievirus and adenovirus receptor (CAR) and its co-receptor decay accelarating factor (DAF) at the cell surface (Fig. 8) (Selinka et al. 2004; Garmaroudi et al. 2015). Nevertheless, virus tropism is usually determined by the expression levels of CAR (Harvala et al. 2005).
Upon binding, the virus-receptor complex is internalized and the viral particle undergoes a conformational change (Milstone et al. 2005): VP4 flips to the outside of the capsid, building a pore to release the viral RNA into the cytoplasm. Within the cell, the host translation machinery translates the viral RNA into one large polyprotein, which subsequently undergoes self-cleavage into the single proteins by the proteases 2A and 3C (Jang et al. 1988). The 3D polymerase then creates a negative strand RNA template, from which the +ssRNA genome is multiplied to be translated and packaged into the virion (Bedard and Semler 2004). Viral proteases 2A and 3C shut off host-translation by cleavage of translation factor eIF4G and PABP (Lloyd et al. 1987).This effectively blocks cap-mediated host translation while ensuring viral translation thorugh the internal ribosomal entry site (IRES) present on the viral genome (Jang et al. 1988; Pelletier et al. 1988). Finally, the newly generated strands of +ssRNA are packed into progeny virions which are released by necrosis-like cell death (van Kuppeveld et al. 1997; Campanella et al. 2004) within 4 – 12 h after infection, as determined in cultured mammalian cells (Althof et al. 2018) (Fig. 8).

Additionally, CVB3 has also been reported to induce autophagosomes (Kemball et al. 2010) to facilitate replication (Wong et al. 2008). To avoid autophagic degradation, the virus inhibits the fusion with the lysosome (Mohamud et al. 2018). Moreover, this has been connected to microvesicle shedding as an alternative path of cell-exit (Robinson et al. 2014).

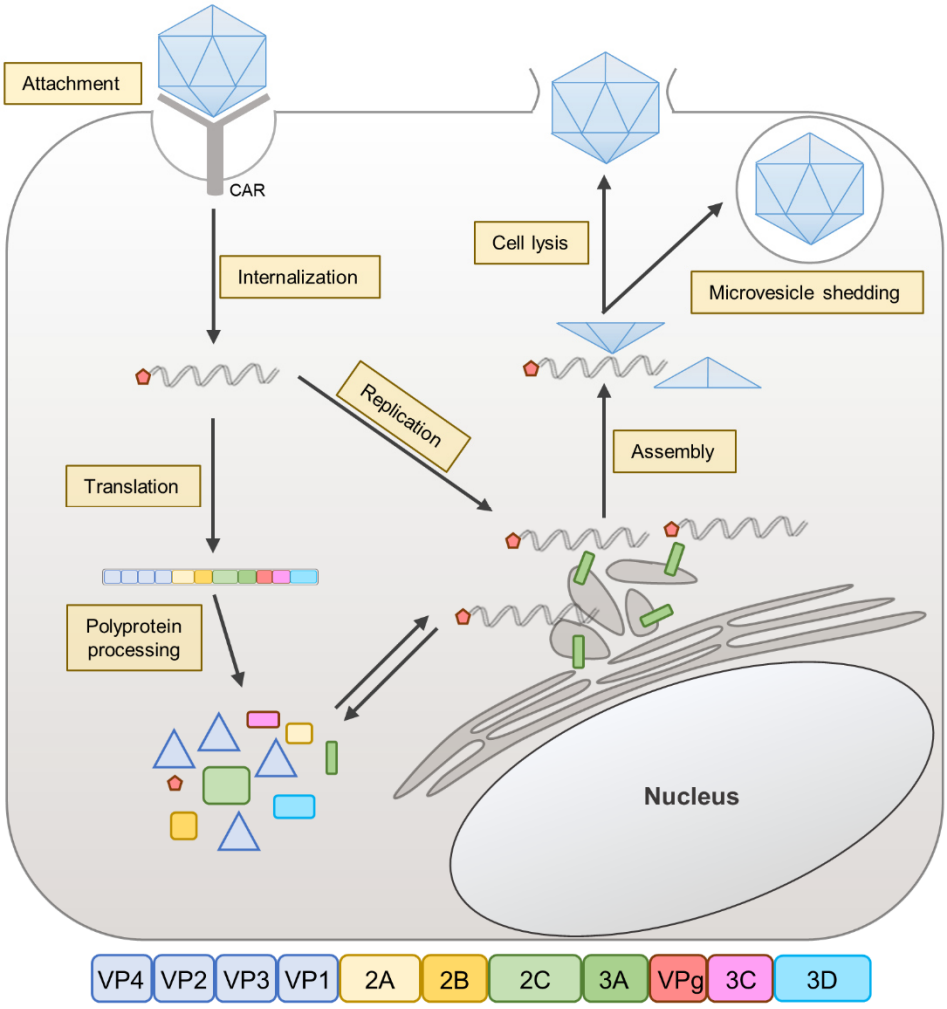

Figure 8: Coxsackievirus B3 replication cycle.
On the cell surface, CVB3 binds to CAR, triggering receptor internalization and the release of the positive sense ssRNA genome into the cytoplasm. Translation of the encoded polyprotein occurs via IRES-mediated binding to the ribosomes. The encoded proteases 2A and 3C cleave out the four structural (VP1-VP4) and seven non-structural (2A, 2B, 2C, 3A, VPg, 3C, and 3D) proteins. At the same time, viral replication organelles are formed at the ER-Golgi membranes. For genome replication, the protein VPg acts as a primer for the 3D polymerase which first synthesizes a negative strand complementary RNA as template for the generation of multiple positive strand genomes. These can either be used for further translation of viral proteins or packaged into a virion together with the structural proteins. The new virus particle is released either by microvesicular shedding or by cell lysis. (Garmaroudi et al. 2015)

Generally, Enteroviruses are transmitted by the fecal-oral route and start their infection cycle in the intestine from where they spread towards polarized and nonpolarized cell types (Coyne et al. 2011). CVB3 is able to infect multiple organs, with cardiac and exocrine pancreatic tissue as the most vulnerable (Cheung et al. 2005). As a lytic virus, CVB3 has

been observed to directly damage cardiac cells (McManus et al. 1993) and many other cell types *in vitro* (Herzum et al. 1994) and *in vivo* (Anderson et al. 1996).

As detailed in section 2.1, the host mobilizes innate immune effectors against CVB3 infection. CVB3 genomic ssRNA and dsRNA replication intermediates are recognized by RIG-I (Francisco et al. 2019) and MDA-5 (Huhn et al. 2010; Wang et al. 2010a) in the cytosol and by TLR3 (Negishi et al. 2008; Sesti-Costa et al. 2017) and TLR7/8 (Triantafilou et al. 2005) in the endosome, inducing transcription of cytokines essential for the antiviral immune response. Heart-specific ablation of type I IFN signaling increased mortality and the development of myocarditis in mice between day 3 and 12 of CVB3 infection (Althof et al. 2014). Correspondingly, an evasion technique of the virus is to target the IFN signaling pathway by cleaving MDA5, MAVS, as well as RIG-I through its proteases 2A and 3C (Feng et al. 2014), underlining the importance of IFN antiviral action. The most abundant ISGs, ISG15 and the IFIT family proteins are thus far the only ones proven to have direct antiviral activity against CVB3 (Szalay et al. 2006; Rahnefeld et al. 2014; Kimura et al. 2019; Kespohl et al. 2020). In the early phase of infection, upregulation of IFIT proteins is required for virus clearance from cardiomyocytes and thus the prevention of CVB3-induced myocarditis (Kimura et al. 2019). Similarly, a lack of ISG15 exacerbated CVB3-induced myocarditis (Rahnefeld et al. 2014) and resulted in increased CVB3 titers in the heart, liver, and spleen (Kespohl et al. 2020).

Together, these studies underline the importance of the type I IFN system and its downstream effectors (Neely et al. 1975) to restrict virus replication and counteract its detrimental sequelae.

2.4.1 CVB3-induced myocarditis

Inflammatory cardiomyopathy, or myocarditis, is described as the inflammation of the heart muscle and is often caused by viral infection. It is estimated to be the cause of around 10% of all unexplained cases of heart failure (Magnani and Dec 2006). The pathophysiological understanding of the course of the disease is mainly derived from mouse models, as it is rarely ever detected at the onset in humans. Adenoviruses as well as enteroviruses are the main causes for viral myocarditis (Why et al. 1994; Maisch 2019), although studies also frequently identified Parvovirus B19 and Human Herpesvirus 6 in endomyocardial biopsy tissue (Mahrholdt et al. 2004; Kuhl et al. 2005; Kindermann et al. 2008; Bock et al. 2010). Most recently, SARS-CoV2 infection was also associated with myocarditis, as evidenced by endomyocardial biopsies of patients (Escher et al. 2020; Wenzel et al. 2020; Bajaj et al. 2021). However, CVB3 is among the few viruses which not only replicate in and lyse human cardiomyocytes (Herzum et al. 1994; Schultheiss et al. 2011) but also induce a similar pathology in mice (Pankuweit and Klingel 2013), making it an ideal model to study the

course of the disease. In the mouse, CVB3 can be detected in several organs within 24 h of infection (Woodruff 1980) with a peak between day 1.5 and day 3 in the liver, pancreas, and spleen (Kespohl et al. 2020), inducing an activation of the innate immune system as determined by increased IFN production (Beling and Kespohl 2018). In the heart tissue, virus replication peaks around 3 days post infection (Kespohl et al. 2020). During this first pathologic phase, which usually passes unnoticed in humans, cardiomyocytes are destroyed through virus-mediated lysis (Dennert et al. 2008). This virus-mediated tissue injury and the resulting infiltration of inflammatory cells into the myocardium leads to the development of acute myocarditis, which manifests around day 8 of infection in mice (McManus et al. 1993). Depending on susceptibility to CVB3, the virus is usually undetectable after day 14 post infection with occasional low-level virus RNA persistence (Flynn et al. 2017). On the other hand, genetically susceptible mouse strains, such as the A.BY/SnJ strain, frequently exhibit higher levels of persistent viral RNA, often associated with chronic myocarditis (Klingel et al. 1992; Jakel et al. 2009).

2.5 Cardiac metabolism

In contrast to the liver, a metabolic hub, which converts glucose into glycogen, produces triacylglycerol (TAG), and provides metabolic substrates for other organs (Rui 2014), the heart is dependent on constant energy production to maintain its contractile functions (Kolwicz et al. 2013). Cardiomyocytes are able to metabolize a variety of substrates supplied by the blood flow, quickly adapting to substrate availability (Neely et al. 1975). Depending on the developmental stage, cardiac ATP production is mainly fuelled by lipid and glucose metabolism (Stanley et al. 2005). The metabolic environment in the fetal heart is considerably different to the adult heart due to a hypoxic nature, resulting in glycolysis as the main energy source (Malandraki-Miller et al. 2018). Shortly after birth, the cardiomyocytes experience a transiently increased cell cycle activity as evidenced by their binucleation, enlargement, and a switch to β-oxidation (Cao et al. 2019). This metabolic switch from glycolysis to β-oxidation is accompanied by an increased number of mitochondria per cardiomyocyte (Ritterhoff and Tian 2017). On average, 60 – 90% of contractile activity in the adult heart is powered by lipid metabolism (Stanley et al. 2005). Lipids in the form of TAG are taken up by fatty acid (FA) translocase FAT/CD36 or by FA binding protein (FABP) (Sharma et al. 2007) and esterified to CoA in the cytoplasm, in order to be transported across the mitochondrial membrane by the carnitine-palmitoyl transferases (CPT) I and II. Sequentially, two carbon atoms are removed from the FA during β-oxidation, a repetitive four-reaction cycle, until the FA chain is completely degraded. During β-oxidation, NADH and $FADH_2$ are generated, which function as electron donors in the mitochondrial respiratory chain. Moreover, Acetyl-CoA is produced and shuttled into the

tricarboxylic acid (TCA) cycle, contributing to further production of NADH and $FADH_2$ (Berg 2012).

Glucose metabolism is responsible for approx. 10 – 40% of cardiac ATP production (Werner et al. 2016). In the heart, glucose is transported across the cell membrane by glucose transporter type 4 (GLUT-4) and 1 (GLUT-1) (Abel 2004). Within the cell, the hexokinase (HK) immediately traps glucose to be used in glycolysis, the pentose phosphate pathway (PPP), hexosamine biosynthesis pathways and glycogen synthesis (Berg 2012). The glycolytic pathway produces two ATP moieties per metabolized glucose molecule, in addition to two NADH used in the respiratory chain. The resulting pyruvate molecules are shuttled into the mitochondria to replenish the TCA cycle.

Furthermore, when substrate supply is low, the heart is also able to metabolize ketone bodies and lactate (Chatham 2002; Werner et al. 2016). Additionally, even though their main degradation site is the liver, amino acids constitute a small but not negligible fraction of energetic fuel for the heart, where especially the branched chain amino acids (BCAA) valine, leucine, and isoleucine are metabolized. BCAA also act as regulators of metabolism and protein degradation, thus emerging as factors of interest in studies on metabolic diseases (Chua et al. 1979; Newgard 2012).

2.5.1 Cardiac metabolic regulation in health

With the heart as the biggest consumer of ATP per gram tissue (Wang et al. 2010b), maintenance of metabolic flux is crucial. Thus, cardiac metabolism experiences constant adaptation through changes in workload, metabolic substrate availability, nutrients, as well as hormones to meet the energy needs of the body. One of the main groups of metabolic regulatory proteins are the transcription factor Peroxisome proliferator-activated receptors (PPAR), i.e., PPARα, as well as the transcriptional coactivators PPAR-gamma coactivator (PGC)-1α and PGC-1β (Pyper et al. 2010). PPARα, itself activated by long chain FAs, regulates gene expression for FA oxidation, while PGC-1α and PGC-1β are also responsible for increasing mitochondrial biogenesis and gene expression for oxidative phosphorylation (Georgiadi et al. 2012; Felker and Mann 2020). In this manner, PPARs adjust the utilization of nutrients within the heart. Furthermore, the energy sensor AMP activated protein kinase (AMPK) regulates cardiac metabolism by monitoring the ATP/AMP ratio within the cell. Low ATP abundance leads to an increase in FA and glucose uptake by AMPK-mediated translocation of CD36 and GLUT-4 to the cell membrane (Feng et al. 2018; Felker and Mann 2020). AMPK activation further downregulates anaplerotic pathways, such as FA synthesis.

Hormones constitute another cause for metabolic adjustments. During development, thyroid hormones (TH) play an important role in cardiac remodeling, acting as critical factors for

maturation and adaptation of the heart (Graham and Huang 2021). For instance, TH are implicated in mitochondrial maturation by modulating posttranscriptional control of PGC-1 (McClure et al. 2005). An example of more direct metabolic influence is the hormone insulin, which increases glucose and FA import and thus metabolization by upregulating GLUT-4 expression and CD36 translocation to the membrane (Bertrand et al. 2008).

Moreover, the abundance of metabolic intermediates acts as negative feedback on the different pathways, i.e., glucose-6-phosphate inhibits HK and high abundance of ATP inhibits glycolytic phosphofructokinase (PFK) activity (Berg 2012). Similarly, glucose-6-phosphate can induce mTOR-mediated cardiac growth in a load-dependent manner (Sen et al. 2013).

Another control mechanism to maintain overall cellular homeostasis and cardiac health is autophagy, leading to the degradation of enzymes (Ronnebaum et al. 2014; Russell et al. 2014), and clearing reactive oxygen species (ROS) (Kubli and Gustafsson 2014). Even though high ROS concentrations lead to oxidative stress, low levels can regulate kinase-driven pathways and act as redox signaling molecules (Nickel et al. 2014; Sag et al. 2014; Reczek and Chandel 2015). In addition to autophagy, enzyme turnover is also realized by the ubiquitin-proteasome system (UPS) (Portbury et al. 2012). While K48-linked polyubiquitination of a protein results in proteasomal degradation and K63-linked ubiquitin chains alter substrate activity as well as being a signal for degradation, monoubiquitination can control protein translocation (Ikeda and Dikic 2008). For instance, the C terminus of HSC70-interacting protein (CHIP) has been shown to polyubiquitinate liver kinase B1 (LKB1), which is directly responsible for phosphorylation and activation of AMPK (Schisler et al. 2013). In this manner, the UPS is involved the fine-tuning of stress-induced activation of AMPK. Moreover, the ubiquitin ligase muscle ring finger-1 (MuRF1) was shown to attach one ubiquitin moiety to PPARα, targeting it for nuclear export and inhibiting PPARα-mediated transcription of FA oxidation genes (Rodriguez et al. 2015).

In summary, the control and maintenance of cardiac metabolism is carried out by an intricate interplay of intracellular sensors, metabolic intermediates, posttranslational modifications, and hormones, which constantly adjust the metabolic flux.

2.5.2 Cardiac metabolic regulation in disease

Cardiovascular disease (CVD) is the leading cause of death worldwide. As the adult mammalian heart has lost its regenerative capacities, it is incapable to replenish myocardial tissue and thus especially vulnerable (Laflamme and Murry 2011). Tissue-damage and subsequent weakening of the heart muscle can lead to extensive remodeling of the myocardium. CVD is caused by a variety of factors, such as diet-induced high blood pressure, congenital conditions, diabetes, or viral infections (Bansal 2020; Fuchs and

Whelton 2020). A prevalent and well-described CVD is myocardial ischemia resulting from hypotension, blockage of the coronary artery, and/or myocardial infarction (Faxon et al. 2004). It is defined by decreased blood flow causing decreased oxygen and metabolic substrate delivery to the heart muscle (Brown et al. 2016). Consequently, ischemic tissue is forced to undergo a variety of metabolic changes to maintain energy production for efficient contractility. Paradoxically, restoring normal blood flow to the tissue often causes further injury (Rodriguez et al. 2006), called ischemia/reperfusion (I/R) injury. The reduced oxygen levels during ischemia force the heart to switch from FA and glucose oxidation towards anaerobic glycolysis for energy production (Das et al. 1987). This leads to production of lactate and subsequently intracellular acidification, which in turn leads to increased calcium levels and eventual cell death (Kalogeris et al. 2012). Another cause of I/R injury is the restoration of normal oxygen levels, which induces oxidative stress and leads to ROS-mediated cellular damage (Yellon and Hausenloy 2007). ROS production, as well as proinflammatory cytokines induce ER stress, leading to activation of the unfolded protein response (UPR) (Minamino et al. 2010). Most components of the UPR pathway have been beneficial in protecting cardiomyocytes from I/R injury (Martindale et al. 2006; Belmont et al. 2010; Toko et al. 2010) and treatment with AMPK was protective against hypoxic injury by inhibiting ER stress (Terai et al. 2005).

Accordingly, the influence of ischemia on metabolic regulators has been studied extensively. For instance, GLUT1 and GLUT4 play a role in regulating the switch to glucose in heart failure, as their translocation to the membrane is induced by ischemia (Young et al. 1997; Shao and Tian 2015). Transgenic mice expressing insulin-independent GLUT1 were protected from aging-associated susceptibility to ischemic injury (Luptak et al. 2007) and GLUT1 overexpression in neonatal mice was shown to enhance cardiac regeneration (Fajardo et al. 2021). Moreover, hexokinase 2 (HK2) association with the mitochondria increases to ensure efficient glucose oxidation (Southworth et al. 2007). Therefore, HK2 overexpression decreased cardiac hypertrophy in mice (Southworth et al. 2007). Additionally, phosphofructokinase (PFK)-2 overexpression enhanced mouse cardiomyocyte contractility in hypoxic conditions but had no effect on I/R injury *in vivo*, suggesting a potential beneficial impact during acute hypoxia without influencing chronic damages (Wang et al. 2008).

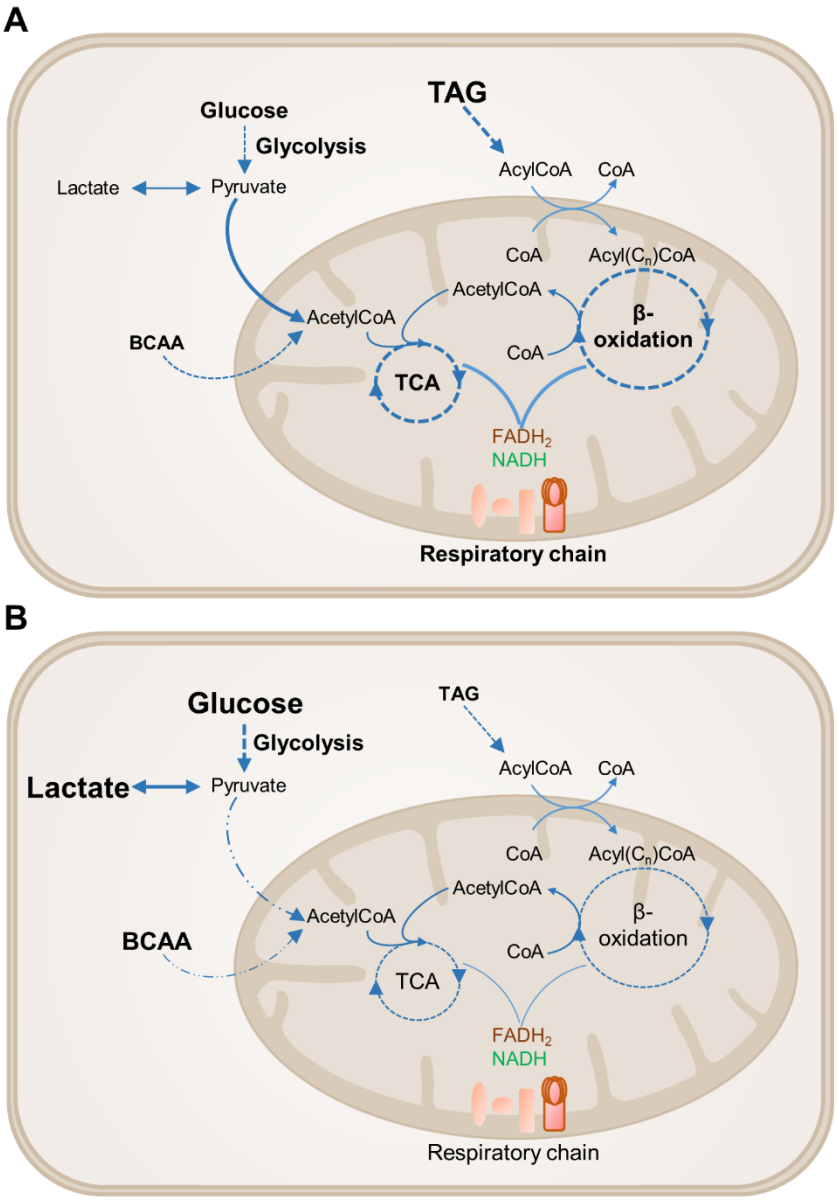

Figure 9: Cardiac metabolism in health and disease.
(A) Within the healthy heart, energy production relies mainly on fatty acid (FA) catabolism. FAs enter the cell as triacylglycerides (TAG). Within the cytoplasm they are esterified to CoA and transported across the mitochondrial membrane where they are degraded in the β-oxidation cycle. The resulting AcetylCoA is shuttled to the tricarboxylic acid (TCA) cycle. The second most important metabolite is glucose, which is metabolized to pyruvate in glycolysis. Pyruvate is shuttled into the mitochondria and metabolized to AcetylCoA and enters the TCA cycle. $FADH_2$ and NADH produced in β-oxidation and TCA cycle are used in mitochondrial respiratory chain to fuel the production of ATP. **(B)** During cardiovascular disease (CVD), the cells experience a metabolic shift. FA catabolism is downregulated in favor of glycolysis. Pyruvate is metabolized to lactate instead of AcetylCoA. Genes involved in β-oxidation and branched chain amino acid (BCAA) catabolism are downregulated, resulting in decreased TCA cycle activity. Subsequently, ATP production by the respiratory chain is downregulated as well. (Schwarzer and Doenst 2016)

The switch from FA oxidation to glycolysis is further accompanied by a reduction in PPARα and subsequently CPTI expression levels (Dewald et al. 2005). While this might be a way to prevent lipotoxicity in ischemia, the role of PPARα remains contradictory. One study showed that PPARα agonist treatment did not improve cardiac function following I/R injury

(Dewald et al. 2005). However, another study reported that PPARα-deficient mice presented with increased infarct size (Yue et al. 2003) and observed an improvement of contractile dysfunction together with reduced infarct size following PPARα agonist treatment (Yue et al. 2003). Moreover, PPARα activation improved the early stage of heart failure in an aortic constriction pressure-overload heart failure model (Kaimoto et al. 2017). Thus, further investigation regarding the PPARα-mediated FA metabolism in cardiac I/R injury is necessary to elucidate the therapeutic potential of PPARα in CVD.

Additionally, humans and mice with cardiomyopathy presented with a downregulation of genes involved in BCAA catabolism, resulting in BCAA accumulation and subsequent BCAA-mediated suppression of mitochondrial respiration (Sun et al. 2016a). Deletion of the mitochondrial branched-chain aminotransferase (BCATm) also resulted in the accumulation of BCAA and in turn increased mechanistic target of rapamycin complex 1 (mTORC1) activation followed by cardiac hypertrophy (Neishabouri et al. 2015). Specifically, leucine accumulation was shown to regulate mTORC1 signaling and was thus able to alter autophagic processes in cardiomyocytes (Meijer et al. 2015).

2.5.3 Metabolism in CVB3 infection

As described for ischemia, a switch from β-oxidation to glucose and lactate as the main energy supply was proposed to be a factor in hypertrophic cardiomyopathy (Yanagawa et al. 2003). Concordantly, human dilated cardiomyocytes exhibit a downregulation of enzymes involved in oxidative phosphorylation and FA β-oxidation (Yanagawa et al. 2003). Similarly, viral cardiomyopathy induces metabolic changes in the myocardium. In accordance with the metabolic switch towards glycolysis, a microarray analysis of CVB3 infected murine heart tissue revealed a downregulation of genes related to fatty acid metabolism and oxidative phosphorylation (Xu et al. 2011).

Moreover, reduced mRNA levels of PPARα, PGC-1α, and PGC-1β were observed in CVB3 induced myocarditis along with increased activation of AMPK (Remels et al. 2018), which could be an indicator for the switch to glycolysis as primary energy source. This was further supported by a downregulation of respiratory chain complex activity in viral myocarditis. Indeed, a prominent dysregulation of cardiac energy metabolism genes became apparent as transcriptome analysis from both, patient biopsies and murine hearts revealed a downregulation of several metabolic genes related to glycolysis, β-oxidation, the tricarboxylic acid cycle, and the electron transport chain (Remels et al. 2018).

This was confirmed by another study which showed that reduced CVB3 susceptibility of C57Bl/6 mice correlated with increased oxidative stress, active apoptosis, and elevated CI and CIII activity of the respiratory chain (Ebermann et al. 2012), indicating that the

maintenance of mitochondrial respiratory function plays a protective role in the development of viral myocarditis.

Moreover, blood glucose, triglyceride (TG), and free fatty acid concentrations were significantly lower in CVB3 infected mice than in uninfected controls, accompanied by a reduction in hepatic glycogen storage (Kespohl et al. 2020). This could indicate an infection-induced increased energy demand, leading to hypoglycemia and malnutrition. Correspondingly, CVB3-induced acute myocarditis presented with a downregulation of hepatic metabolic proteins involved in FA oxidation and oxidative phosphorylation and an upregulation of enzymes involved in carbohydrate catabolism (Kespohl et al. 2020).

Taken together, metabolic remodeling appears to be a prevalent factor in the development of CVD, including viral cardiomyopathy.

2.5.4 ISG15 in metabolism

ISG15 and more specifically ISGylation has previously been implicated in the regulation of metabolic function. For instance, several proteins within the mitochondrial inner membrane were found to be ISGylated (Baldanta et al. 2017). As ISGylation is considered a cotranslational process (Durfee et al. 2010), the mitochondrial targets are most likely modified in the cytoplasm and then transported to the mitochondria (Baldanta et al. 2017). Proteomic analysis of bone marrow derived macrophages (BMDM) revealed that loss of ISG15 results in decreased oxidative phosphorylation and mitophagy (Fig. 10, (Baldanta et al. 2017)). This observation was confirmed in pancreatic cancer stem cells, as cells lacking ISG15 displayed a decrease in oxidative phosphorylation in addition to increased mitochondrial dysfunction and impaired mitophagy (Alcala et al. 2020). Thus, one mode of action of ISG15 might be the maintenance of mitochondrial function. Accordingly, treatment with IFN induced oxidative phosphorylation in an ISG15-dependent manner, yet ISG15 had no influence on complex formation of the electron transport chain (ETC), suggesting that the increase in function is conveyed through another mechanism (Baldanta et al. 2017). Increased function of the ETC corresponded with increased viral resistance against VACV infection, indicating that ISG15-mediated antiviral capacity is in part conveyed through its impact on mitochondrial function (Baldanta et al. 2017).

A study of the hepatic ISGylome and ubiquitylome in *L. monocytogenes* infection found a significant enrichment of ISGylated proteins involved in metabolic processes, such as glucose metabolism and lipid oxidation (Zhang et al. 2019). Even though there was evidence that in proteins related to cofactor and coenzyme binding ubiquitin modifications were replaced with ISGylation, metabolic proteins appear to have been specifically targeted by ISG15 (Zhang et al. 2019). Moreover, several enzymes, like glucose-6-phosphate isomerase (GPI) and phosphoglycerate kinase (PGK) 1 were modified at lysine residues

within active sites or dimerization domains, indicating a functional implication of ISGylation in metabolism (Zhang et al. 2019). Additionally, mitochondrial proteins were found to be ISGylated, a subset of which were situated within the inner mitochondrial membrane (Zhang et al. 2019), supporting the previous observation of ISG15's influence on mitochondria (Baldanta et al. 2017). Furthermore, ISGylation within the FKBP/Rapamycin binding domain could implicate ISG15 in the functional regulation of mTOR, downregulating its role in growth and metabolism and directing it towards its autophagic function to help with the clearance of the bacterial pathogen (Zhang et al. 2019).

In CVB3 infection, ISG15 was reported to alter the central liver metabolism, increasing oxidative phosphorylation, and promoting gluconeogenesis (Kespohl et al. 2020). CVB3 infection of HeLa cells induced an increase in glucose consumption and lactate production, which was exacerbated in ISG15ko HeLa cells (Kespohl et al. 2020). Concordantly, ISG15-deficient mice presented with a hypoglycemic state as determined by blood glucose and hepatic glycogen analysis. This was further intensified in CVB3 infection, indicating a role of ISG15 in glucose homeostasis (Fig. 10, (Kespohl et al. 2020)). Analysis of the liver proteome revealed that lack of ISG15 resulted in premature downregulation of metabolic proteins (Kespohl et al. 2020). Furthermore, the finding that $ISG15^{-/-}$ mice were unable to increase their hepatic oxygen consumption in response to infection (Kespohl et al. 2020) is in line with previous observations (Fig. 10, (Baldanta et al. 2017; Alcala et al. 2020)).

A direct inhibitory function of ISGylation on glycolysis was reported in primary adipocytes (Yan et al. 2021) further substantiating a role of ISG15 in metabolic regulation. IRF3-mediated expression of ISG15 and the ISGylation machinery in primary adipocytes led to the covalent modification of most glycolytic enzymes. Concordantly, ISG15-deficiency induced a significant increase in glycolytic flux (Fig. 10, (Yan et al. 2021)), while overexpression led to a decrease in lactate levels, substantiating the hypothesis of a functional influence of ISGylation on glycolytic enzymes (Zhang et al. 2019; Kespohl et al. 2020). Moreover, ISGylation of a lysine residue within its NAD-binding domain inhibited LDH activity (Fig. 10). In this manner, ISG15 inhibits adipocyte thermogenicity and supports IRF3-mediated promotion of obesity and glucose intolerance (Yan et al. 2021).

Together, these studies present compelling evidence for a regulatory function of ISG15 influencing metabolic pathways in virus-, bacteria-, and obesity-induced inflammation.

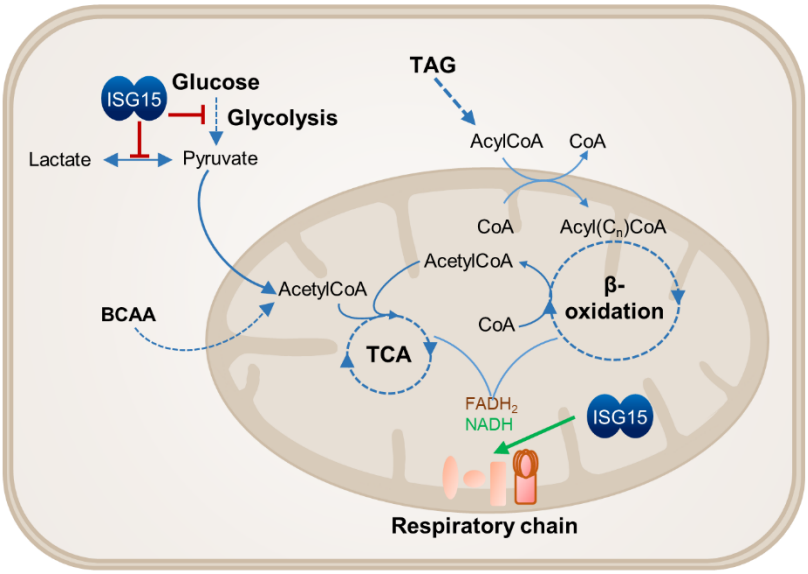

Figure 10: Influence of ISG15 on metabolic pathways.
ISG15 indirectly promotes the activity of mitochondrial respiratory chain. To date, no covalent modification of respiratory chain complexes has been observed. Although ISGylated proteins have been found within the inner mitochondrial membrane, no positive regulatory mechanism has been elucidated (Baldanta et al. 2017; Alcala et al. 2020; Kespohl et al. 2020). In contrast, ISG15 has been shown to downregulate glycolysis in primary adipocytes and is involved in hepatic glucose homeostasis. Furthermore, lactate dehydrogenase (LDH) activity is directly inhibited by ISGylation (Kespohl et al. 2020; Yan et al. 2021).

2.6 Project outline

The importance of the type I IFN response and especially ISGylation against CVB3 infection is well documented (Althof et al. 2014; Rahnefeld et al. 2014; Kespohl et al. 2020). ISGylation has been shown to reduce cardiac virus load, alleviate cardiac tissue inflammation and prevent the onset of chronic myocarditis (Rahnefeld et al. 2014), which is further improved in impaired deISGylation conditions (Kespohl et al. 2020). However, it remains unclear which mechanisms and pathways are influenced by ISG15 and how exactly the protective effect of ISGylation on the myocardium is conferred.

Thus, this project aimed to determine the cardiac ISGylation targets in CVB3 infection *in vivo* at the peak of type I IFN-signaling on day 3 as well as during acute myocarditis on day 8 (Althof et al. 2014; Kespohl et al. 2020). First, the cardiac proteome of wildtype, $ISG15^{-/-}$, and $USP18^{C61A/C61A}$ mice infected with CVB3 was analysed to investigate whether infection leads to altered protein expression in $ISG15^{-/-}$ mice. Additionally, the ISGylome was identified by immunoprecipitation of GG-modified peptides from cardiac lysates with subsequent LC-MS/MS analysis (Zhang et al. 2019). Putative ISGylation targets were validated in an *in vitro* overexpression model and the influence of ISG15 on protein stability and activity was investigated.

With regard to the impact of ISG15 and ISGylation on metabolic processes (Baldanta et al. 2017; Alcala et al. 2020; Yan et al. 2021), namely reprogramming of the central liver metabolism in CVB3 infection (Kespohl et al. 2020), the second aim of this study was to elucidate the influence of ISG15 on cardiac metabolic function in CVB3 infection. To this end, the mitochondrial activity was analysed by (i) Seahorse metabolic measurement in CVB3 infected primary cardiomyocytes and (ii) cardiac tissue, as well as (iii) fluorescent staining of mitochondria with subsequent immunofluorescent and flow cytometric analyses. Furthermore, the influence of ISGylation on individual metabolic enzymes found in the cardiac ISGylome analysis was analyzed *in vitro*.

3 Material

3.1 Chemicals and reagents

Chemical	Manufacturer
2-Chloroacetamide	Sigma Aldrich, St. Louis, MO / USA
2-Propanol	AppliChem, Darmstadt / Germany
3x FLAG peptide	Sigma Aldrich, St. Louis, MO / USA
Acetonitrile	Biosolve BV, Valkenswaard / The Netherlands
Agar	AcroOrganics, Fair Lawn, NJ / USA
Agarose	Serva, Heidelberg / Germany
Agarose, low gelling temperature	Sigma Aldrich, St. Louis, MO / USA
AlbuMAX™ II	Thermo Fisher Scientific, Waltham, MA / USA
Ampicillin	AppliChem, Darmstadt / Germany
Antimycin A from Streptomyces sp.	Sigma Aldrich, St. Louis, MO / USA
APS	AppliChem, Darmstadt / Germany
B-27 Supplements	Thermo Fisher Scientific, Waltham, MA / USA
BSA	AppliChem, Darmstadt / Germany
Carbonylcyanid-4-trifluormethoxyphenylhydrazon (FCCP)	Sigma Aldrich, St. Louis, MO / USA
CHAPS	Thermo Fisher Scientific, Waltham, MA / USA
Chloroforme=Trichlormethane	AppliChem, Darmstadt / Germany
cOmplete, EDTA-free Protease Inhibitor Cocktail	Roche, Basel/Switzerland
Coomassie G250	Sigma Aldrich, St. Louis, MO / USA
Difco™ Agar	Thermo Fisher Scientific, Waltham, MA / USA
Distilled water	Gibco/Life Technologies, Carlsbad, CA / USA
DMEM	Gibco/Life Technologies, Carlsbad, CA / USA
DMEM 5030	Merck Millipore, Billerica, MA / USA
dNTP	Invitrogen/ Life Technologies, Carlsbad, CA / USA
DTT	AppliChem, Darmstadt / Germany
EDTA	Boehringer, Ingelheim / Germany
EGTA	Boehringer, Ingelheim / Germany
Ethanol	Merck Millipore, Billerica, MA / USA
FCS	Sigma Aldrich, St. Louis, MO / USA
Forene	Abbvie, North Chicago, IL / USA
GelRed	VWR, Radnor, PA / USA
Glucose	Thermo Fisher Scientific, Waltham, MA / USA
GlutaMAX	Gibco/Life Technologies, Carlsbad, CA / USA
Glycerol	AppliChem, Darmstadt / Germany

Chemical	Manufacturer
HEPES 2-[-4-hydroxyethyl-1-piperazinyl]-ethanesulfonic acid)	AppliChem, Darmstadt / Germany
KCl	Carl Roth, Karlsruhe / Germany
KH_2PO_4	Carl Roth, Karlsruhe / Germany
$KHCO_3$	AppliChem, Darmstadt / Germany
LB Medium (Powder according to Lennox)	AppliChem, Darmstadt / Germany
LB-Agar	AppliChem, Darmstadt / Germany
MEM	Gibco/Life Technologies, Carlsbad, CA / USA
Methanol	Merck Millipore, Billerica, MA / USA
Milk powder	AppliChem, Darmstadt / Germany
Monensin	Sigma Aldrich, St. Louis, MO / USA
MTT	Sigma Aldrich, St. Louis, MO / USA
Myxothiazol	Thermo Fisher Scientific, Waltham, MA / USA
Na_3VO_4	Thermo Fisher Scientific, Waltham, MA / USA
$Na_4P_2O_7$	Sigma Aldrich, St. Louis, MO / USA
NaCl	AppliChem, Darmstadt / Germany
NaF	Thermo Fisher Scientific, Waltham, MA / USA
$NaHCO_3$	Carl Roth, Karlsruhe / Germany
$NaHPO_4$	Carl Roth, Karlsruhe / Germany
NaOH	Carl Roth, Karlsruhe / Germany
NaPP	Thermo Fisher Scientific, Waltham, MA / USA
NEM	Sigma Aldrich, St. Louis, MO / USA
NH_4Cl	AppliChem, Darmstadt / Germany
Non-Essential Amino Acids	Thermo Fisher Scientific, Waltham, MA / USA
Nonidet P 40	Sigma Aldrich, St. Louis, MO / USA
Oligomycin A	Sigma Aldrich, St. Louis, MO / USA
OptiMEM	Gibco/Life Technologies, Carlsbad, CA / USA
Ortho-phosphoric acid	Carl Roth, Karlsruhe / Germany
PBS	Biochrom, Berlin / Germany
PhenylChloroforme Isoamylalcohol	Carl Roth, Karlsruhe / Germany
Polyethylenimin	Polysciences, Warrington, PA / USA
Ponceau S	AppliChem, Darmstadt / Germany
Puromycin	Merck Millipore, Billerica, MA / USA
RNase inhibitor	Roche, Basel/Switzerland
Rotenone	Sigma Aldrich, St. Louis, MO / USA
Roti®Block	Carl Roth, Karlsruhe / Germany
RotiHistoFix 10%	Carl Roth, Karlsruhe / Germany
Rotiphorese	Carl Roth, Karlsruhe / Germany
SDS	AppliChem, Darmstadt / Germany
Seahorse XF Calibrant Solution	Agilent, Santa Clara, CA / USA
Sodium pyruvate	Gibco/Life Technologies, Carlsbad, CA / USA
Streptomycin/Penciliin	Gibco/Life Technologies, Carlsbad, CA / USA

Chemical	Manufacturer
TEAB buffer	Sigma Aldrich, St. Louis, MO / USA
TEMED	VWR, Radnor, PA / USA
TFA	Biosolve BV, Valkenswaard / The Netherlands
Tris Base	AppliChem, Darmstadt / Germany
Triton X100	AcrosOrganics, Fair Lawn, NJ / USA
Trizol	Ambion/Life Technologies, Carlsbad, CA / USA
Tween 20	AppliChem, Darmstadt / Germany
Urea	AppliChem, Darmstadt / Germany

3.2 Cell culture media

Medium	Composition
2x DMEM Plaque Assay	DMEM 20% (v/v) FCS 2% (v/v) Pen/Strep 7.5% (w/v) NaHCO3 2 mM sodium pyruvate
Eagle Medium	MEM 1% Pen/Strep 27 mM $NaHCO_3$
Eagle Overlay	For 25 ml: 5.7 ml 3.2% Difco™ Agar 17 ml Eagle Medium 2.3 ml FCS
HeLa pBabe-Puro FLAG-His ISG15 medium	MEM 10% (v/v) FCS 1% (v/v) Pen/Strep 1% (v/v) Glutamax
HeLaV medium	MEM 5% (v/v) FCS 1% (v/v) Pen/Strep 1% (v/v) NEAA 2% (v/v) HEPES
Low glucose medium	DMEM low Glucose (1 g/l) 5% FCS 1% Pen/Step 1% 2mM L-Glutamin
PK-15 medium	DMEM high Glucose (4.5 g/l) 5% FCS 1% Pen/Step 1% 2 mM L-Glutamin
Primary cardiomyocyte culture medium	DMEM 10% (v/v) FCS 1% (v/v) Pen/Strep
Seahorse Assay Medium	DMEM 5030 2 mM Glutamin, 10 mM Glukose
Standard cell culture medium	DMEM 10% (v/v) FCS 1% (v/v) Pen/Strep

3.3 Buffers and solutions

Name	Content
Bradford	0.1 mg/ml Coomassie G250 4.75% (v/v) Ethanol 8.5% (v/v) phosphoric acid in H_2O dest.
Cell lysis buffer	20 mM HEPES 8 mM EDTA 2 mM EGTA 1% CHAPS 50 mM NaF 5 mM NaPP 2 mM Na_3VO_4 5 mM NEM 1x cOmplete Protease Inhibitor Cocktail
Crystal violet staining solution	0.2% (w/v) Cristal Violet 20% (v/v) Ethanol In H_2O dest.
DNA loading dye (6x)	50% Glycerin 50 mM EDTA 0.1-0.2% Bromphenol blue 0.1-0.2 % Xylencyanol
Genomic DNA lysis buffer	100 mM Tris 5 mM EDTA 200 mM NaCl 0.2% (w/v) SDS
Genomic DNA lysis buffer USP18	10 mM Tris 10 mM EDTA 150 mM NaCl 0.1% (w/v) SDS
Laemmli buffer (6x)	375 mM Tris (pH 6.8) 12% SDS 0.6 M DTT 60% (v/v) glycerol 0.03% (w/v) Bromophenol blue in H_2O dest.
MTT	5 mg/ml MTT in PBS
PBS	10 mM Na_2HPO_4 1.8 mM KH_2PO_4 2.7 mM KCl 137 mM NaCl in H_2O dest. pH 7.2
Plaque Assay fixation	75% (v/v) Methanol 25% (v/v) Acetic Acid
Ponceau Red	0.1% (w/v) Ponceau S 5% (v/v) Acetic Acid in H_2O dest.
Resolving gel buffer (pH 8.6)	1.5 M Tris 0.4% (w/v) SDS

Name	Content
SDS page running buffer	25 mM Tris Base 192 mM Glycine 1% (w/v) SDS
Semi dry transfer buffer	Anode: 60 mM Tris Base 40 mM CAPS 15% (v/v) Ethanol Cathode: 60 mM Tris Base 40 mM CAPS 0.1% SDS
Stacking gel buffer (pH 6.8)	0.5 M Tris 0.4% (w/v) SDS
TAE buffer (pH 8.3)	1 mM EDTA 0.1% (v/v) Acetic Acid 40 mM Tris in H_2O dest.
Tank blot buffer	25 mM Tris 192 mM Glycin in H_2O dest.
TBS	2 mM Ca_2Cl 2 mM $MgCl_2$ 150 mM NaCl 10 mM Tris in H_2O dest.
Western blot blocking buffer	5% milk powder (w/v) in PBS 1x Roti®Block
Western blot Wash buffer	0.05% (v/v) Tween20 in PBS

3.4 Enzymes

Enzyme	Manufacturer
BamHI	Thermo Fisher Scientific, Waltham, MA / USA
Benzonase Nuclease	Novagen/Merck, Darmstadt / Germany
DNA T4 Ligase	New England Biolabs, Ipswich, MA / USA
DNAseI	Sigma Aldrich, St. Louis, MO / USA
DNAseI	Invitrogen/Life Technologies, Carlsbad, CA / USA
EcoRI	Thermo Fisher Scientific, Waltham, MA / USA
FastAP Thermosensitive Alkaline Phosphatase	Thermo Fisher Scientific, Waltham, MA / USA
Lysyl Endopeptidase ® C	FUJIFILM Wako Pure Chemical Corporation, Japan
M-MLV Reverse transcriptase	Promega, Madison, WI / USA
OneTaq Polyerase	New England Biolabs, Ipswich, MA / USA
PmeI	Thermo Fisher Scientific, Waltham, MA / USA
ProteinaseK	QIAGEN, Venlo / The Netherlands
Q5 High fidelity DNA polymerase	New England Biolabs, Ipswich, MA / USA
Sequencing grade Trypsin, porcine	Promega, Madison, Wisconsin / USA

Enzyme	Manufacturer
SgfI / AsisI	Thermo Fisher Scientific, Waltham, MA / USA
Trypsin/EDTA 0.05%	Gibco/ Life Technologies, Carslbad, CA / USA
Trypsin/EDTA 0.25%	Biochrom, Berlin / Germany
XbaI	Thermo Fisher Scientific, Waltham, MA / USA
XhoI	Thermo Fisher Scientific, Waltham, MA / USA

3.5 Cytokines

Cytokine	Manufacturer
Recombinant human IFN-β	Peprotech, Rocky Hill, NJ / USA
Recombinant murine IFN-β	Sigma Aldrich, St. Louis, MO / USA

3.6 Kits

Kit	Manufacturer
µMACS HA Isolation Kit	Miltenyi Biotec, Bergisch Gladbach / Germany
Hexokinase (HK) Activity Assay Kit	Cell Biolabs, Inc., Kampenhout / Belgium
Lipofectamine RNAiMax	Invitrogen/Life Technologies, Carlsbad, CA / USA
Micro BCA™ Protein Assay	Thermo Fisher Scientific, Waltham, MA / USA
PCR Cleanup Micro Kit	Roche, Basel / Switzerland
Phosphofructokinase (PFK) Activity Assay Kit	PromoCell GmbH, Heidelberg / Germany
Plasmid Maxi Kit	QIAGEN, Venlo / The Netherlands
Plasmid Plus Maxi Kit	QIAGEN, Venlo / The Netherlands
PTMScan® Ubiquitin Remnant Motif (K-ε-GG)	Cell Signaling Technology, Danvers, MA / USA
QIAquick Gel Extraction Kit	QIAGEN, Venlo / The Netherlands
TaqMan Fast Univ. PCR Master Mix (2x)	Thermo Fisher Scientific, Waltham, MA / USA

3.7 Molecular weight markers

Weight marker	Manufacturer
100 bp DNA marker	Rapidozym, Berlin / Germany
1 kb DNA ladder	Carl Roth, Karlsruhe / Germany
PAGERulerPlus	Thermo Fisher Scientific, Waltham, MA / USA

3.8 Antibodies

Antigen	Species/ Clone	Purpose / Dilution	Manufacturer
ANTI-FLAG® M2 Affinity Gel	mouse monoclonal, IgG1, clone: M2	Used for immunoprecipitation	Sigma Aldrich, St. Louis, MO / USA
Anti-GFP (Green Fluorescent	rat monoclonal,	Used for immunoprecipitation	BIOZOL Diagnostica

Antigen	Species/ Clone	Purpose / Dilution	Manufacturer
Protein) mAb-Magnetic Beads	IgG2a kappa, clone: RQ2		Vertrieb GmbH, Eching / Germany
FLAG-Tag	mouse monoclonal, clone: M2	1:10000 in 5% non-fat milk powder solution	Sigma Aldrich, St. Louis, MO / USA
GAPDH	mouse monoclonal, clone: GT239	1:25000 in Roti®-Block	GeneTex, Irvine, CA / USA
GAPDH	rabbit polyclonal	1:25000 in Roti®-Block	St Cruz, Dallas, TX / USA
GFP	rabbit polyclonal	1:2000 in 5% non-fat milk powder solution	Thermo Fisher Scientific, Waltham, MA / USA
Halo-Tag	mouse monoclonal, clone: G9211	1:1000 in Roti®-Block	Promega, Madison, Wisconsin / USA
HA-Tag	mouse monoclonal, clone: HA.C5	1:1000 in 5% non-fat milk powder solution	Abcam, Cambridge, UK
HA-Tag	rabbit polyclonal	1:5000 in 5% non-fat milk powder solution	Abcam, Cambridge, UK
IFIT1	mouse polyclonal	1:1000 in Roti®-Block	Abcam, Cambridge, UK
Ifit1	rabbit polyclonal	1:1000 in Roti®-Block	Abcam, Cambridge, UK
IFIT3	mouse polyclonal	1:1000 in Roti®-Block	Abcam, Cambridge, UK
Ifit3	rabbit polyclonal	1:1000 in Roti®-Block	Abcam, Cambridge, UK
ISG15 (human)	rabbit polyclonal	1:10000 in Roti®-Block	Lab Stock, AG Kloetzel/Beling
ISG15 (murine)	rabbit polyclonal	1:1000 in 5% non-fat milk powder solution	Lab stock Klaus-Peter Knobeloch, Freiburg
OAS3	rabbit polyclonal	1:5000 in Roti®-Block	Atlas antibodies
Oas3	mouse monoclonal, clone: D-7	1:1000 in Roti®-Block	Santa Cruz Biotechnology, Dallas, TX / USA
Pierce™ Anti-HA Magnetic Beads	mouse monoclonal, IgG1, clone: 2-2.2.14	Used for immunoprecipitation	Thermo Fisher Scientific, Waltham, MA / USA
VP1	mouse monoclonal, clone: 31A2	1:2000 in Roti®-Block	Mediagnost, Reutlingen / Germany
VP1	mouse monoclonal, clone: 5-D8/1	1:2000 in 5% non-fat milk powder solution	DAKO / Agilent, Santa Clara, CA / USA
α-Tubulin	mouse monoclonal, clone: GT114	1:400000 in Roti®-Block	GeneTex, Irvine, CA / USA
β-Actin	mouse monoclonal, clone: C4	1:40000	Merck Millipore, Billerica, MA / USA

3.9 Secondary antibodies

Specificity	Fluorochrome	Manufacturer
Goat anti mouse	IRDye® 800CW	LI-COR, Lincoln, NE / USA
Goat anti mouse	IRDye® 680LT	LI-COR, Lincoln, NE / USA
Goat anti rabbit	IRDye® 680LT	LI-COR, Lincoln, NE / USA
Goat anti rabbit	IRDye® 800CW	LI-COR, Lincoln, NE / USA

3.10 Immunofluorescence Dyes

Dye	Manufacturer
MitoTracker® Deep Red FM	Cell Signaling Technology, Danvers, MA / USA
ROTI-Mount Fluoro-Care DAPI	Carl Roth

3.11 DNA Oligos

Primer	direction	5‘ → 3‘ sequence	Application
ISG15 wt	forward	GCCCCCATCCAGAGCCAGTGTT	ISG15$^{-/-}$ genotyping
ISG15 wt/ko	reverse	AGCCCCGATGAGGATGAGGTGT	
ISG15 ko	forward	CGCGAAGGGGCCACCAAAGAA	
UBP43	forward	TCAGAGAGAAGCACGGTGTC	USP18C61A genotyping
	reverse	TCAGAGATCCACCTGCCTTT	
Primer random p(dN)6		ROCHE	cDNA synthesis
Human HPRT	forward	AGTCTGGCTTATATCCAACACTTCG	qRT-PCR Primer
	reverse	GACTTTGCTTTCGGTCAGG	
Murine HPRT	forward	ATCATTATGCCGAGGATTTGGAA	
	reverse	TTGAGCACACAGAGGGCCA	
CVB3	forward	CCCTGAATGCGGCTAATCC	
	reverse	ATTGTCACCATAAGCAGCCA	
HK2 K419R	forward	GCTCTGTCTACAAGAGACATCCCCATTTTGC	Site-directed mutagenesis
	reverse	GCAAAATGGGGATGTCTCTTGTAGACAGAGC	
LDH K59R	forward	GGAAGACAAACTCAGGGGCGAGATGATGG	
	reverse	CCATCATCTCGCCCCTGAGTTTGTCTTCC	
PFK K372R	forward	GATGAAGCCATTAGGCTGAGAGGCCGGAGC	
	reverse	GCTCCGGCCTCTCAGCCTAATGGCTTCATC	
PFK K727R	forward	CAGTAACTGAGCTGAGGGACCAGACAGAC	
	reverse	GTCTGTCTGGTCCCTCAGCTCAGTTACTG	

3.12 qRT-PCR Probes

Target	Sequence 5' → 3'
CVB3	FAM-TGCAGCGGAACCG-MGB
Human HPRT	FAM-TTTCACCAGCAAGCTTGCGACCTTGA-MGB
Murine HPRT	FAM-TGGACAGGACTGAAAGACTTGCTCGAGATG-TAMRA

3.13 Taqman Assays

Target Gene	Assay ID	Manufacturer
IFIT1	Hs00356631_g1	Thermo Fisher Scientific, Waltham, MA / USA
Ifit1	Mm00515153_m1	
IFIT3	Hs00155468_m1	
Ifit3	Mm01704846_s1	
OAS3	Hs00196324_m1	
Oas3	Mm00460944_m1	

3.14 Plasmids

Gene	Species	Vector	Tag + Location	Source / Reference
Aldoa	Mouse	pCMV3	C-term. FLAG	Sinobiological, #MG52539-CF
Ech1	Mouse	pCMV6	C-term. FLAG	Origene, #MR204801
Gapdh	Mouse	pCMV6	C-term. FLAG	Origene, #MR204934
HERC5	Human	pTriEx2	-	(Rahnefeld et al. 2014) Lars Ketscher / Klaus-Peter Knobeloch, University Clinic Freiburg, Freiburg / Germany
Hk2	Mouse	pCMV6	C-term. FLAG	Origene, #MR211170
IFIT1	Human	pcDNA3.1	N-term. 3xFLAG	Addgene #53554
IFIT3	Human	pcDNA3.1	N-term. 3xFLAG	Addgene #53553
ISG15	Mouse	pcDNA3.1	N-term. HA	(Zhang et al. 2019) Lars Ketscher / Klaus-Peter Knobeloch, University Clinic Freiburg, Freiburg / Germany
ISG15	Human	pcDNA3.1	N-term. HA	(Rahnefeld et al. 2014) Nicole Lange/Peter-Michael Kloetzel, Charité – Universitätsmedizin Berlin, Berlin / Germany
Ldha	Mouse	pCMV3	C-term. FLAG	Sinobiological, #MG51207-CF
Mdh1	Mouse	pCMV3	C-term. FLAG	Sinobiological, #MG51330-CF
OAS3	Human	pCMV6	C-term. FLAG	Origene, #RC222722
Pfkm	Mouse	pCMV3	C-term. FLAG	Sinobiological, #MG52541-CF
Pygm	Mouse	pCMV3	C-term. FLAG	Sinobiological, #MG52459-CF
UBE1L	Human	pcDNA3.1	-	(Rahnefeld et al. 2014) Dong Er Zhang, Moores UCSD Cancer Center, University of California,

Gene	Species	Vector	Tag + Location	Source / Reference
				San Diego, La Jolla, California / USA
UbcM8 (Ube2L6)	Mouse	pcDNA3.1	-	(Rahnefeld et al. 2014) Dong Er Zhang, Moores UCSD Cancer Center, University of California, San Diego, La Jolla, California / USA
Xdh	Mouse	pCMV6	C-term. FLAG	Origene, # MR221034
eGFP		pEGFP-C3	C-term. eGFP	Elke Krüger, Charité – Universitätsmedizin Berlin, Berlin / Germany

3.15 Small interfering RNAs

Target	Supplier
ON-TARGET Plus Control Pool	Dharmacon, Lafayette, CO / USA
ON-TARGET Plus SMART Pool Human OAS3	

3.16 Consumables

Consumable	Supplier
500 mm µPAC™ column	PharmaFluidics, Gent / Belgium
BD Vacutainer K2E EDTA	BD Biosciences, Franklin Lakes, NJ / USA
C18 Reprosil-HD column (400 mm), 100 µm I.D., 1.9 µm beads	Dr. Maisch, Ammerbuch-Entringen / Germany
C18 Reprosil-HD pre column (20 mm), 100 µm I.D., 5 µm beads	Dr. Maisch, Ammerbuch-Entringen / Germany
Cell Scraper	Sarstedt, Nümbrecht / Germany
Microvette	Sarstedt, Nümbrecht / Germany
Millex-GP-Filter, 0,22 µm	Merck Millipore, Billerica, MA / USA
Odyssey Nitrocellulose Membranes	LI-COR, Lincoln, NE / USA
Peptide Cleanup C18 Pipette Tips	Agilent, Santa Clara, CA / USA
Seahorse XFe24 FluxPak	Agilent, Santa Clara, CA / USA
Sep-Pak SampliQ C18 Cartridges	Agilent, Santa Clara, CA / USA
Tissue culture flasks	Sarstedt, Nümbrecht / Germany
Vacuette	Greiner Bio One, Kremsmünster, Austria
Well plates / dishes	Sarstedt, Nümbrecht / Germany
Whatman	GE Healthcare, Chicago, IL / USA
Zirconium pellets 2 mm	Carl Roth, Karlsruhe / Germany

3.17 Software

Software	Version	Supplier
DNASTAR Lasergene	15	DNASTAR, Inc., Madison, WI / USA
FlowJo	10.6.1	FlowJo, Ashland, OR / USA
Image Studio Lite	5.2	LI-COR, Lincoln, NE / USA
ImageJ	1.48v	Wayne Rasband (NIH)

Software	Version	Supplier
MaxQuant	1.6.11.0	(Tyanova et al. 2016a) Max-Planck-Institute of Biochemistry
MS Office	2016	Mircosoft, Redmond, WA / USA
NIS Elements Viewer	5.21.00	Nikon Europe B.V. Amsterdam / The Netherlands
Perseus	1.6.1.2	(Tyanova et al. 2016b) Max-Planck-Institute of Biochemistry
Prism	7.0	GraphPad Software, San Diego, CA / USA
StepOne	2.3	Thermo Fisher Scientific, Waltham, MA / USA
Wave	2.6.0	Agilent Technologies

4 Methods

4.1 Animal experiments

4.1.1 Housing & breeding

Mice were maintained in the animal facilities of the Charité FEM under specific-pathogen free conditions and were provided with food and water *ad libitum*. ISG15$^{-/-}$, USP18$^{C61A/C61A}$, and Ube1L$^{-/-}$ mice were originally described elsewhere (Osiak et al. 2005; Kim et al. 2006; Ketscher et al. 2015). All mouse experiments were performed according to the German Animal Protection Act and were approved by the Committee on the Ethics of Animal Experiments of Berlin State authorities (permit numbers: G0272/14, G0070/18, G0119/20, T0032/07). All efforts to minimize suffering were made.

Tab. 1: List of mouse strains

Strain	Genotype	Origin
C57BL/6J	wildtype	Mouse strain maintained at the animal house facility at Charité Universitätsmedizin Berlin
	ISG15$^{-/-}$	Klaus-Peter Knobeloch (Osiak et al. 2005)
	Ube1L$^{-/-}$	Dong-Er Zhang (Kim et al. 2006)
	USP18$^{C61A/wt}$	Klaus-Peter Knobeloch (Ketscher et al. 2015)

4.1.2 Genotyping

Tissue biopsies were resuspended in 500 µl lysis buffer (Section 3.3) supplemented with 100 µg/ml ProteinaseK and digested overnight at 55°C under agitation. Samples were then centrifuged at 17,000 rcf for 10 min, removing all cell debris. Supernatants were isolated and DNA was precipitated by addition of isopropyl alcohol and a 15 min centrifugation at 17,000 rcf. Pellets were washed with 70% ethanol and resuspended in 30 µl of nuclease-free H_2O. Gene disruption was confirmed by PCR using the primer pairs listed in section 3.11.

4.1.3 Virus infection and organ preparation

For infection, 4 – 6 week old male mice received an intraperitoneal injection of $1x10^5$ plaque-forming units (pfu) of Coxsackievirus B3 (Nancy strain: GenBank M33854.1, [https://www.ncbi.nlm.nih.gov/]). Uninfected mice served as control. Mice were anesthetized by isoflurane inhalation and euthanized by an overdose of isoflurane at 0, 3, and 8 days post-infection. Blood was either collected through retro-orbital or cardiac punctuation of anesthetized or euthanized animals, respectively. If heart tissue was used for proteomic analysis, hearts were perfused with 10 ml of PBS, weighed, flash-frozen in

liquid nitrogen and stored at -80°C until further use. For seahorse analysis, the left ventricle of unperfused hearts was removed for small tissue biopsies. All other organs of interest were harvested, washed with PBS, flash-frozen in liquid nitrogen, and stored at -80°C until further use. The right tibia was isolated and remaining muscle tissue digested in PBS with 100 µg/ml ProteinaseK at 55°C overnight under agitation. Subsequently, tibia length was determined using a sliding caliper. Histological analysis was performed by Prof. Dr. Karin Klingel at the Universitätsklinikum Tübingen, Tübingen, Germany in a blinded fashion by evaluating the inflammation score of hematoxylin and eosin (H&E) staining of pancreatic tissue.

4.1.4 Blood sampling

Blood samples were obtained by retro-orbital or cardiac puncture of euthanized mice and collected in Microvette® tubes (Sarstedt) for serum collection. Blood samples were centrifuged at 10,000 rcf for 5 min at room temperature (RT) and the obtained serum was aliquoted and stored at -80°C.

4.2 Proteomics

4.2.1 Proteomic sample preparation & GG-Enrichment

Three mice per genotype and condition ($USP18^{C61A/C61A}$, $USP18^{wt/wt}$, and $ISG15^{-/-}$) were infected as described in section 4.1.3, monitored, and weighed daily. At the indicated time points, animals were sacrificed and whole hearts were collected and flash-frozen in liquid nitrogen. Tissue preparation was described elsewhere (Zhang et al. 2019). Briefly, whole hearts were homogenized in 10 mL lysis buffer containing 8 M urea, 20 mM HEPES pH 8.0 using a Turrex tissue homogenizer and sonicated by three pulses of 10 s at an amplitude of 20%. Debris was removed by centrifugation for 15 min at 15,000 rcf. Protein concentration was determined by Bradford assay and 10 mg of total protein were used for further analysis. Samples were reduced by adding 5 mM dithiothreitol (DTT) and incubated at 55°C for 30 min. Alkylation was achieved by addition of 10 mM Chloroacetamide and incubation for 15 min in the dark. Samples were diluted with 20 mM HEPES pH 8.0 to 4 M urea concentration for endo-Lys C digestion (1/200, w/w) at 37°C for 4 h under agitation. Samples were further diluted with 20 mM HEPES to 2 M urea concentration for overnight Trypsin digestion (1/200, w/w) at 37°C and under agitation. Immunocapture of GG-modified peptides was then performed using the PTMScan® Ubiquitin Remnant Motif (K-ε-GG) Kit (Cell Signaling Technology) according to manufacturer's instructions. Briefly, digests were acidified to 1% TFA and peptides were spun down at 1500 rcf for 15 min at RT to remove undigested proteins. Peptide purification on Sep-Pak C18 cartridges (Waters) was performed prior to a 48 h lyophilization step. Lyophilizate was re-dissolved in 1.4 ml 1x

immunoprecipitation buffer supplied with the kit. An aliquot of 100 µg was taken for shotgun proteomic analysis, while the rest of the samples were used for immunocapture of GG-modified peptides. After elution with 1.5% TFA, the purified GG-modified peptides were dried in a SpeedVac (Eppendorf) and stored at -20°C until LC-MS/MS analysis.

4.2.2 LC-MS/MS of GG-modified peptides

The LC-MS/MS measurements were performed by the ViB Proteomics Core at the VIB-UGent Center for Medical Biotechnology in Ghent, Belgium. The purified peptides were processed as previously described (Zhang et al. 2019). In brief, samples were dissolved in 30 µl loading solvent (0.1% TFA in water/acetonitrile (ACN) (98:2, v/v)) from which 15 µl of samples were injected into an Ultimate 3000 RSLCnano system in-line connected to a Q Exactive HF mass spectrometer (ThermoFisher Scientific). Samples were injected at 10 µl/min for 4 min in loading solvent. Peptides were trapped on a 20 mm pre-column (100 µm internal diameter (I.D.), 5 µm beads C18 Reprosil-HD, Dr. Maisch, Germany) and loaded onto a 400 mm analytical column (made in-house, 75 µm I.D., 1.9 -µm beads C18 Reprosil-HD, Dr. Maisch). Peptides were eluted from the column by a non-linear gradient from 2% to 56% solvent B (0.1% formic acid (FA) in water/acetonitrile (2:8, v/v)) over 120 minutes at a constant flow rate of 250 nl/min, followed by 10 min in 97% solvent B. The column was re-equilibrated with 98% solvent A (0.1% FA in water) for 20 min. The temperature of the column was at a constant 50°C within a column oven (CoControl 3.3.05, Sonation). Operation of the mass spectrometer was in data-dependent mode, switching between MS and MS/MS acquisition for the 16 most abundant ion peaks per MS spectrum in an automated fashion. Acquisition of full-scan MS spectra (375-1,500 m/z) was achieved at a resolution of 60,000 (at 200 m/z) in the orbitrap analyzer after accumulation to a target value of $3x10^6$ for a maximum of 60 ms. Above a threshold of $8{,}3x10^3$, the most intense ions were isolated in the trap with an isolation window of 1.5 Da for maximum 120 ms to a target AGC value of $1x10^5$ and a minimum AGC value $1x10^3$. Precursor ions with either an unassigned charge state, a charge state equal to 1, or a charge state >7 were excluded. Peptide match was set on “preferred” and isotopes were excluded. Dynamic exclusion time was set to 12 s. Fragmentation was performed at a normalized collision energy of 28%. MS/MS spectra (200-2,000 m/z) were acquired at fixed first mass 145 m/z at a resolution of 15,000 (at 200 m/z) in the Orbitrap analyzer. MS/MS spectrum data type was set to profile. The polydimethylcyclosiloxane background ion at 445.12003 was used for internal calibration (lock mass).

4.2.3 LC-MS/MS for shotgun analysis

For the shotgun analysis, ~3µg of peptides in 30 µl loading solvent were injected into an Ultimate 3000 RSLCnano system in-line connected to a Q Exactive HF mass spectrometer (ThermoFisher Scientific). Samples were injected at 10 µl/min for 4 min in loading solvent. Peptides were trapped on a 20 mm pre-column (100 µm internal diameter (I.D.), 5 µm beads, C18 Reprosil-HD, Dr. Maisch, Germany) and on a 500 mm long micro pillar array column (µPAC™, PharmaFluidics) with C18-endcapped functionality. This column consists of 300 µm wide channels that are filled with 5 µm porous-shell pillars at an inter pillar distance of 2.5 µm. With a depth of 20 µm, this column has a cross section equivalent to an 85 µm inner diameter capillary column. Peptide elution and detection on the mass spectrometer was performed as described in section 4.2.2 with the following changes: Acquisition of full-scan MS spectra in the orbitrap analyzer was achieved after accumulation to a target value of $3x10^6$ for a maximum of 60 ms. Above a threshold of $1.3x10^4$, the most intense ions were isolated in the trap with an isolation window of 1.5 Da for maximum 80 ms to a target AGC value of $1x10^5$ and a minimum AGC value $1x10^3$.

4.2.4 Data Analysis of proteomic analysis

Data analysis was performed with MaxQuant (version 1.6.1.0) employing the Andromeda search engine. The default settings included a false discovery rate (FDR) set at 1% on peptide and protein level. To analyze GG-enriched samples and shotgun samples, two different searches were performed. Spectra were interrogated against mouse proteins within the Uniprot/Swiss-Prot database (release version of June 2020 containing 21,982 mouse protein sequences [www.uniprot.org]) and proteins from Coxsackievirus B Nancy strain (GenBank M33854.1, [https://www.ncbi.nlm.nih.gov/]). The mass tolerance was set at 4.5 ppm for precursor ions and at 20 ppm for fragment ions. C-terminal arginine and lysine (trypsin) were set as enzyme specificity, allowing cleavage at arginine/lysine-proline bonds with a maximum of three and two missed cleavages for GG-enriched and shotgun samples, respectively. Cysteine carbamidomethylation was set as a fixed modification. Oxidation of methionine and acetylation of N-termini were set as variable modifications. A minimum score of 30 was set for modified peptides. GG modification of lysine residues was set as an additional variable modification in the GG-enriched samples. Matching between runs was enabled for GG-enriched samples only, with an alignment time window of 20 min and a matching time window of 1 min. In the shotgun samples, only proteins with at least one unique peptide were retained, thus identifying 2926 mouse proteins (Tab. S1). For the GG-enrichment, 668 and 791 potential GG-modification sites were identified for day 3 (Tab. S5) and day 8 (Tab S9) of CVB3 infection, respectively.

Subsequent data analysis was performed with the Perseus software (version 1.6.2.1) (Cox and Mann 2012; Tyanova et al. 2016a; Tyanova et al. 2016b; Rudolph and Cox 2019). GlyGly (K) sites table from MaxQuant was loaded into Perseus. Reverse hits and potential contaminants were removed. The site table was expanded and the site intensities log2 transformed. Normalization was achieved by subtracting the median intensity prior to grouping the samples and removing sites with less than three valid values in at least one group. Missing values were imputed from the normal distribution with intensity values around the detection limit (width 0.3, down shift 1.8). To reveal sites that were significantly regulated, sample groups were defined based on infection (uninfected vs. CVB3 infected) and genotype (USP18$^{wt/wt}$ vs. ISG15$^{-/-}$ vs. USP18$^{C61A/C61A}$), and a two-way ANOVA test was performed to compare the intensities of the sites in the infection group with the genotype group. This test calculates two *p*-values for each site (-log *p*-value) for both, infection and genotype and a third *p*-value for the interaction between infection and genotype. For day 3 and day 8, 118 and 176 GG-modification sites with a *p*-value ≤ 0.05 in at least one of the three comparisons were considered to be significantly regulated (displayed in heatmap in Fig. 18 After non-supervised hierarchical clustering and listed in Tab. S5 and Tab. S9). For the shotgun data, the proteinGroups table from MaxQuant was loaded into Perseus, reverse hits, potential contaminants, and proteins only identified by sites were removed. LFQ intensities were log2 transformed. Samples were grouped into replicates and proteins with less than three valid values per replicate were removed. Samples were further grouped into infection time point (uninfected vs. CVB3 infected day 3 vs. CVB3 infected day 8) and according to genotype. Missing values were imputed from a normal distribution around the detection limit (width 0.3, down shift 1.8). To reveal significantly up- or downregulated proteins between uninfected and CVB3 infected samples, the *t*-test available in Perseus software was used together with False Discovery Rate (FDR) calculation to correct for multiple testing (FDR = 0.05, S_0 = 1) (Tab. S14 and Fig. 13 C). After grouping the samples as described above, significantly regulated proteins were determined by a two-way ANOVA as described above for the GG-sites. 319 proteins with a *p*-value ≤ 0.01 in at least one group were considered to be significantly regulated. The intensities were z-scored and displayed in a heatmap (Fig. 13 D) after non-supervised hierarchical clustering and listed in a table (Tab. S1). The heatmaps of both, GG-enrichment and shotgun analysis, reveal distinct clusters grouping proteins with a similar distribution pattern across all samples. Gene Ontology enrichment analysis was performed using the Gene Ontology consortium bioinformatics resources (www.geneontology.org) (Ashburner et al. 2000; The Gene Ontology 2017; Kramarz and Lovering 2019). The Panther engine was used to determine

the enrichment of GO terms by calculating the fold change enrichment compared to all mouse genes/proteins and the Fisher exact test p-values with their FDR correction.
All mass spectrometry data have been deposited to the ProteomeXchange Consortium via the PRIDE partner repository (data set identifier: PXD032078) under the project name “Proteomics-based identification of ISG15 modification sites in vivo upon Coxsackie virus infection”.

4.3 Cell culture

4.3.1 Cell lines

Cells were handled under sterile conditions and cultured at 37°C and 5% CO_2 in their respective full medium (section 3.2). Serial passaging was achieved by trypsinization as follows. Cellular monolayers were washed with PBS to remove remaining medium and incubated with 0.05% trypsin for 3 – 5 min at 37°C, 5% CO_2 until fully detached from the surface. Full medium was added to stop the reaction. For long-term storage, cells were harvested, centrifuged at 300 rcf for 10 min and resuspended in 500 µl fetal calf serum (FCS) per cryovial. After addition of another 500 µl FCS supplemented with 20% dimethyl sulfoxide (DMSO), cryovials were frozen in a Nalgene® Cryo freezing container at -80°C prior to storage in liquid nitrogen.

4.3.2 Primary cardiomyocytes

Primary cardiomyocytes were isolated and cultured from embryonic mouse hearts at E14 as described previously (Opitz et al. 2011). Briefly, embryonic hearts were isolated under a microscope and incubated in 0.05% trypsin at 4°C overnight. Subsequent to a 15 min incubation at 37°C, cells were dissociated by carefully pipetting up and down in full medium (section 3.2) and seeded at a density of $3x10^5$ cells per 12-well or $4x10^4$ cells per well in a Seahorse 96-well culture plate (Agilent). After three days, medium was changed to Dulbecco’s Modified Eagle’s Medium (DMEM) supplemented with 1% B-27 cocktail and 1% Penicillin/Streptomycin (Pen/Strep). For glycolytic Seahorse measurements, DMEM with low glucose (1 g/l) was used.

4.3.3 Transfection

4.3.3.1 Plasmid transfection

For transient overexpression of a gene of interest, HeLa cells were grown to ~80% confluence. Transfection was performed using polyethylenimine (PEI). A 1 mg/ml stock solution of 25 kDa linear PEI was prepared in nuclease-free H_2O and pH was adjusted to 7.4 using hydrochloric acid (HCL) prior to sterile filtering through a 0.22 µm filter and stored at -80°C. Transfection mixes for 6-well or 10 cm dish format were prepared using 3 µg DNA

in 100 µl and 10 µg DNA in 250 µl 0.9% sodium chloride (NaCl) solution, respectively. A separate PEI solution was prepared in 0.9% NaCl using 2.6 µg PEI per µg DNA. Equal volumes of PEI solution were carefully added to DNA solutions, mixed, and incubated for 15 – 20 min at RT prior to addition to the cells. Medium was changed after ~8 h.
ISGylation target gene expression was induced in HeLa cells by transfection of FLAG-tagged GAPDH, ECH1, HK2, IFIT1, IFIT3, MDH1, LDH A, ALDO A, OAS3, PFKM, PYGM or XDH (section 3.14) using PEI. ISG15 and the ISGylation machinery expression was induced by transfection of HA-tagged mISG15, as well as untagged UBE1L, UbcM8, and HERC5 (section 3.14) using PEI. A subset of the IFIT1 and IFIT3 experiments were performed by Meike Kespohl, Charité Universitätsmedizin Berlin, as indicated in the corresponding figure legends.

4.3.3.2 siRNA transfection

Transient knockdown of OAS3 was achieved by targeting *OAS3* mRNA with complementary small interfering RNA (siRNA), inducing its degradation. HeLa cells were grown to ~70% confluence in a 12-well plate and medium was replaced by 600 µl OptiMEM. 100 nM siRNA and 1 µl RNAiMax (ThermoFisher Scientific) were mixed in OptiMEM and incubated for 10 min at RT. Per 12-well, a final concentration of 25 nM of siRNA was added in 200 µl transfection mix. Cells were incubated for 4 h, after which the transfection mix was replaced by standard medium. For efficient gene silencing, cells were incubated for at least 24 h prior to analysis.

4.4 Biochemical methods

4.4.1 Cell lysis

Cells were scraped in medium and collected in Eppendorf tubes prior to centrifugation at 2,000 rcf for 3 min. Pellets were washed with PBS and resuspended in cell lysis buffer (section 3.3) (30 µl per 12-well, 50 µl per 6-well, 100 – 125 µl per 10 cm dish). For samples only processed for SDS PAGE and western blot, cells were washed with PBS prior to scraping in lysis buffer. Samples were incubated on ice for 20 min prior to centrifugation at 16,000 rcf for 10 min at 4°C. Aliquots were taken for Bradford assay.

4.4.2 Protein assays

4.4.2.1 Bradford Assay

Depending on pellet size and expected concentration, cell lysates were diluted 1:20 or 1:40 in PBS. 5 µl of a serial bovine serum albumin (BSA) dilution (0.1 – 1 µg), a blank (PBS), as well as the samples were plated in 96-well plates in triplicates. 200 µl of Bradford reagent

was added and the optical density (OD) was measured at 595 nm. Samples were prepared at a concentration of 0.5 – 2 µg/µl in 1x Laemmli buffer for SDS PAGE (section 4.4.3) or used for immunoprecipitation (section 4.4.2.3).

4.4.2.2 Micro BCA

Micro BCA™ (Thermo Fisher Scientific) of primary cardiomyocytes and cardiac tissue stances was performed according to manufacturer's instructions. Briefly, cell and tissue samples were homogenized in ddH_2O and 150 µl of 1:3 diluted sample and standard serial BSA dilution were plated in a 96-well plate. 150 µl of Micro bicinchoninic acid assay (BCA) working reagent was added prior to covering and incubating at the plates 37°C for 2 h. OD was measured at 562 nm and sample concentration was calculated based on the standard curve.

4.4.2.3 Immunoprecipitation

HeLa cells were transfected with HA-tagged mISG15 and untagged hUbe1L, UbcM8, hHERC5 and the FLAG-tagged ISGylation target (identified in GG-IP LC-MS/MS or generated in site-directed mutagenesis). Cells were lysed in in cell lysis buffer (section 3.3) and total protein concentration was determined by Bradford assay (section 4.4.2.1). 1 – 2 mg of protein each were used for FLAG- and HA-immunoprecipitation using FLAG-M2 Affinity gel (Merck), µMACS HA isolation kit (Milteny Biotec) or Anti-HA magnetic beads (Pierce) according to manufacturer's instructions. For elution, beads were incubated either with Laemmli buffer for 10 min at RT or with 100 µg/ml 3x FLAG peptide for 15 min at 4°C. Samples were analyzed by SDS-polyacrylamide gel electrophoresis (SDS-PAGE).

4.4.3 SDS PAGE & western blot

Polyacrylamide (PA) gels were prepared according to Tab. 2 and Tab. 3 for electrophoretic separation of proteins, and 10 – 20 µg of protein lysates were loaded onto the gel together with a molecular weight marker. Gels were run at 60 V in the stacking gel.

Tab. 2: pipetting scheme for SDS separating gels

	H2O	**1.5 M Tris-HCl pH 8.6**	**40% (30%) Acrylamide**
8%	7.5 ml (6.6 ml)	3.5 ml	2.8 ml (3.7 ml)
10%	6.8 ml (5.6 ml)	3.5 ml	3.5 ml (4.7 ml)
12%	6.1 ml (4.7 ml)	3.5 ml	4.2 ml (5.6 ml)
15%	5.1 ml (3.4 ml)	3.5 ml	5.3 ml (7.0 ml)
+ 140 µl 10% SDS + 13 µl TEMED + 47 µl 10% APS			

Tab. 3: pipetting scheme for SDS stacking gels

	H_2O	2 M Tris-HCl pH 6.8	40% (30%) Acrylamide
3.8%	4.9 ml (4.7 ml)	375 µl	570 µl (750 µl)
+ 60 µl 10% SDS + 7 µl TEMED + 33 µl 10% APS			

When the dye front reached the separating gel, voltage was increased to 100 – 140 V until the dye front was completely run out of the gel. Western blot analysis was performed according to standard protocols. Briefly, proteins were transferred from the gel onto a nitrocellulose membrane in a sandwich consisting of layers of Whatman paper, nitrocellulose membrane, SDS gel, whatman paper using two blotting techniques as follows. For tank blotting, the blotting cassette was submerged in transfer buffer and proteins were transferred at 100 V for 60 min using a Mini Protean Tetra cell (BIORAD). Smaller proteins were transferred with the semi-dry blotting technique using a Peqlab semi dry blotter for 35 minutes at 12 V. Following the transfer, membranes were stained with Ponceau red staining solution to confirm successful transfer. Membranes were dried prior to removal of excess Ponceau staining and blocking unspecific binding sites on the membrane in either 5% non-fat milk powder or Roti®-Block solution for 30 – 60 min. Membranes were then incubated overnight at 4°C with primary antibody (section 3.8). Subsequently, membranes were washed three times with PBS-T to remove weak antibody binding and incubated for 1 h at RT in secondary antibody (section 3.9). Membranes were washed three times in PBS prior to signal acquisition by an Odyssey® CLx imager (LI-COR® Biosciences).

4.4.4 Enzyme activity assays

Activity assays were performed with kits (see material section 3.6) according to manufacturer's instructions. Activity was measured by Nicotinamide adenine dinucleotide (NADH) generated during enzymatic substrate turnover. Briefly, samples were taken up in assay buffer of the respective kit. Hexokinase FLAG-IP eluates were diluted 1:5 in assay buffer and 10 µl of dilution was used for analysis in a 96-well plate. For the Phosphofructokinase activity assay, 25 µl of FLAG-IP eluates were used. Reaction mix containing assay buffer, substrates, developers, ATP, and enzyme mix was prepared according to manufacturer's instructions, and added to wells prior to kinetic measurement at 37°C for 60 min at 450 nm. A standard curve with set concentrations served as reference to calculate the amount of NADH generated by the enzyme. Enzyme activity was calculated by dividing the amount of generated NADH by the time and the sample volume per well. Values were then multiplied by the dilution factor to yield the activity in nmol/min/ml or mU/ml. As the cotransfection of the enzymes together with ISG15 and the ISGylation

machinery in ISG15ko HeLa cells resulted in varying expression levels of the ISGylated enzymes (as seen on western blot, data not shown) depending on the plasmid combination, signal intensities on the western blot were used to determine the fold change in expression levels, which were then factored into the activity calculations to be able to compare enzyme activities between conditions.

4.4.5 Seahorse metabolic measurement

The mitochondrial oxidative and glycolytic metabolism of primary cardiomyocytes and heart samples was analyzed on an XFe 96-well Extracellular Flux Analyzer (Agilent). Assessment of mitochondrial function was performed by evaluation of basal oxygen consumption and extracellular acidification rate in DMEM-based assay medium supplemented with 2 mM glutamine and 10 mM glucose. For primary cardiomyocytes, assay medium was further supplemented with 3 µg/ml AlbuMAX™ II. For analysis of mitochondrial oxidative phosphorylation, 25 µl of 0.75 µM Oligomycin, 1 µM carbonyl cyanide-p-trifluoromethoxyphenylhydrazone (FCCP), and 0.75 µM Rotenone + 0.75 µM Antimycin A in assay medium without AlbuMAX™ II were sequentially injected into the wells. Oxygen Consumption Rate (OCR) was measured in pmol/min per well. The Extracellular Acidification Rate (ECAR) was measured by changes in mpH/min per well.

For glycolytic analysis, assay medium was prepared without glucose. During measurement, 25 µl of 10 mM Glucose, 0.75 µM Rotenone + 1 µM Myxothiazol, and 1 µM FCCP + 200 mM Monensin in assay medium without AlbuMAX™ II were added sequentially.

Data were normalized to total protein content of each well, as measured by the Micro BCA Protein Assay Kit (Thermo Fisher Scientific). Outliers were determined after analysis by Grubbs' test in GraphPad Prism 7 and excluded. Since cell density directly influences the intracellular flux, measurements from wells with insufficient and too large amounts of protein content can potentially falsify the results. After n = 6 plate measurements, the mean protein content per plate was calculated to be 18.75 ± 6.25 µg/well. Allowing for an additional 20% of the mean protein amount, a range of usable values was set between ≤9 and ≥29 µg per well.

Mitochondrial oxygen consumption was additionally determined *in vivo* in 1 mm murine cardiac biopsies of the left ventricle (see section 4.1.3). Per ventricle, 5 biopsies were taken and added to one well each, prior to being secured by a micro sieve. As tissue does not react to oligomycin treatment, only FCCP, Antimycin A, and Rotenone were used as inhibitors at 5 mM and 2.5 mM concentration, respectively. Protein content of each biopsy was determined by MicroBCA (section 4.4.2.2). Data analysis was performed by Eva Wirth at Charité Universitätsmedizin Berlin.

4.4.6 Immunofluorescence

Mitochondrial membrane potential analysis was performed by immunostaining with MitoTracker® Deep Red (MTDR). Wildtype and ISG15$^{-/-}$ primary cardiomyocytes were seeded onto 13 mm glass coverslips and infected with CVB3 at an MOI of 1 for 8 h or treated with 16 µM FCCP for 4 h prior to staining with 500 nM MTDR for 30 min at 37°C, 5% CO_2. Cells were subsequently fixed and permeabilized with ice-cold methanol for 20 min at -20°C and washed three times with ice-cold PBS for 5 min. Coverslips were mounted onto slides with ROTI-Mount Fluoro-Care DAPI and stored at 4°C. Images were acquired on a Nikon Scanning Confocal A1Rsi+ microscope using a Plan Fluor 40 x oil objective (NA = 1.3) and analyzed with ImageJ. Distributions of MTDR signal density were compared in a quantitative manner by analyzing confocal images in an 8-bit grey scale in ImageJ. A region of interest was defined manually, tracing one cell per image excluding the nucleus and the mean signal intensity was determined. Total intensity was normalized to 10% of the mean intensity and a histogram was created to determine the number of pixels with a particular signal intensity value. The intensity distributions were represented as the percentage of pixels with a certain normalized intensity.

The confocal immunofluorescence images were further analyzed by Niclas Gimber of the Advanced Medical BioImaging Core Facility at Charité Universitätsmedizin Berlin, using an autocorrelation-based image correlation spectroscopy (ICS). Briefly, Otsu's method was used for MTDR signal detection and images were then shifted pixel-wise against each other to achieve autocorrelation. Pearson correlation was calculated and plotted. The python script is custom-written and available as a Jupyter Notebook under https://github.com/ngimber/ImageCorrelationSpectroscopy.

4.4.7 Flow Cytometry

Mitochondrial membrane potential was further analyzed by flow cytometry. Wildtype and ISG15$^{-/-}$ primary cardiomyocytes were infected with CVB3 at an MOI of 1 for 8 h or treated with 16 µM FCCP for 4 h prior to staining with 2 nM MTDR for 30 min at 37°C, 5% CO_2. Cells were subsequently trypsinized, spun down at 200 rcf for 3 min and the pellets were resuspended in PBS supplemented with 2% FCS and 2 mM EDTA. Fluorescence intensity of MTDR was measured by flow cytometry using the FACSCalibur (BD Biosciences) platform. Median fluorescence intensity per condition was calculated using the software FlowJo (10.6.1).

4.5 Molecular biology methods

4.5.1 Polymerase Chain Reaction

The polymerase chain reaction (PCR) was employed for genotyping of transgenic mice, cloning of DNA fragments into expression plasmids, or mutagenesis. While genotyping only requires standard fidelity polymerases (i.e. OneTaq, (NEB Biolabs)), DNA cloning and mutagenesis require high-fidelity polymerases with proofreading activity (i.e. Q5 (NEB Biolabs) or Phusion (Thermo Fisher Scientific)). Specific primer pairs framing the sequence of interest were designed and are listed in section 3.11. Amplification was performed using a PCR thermocycler (Peqlab) with optimized conditions depending on PCR fragment length, primer melting temperature and polymerase.

4.5.2 Plasmid cloning

In order to insert a sequence of interest into an expression plasmid, primers with restriction enzyme site overhangs flanking the sequence were designed. After purification with the PCR Cleanup Micro Kit (Roche), plasmid and insert were digested with the respective FastDigest restriction enzymes (section 3.4) at a concentration of 1-10 units per 1 µg DNA. Purification was achieved by agarose gel separation and excision, followed by cleanup with the QIAquick Gel Extraction Kit (Qiagen). Vector backbone and insert were ligated in 1:3 or 1:5 molar ratio, respectively, using T4 ligase in T4 ligase buffer (NEB Biolabs) for 30-60 min at 37°C. The reaction was terminated with a 10 min incubation at 65°C and 5 µl of ligation product were transformed into competent *Escherichia coli* (*E. coli*) (section 4.5.4). Successful clones were confirmed by sequencing analysis performed by LGC Genomics GmbH.

4.5.3 Site-directed mutagenesis

To mutate a lysine (K) residue within a protein into an arginine (R), a single base pair is changed within the genetic code. The codon for K is either AAA or AAG, while R is encoded for by AGG or AGA. Thus, only the middle amino acid A of the K-codon is required to change into G in order to switch the amino acid to R. Mutagenesis primers containing the A to G exchange were designed for HK2 K419, PFK K327 and K727, and LDH K59 (section 3.11). Phusion polymerase was used for amplification, due to its proofreading ability. PCR mixtures were digested with the restriction enzyme DpnI, which cleaves methylated DNA. Since the plasmids generated by PCR do not contain methylations, only the template DNA was digested, leaving the mutated plasmids intact. 5 µl of DpnI digested PCR product was transformed into *E. coli*. The desired mutations were confirmed by genomic analysis (LGC Genomics GmbH or Eurofins Genomics).

4.5.4 Transformation

DNA constructs were transformed into chemically competent Top 10 bacteria via heat shock. Bacteria were thawed on ice and incubated with 0.5 – 5 µl of DNA for 20 min prior to heat shock for 30 s at 42°C. Subsequently, bacteria were incubated on ice for 2 min and resuspended in 500 µl LB medium. After 1 h of incubation at 37°C, shaking at 800 rpm, bacteria were spread onto LB agar plates containing 100 µg/ml ampicillin or 50 µg/ml kanamycin and grown overnight at 37°C. Single colonies were picked and grown in 3 ml of LB medium containing the appropriate antibiotic for plasmid isolation. The culture was grown overnight at 37°C at 180 rpm. Plasmid DNA isolation is described in section 4.5.5.

4.5.5 DNA preparation

Plasmid DNA isolation from bacteria was performed according to a modified protocol from Qiagen Plasmid Mini Kit. 2 ml of the 3 ml overnight culture were spun down at 17,000 rcf and resuspended in 250 µl Resuspension Buffer P1. 250 µl of Lysis buffer P2 were added and tubes were inverted several times prior to addition of P3 Neutralization Buffer. Cell debris and proteins were spun down for 10 min at 17,000 rcf and DNA was precipitated with 500 µl 2-propanol followed by another 10 min centrifugation step at 17,000 rcf. DNA pellets were washed with 1 ml 70% ethanol and dried prior to resuspension in 25 µl nuclease free H_2O. Large scale plasmid preparations were grown in 150 ml overnight cultures and isolated with the QIAGEN Plasmid Maxi Kit according to manufacturer's instructions.

4.5.6 RNA isolation

Tissue samples were homogenized in 0.5 – 1 ml TRIzol™ reagent using 2.0 mm zirconium pellets in combination with a FastPrep FP120 device (BIO 101 Savant). Cell pellets were resuspended in 250 µl TRIzol™ per 12-well and incubated for 5 min at RT. 200 µl chloroform was added and samples were shaken vigorously for 15 sec prior to incubation for 3 min at RT. Centrifugation of 17,000 rcf separated the liquid into two phases, polar and non-polar, with a protein disc in between. The upper aqueous phase containing the RNA was collected and nucleic acids were precipitated with 2-propanol at a ratio of 500 µl 2-propanol per 1 ml TRIzol™ reagent. Samples were incubated at RT for 30 min or overnight at -20°C and subsequently centrifuged for 15 min at 17,000 rcf / 4°C. Precipitated nucleic acids were washed with 1 ml 70% ethanol, air-dried and resuspended in 30 µl nuclease free H_2O.

4.5.7 cDNA synthesis

RNA (250-1000 ng) in 9 µl nuclease free H_2O was digested with 1 U DNAseI for 15 min at 37°C. Enzyme was deactivated by incubation at 75°C for 5 min. 1 µg random hexamer primers were added and incubated for 10 min at 70°C prior to cDNA synthesis. The RNA-

hexamer mix was supplemented by 200 U M-MLV Reverse Transcriptase, 4 µl 5x M-MLV reaction buffer, 0.5 mM dNTPs and 20 U RNAse Inhibitor to a total volume of 20 µl and incubated for 1 h at 37°C. cDNA was stored at -20°C.

4.5.8 qRT-PCR

To analyze the cellular transcriptome and CVB3 RNA load, quantitative real-time PCR (qPCR) was performed. 12.5 ng cDNA, 2.2 µM of forward and reverse primer, 200 nM probe and Fast Universal PCR Mastermix were combined in a 13 µl PCR reaction mix. Commercially available ABI probes and primer mixes are listed in sections 3.11 – 3.13 and used according to manufacturer's instructions. Amplification was performed on an ABI Prism detection system with the following program: 95 °C/20 s, 40 x (95 °C/1 s, 60 °C/20 s). The housekeeping gene hypoxanthine guanine phosphoribosyltransferase (HPRT) was used for relative quantification according to the ΔC_T or $\Delta\Delta C_T$ method.

4.6 Virology methods

4.6.1 Coxsackievirus B3 propagation

Green Monkey Kidney (GMK) cells were grown to ~90% confluence in a T175 tissue culture flask. Cells were washed with PBS prior to infection with ~$1.5x10^8$ pfu CVB3 in 5 ml medium for 1 h. Subsequently, 20 ml of medium were added and cells were incubated for another 8 – 10 h, until a cytopathic effect was detected. Cells and supernatant were collected together and underwent three freeze-thaw cycles to release intracellular virus into the supernatant. Cell debris was collected and removed by centrifugation at 485 rcf for 10 min and virus titers of the supernatant were determined by plaque assay.

4.6.2 Plaque assay

To determine infectious virus particles in cellular homogenates or cell culture supernatants, samples were centrifuged for 5 min at 2,000 rcf prior to serial dilution up to 10-fold in DMEM without supplements. GMK cells at 70% confluence in a 12-well format were incubated with 200 µl of virus dilution per well for 1 h at 37°C, 5% CO_2 with gentle agitation every 15 min. Virus solution was aspirated and infected monolayers were overlaid with 0.6% agar in DMEM. After the agar overlay solidified, plates were incubated at 37°C, 5% CO_2, for 2 days. Plaque assay fixation buffer (section 3.3) was added for 10 min before the overlay was carefully removed. Cells were stained in crystal violet solution for 1 – 4 h and plates were rinsed in water. Clear areas on violet background were considered plaques and counted to calculate viral titers.

Alternatively, viral dilutions were pipetted in PBS and added to confluent HeLa Vero cells in 24-well format at 300 µl/well for 30 min at 37°C, 5% CO_2. After removal of supernatant, cells

were overlaid with 500 µl Eagle overlay (section 3.2) and incubated for 2 days at 37°C, 5% CO_2. Cells were fixed and stained with 25 µl of 1:1 MTT-PBS solution for 1 h and plaques were counted as described above.

4.6.3 Infection of cells

Cell numbers were determined with a Neubauer counting chamber to calculate the MOI for *in vitro* infections. Virus was diluted in DMEM without supplements and added in half the standard amount per well for 1 h at 37°C, 5% CO_2. Cells were then incubated in standard culture medium for the indicated timepoints.

4.7 Statistics

Statistical analysis was performed in GraphPad Prism (GraphPad Software, La Jolla) or in Perseus (MaxQuant, Martinsried). Data was plotted as individual points with a summary given as mean ± standard error of the mean (SEM). Virus titers and other logarithmic data were transformed logarithmically prior to data plotting and statistical analysis. The significance levels were set at 0.05 unless indicated otherwise. For two-group comparisons, unpaired Student's *t*-tests were used. In the case of unequal variances, as determined by an *F*-test, the unpaired Student's *t*-test with Welch correction was used. One-sample *t*-tests were used if values were normalized to an internal control. Multiple group comparison was achieved by a one-way or two-way ANOVA followed by Sidak's multiple comparison test.

5 Results

5.1 Analysis of the cardiac proteome at multiple stages of CVB3 infection

To investigate CVB3 infection-induced changes in cardiac protein expression and abundances, the proteome was analysed by liquid chromatography-tandem MS (LC-MS/MS) during the peak of cardiac ISGylation on day 3 (Kespohl et al. 2020) and acute myocarditis on day 8 (Rahnefeld et al. 2014). Furthermore, the influence of ISG15 and ISGylation on protein abundances was determined. To this end, heart tissue of wildtype (wt), ISG15$^{-/-}$, and USP18$^{C61A/C61A}$ (C61A) mice was analysed on day 0, day 3 and day 8 post-infection (Fig. 11 A).

On day 3 and 8, a total of 3023 and 1570 proteins were identified and quantified, respectively (Tab. S1). A principal component analysis (PCA) of the quantified proteome showed clustering of uninfected and infected samples (Fig. 11 B), indicating no discernible difference on the proteomic level between the genotypes. Subsequently, proteomes of CVB3-infected mice and uninfected controls were compared in order to reveal which proteins were up- and downregulated during infection. The resulting volcano plot (Fig. 11 C, Tab. S14) showed 64 significantly regulated proteins. Most upregulated upon virus-infection were proteins of the antiviral response, such as IFIT1/2/3, interferon-inducible GTPase (IIGP) 1, sterile alpha motif (SAM) domain and histidine-aspartate (HD) domain containing protein (SAMHD) 1, STAT1, as well as ISG15.

When testing the protein expression of ISG15$^{-/-}$ mice against both, wildtype and USP18$^{C61A/C61A}$, no significantly regulated proteins were found apart from the mitochondrial NAD(P) transhydrogenase (NNT) which was upregulated in ISG15$^{-/-}$ mice (Fig. 12 A-C). This is likely due to a mixed background of the ISG15$^{-/-}$ animals, as C57BL/6 subtype J mice display a mutation in the *Nnt* gene causing a lack of NNT protein, while C57BL/6 subtype N mice express NNT normally (Mekada et al. 2009; Simon et al. 2013). Nonetheless, these analyses showed that the antiviral protein expression is not impaired in ISG15-deficient mice.

Furthermore, a two-way ANOVA test was performed prior to z-scoring of differentially regulated proteins. A z-score calculation forms the mean of all intensities within one row and subtracts it from each individual intensity, allowing the visualization of more subtle changes in protein abundance than a volcano plot. Non-hierarchical clustering formed a heatmap, revealing a total of 319 significantly regulated proteins, grouped in four distinct clusters (Fig. 11 D, Tab. S1). 135 proteins were upregulated in CVB3-infection conditions (cluster 1), with an additional 17 proteins that were specifically upregulated on day 8 (cluster 2). Moreover, 110 proteins were downregulated on both days of infection (cluster 4)

with an additional 57 proteins that were downregulated only on day 8 of infection (cluster 3). Again, no difference between the genotypes was observed.

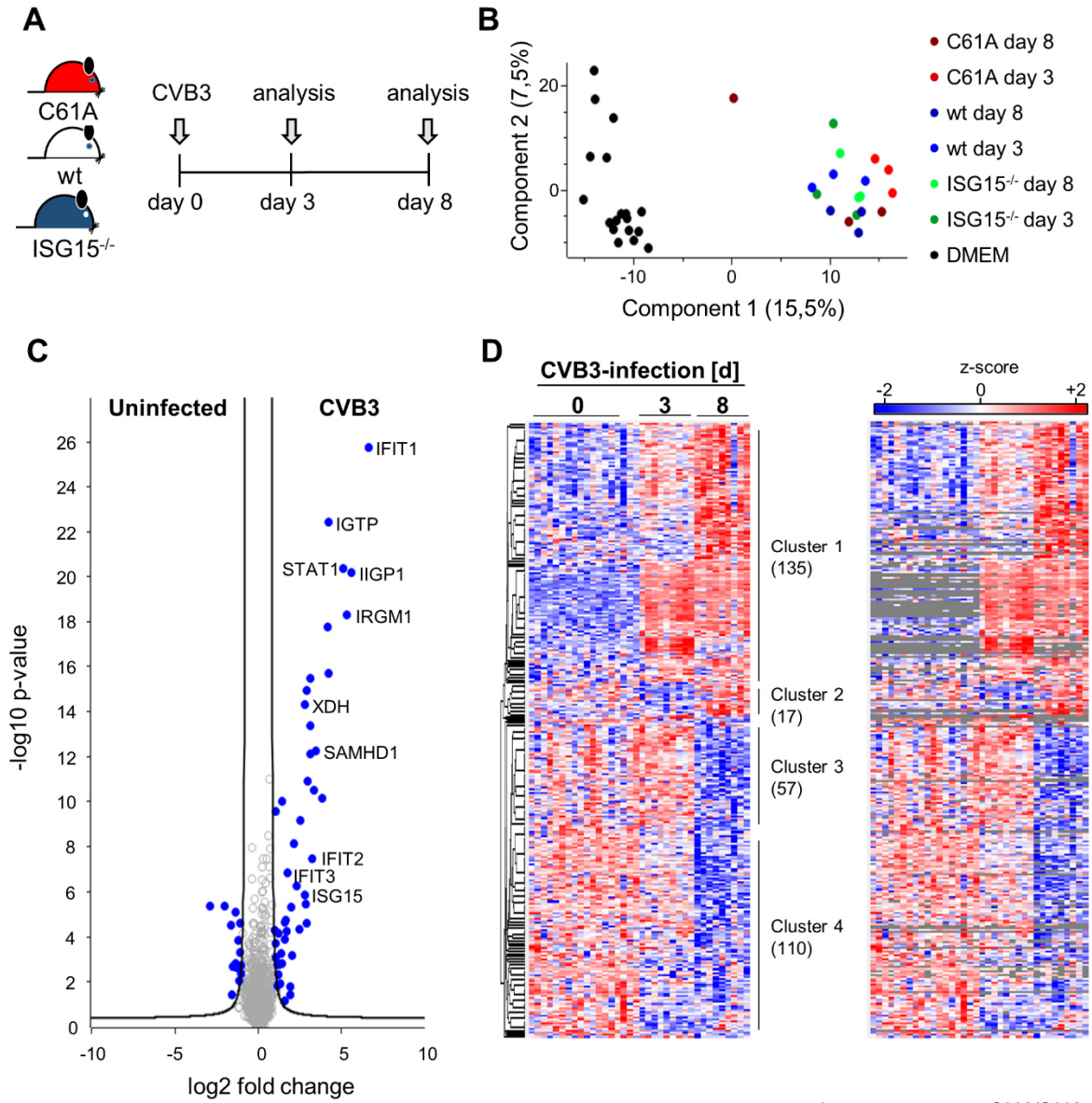

Figure 11: Proteome analysis of CVB3 infected wildtype, ISG15$^{-/-}$, and USP18$^{C61A/C61A}$ mice.

(A) Wildtype (wt), ISG15$^{-/-}$, and USP18$^{C61A/C61A}$ (C61A) mice were infected with 1x10^5 pfu of CVB3 Nancy strain and analysed on day 0, day 3, and day 8 of infection (n=3 per condition). **(B)** Principal Component analysis of proteomic samples depicting a two-dimensional principal subspace to visualize correlation patterns between the samples. **(C)** Volcano Plot of infected vs. uninfected samples showing significantly regulated proteins. The log2 fold change is shown on the x-axis, while the -log10 p-value calculated by a *t*-test is shown on the y-axis. Significantly regulated proteins are colored in blue and representative proteins are labelled. **(D)** Non-supervised hierarchical clustering of significantly regulated proteins displayed in a heatmap. The relative abundance of each protein is based on the z-score in a colour coded manner (red=high abundance, blue=low abundance). The right side shows heatmap with imputed values in gray. Four major clusters can be observed corresponding to proteins upregulated on both days of infection (cluster 1), upregulated on day 8 (cluster 2), downregulated on day 8 (cluster 3) and downregulated on both days of infection (cluster 4). The number of proteins within each cluster is stated in brackets.

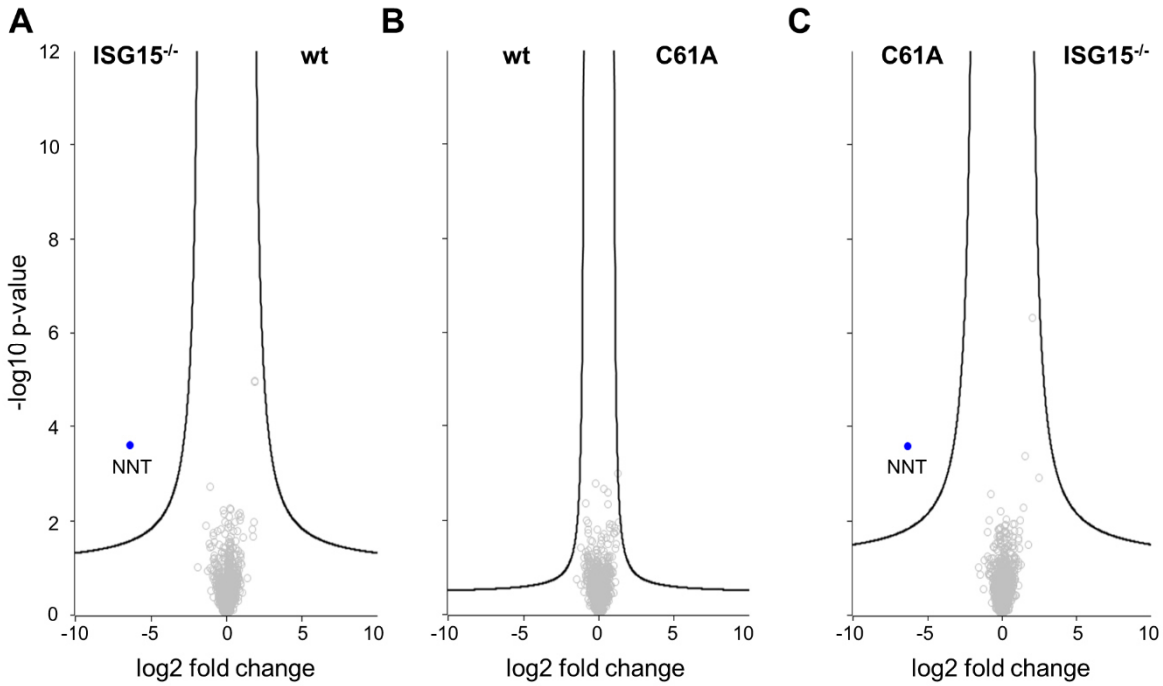

Figure 12: Comparison of protein expression between genotypes.
To determine cardiac proteins that were significantly regulated between wildtype (wt), ISG15$^{-/-}$, and USP18$^{C61A/C61A}$ mice, their quantified proteomes were subjected to a *t*-test and displayed in volcano plots as follows: **(A)** ISG15$^{-/-}$ vs. wildtype (wt), **(B)** wildtype vs. USP18$^{C61A/C61A}$ (C61A), and **(C)** USP18$^{C61A/C61A}$ (C61A) vs. ISG15$^{-/-}$. The x-axis depicts the log2 fold change of protein expression and the y-axis the -log10 *p*-value. Significant proteins are colored in blue and labelled. NNT = NAD(P) transhydrogenase.

To obtain a functional overview of the proteins within each cluster, a systematic gene ontology (GO) enrichment analysis was performed (Fig. 13). GO enrichment analysis sorts a list of given proteins in three categories: cellular component, molecular function, and biological process. To gain insight into the processes that are up- or downregulated over the course of CVB3 infection, the focus was laid on the category biological process. The results for the categories of molecular function and cellular component are listed in supplemental Tab. S3 and Tab. S4, respectively. Proteins from the cluster “upregulated in infection” were included in the GO analysis for the cluster “upregulated on day 8”. Similarly, the proteins from “downregulated in infection” were included in the GO analysis for the cluster “downregulated on day 8”. Since proteins are often sorted in several redundant GO terms, a representative set of terms was chosen for display (Fig. 13). The full results are listed in Tab. S2 (Supplements).

During CVB3 infection, upregulated proteins are part of the innate immune system and involved in cytokine production as well as the defense response to viral infection (Fig. 13 A). With over 100-fold enrichment, “antigen processing and presentation of exogenous peptide antigen via MHC class I, TAP-dependent” (GO:0002479) was the most enriched term (Fig. 13 A, Tab. S2), closely followed by lipoprotein mediated signaling (GO: 0055095) (Tab. S2). Notably, “ISG15-protein conjugation” (GO: 0032020) was ~68-fold enriched in

infection, emphasizing the importance of ISGylation in the antiviral immune response against CVB3. Further processes related to innate immunity, such as cellular responses to interferon alpha (GO:0035457), interferon beta (GO: 0035458), and interferon gamma (GO: 0071346) were enriched as well, next to cytokine response and the defense response to virus (Fig. 13 A). Only a few metabolic terms were upregulated in infection which were mostly redundant, i.e., “ATP metabolic process” (GO:0046034) and “deoxyribonucleoside triphosphate metabolic process” (GO:0009200) (Fig. 13 A, Tab. S2). Since the proteins that were upregulated on both days of infection were also used for the GO analysis of the cluster “upregulated on day 8”, most enriched terms remained the same between both clusters, with only minor changes in the fold enrichment (Tab. S2). At 8 days post infection, more GO terms related to metabolic processes were enriched. Aside from “mitochondrial ATP synthesis coupled proton transport” (GO:0042776) (Tab. S2) and “ATP metabolic process” (GO:0046034) (Fig. 13 A), all other metabolic GO terms were nucleoside-related (i.e., GO:0009206, GO:0009201, and GO:0009144) (Tab. S2).

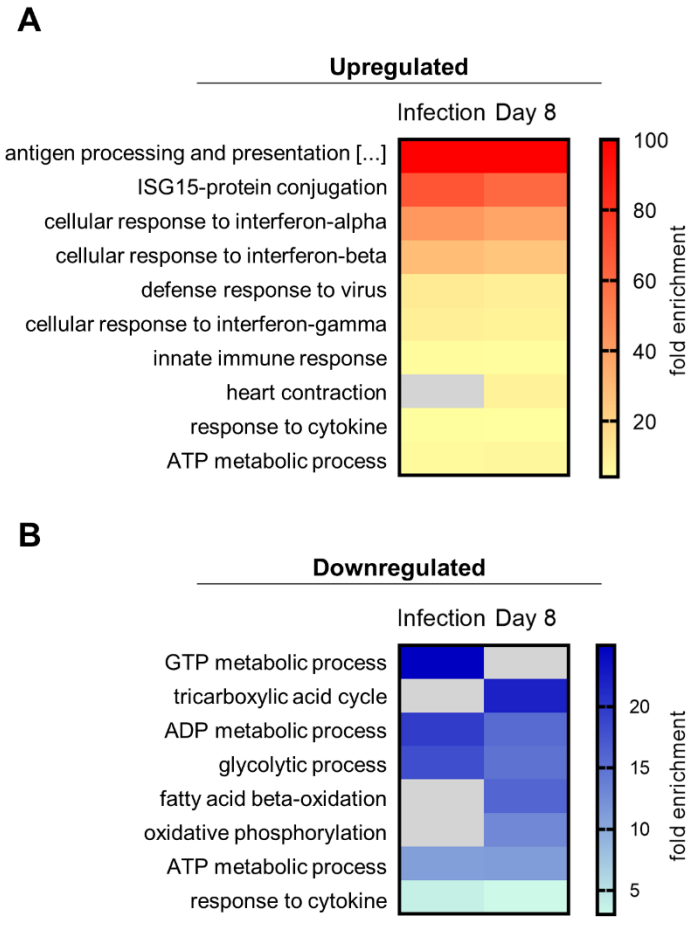

Figure 13: Gene Ontology enrichment analysis of the proteome in CVB3 infection.
Heatmap based clusters were subjected to gene ontology (GO) enrichment analysis of proteins **(A)** upregulated in CVB3 infection in general (Infection) and on day 8 specifically (Day 8) and **(B)** downregulated in CVB3 infection and on day 8 specifically. Representative GO terms and corresponding fold enrichment are depicted.

On the other hand, proteins downregulated during infection were almost exclusively part of metabolic processes, such as glycolytic, GTP and ADP metabolic (GO:0006096, GO:0046039, GO:0046031) processes (Fig. 13 B, Tab. S2). Specifically during acute myocarditis on day 8 post infection, downregulated proteins were part of the “tricarboxylic acid cycle” (GO:0006099), “oxidative phosphorylation” (GO:0006119), and “fatty acid beta-oxidation” (GO:0006635) (Fig. 13 B).

Together, the proteome analysis of CVB3 infected mice shows that the initialization of the cardiac antiviral state is independent of ISG15 and ISGylation. As the infection progresses, expression of metabolic proteins decreases, pointing towards infection-induced changes in cardiac energy metabolism.

5.2 Influence of ISG15 on cardiac respiratory function

To examine potential metabolic alterations suggested by a downregulation of proteins involved in cardiac metabolism during CVB3 infection, the mitochondrial energy production was assessed by Seahorse metabolic measurement. Furthermore, the influence of ISG15 on cardiac mitochondrial function was investigated.

5.2.1 Impact of ISG15 on oxidative phosphorylation in primary cardiomyocytes

Primary cardiomyocytes were infected with CVB3 MOI 1 for 8 h and the cellular oxygen consumption rate (OCR) was measured with a Seahorse XFe96 analyzer to gain insight into the cellular respiratory chain activity. During measurement, three inhibitors were sequentially added to the cells (section 4.4.5). Their influence on OCR is depicted in Fig. 14. Oligomycin blocks the ATP synthase, causing OCR rates to decrease as the respiratory chain is halted (Fig. 14 A). FCCP acts as an uncoupling agent of the respiratory chain complexes by transporting protons across the inner mitochondrial membrane, resulting in maximal activity of the chain complexes and thus maximal cellular oxygen consumption. Finally, Rotenone and Antimycin A inhibit complex I and complex III of the respiratory chain, respectively, which leads to complete shutdown of oxidative phosphorylation (Fig. 14 A). Based on the measured OCR levels, this allows for calculation of maximal respiration, ATP turnover, spare capacity, and proton leak across the mitochondrial membrane (Fig. 14 B). All measurements were normalized to protein content per well, as determined by a MicroBCA assay, and then set relative to untreated cells (Fig. 15).

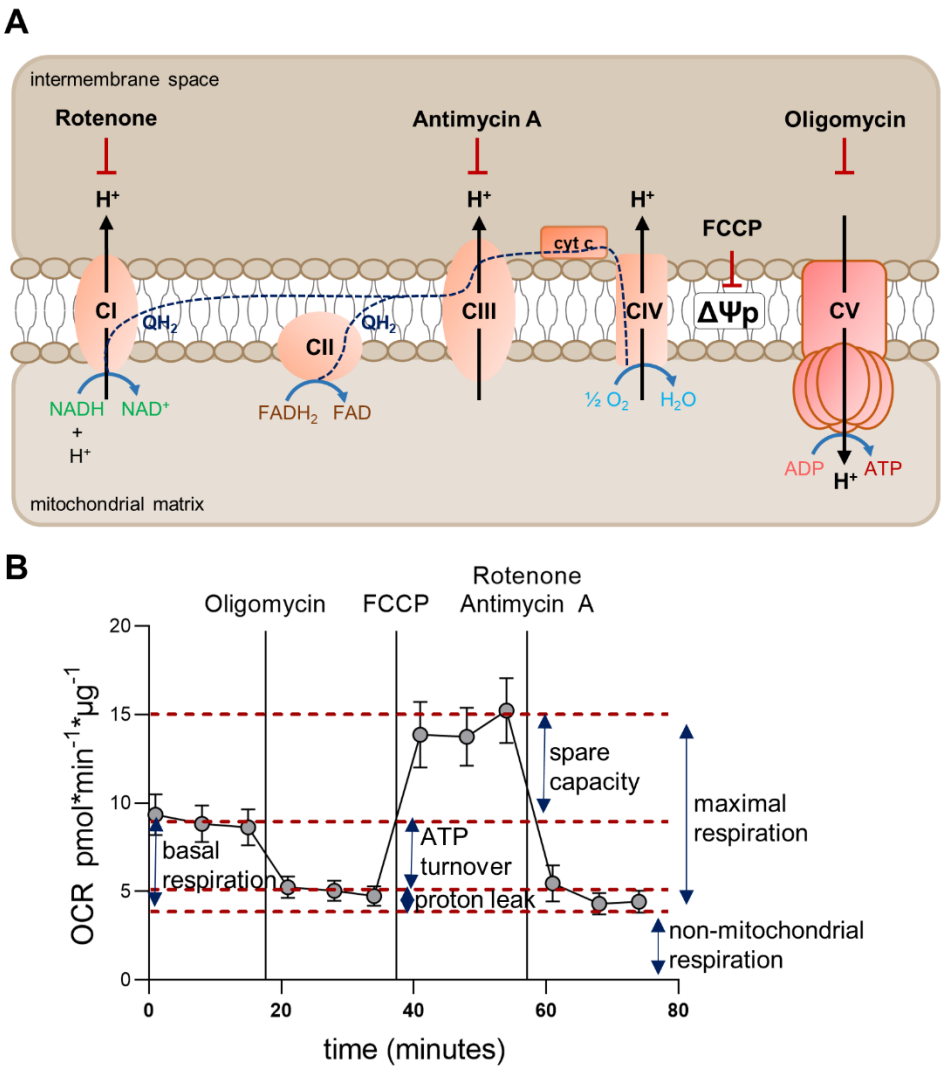

Figure 14: Seahorse measurement and injection strategy of mitochondrial stress test. **(A)** Within the inner mitochondrial membrane sits the respiratory chain. Electrons from NADH and $FADH_2$ are used by complex I (CI) and III (CIII) to form ubiquitinol (QH_2) while pumping protons into the intermembrane space, creating the mitochondrial membrane potential (ΔΨp). The proton gradient fuels the ATP synthase (CV). The inhibitors used during Seahorse measurement and their mechanism of action are depicted. Rotenone inhibits activity of CI, while Antimycin A inhibits CIII. FCCP counteracts the membrane potential, while Oligomycin blocks ATP synthase activity. **(B)** Oxygen consumption rate (OCR) over time normalized to the protein content of wildtype cardiomyocytes is displayed. After three measurement cycles under basal conditions, the indicated inhibitors are injected causing changes in OCR. These changes then allow for calculation of different parameters: basal and maximal respiration, spare capacity, ATP turnover, and proton leak. Non-mitochondrial respiration is the remaining cellular oxygen consumption, after the respiratory chain is inhibited.

CVB3 infection resulted in a significant increase in basal OCR levels as compared to untreated levels in wildtype cardiomyocytes (Fig. 15 B). In contrast, OCR levels in $ISG15^{-/-}$ cells only were only marginally higher in response to infection, leading to a significant difference between wildtype and $ISG15^{-/-}$ cells (Fig. 15 B). Furthermore, CVB3 infection induced a 2-fold increase in the maximum capacity of both, wildtype and $ISG15^{-/-}$ cells, showing that the cells reacted to an increase in energy demand with increased

mitochondrial chain capacity (Fig. 15 C). Here too, ISG15$^{-/-}$ cells displayed a significantly lower maximal respiration in CVB3 infection than the wildtype (Fig. 15 C).

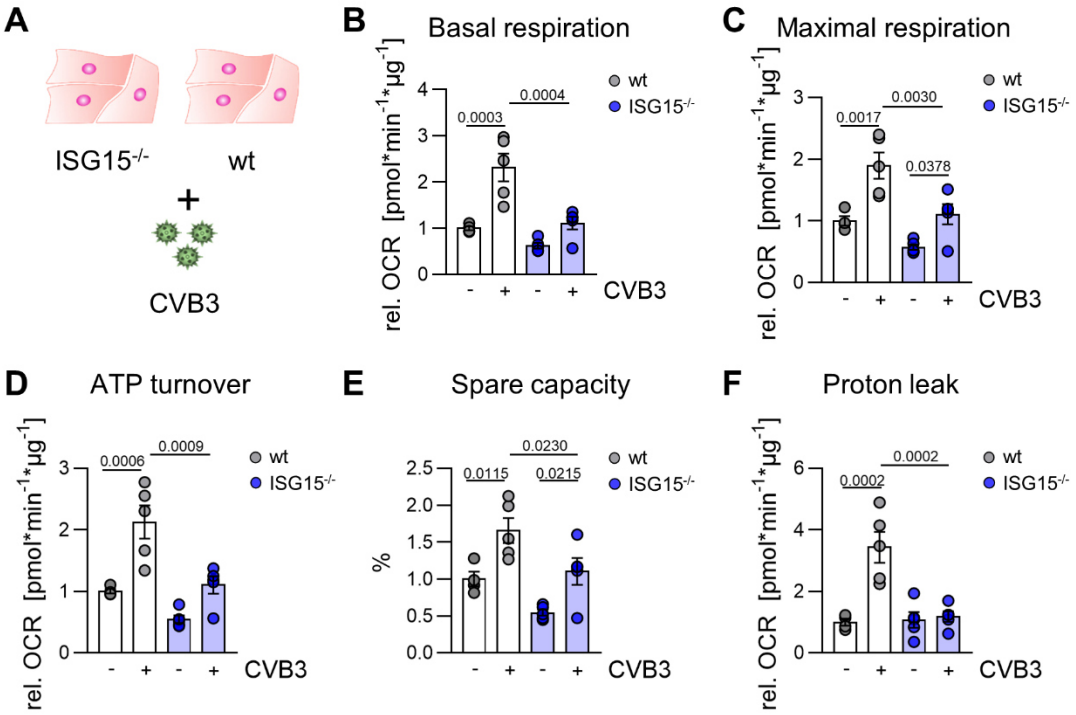

Figure 15: Measurement of mitochondrial respiration in primary cardiomyocytes.
(A) Primary cardiomyocytes of wildtype (wt) and ISG15$^{-/-}$ mice were infected with CVB3 at an MOI of 1 for 8 h prior to analysis oxygen consumption in a Seahorse XF Analyzer. **(B-F)** Calculated parameters based on OCR per µg protein: **(B)** basal respiration, **(C)** maximal respiration, **(D)** ATP turnover, **(E)** spare capacity, and **(F)** proton leak. A representative of n=5 experiments is shown. Significances calculated with two-way ANOVA and Sidak's multiple comparisons test.

Similar to the basal OCR levels (Fig. 15 A), ATP turnover levels in infected wildtype cells were significantly increased (Fig. 15 D) and infected ISG15$^{-/-}$ cells showed significantly reduced levels in infection as compared to wildtype (Fig. 15 D). The spare capacity, the difference between basal and maximal respiration, was significantly increased in both genotypes, yet still significantly lower in infected ISG15$^{-/-}$ cells (Fig. 15 E). Finally, wildtype cells exhibited increased proton leak in infection, while ISG15$^{-/-}$ cells did not (Fig. 15 F). On the one hand, proton leak can be an indicator for damaged mitochondria, on the other hand it could be a mechanism of the cell to regulate the mitochondrial ATP production (Divakaruni and Brand 2011). Therefore, the results of the proton leak calculation could indicate either increased mitochondrial stress or higher basal respiration in wildtype cells.

In summary, the Seahorse analysis shows that CVB3 infection of primary cardiomyocytes leads to increased mitochondrial respiratory activity. Furthermore, this increase appears to be dependent on ISG15, as ISG15$^{-/-}$ cardiomyocytes displayed significantly lower OCR levels in CVB3 infection than wildtype cells.

5.2.2 Impact of ISG15 on mitochondrial membrane potential in primary cardiomyocytes

The results of the Seahorse metabolic measurements suggest an infection-induced increase in mitochondrial respiratory activity (section 5.2.1). An increase in oxidative phosphorylation is directly coupled to an increase in mitochondrial membrane potential, as the respiratory chain complexes I and III act as proton pumps. The fluorescent dye MitoTracker® Deep Red (MTDR) FM traverses the mitochondrial membrane in dependence of the membrane potential and accumulates within mitochondria (Lugli et al. 2005; Xiao et al. 2016). Employing MTDR, the mitochondrial membrane potential of cardiomyocytes was assessed to confirm the observed increase in oxidative phosphorylation. FCCP treatment served as a positive control for mitochondrial damage, as it collapses the mitochondrial proton gradient and thus leads to decreased MTDR accumulation (Mot et al. 2016).

Wildtype and ISG15$^{-/-}$ cardiomyocytes were infected with CVB3 at an MOI of 1 prior to staining with MTDR and confocal fluorescence microscopy images were taken to visualize mitochondria and calculate fluorescence intensity (Fig. 16 A). ImageJ was used to define the maximum fluorescence intensity image within a confocal z-stack and a region of interest was traced around a single cell, excluding the nucleus. A histogram then separated the number of pixels with a given intensity, which allows a more detailed analysis than considering total intensities only.

The average intensity and the corresponding percentage of pixels was plotted, and the resulting graphs were subjected to a two-way ANOVA (Fig. 16 B). These analyses revealed that, compared to wildtype cardiomyocytes, ISG15$^{-/-}$ cells already showed a slight but significant decrease in MTDR intensity under steady state conditions, indicating a lower baseline mitochondrial membrane potential. Upon treatment with FCCP, the intensity peak narrowed and increased for both genotypes reflecting the diffuse MTDR signal (Fig. 16 A, B) and thus mitochondrial damage. When infected with CVB3, mitochondria of wildtype cells did not display a change in MTDR intensity as compared to uninfected controls. However, the average fluorescence intensity per pixel of ISG15$^{-/-}$ cells was significantly lower during infection (Fig. 16 B), indicating an infection-induced decrease in mitochondrial membrane potential. This finding is in accordance with the decreased oxidative phosphorylation levels in cardiomyocytes (Fig. 15 B).

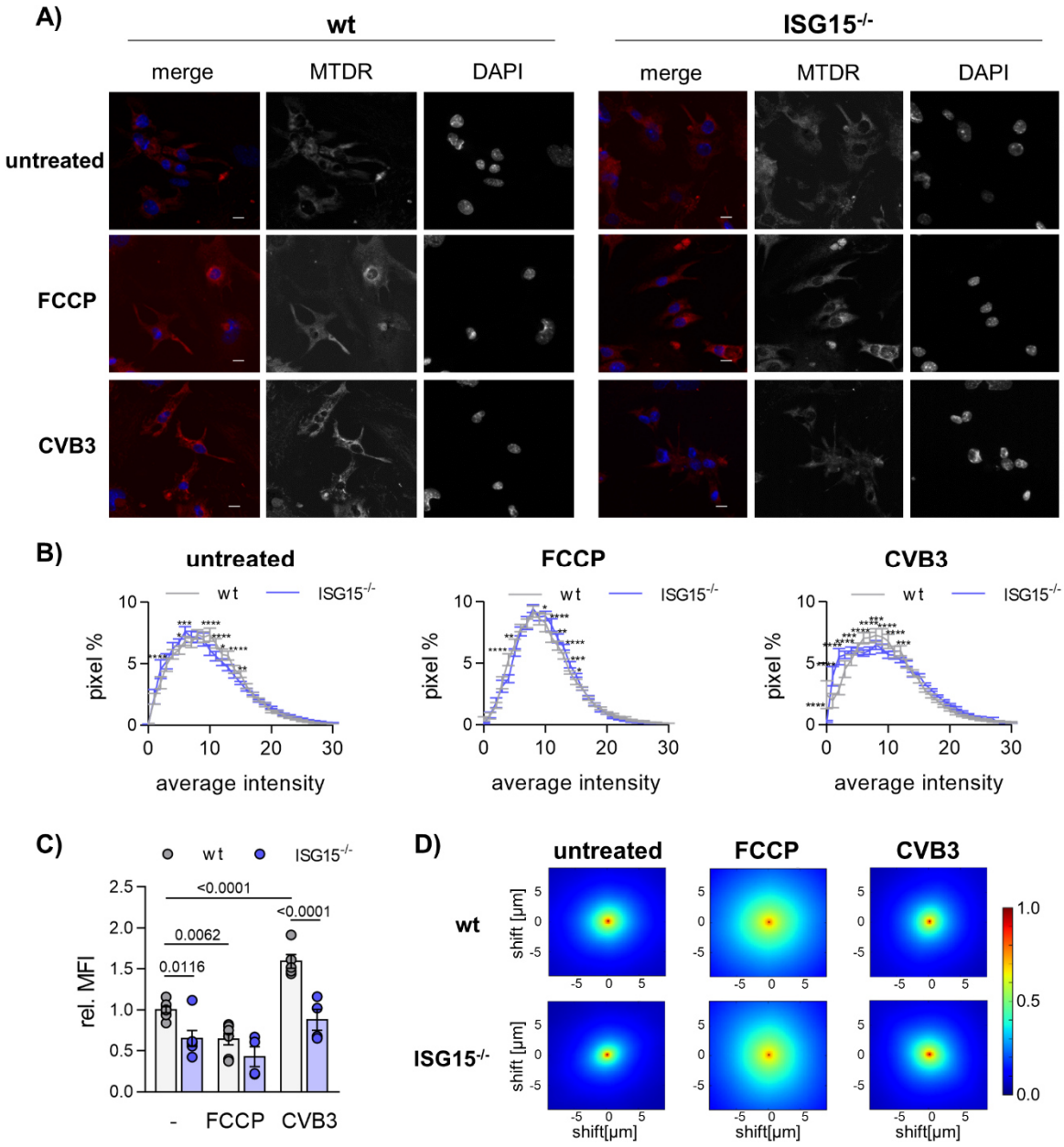

Figure 16: Determination of mitochondrial membrane potential in primary cardiomyocytes.
(A) Confocal microscopy of wildtype (wt) and ISG15$^{-/-}$ primary cardiomyocytes infected with CVB3 MOI 1 for 6h or treated with FCCP. Sum of intensity Z-projection of optical sections with MitoTracker™ Deep Red (red) and DAPI (blue) staining. Scale bar: 10 µm. **(B)** Quantitative comparison of MitoTracker™ Deep Red fluorescence intensity distributions (n=24) depicted in (A). Significances were calculated with a two-way ANOVA. **(C)** Flow cytometric analysis of MitoTracker™ Deep Red fluorescence in primary cardiomyocytes as described in (A). Median fluorescence intensities (MFI) relative to wildtype control are depicted. Significances were calculated with a two-way ANOVA. **(D)** Autocorrelation-based image correlation spectroscopy of MitoTracker™ Deep Red fluorescence depicted in (A). Auto-correlation is shown as 2D plots of confocal images shifted against each other on the x/y axes to determine cluster sizes.

Additionally, MTDR intensity was assessed by flow cytometry using the same experimental setup. The relative mean fluorescence intensity (MFI) of MTDR intensity normalized to wildtype uninfected control is displayed in Fig. 16 C. This analysis confirmed the significant

difference in baseline membrane potential between wildtype and ISG15$^{-/-}$ cells. FCCP treatment further reduced MTDR signal both genotypes. Additionally, a significant increase in MTDR intensity in wildtype cells during CVB3 infection was observed. ISG15$^{-/-}$ cells on the other hand showed only a slightly increased MTDR intensity upon infection (Fig. 16 C). Aiming to dissect whether the increased proton leak measured in wildtype cells during Seahorse analysis (Fig. 15 F) was due to increased mitochondrial damage and thus changes in morphology, image cross correlation (ICC) analysis was performed. Shifting each image against itself on the x/y axis allows for cluster size assessment collapsed into a 1D-Pearson correlation coefficient plot (Fig. 16 D). The ICC revealed no difference in mitochondrial shape between wildtype and ISG15$^{-/-}$ cells, neither in uninfected control conditions nor under CVB3 infection. This indicates that the change in mitochondrial membrane potential is not accompanied by changes in mitochondrial structure, i.e., due to mitochondrial fission or mitophagy.

Together, these experiments confirm an increase in mitochondrial oxidative phosphorylation in CVB3 infected wildtype cardiomyocytes, while ISG15$^{-/-}$ cells respond to the infection-induced energy demand with significantly lower respiratory activity, reflected by the mitochondrial membrane potential. The protective effect of ISG15 on the membrane potential is already apparent in steady state conditions yet further exacerbated in CVB3 infection.

5.2.3 Impact of ISG15 on cardiac oxidative phosphorylation in CVB3 infected mice

The downregulation of proteins involved in metabolism (Fig. 13 B) was observed in both, wildtype and ISG15$^{-/-}$ cardiac tissue. However, a difference in oxidative phosphorylation was observed in CVB3 infected wildtype and ISG15$^{-/-}$ primary cardiomyocytes (Fig. 15 B), suggesting a functional influence of ISG15 on mitochondrial energy production. To investigate whether this effect was replicable *in vivo* under the influence of systemic inflammatory mediators, the cardiac respiratory activity was analysed during CVB3 infection.

To avoid any NNT-derived phenotype introduced by the mixed subtype of the ISG15$^{-/-}$ mice (section 5.1), wildtype and ISG15$^{-/-}$ littermates from heterozygous breeding were analysed. Moreover, Ube1L$^{-/-}$ mice served as control to distinguish whether any influence of ISG15 was mediated by its free or conjugated form. Mice were infected with CVB3 Nancy strain and sacrificed on day 0 and day 3 post-infection. At the scheduled day of section, biopsies of the left ventricle were analyzed for oxygen consumption in a Seahorse XFe96 analyzer (Fig. 17 A). For each genotype, values were normalized to their uninfected control.

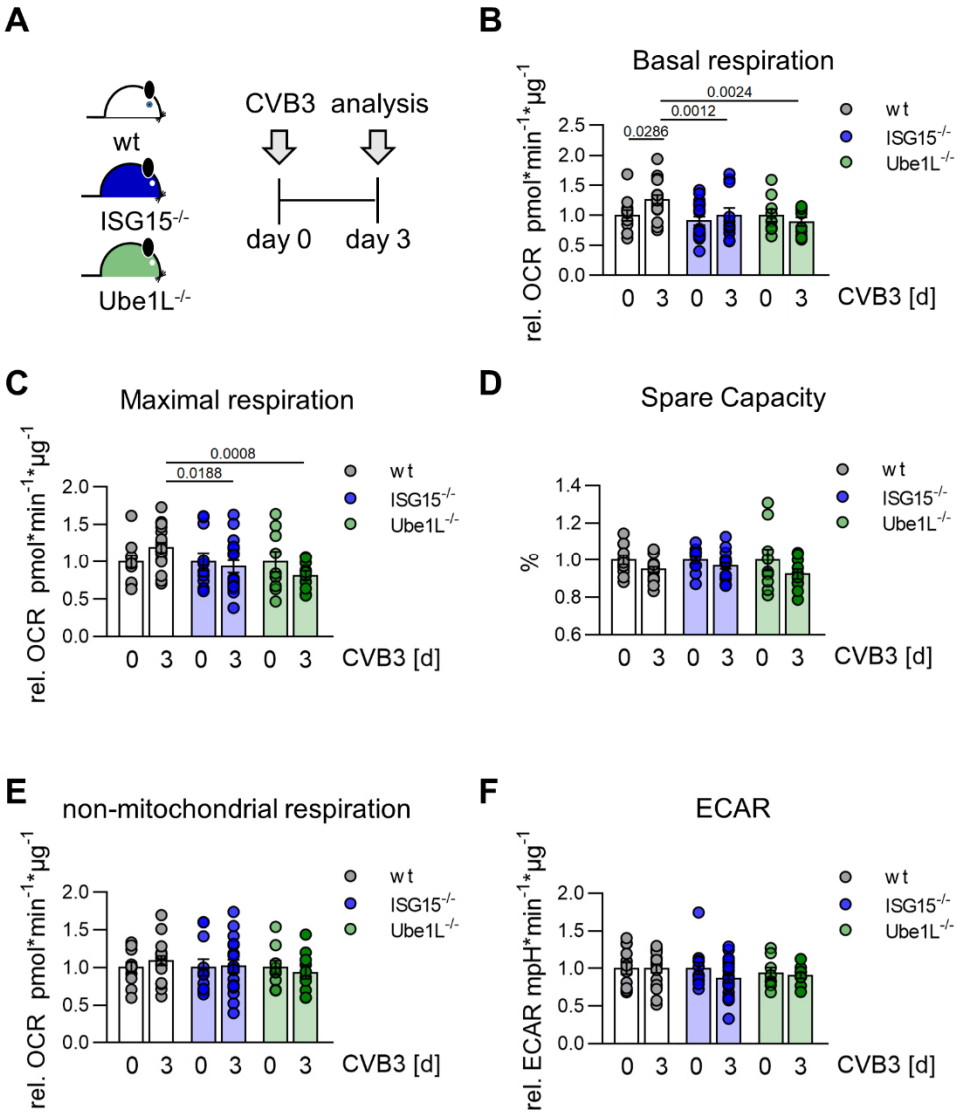

Figure 17: Measurement of mitochondrial respiration *in vivo*.
(A) Wildtype (wt), ISG15$^{-/-}$, and Ube1L$^{-/-}$ mice (n≥9) were infected with 1x10^5 pfu of CVB3 Nancy strain and analysed on day 0 and 3 of infection. Biopsies of the left ventricle were taken for Seahorse measurement. **(B-F)** Data were normalized to protein content, summarized as mean ± SEM and *t*-tests were performed for statistical evaluation. **(B)** Basal OCR levels displayed relative to uninfected controls. **(C)** Maximal OCR was determined by addition of uncoupling agent FCCP. **(D)** Spare capacity of each group was calculated from basal and maximal values. **(E)** Non-mitochondrial OCR was determined by complete inhibition of mitochondrial respiratory chain. **(F)** Extracellular acidification rate (ECAR) was determined by pH-measurement. Significances were determined by student's *t*-test.

In infection, wildtype OCR levels increased significantly while levels in ISG15$^{-/-}$ and Ube1L$^{-/-}$ mice remained unchanged (Fig. 17 B), resulting in significantly different basal respiration levels between wildtype and ISG15- and ISGylation-deficient cardiac tissue. Maximal respiration was also higher in infected wildtype heart biopsies than in infected ISG15$^{-/-}$ and Ube1L$^{-/-}$ mice. The spare respiratory capacity (Fig. 17 C) remained unchanged in all genotypes, as did the non-mitochondrial respiration levels (Fig. 17 E) and the extracellular acidification rate (ECAR) (Fig. 17 F). ECAR is determined by pH measurement

of the assay medium. Factors such as glycolysis, but also CO_2 generation by the cells contribute to alterations in pH (section 4.3.6.2) (Mookerjee and Brand 2015)

Together, the *in vivo* analysis of mitochondrial respiratory function suggests that CVB3 infection results in a higher cardiac ATP demand which is met by increased oxidative phosphorylation. This is complemented by the results observed in primary cardiomyocytes (Fig. 15 and 17). The increase in OCR appears to be dependent on ISG15 and more specifically on ISGylation, as ISG15$^{-/-}$ and Ube1L$^{-/-}$ hearts exhibit significantly lower oxygen consumption levels during infection than wildtype mice.

5.3 Analysis of the cardiac ISGylome and ubiquitylome at different stages of CVB3 infection

ISGylation is known to counteract CVB3-mediated morbidity resulting in an increased survival and a decrease in cardiac inflammation and viral titers (Rahnefeld et al. 2014), whereas catalytic inactivation of USP18 reduces cardiac CVB3 titers as ISGylation is increased (Kespohl et al. 2020). This antiviral effect correlates with ISG15/ISGylation-mediated increased cardiac oxygen consumption (Fig. 15 and 17). However, it remains unclear which proteins are covalently modified by ISG15 in the infected heart muscle. Thus, the cardiac ISGylome was analyzed in an MS-based approach to identify ISGylated proteins.

Wildtype, ISG15$^{-/-}$, and USP18$^{C61A/C61A}$ mice were analyzed on day 3 and day 8 post-CVB3 infection while uninfected mice served as control. Proteolytic digestion of cardiac proteins with Trypsin and LysC leaves characteristic double-glycine (GG) - remnants where ubiquitin or ISG15 were bound to lysine residues (Fig. 18 A). These GG-remnants allow for immunoprecipitation-based enrichment of modified peptides prior to LC-MS/MS analysis. To separate GG-remnants stemming from ubiquitination and ISGylation, the analysis of samples from ISG15$^{-/-}$ mice is crucial. The GG-modifications identified in all three genotypes are most likely remnants of ubiquitination, while those not found in the ISG15$^{-/-}$ mice are bona fide ISGylation sites (Fig. 18 B). The ones only present in the USP18$^{C61A/C61A}$ context are considered ISGylation sites that were detected due to defective deISGylation capacity of USP18 and are thus referred to as hyperISGylation sites (Zhang et al. 2019) (Fig. 18 B). This method provides no control for GG-modifications stemming from Nedd8-modifications, which is discussed in section 6.3.

Following a two-way ANOVA, non-supervised hierarchical clustering revealed distinct groupings of GG-modifications (Fig. 18 C and D). On day 3, 124 GG-modification sites were identified and 114 significantly regulated, 26 of which appeared in the hyperISGylation cluster, 25 in the ISGylation cluster, 22 in the ubiquitin cluster and 51 that were considered to be basal ubiquitination, only found in the uninfected controls (Fig. 18 C, Tab. S5).

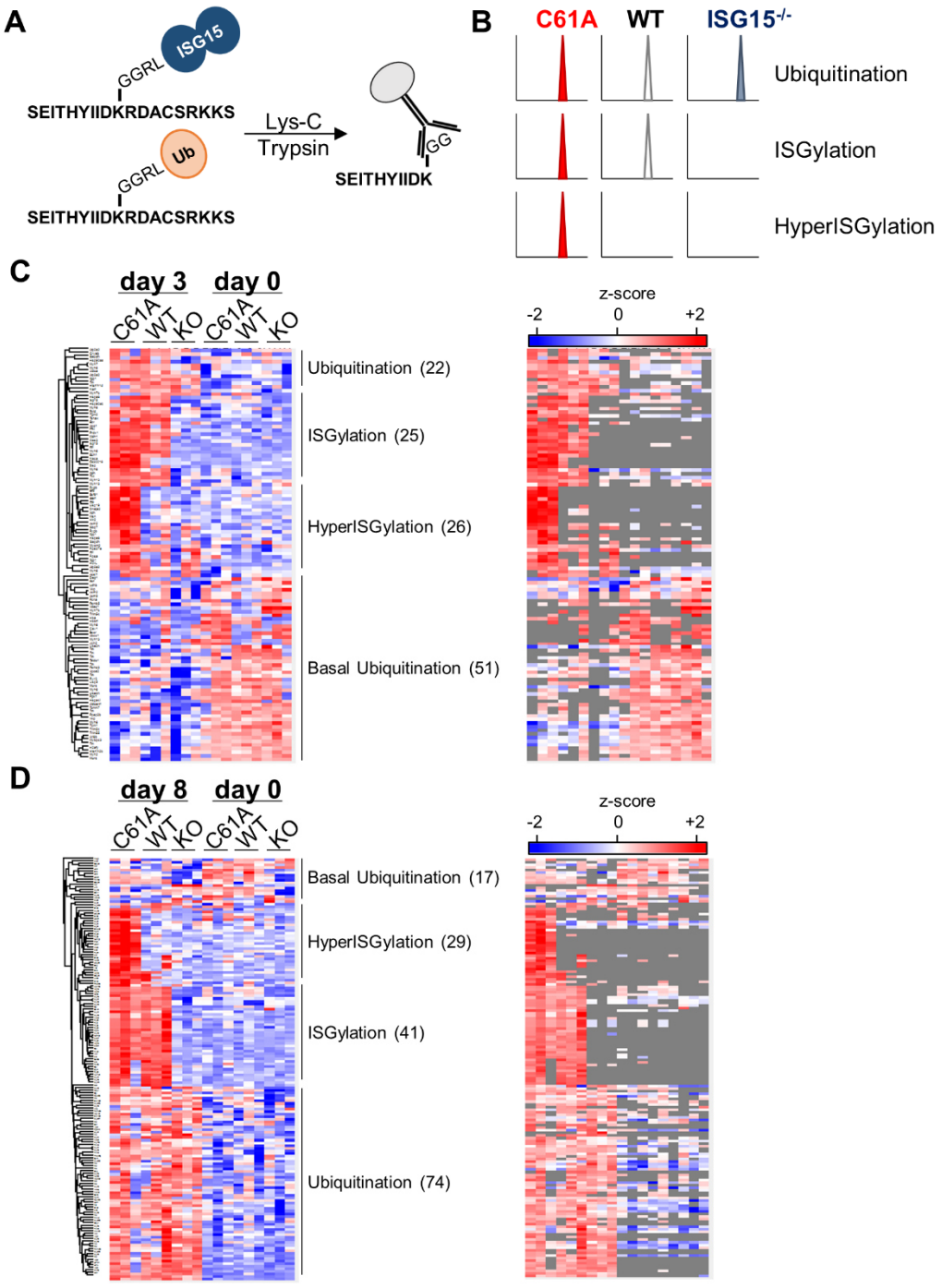

Figure 18: ISGylome and ubiquitylome analysis of CVB3 infected wildtype, ISG15$^{-/-}$, and USP18$^{C61A/C61A}$ mice.

(A) Cardiac proteins modified with ISG15, or ubiquitin were digested with LysC and Trypsin, leading to GG-remnants which were enriched by immunoprecipitation and analysed by LC-MS/MS. **(B)** GG-modifications found in all three employed genotypes (C61A=USP18^{C61A}, WT=wildtype, ISG15$^{-/-}$, n=3) were considered to be remnants from ubiquitination, GG-remnants missing in ISG15$^{-/-}$ context were considered to be ISGylation and GG-remnants only found in C61A mice are considered hyperISGylation. **(C-D)** Non-supervised hierarchical clustering of significantly regulated GG-modifications displayed in a heatmap. The relative abundance is based on the z-score in a colour coded manner (red=high abundance, blue=low abundance). The right side shows heatmap with the missing values in gray. Four major clusters can be observed corresponding to basal ubiquitination, infection-induced ubiquitination, ISGylation and hyperISGylation sites. Site analysis was performed on day 3 **(C)** and day 8 **(D)** post-CVB3 infection.

Out of a total of 285 identified and 161 significantly regulated GG-modification sites on day 8, 29 were determined to be hyperISGylation, 41 were ISGylation, while 74 sites were found in all three genotypes and thus ubiquitination, and 17 sites were basal ubiquitination (Fig. 18 D, Tab. S9).

Even though site comparison between infection time points is difficult since the samples were not analysed on the same day, it is worth noting that the increase of bona fide ISGylation sites from day 3 to day 8 was not accompanied by an increased amount in modified proteins (Tab. S5 and Tab. S9). On day 3, the 41 ISGylation sites were found on 37 proteins, while on day 8, 70 sites were identified on 41 proteins. Thus, most proteins have either several putative ISGylation sites or are multi-ISGylated. Moreover, an upregulation of infection-specific ubiquitination was observed, from 19 ubiquitinated proteins on day 3 to 44 proteins on day 8 (22 and 74 ubiquitination sites, respectively).

Tab. 4: Novel targets of ISGylation. Proteins identified for the first time to be covalently modified by ISG15.

Uniprot	Protein	Gene	Day p.i.
G3UWE2	Interferon-gamma-inducible GTPase Ifgga4 protein	*F830016B08Rik*	3
P04247	Myoglobin	*Mb*	8
P13541	Myosin-3	*Myh3*	3
Q5SX39	Myosin-4	*Myh4*	3
Q02566	Myosin-6	*Myh6*	8
Q91Z83	Myosin-7	*Myh7*	8
O08638	Myosin-11	*Myh11*	8
B1AR69	Myosin-13	*Myh13*	3
Q6URW6	Myosin-14	*Myh14*	8
P51667	Myosin regulatory light chain 2	*Myl2*	8
Q14BI5	Myomesin 2	*Myom2*	8
P47857	ATP-dependent 6-phosphofructokinase, muscle type	*Pfkm*	8
Q9DBC7	cAMP-dependent protein kinase type I-alpha regulatory subunit	*Prkar1a*	8
Q8CI94	Glycogen phosphorylase, brain form	*Pygb*	3 & 8
Q9WUB3	Glycogen phosphorylase, muscle form	*Pygm*	8

Comparison of the ISG15 targets identified in this study and previously published ones (Giannakopoulos et al. 2005; Zhao et al. 2005; Takeuchi et al. 2006; Wong et al. 2006;

Durfee et al. 2010; Radoshevich et al. 2015; Perng and Lenschow 2018; Zhang et al. 2019) revealed 15 novel putative targets for ISG15 (Tab. 4). Out of the 111 ISGylation sites identified in this study, 11 were found to be ISGylated on both, day 3 and day 8 of CVB3 infection. Moreover, when comparing the herein identified sites to the recent study by Zhang, Thery et al., 38 sites overlapped (Zhang et al. 2019). Thus, 62 novel ISGylation sites are reported here.

A total of 30 overlapping GG-modifications on both days were identified (including ubiquitination and basal ubiquitination), 8 of which are found to change clusters from day 3 to day 8.

Tab. 5: GG-site cluster changes. GG-modification sites found on both day 3 and day 8 and their respective cluster affiliation based on the heatmaps (Fig. 18).

Uniprot	Protein	Gene	Site	day 3	day 8
Q91Z40	Submitted name: Gbp6 protein	*Gbp7*	634	HyperISGylation	Ubiquitination
P63017	Heat shock cognate 71 kDa protein	*Hspa8*	159	ISGylation	HyperISGylation
P26040	Ezrin	*Ezr*	79	ISGylation	Ubiquitination
E9Q557	Desmoplakin	*Dsp*	320	ISGylation	HyperISGylation
Q00519	Xanthine dehydrogenase	*Xdh*	905	ISGylation	Ubiquitination
P40142	Transketolase	*Tkt*	319	ISGylation	Ubiquitination
B1AR69; **G3UW82;** **P13541;** **Q02566;** **Q5SX39;** **Q91Z83**	Myosin-13; Myosin-2; Myosin-3; Myosin-6; Myosin-4; Myosin-7	*Myh13;* *Myh2;* *Myh3;* *Myh6;* *Myh4;* *Myh7*	407; 408; 406; 406; 408; 405	ISGylation	Ubiquitination
P16858	Glyceraldehyde-3-phosphate dehydrogenase	*Gapdh*	213	Ubiquitination	basal Ubiquitination

Two sites changed from ISGylation to hyperISGylation, five sites changed from ISGylation (or hyperISGylation) to ubiquitination, and one site changed from ubiquitination to basal ubiquitination (Tab. 5). This might hint towards ISGylation blocking ubiquitination sites, as certain sites appear to be modified by ISGylation during early infection and are later found

in the ubiquitination cluster. However, the two sample sets should have been analyzed at the same time to allow a comprehensive analysis of modification changes.

The ISGylation and ubiquitination clusters (Fig. 18 C and D) were subjected to systematic GO enrichment analysis using the Panther Classification System (Ashburner et al. 2000; Mi et al. 2013; The Gene Ontology 2019). As with the shotgun analysis (Section 5.1), the focus of the GO analysis was laid on the Biological Process of the bona fide ISGylation and ubiquitination targets. The hyperISGylation and ISGylation clusters were analysed together since they both contain putative ISGylation sites.

On day 3 post-infection, GO analysis revealed an enrichment of ISG15-modification on key proteins in the regulation of viral replication and the host defense, such as STAT1, IIGP1, OAS3, as well as IFIT1 and 3 (Fig. 19 A, Table S5). In addition to the immunologic GO terms, metabolic terms such as “glycolytic process” and “ATP metabolic process” were also highly enriched, including the proteins HK2, and PFK (Fig. 19 A, Table S5).

On day 8, the ISGylation clusters consisted almost exclusively of metabolic proteins involved in glycolysis and ATP generation with only one immunologic term, namely “cellular response to interferon-alpha” containing IFIT1 and IFIT3 (Fig. 19 B, Table S9).

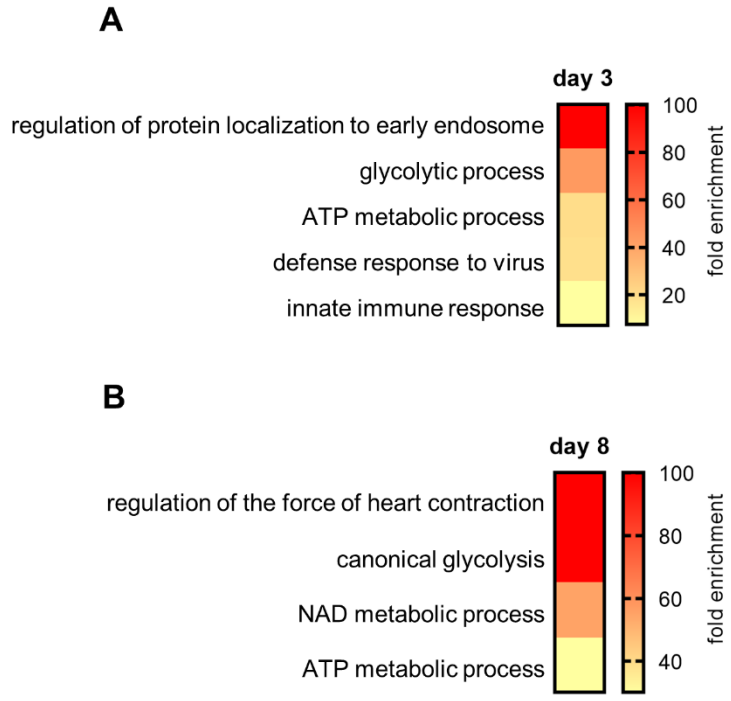

Figure 19: Gene Ontology enrichment analysis of the ISGylome in CVB3 infection.
Heatmap based ISGylation clusters were subjected to gene ontology (GO) enrichment analysis of proteins. ISGylation and hyperISGylation clusters were combined for this analysis. **(A)** ISGylation in CVB3 infection on day and **(B)** on day 8. Representative GO terms and corresponding fold enrichment are depicted.

On day 3, infection-induced ubiquitination targets were mostly involved in cardiac processes, such as “cardiac muscle hypertrophy”, and “regulation of the force of heart contraction” (Fig. 20). On day 8 post-infection, proteins affiliated with cardiac terms, but also

immunologic and structural terms were ubiquitinated. The uninfected controls revealed the basal ubiquitination in the healthy heart, reflecting cytoskeletal activity as well as cardiac function (Tab. S6).

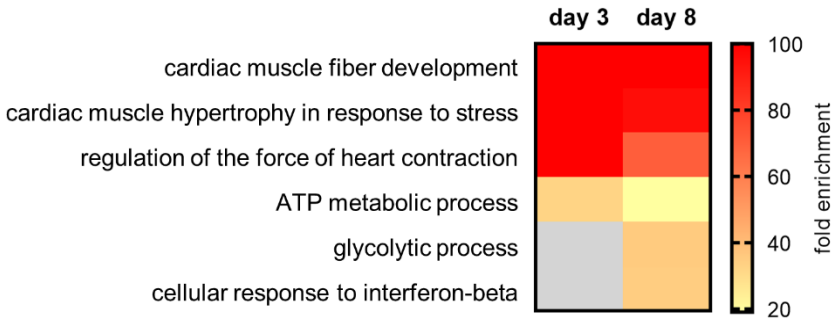

Figure 20: Gene Ontology enrichment analysis of the ubiquitylome in CVB3 infection. Heatmap based infection induced ubiquitination clusters were subjected to gene ontology (GO) enrichment analysis of proteins. Representative GO terms and corresponding fold enrichment scores of ubiquitination in CVB3 infection on day 3 and day 8 are depicted.

The analyses for both, Cellular Component (Tab. S8 and S12) and Molecular Function (Tab. S7 and S11) complemented the Biological Function described above. The infection-induced ubiquitination cluster on day 3 did not contain enough proteins for a comprehensive analysis for Molecular Function (Tab. S8).

In summary, these data reveal a distinct ISGylation profile during CVB3 infection. In the early phase, proteins belonging to the immune response are modified. Strikingly, during early infection as well as during acute myocarditis, an enrichment in metabolic target proteins is evident. Additionally, infection-induced ubiquitination targets are part of cardiac and metabolic processes.

5.4 Investigation of ISGylation targets

Most of the ISGylation targets identified in this study have already been reported to be modified by ISG15. However, they were mainly found through MS-based identification (Giannakopoulos et al. 2005; Zhao et al. 2005; Wong et al. 2006; Radoshevich et al. 2015; Zhang et al. 2019; Yan et al. 2021), which do not exclude false positives or other modification origins. Thus, it is important to validate bona fide ISGylation targets prior to analyses of possible functional effects. As this study found putative ISGylation targets belonging to the immune response as well as metabolism (section 5.3), follow-up investigations were split into two parts. First, a selection of immunologic ISG15-target proteins was validated and investigated (sections 5.4.1 – 5.4.2). Then, the focus was laid on ISGylated proteins involved in metabolism (sections 5.4.3 – 5.4.5).

5.4.1 Validation of IFIT1, IFIT3, and OAS3 as ISGylation targets

The analysis of the ISGylome revealed IFIT1, IFIT3, and OAS3 to be covalently modified by ISG15 during CVB3 infection. To validate this finding, two co-immunoprecipitation

approaches were conducted, precipitating either ISG15 or the target proteins to analyze their interaction.

For the first approach, the ISG15 pulldown, HeLa cells constitutively expressing FLAG-tagged ISG15 and vector control cells (Radoshevich et al. 2015) were treated with IFNβ to induce the expression of endogenous target proteins. A FLAG-immunoprecipitation was performed and endogenous IFIT1, IFIT3, and OAS3 were detected in western blot (Fig. 21 A and B). The total cell lysates (TCL) showed a strong ISGylation signal due to IFNβ treatment (Fig. 21 A and B, lanes 1 and 2), yet the FLAG pulldown revealed an enrichment in FLAG-ISG15-modification only in the constitutively overexpressing cells (Fig. 21 A and B, lanes 4). IFIT1 (Fig. 21 A, upper panel), IFIT3 (Fig. 21 B, middle panel), and OAS3 (Fig. 21 B) were all detected in both, ISG15 overexpressing cells as well as in the control cells, albeit to a lower extent in the latter. This suggests that all three proteins bind at least in part to the FLAG-beads used for precipitation. However, for IFIT1 and IFIT3, higher molecular weight modification bands were co-precipitated in the FLAG-ISG15 HeLa cells, which were not detected in the control cells (Fig. 21 A, lane 4). On the other hand, OAS3 did not show any higher molecular weight bands and only a slight increase in the FLAG-pulldown as compared to control cells (Fig. 21 B, lane 3 and 4).

Next, these results were confirmed by the second co-immunoprecipitation approach: the pulldown of the target proteins. Here, FLAG-tagged IFIT1, IFIT3, and OAS3 were co-transfected with HA-ISG15 and the ISGylation machinery (E1/E2/E3) followed by a FLAG-immunoprecipitation and western blotting. Controls without either the target, ISG15, or the machinery allowed to distinguish ISG15-modification from other modifications. As seen in Fig. 21, IFIT1 (Fig. 21 C), IFIT3 (Fig. 21 D), as well as OAS3 (Fig. 21 E) were confirmed as targets of ISG15-modification. For IFIT1, the FLAG-immunoblot showed a modification band approximately 15 kDa above IFIT1, which could be the ISGylated IFIT1 (Fig. 21 C, lane 5). Of note, this modification band was also apparent in the FLAG-immunoblot of the control lacking HA-tagged ISG15 (Fig. 21 C, lane 7). However, as HeLa cells express endogenous ISG15, which is induced by transfection of plasmids, this band is likely endogenously ISGylated IFIT1.

FLAG-immunoblots for IFIT3 (Fig. 21 D, lane 5) and OAS3 (Fig. 21 E, lane 5) do not show any higher molecular weight modification bands. However, in the HA-immunoblots of all three target immunoprecipitations, clear modification bands were observed, which were detected at and above of the apparent molecular weight of the target (Fig. 21 C – D, middle panel). Thus, IFIT1, IFIT3, and OAS3 were all confirmed as ISGylation target proteins.

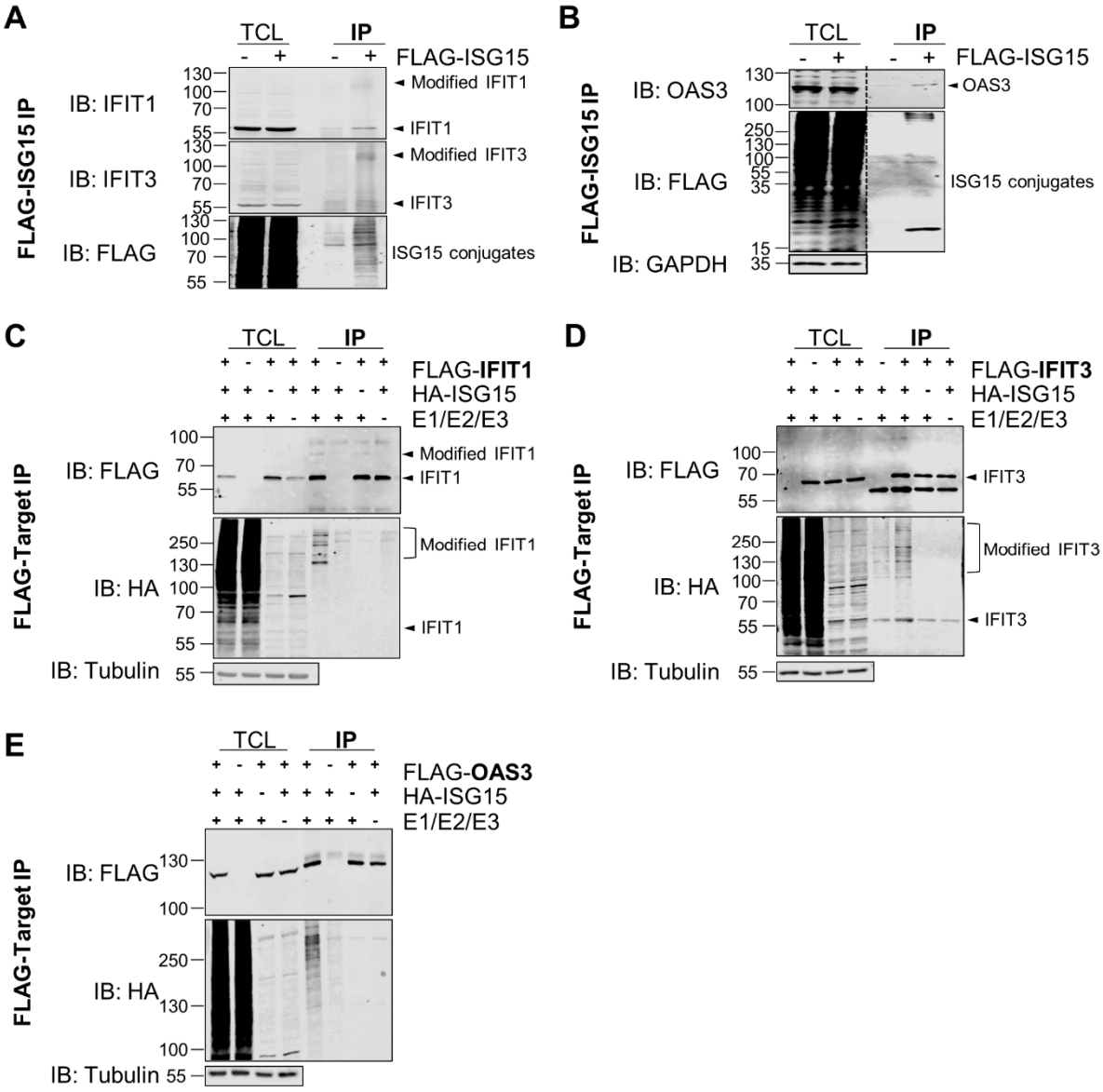

Figure 21: Validation of ISG15-modification of IFIT1, IFIT3, and OAS3.
(A-B) 3xFLAG-6xHis-ISG15-HeLa cells and controls were stimulated with IFNβ for 24 hours prior to FLAG-immunoprecipitation (IP) of ISG15. Total cell lysates (TCL) and FLAG-enrichment were immunoblotted against FLAG-ISG15, IFIT1 and IFIT3 (A), as well as OAS3 (B). Data are representatives of three independent experiments. **(C-E)** HeLa cells were transfected with a four-plasmid combination (HA-ISG15, Ube1L, Ube2L6, Herc5) and FLAG-tagged targets IFIT1 (C), IFIT3 (D), or OAS3 (E). Lysates were subjected to FLAG-immunoprecipitation and TCL and FLAG-IP samples were immunoblotted against FLAG, HA, and a loading control (Tubulin). Data are representatives of three independent experiments. (A), (C), and (D) were published in (Kespohl et al. 2020). Data in (A) were generated by Meike Kespohl.

5.4.2 Impact of ISG15 and ISGylation on IFIT1, IFIT3, and OAS3 stability

5.4.2.1 Impact of ISG15 on expression levels in CVB3 infected mice

ISG15 was recently described to influence DNA processing by accelerating replication fork progression (Raso et al. 2020). Thus, another potential influence of ISG15 on DNA, namely gene transcription, was investigated. To this end, mRNA was extracted from heart tissue of

wildtype and ISG15$^{-/-}$ mice at 0, 1.5, 3, 6 and 8 days post-CVB3 infection for qRT-PCR analysis of *Ifit1*, *Ifit3*, and *Oas3* expression (Fig. 22).

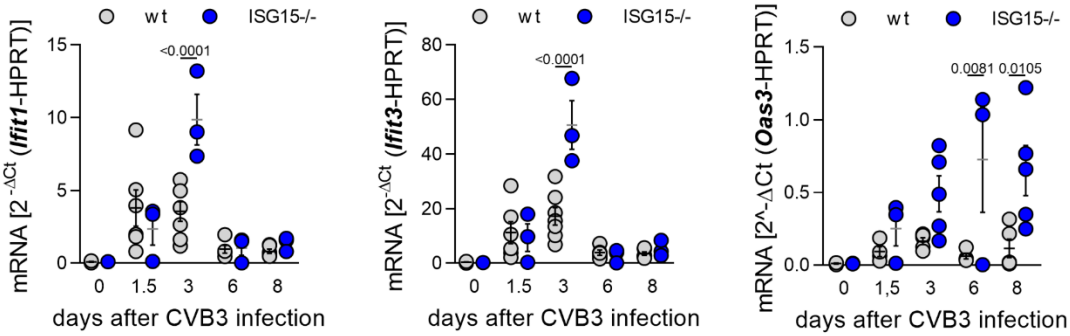

Figure 22: *Ifit1*, *Ifit3*, and *Oas3* gene transcription and protein expression levels in dependence of ISG15 *in vivo*.
Wildtype (wt) and ISG15$^{-/-}$ mice (n≥3) were infected with 10^5 pfu CVB3 Nancy strain for 3 and 8 days. Hearts were collected for analyses. Cardiac mRNA levels of *Ifit1*, *Ifit3*, and *Oas3* in relative to a housekeeping gene (HPRT). $2^{\Delta\Delta Ct}$ values are depicted. IFIT1/3 data were collected by Meike Kespohl and published in (Kespohl et al. 2020).

The mRNA of IFIT1 and IFIT3 in wildtype animals increased until day 3, then remained stable at low levels until day 8 (Fig. 22 A, panel 1 and 2). On day 3, their mRNA levels were significantly higher in ISG15$^{-/-}$ mice, suggesting an influence of ISG15 on *Ifit1* and *Ifit3* gene transcription. OAS3 mRNA levels remained relatively low in wildtype animals over the course of infection while levels in the ISG15$^{-/-}$ hearts increased until day 6 and only slightly decreased on day 8 with a significant difference towards wildtype levels on day 6 and day 8 (Fig. 22 A, panel 3).

Next, protein levels of IFIT1, IFIT3, and OAS3 were analysed by immunoblotting of heart lysates (data not shown). However, no conclusive evidence of IFIT1/3 protein levels could be gained in this approach. Moreover, OAS3 protein levels were undetectable in tissue lysates (data not shown), confirming the proteome analysis (Tab. S1), which also did not detect OAS3.

Even though higher levels of IFIT1, IFIT3, and OAS3 mRNA are present in ISG15$^{-/-}$ mice, this appears not to be reflected on the protein level. This might indicate an influence of ISG15 on protein expression or stability, or both.

5.4.2.2 Impact of ISG15 on IFIT1, IFIT3, and OAS3 expression levels *in vitro*

To further address the question how ISG15 influences IFIT1/3 and OAS3 protein expression, ISG15-deficient (ISG15ko) and control (ISG15wt) HeLa cells generated by CRISPR-Cas9 technology (Kespohl et al. 2020) were treated with 100 U/ml IFNβ and analysed for mRNA (Fig. 23 A) and protein expression of IFIT1 (Kespohl et al. 2020), IFIT3 (Kespohl et al. 2020), and OAS3 at the indicated timepoints (Fig. 23 B).

IFIT1 mRNA levels started to increase at 2 h of IFNβ-stimulation with notably higher mRNA levels in the ISG15$^{-/-}$ cells at 4 h and 8 h post-stimulation (Fig. 23 A panel 1, (Kespohl et al. 2020)). IFIT3 showed a similar trend but the difference in mRNA levels between ISG15ko and control cells only became apparent at 8 h of IFNβ-stimulation (Fig. 23 A, panel 2, (Kespohl et al. 2020)). Interestingly, this was not reflected on the protein levels of IFIT1 and IFIT3. After 8 h of IFNβ-stimulation, lower levels IFIT1 and IFIT3 protein were observed in the ISG15ko cells as compared to control cells (Fig. 23 B, (Kespohl et al. 2020)). This difference is limited to the early expression, as it was not apparent at 24 h of IFNβ-treatment. The negative feedback of ISG15 on type I IFN signaling (Zhang et al. 2015) could explain the increased mRNA levels of both, IFIT1 and IFIT3 in ISG15ko cells. However, protein levels show the exact opposite at the 8 h timepoint, suggesting that ISG15 might influence the stability of IFIT1 and IFIT3. The equal protein levels at 24 h post-stimulation could be due to higher mRNA production and thus more protein expression, potentially counteracting any observed stabilizing effects.

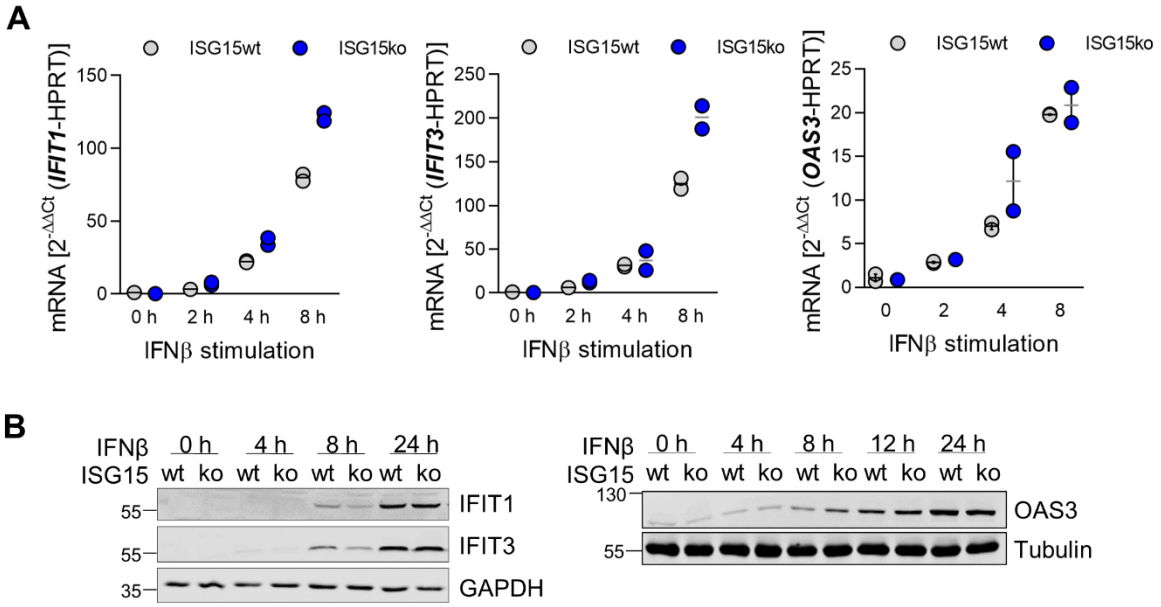

Figure 23: *Ifit1*, *Ifit3*, and *Oas3* gene transcription and protein expression levels in dependence of ISG15 *in vitro*.
(A) ISG15 knockout (ISG15ko) and wildtype control (ISG15wt) HeLa cells were generated with the CRISPR CAS9 technology. ISG15ko and ISG15wt cells were treated with IFNβ for the indicated timepoints and mRNA transcription of *IFIT1*, *IFIT3*, and *OAS3* were analysed by qRT-PCR relative to a housekeeping gene. $2^{\Delta\Delta Ct}$ values of a representative experiment (n=3) are depicted. **(B)** ISG15ko and ISG15wt HeLa cells were treated with IFNβ for the indicated timepoints, and lysates were analysed for expression of IFIT1, IFIT3, and OAS3 by western blot. GAPDH and Tubulin were used as loading controls. IFIT1/3 data in (A) and (B) were collected by Meike Kespohl and published in (Kespohl et al. 2020).

The same experimental setup was performed for OAS3. After stimulation with IFNβ, OAS3 mRNA levels differed between ISG15ko and control cells at 4 h but not at 8 h post-stimulation (Fig. 23 A, panel 3). By comparison, OAS3 protein levels at 8 h and 12 h of IFNβ-stimulation were only slightly higher in the ISG15ko cells than in the control (Fig. 23 B).

Here too, the lack of ISG15-mediated negative feedback on IFNβ-signaling (Zhang et al. 2015) could explain the higher levels of OAS3 mRNA in ISG15ko cells. As the initial difference in OAS3 mRNA levels dissipated over longer stimulation periods (Fig. 23 A, panel 3), the protein levels stabilized over time as well (Fig. 23 B), suggesting no lasting effect of ISG15 on OAS3 expression under the conditions of this *in vitro* experimental setup.
To investigate the opposing effects of ISG15 on mRNA and protein levels of IFIT1, IFIT3, and OAS3 expression, an experimental setup independent of IFNβ-mediated transcriptional regulation was used. IFIT1, IFIT3, and OAS3 cDNA was transfected into ISG15-deficient and control HeLa cells and their protein levels were investigated over a 24 h timeframe.
FLAG-tagged IFIT1 expression increased over time in wildtype cells, peaking at 24 h post-transfection (Fig. 24 A, first panel, (Kespohl et al. 2020)). In contrast, expression was delayed in the ISG15ko cells and was still severely lower in the ISG15$^{-/-}$ cells after 24 h as compared to wildtype. Similarly, IFIT3 expression was distinctly lower in ISG15ko cells at 8 h and 24 h post-transfection (Fig. 24 A, third panel, (Kespohl et al. 2020)), indicating an effect of ISG15 on the expression of both, IFIT1 and IFIT3. However, OAS3 expression was unaffected by the absence of ISG15 (Fig. 24 B), thus suggesting that the positive effect is specific to IFIT1 and IFIT3.

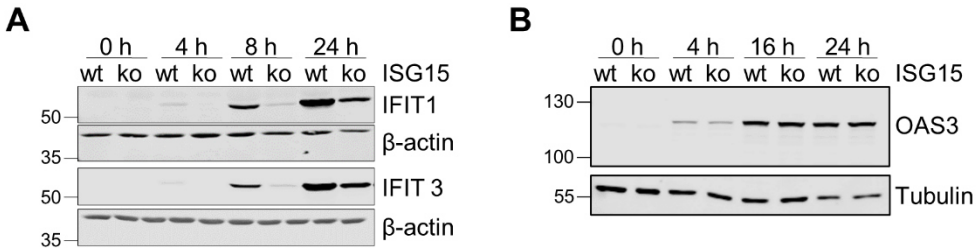

Figure 24: IFIT1, IFIT3, and OAS3 overexpression levels in dependence of ISG15 *in vitro*.
(A-B) ISG15ko and ISG15wt HeLa cells were transfected with plasmids encoding for IFIT1, IFIT3 (A), and OAS3 (B). Protein expression was analysed at the indicated timepoints by western blot. A representative experiment of n=3 is depicted. IFIT1/3 data in (A) were collected by Meike Kespohl and published in (Kespohl et al. 2020).

5.4.2.3 Impact of ISG15 on IFIT1, IFIT3, and OAS3 degradation

To investigate whether ISG15 and ISGylation influence the degradation of IFIT1, IFIT3, and OAS3, ISG15$^{-/-}$ and wildtype control HeLa cells were treated with IFNβ prior to a pulse-chase with cycloheximide (CHX) for 4, 8, 12 and 24 hours.
Cycloheximide inhibits protein translation by interfering with tRNA translocation in the ribosomes and is thus common reagent to investigate the half-life of a protein. Protein levels were analysed by western blot (Fig. 25) and quantified with the ImageStudio Lite Software.

Neither IFIT1 (Fig. 25 A), nor IFIT3 (Fig. 25 B), nor OAS3 (Fig. 25 C) half-life was influenced by ISG15. As OAS3 expression levels also did not appear to be modified by ISG15 (Fig. 24 B), it was concluded that OAS3 protein expression and stability are not impacted by ISG15.

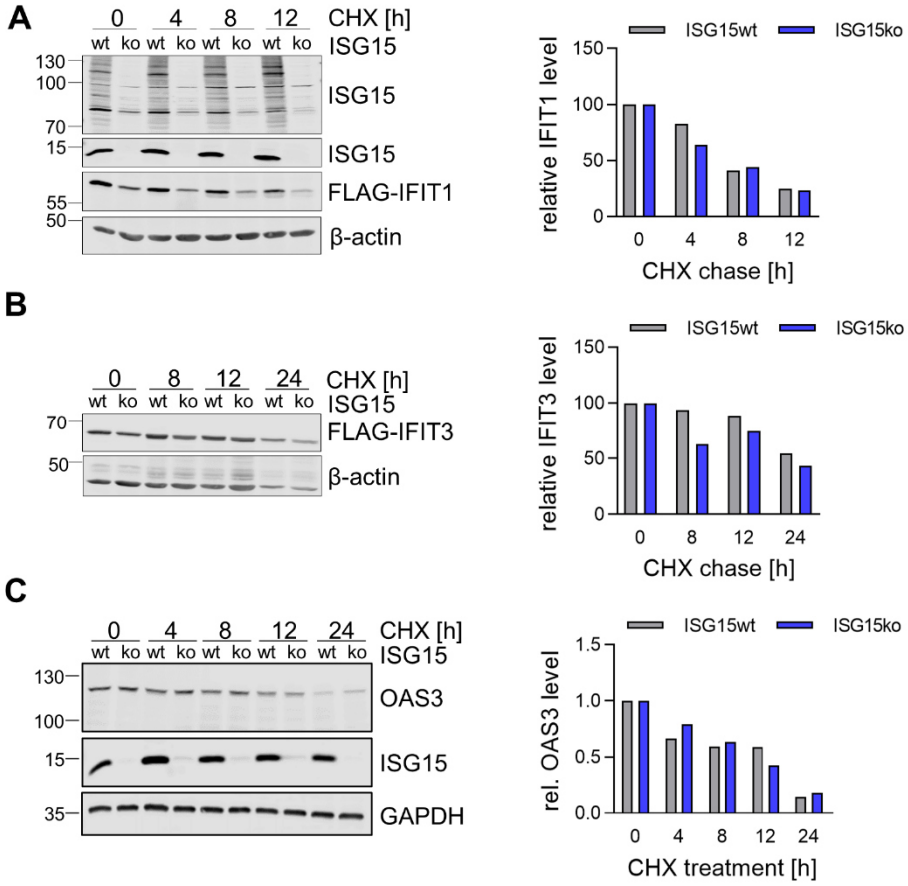

Figure 25: Impact of ISG15 on IFIT1, IFIT3, and OAS3 protein degradation.
(A-C) ISG15ko and ISG15wt HeLa cells were treated with IFNβ for 24 h prior to treatment with cycloheximide (CHX) to block protein translation. Protein levels of IFIT1 (A), IFIT3 (B), and OAS3 (C) were analysed by western blot and quantified based on loading controls with the ImageStudio Lite software. A representative experiment of n=3 is depicted. IFIT1/3 data in (A) and (B) were collected by Meike Kespohl.

5.4.2.4 Impact of ISGylation on IFIT1 and IFIT3 protein expression

To investigate whether the stabilizing effect on IFIT1/3 protein expression is mediated by free or conjugated ISG15, IFIT1/3 were transfected in ISG15ko cells in which ISG15 was rescued by exogenous expression of either ISG15-LRGG or an unconjugable ISG15-LRAA mutant (Fig. 26 A).

GFP expression served as control. Subsequently, ISGylation was induced by stimulation with IFNβ. Compared to the GFP control condition, IFIT1/3 levels were increased in the cells rescued by ISG15 (Fig. 26 B, (Kespohl et al. 2020)). Remarkably, IFIT1/3 expression was not rescued in the cells reconstituted with the unconjugable LRAA variant, strongly

indicating that protein expression of IFIT1/3 is positively influenced by ISGylation (Kespohl et al. 2020).

In summary, ISG15 and more specifically ISGylation exerts a stabilizing effect on IFIT1 and IFIT3 protein levels (Kespohl et al. 2020). This stabilization is independent of protein degradation.

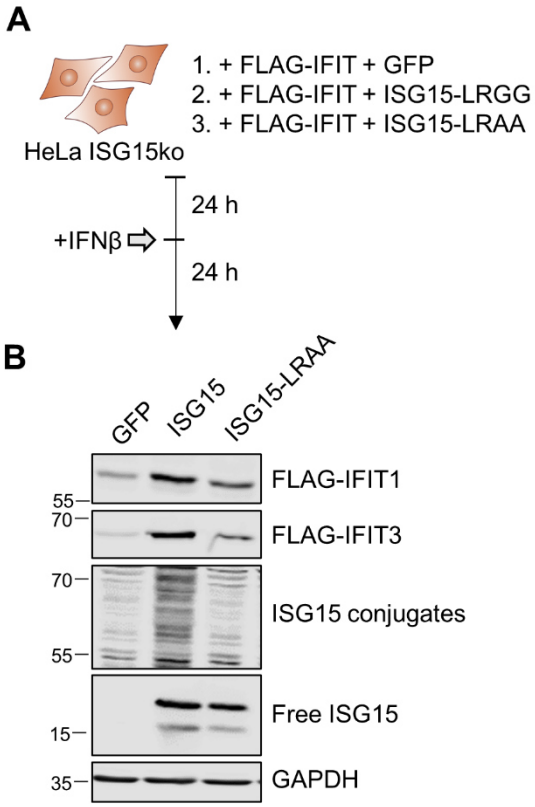

Figure 26: Impact of ISG15 expression rescue on IFIT1 and IFIT3 expression.
(A) ISG15ko HeLa cells were cotransfected with FLAG-tagged IFIT1 or IFIT3 together with either conjugable or unconjugable ISG15 (-LRGG and -LRAA, respectively) or a GFP control. After 24 h, cells were treated with IFNβ for another 24 h. **(B)** IFIT expression levels were analysed by western blot. Antibodies against FLAG-tag, ISG15, and GAPDH were used. Experiment was performed by Meike Kespohl and published in (Kespohl et al. 2020).

5.4.2.5 Impact of OAS3 on CVB3 infection

Even though no effect of ISG15/ISGylation on OAS3 protein expression and stability was apparent, the identified modification site K858 (Tab. S5) is located in close proximity to S855, an ATP binding site, and Mg^{2+} binding sites D867 and D869, suggesting a functional influence on OAS3-mediated oligoadenylate synthesis and thus antiviral activity (Silverman 2007). OAS3 has proven antiviral activity against West Nile, Sindbis, Influenza and VACV (Li et al. 2016) yet nothing is known about its impact on CVB3 infection. The antiviral effect of IFIT1/2/3 on CVB3 infection was recently demonstrated *in vitro* in IFIT1/2/3 triple-knockout cardiomyocytes by Kimura et al. in 2019 (Kimura et al. 2019).

Thus, the influence of OAS3 expression on CVB3 infection was analysed in an *in vitro* approach. First, OAS3 expression was inhibited by siRNA treatment prior to infection with CVB3 at an MOI of 0.1 and 1 (Fig. 27 A) with scrambled (Scr) siRNA as control. VP1 expression as an indicator of viral protein translation was analysed by immunoblot. Additionally, FLAG-tagged OAS3 was overexpressed prior to CVB3 infection at an MOI of 0.1. VP1 expression was analysed by immunoblot and compared to a GFP transfected control (Fig. 27 B).

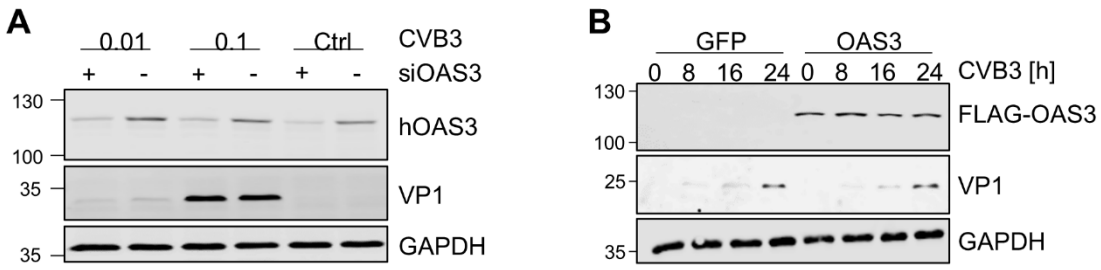

Figure 27: Impact of OAS3 expression on CVB3 infection in vitro
(A) OAS3 expression was knocked down with siRNA in HeLa cells. Scrambled (Scr) siRNA served as a control. Cells were subsequently infected with CVB3 at an MOI of 0.01 and 0.1 for 24 h and viral replication was assessed by VP1 expression on a western blot. **(B)** FLAG-tagged OAS3 was overexpressed in HeLa cells prior to CVB3 infection at an MOI of 0.1 for the indicated timepoints. GFP transfection served as negative control. The influence of OAS3 overexpression on viral replication was determined by VP1 expression. Antibodies against VP1, OAS3, FLAG, and GAPDH were used. Representative experiments of n=3 are depicted.

Despite successful manipulation of OAS3 expression, no difference in VP1 levels was detected in either downregulation (Fig. 27 A) or overexpression (Fig. 27 B) of OAS3, suggesting no effect of OAS3 expression on CVB3 infection in these specific *in vitro* experimental setups.

5.4.3 Validation of metabolic enzymes as ISGylation targets

Aside from ISGs as targets of ISGylation, a number of metabolic enzymes were found to be putative targets of ISG15-modification during CVB3 infection. As reflected by the GO analysis (Fig. 19), glycolytic enzymes were especially enriched among the ISG15-modification targets (Fig. 28).

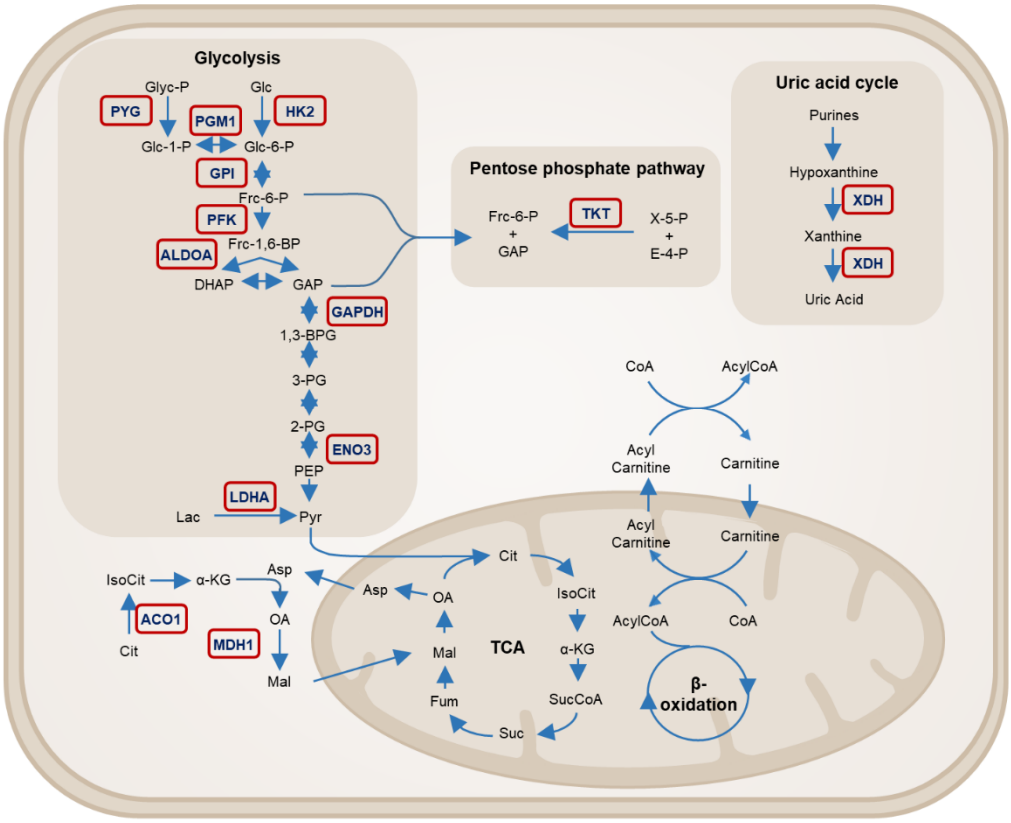

Figure 28: Diagram of metabolic pathways influenced by ISGylation as determined in the ISGylome analysis.
Metabolic enzymes that were found to be ISGylated in CVB3-infected cardiac tissue are depicted in their respective pathways. In glycolysis, PYG, PGM1, HK2, GPI, PFK, ALDOA, GAPDH, ENO3, and LDHA were modified by ISG15. Moreover, TKT of the pentose phosphate pathway and XDH of the uric acid cycle were ISGylated. The cytosolic forms of ACO1 and MDH1 were targets of ISGylation as well.

To verify their ISGylation, a selection of nine ISGylated enzymes were confirmed in a similar manner as IFIT1, IFIT3, and OAS3; FLAG-tagged fructose-bisphosphate aldolase A (ALDOA), delta(3,5)-delta(2,4)-dienoyl-CoA isomerase (ECH1), glyceraldehyde-3-phosphate dehydrogenase (GAPDH), hexokinase 2 (HK2), lactate dehydrogenase A (LDHA), malate dehydrogenase (MDH1), phosphofructokinase (PFK), glycogen phosphorylase (PYG) and xanthine dehydrogenase/oxidase (XDH) were transfected into HeLa cells together with HA-tagged ISG15 and the ISGylation machinery. As internal controls, each of the three components was replaced by an empty vector. A target is confirmed to be ISGylated if the FLAG-immunoprecipitation shows modification bands at higher molecular weight that are also detected in the HA-immunoblot.

ISGylation can be further confirmed by a FLAG signal in the HA-immunoprecipitation of HA-ISG15. Higher molecular weight bands visible on the immunoblot can either be due to multi-ISGylation, a mix of ISGylation and other posttranslational modifications such as ubiquitination, or a complex formation potentially initiated by ISGylation. Non-covalent association with ISG15 would result in the detection of free ISG15 and a lack of higher molecular weight target bands in the FLAG-target immunoprecipitation. No free ISG15 was detected in any target immunoprecipitation (data not shown).

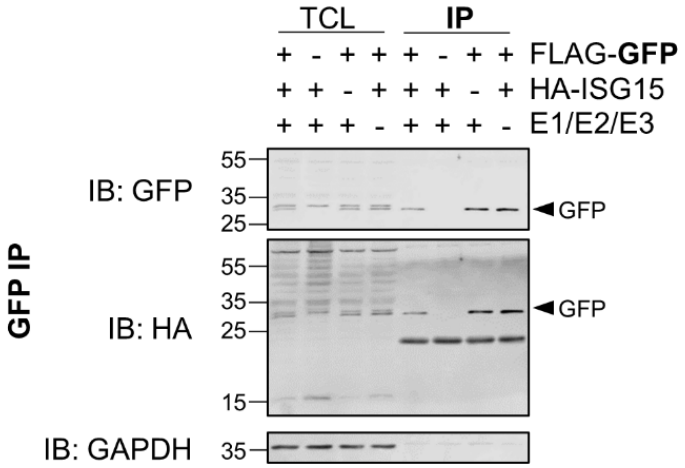

Figure 29: Target validation of GFP.
HeLa cells were transfected with EGFP control vector and a four-plasmid combination (HA-ISG15, Ube1L, Ube2L6, Herc5). GFP was enriched by immunoprecipitation and its modification was assessed by western blot. Antibodies against GFP, HA, and GAPDH were used. A representative of n=2 experiments is depicted.

To exclude that the experimental setup results in unspecific ISGylation of all transfected proteins, the experiment was performed with GFP, a protein known not to be ISGylated (Durfee et al. 2010). A GFP immunoprecipitation revealed a clear enrichment of the protein (Fig. 29, lane 5-8). However, no modification with ISG15 was detectable, neither in the GFP immunoblot nor the HA-ISG15 immunoblot (Fig. 29, lane 5). This validates the experimental setup and confirms the validity of the results achieved below.

5.4.3.1 Validation of HK2 as ISGylation target

HK2 is the enzyme responsible for trapping hexoses within the cell by catalyzing their phosphorylation (i.e., glucose to glucose-6-phosphate and fructose to fructose-6-phosphate), ensuring their continued processing in the glycolytic pathway. The LC-MS/MS analysis revealed one putative ISGylation site at K419 (Tab. S5). The FLAG-immunoblot showed marked enrichment of FLAG-tagged HK2 (Fig. 30, lane 5-8). Together with the ISGylation machinery and ISG15, a clear modification band just above the 130 kDa mark was visible in the FLAG-immunoblot (Fig. 30, lane 5), that overlapped with the signal in the HA-immunoblot, confirming that this higher molecular weight modification is indeed ISGylation. Interestingly, the modification band indicated by the arrow in Fig. 32 was also

slightly detected in the condition lacking HA-ISG15. Since transfection of cells induces ISG15 expression, this modification band is likely due to ISGylation with endogenous ISG15. In the HA-blot, three more ISGylated bands were detected, which are likely multi-ISGylated versions of HK2 or HK2-containing ISGylated protein complexes. When ISG15 was enriched by HA-immunoprecipitation, HK2 appeared to bind to the anti-HA magnetic beads (Fig. 32, lower panel, lane 5-8). Nonetheless, only the condition containing all relevant plasmids (Fig. 32, lower panel, lane 5) showed modification bands on the FLAG-immunoblot. This confirms that HK2 is indeed a substrate for ISGylation.

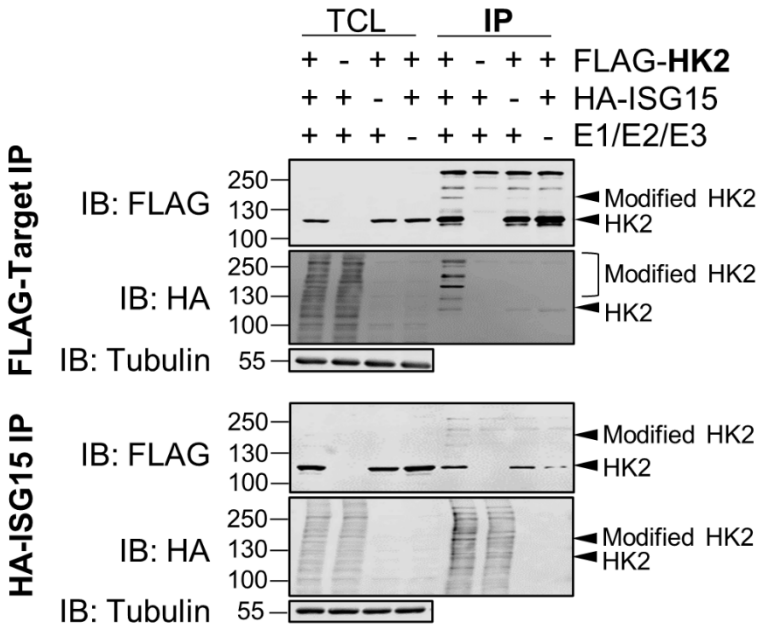

Figure 30: Target validation of hexokinase 2.
HeLa cells were transfected with FLAG-tagged HK2 and a four-plasmid combination (HA-ISG15, Ube1L, Ube2L6, Herc5). FLAG-tagged target and HA-tagged ISG15 were enriched by FLAG- and HA-immunoprecipitation, respectively. HK2 modification was assessed by western blot. Antibodies against FLAG, HA, and Tubulin were used. A representative of n=3 experiments is depicted.

5.4.3.2 Validation of PYG as ISGylation target

PYG is part of the glycogen metabolism catalyzing the cleavage of glycogen into glucose-1-phosphate to be used in glycolysis. The HA-immunoprecipitation did not show a distinct co-immunoprecipitation of PYG in the FLAG-immunoblot (Fig. 31, lower panel, lane 5-8), although the ISGylation pattern in the HA blot was distinctly different between the conditions with and without PYG (Fig. 31, lower panel, lane 5-6). Since it modifies a plethora of proteins within the cell, ISG15-immunoprecipitation might not enrich a single target to a quantity detectable by western blot. Thus, the lack of a putative target in ISG15-immunoprecipitation does not exclude ISGylation of this protein.

Indeed, in the FLAG-immunoprecipitation, which showed a clear enrichment of FLAG-tagged PYG (Fig. 31, upper panel, lane 5-8), two clear modification bands are detected

(Fig. 31, upper panel, lane 5). One at approximately 15 kDa higher than the unmodified PYG, which could be a mono-ISGylation. Another modification band was visible just above 130 kDa. Both modifications were also detected in the HA-blot (Fig. 31, lane 5), confirming PYG to be a target of ISGylation.

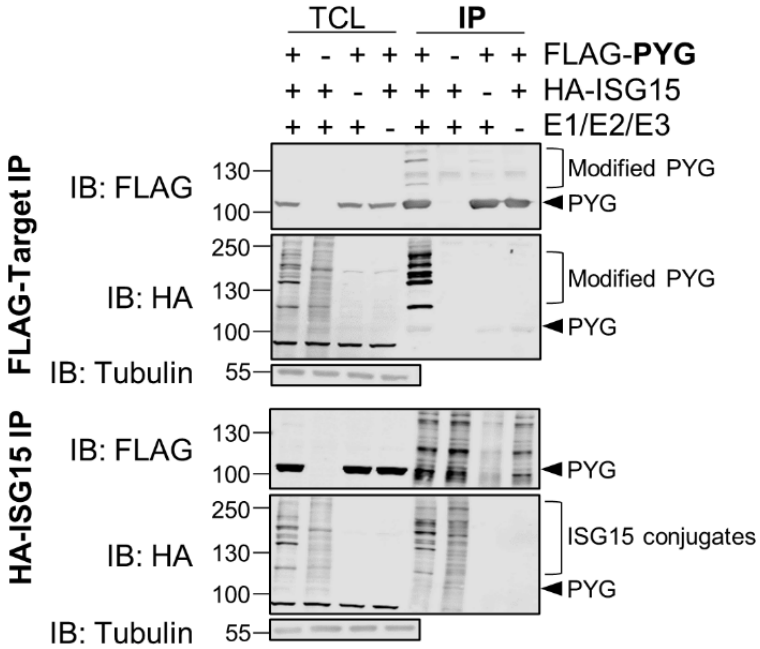

Figure 31: Target validation of glycogen phosphorylase.
HeLa cells were transfected with FLAG-tagged PYG and a four-plasmid combination (HA-ISG15, Ube1L, Ube2L6, Herc5). FLAG-tagged target and HA-tagged ISG15 were enriched by FLAG- and HA-immunoprecipitation, respectively. PYG modification was assessed by western blot. Antibodies against FLAG, HA, and Tubulin were used. A representative of n=3 experiments is depicted.

5.4.3.3 Validation of PFK as ISGylation target

The phosphorylation of fructose-6-phosphate to fructose-1,6-bisphosphate is catalyzed by PFK. FLAG-immunoprecipitation substantially enriched PFK (Fig. 32, upper panel, lane 5-8), and two clear modification bands can be observed when cotransfected with HA-ISG15 and the ISGylation machinery (Fig. 32, upper panel, lane 5), as well as in the control condition without HA-ISG15 (Fig. 32, upper panel, lane 7). This modification is likely due to endogenous ISG15 induced by the transfection.

The HA-immunoprecipitation revealed that PFK, like HK2, binds to the anti-HA magnetic beads to some extent (Fig. 32, lower panel, lanes 5-8). However, HA-ISG15 pulldown also showed a modification-band around 130 kDa in the FLAG-immunoblot as seen in the FLAG-PFK pulldown (Fig. 32, lower panel, lane 5). Thus, the HA-immunoblot confirmed PFK-ISGylation.

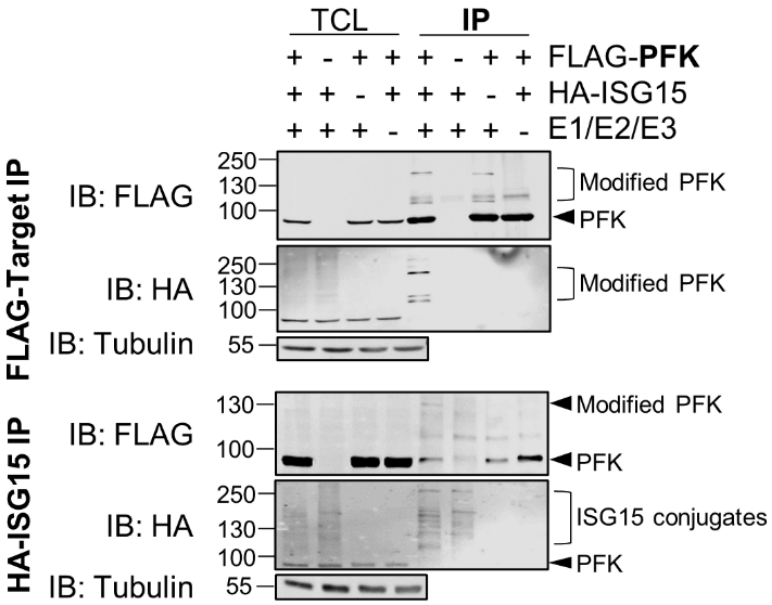

Figure 32: Target validation of phosphofructokinase.
HeLa cells were transfected with FLAG-tagged PFK and a four-plasmid combination (HA-ISG15, Ube1L, Ube2L6, Herc5). FLAG-tagged target and HA-tagged ISG15 were enriched by FLAG- and HA-immunoprecipitation, respectively. PFK modification was assessed by western blot. Antibodies against FLAG, HA, and Tubulin were used. A representative of n=3 experiments is depicted.

5.4.3.4 Validation of ALDOA as ISGylation target

ALDO A is the muscle specific form of the enzyme that catalyzes the formation of glyceraldehyde phosphate (GAP) and dihydroxyacetone phosphate (DHAP) from fructose-1,6-bisphosphate.

In the same manner as PFK, ALDOA was enriched in the FLAG-immunoprecipitation (Fig. 33, upper panel, lane 5-8), with higher weight modification bands in both conditions with and without HA-ISG15 (Fig. 33, upper panel, lane 5 and lane 7), suggesting that endogenous ISG15 is induced by transfection. The HA-immunoprecipitation showed that ALDOA binds to the anti-HA magnetic beads (Fig. 33, lower panel, lane 5-8). Nonetheless, a higher weight modification band was detected in the FLAG-immunoblot as well as in the HA-immunoblot (Fig. 33, lower panel, lane 5). The HA-immunoblot showed a different ISGylation pattern as the control lacking ALDOA (Fig. 33, lower panel, lane 5-6), suggesting that ALDOA is indeed ISGylated.

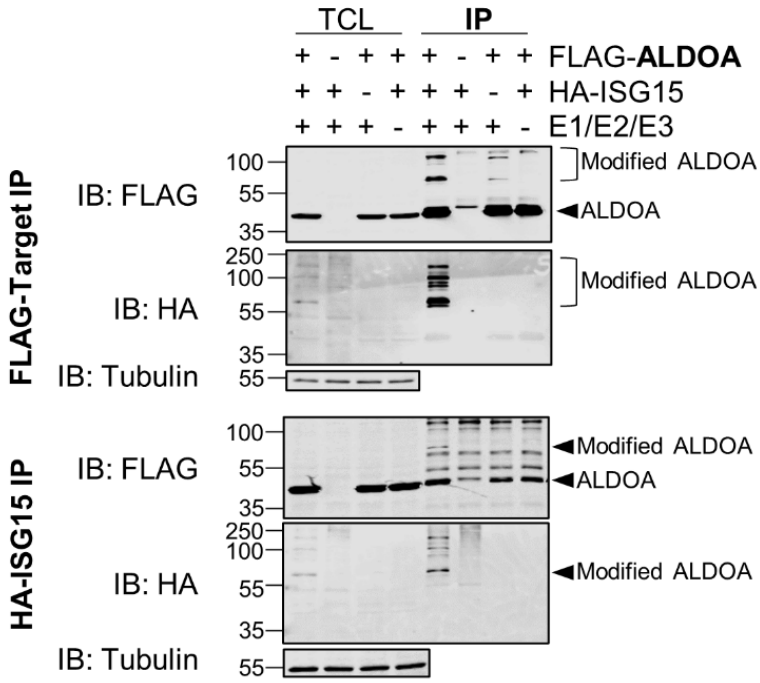

Figure 33: Target validation of aldolase A.
HeLa cells were transfected with FLAG-tagged ALDOA and a four-plasmid combination (HA-ISG15, Ube1L, Ube2L6, Herc5). FLAG-tagged target and HA-tagged ISG15 were enriched by FLAG- and HA-immunoprecipitation, respectively. ALDOA modification was assessed by western blot. Antibodies against FLAG, HA, and Tubulin were used. A representative of n=3 experiments is depicted.

5.4.3.5 Validation of GAPDH as ISGylation target

GAPDH is one of the key enzymes in glycolysis, catalyzing the transformation of glyceraldehyde-3-phoshpate to 1,3-bisphosphoglycerate. Together with enolase, it has been previously described as ISGylation target (Wong et al. 2006). In this study, it was not only confirmed to be modified by ISG15 *in vivo* but also to have at least two modification sites (Tab. S5 and S9). The FLAG-immunoprecipitation revealed an enrichment of two higher molecular weight modifications which overlap with the HA-mISG15 signal (Fig. 34, upper panel, lane 5). An additional band between the 100 and 250 kDa marker did not appear in the FLAG-immunoblot and could therefore be a larger ISGylated interaction protein that co-precipitated with GAPDH. The HA-immunoprecipitation revealed a FLAG signal at the height of mono-ISGylated GAPDH which overlapped with a band in the HA-immunoblot, confirming ISGylation of GAPDH (Fig. 34, lower panel, lane 5).

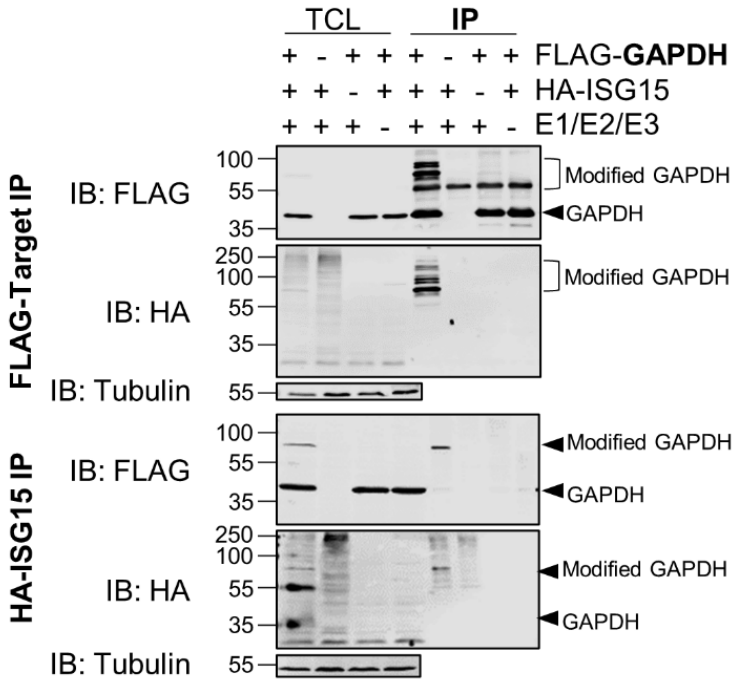

Figure 34: Target validation of glyceraldehyde dehyrogenase.
HeLa cells were transfected with FLAG-tagged GAPDH and a four-plasmid combination (HA-ISG15, Ube1L, Ube2L6, Herc5). FLAG-tagged target and HA-tagged ISG15 were enriched by FLAG- and HA-immunoprecipitation, respectively. GAPDH modification was assessed by western blot. Antibodies against FLAG, HA, and Tubulin were used. A representative of n=3 experiments is depicted.

5.4.3.6 Validation of LDH as ISGylation target

The interconversion of lactate and pyruvate is catalyzed by the LDH. As seen in Fig. 37, there is evidence of a mono-ISGylation of LDH already in the TCL, where a modification band was detected at approximately 15 kDa above the expected molecular weight of LDH at 36 kDa (Fig. 35, lower panel, lane 1).

Moreover, this band was enriched in the FLAG-immunoprecipitation and detected in the HA-immunoprecipitation on both, FLAG and HA-immunoblots (Fig. 35, upper and lower panel, lane 5). It was also slightly visible in the control lacking HA-ISG15 which could again be endogenous ISG15 being attached to the target (Fig. 35, upper panel, lane 7). Additionally, FLAG-immunoprecipitation revealed a higher molecular weight band above 100 kDa, which gave a strong signal in the HA-immunoblot as well (Fig. 35, upper panel, lane 5). In the HA-immunoblot, further modification bands were detected, which could be ISGylated non-covalent interaction partners of LDH.

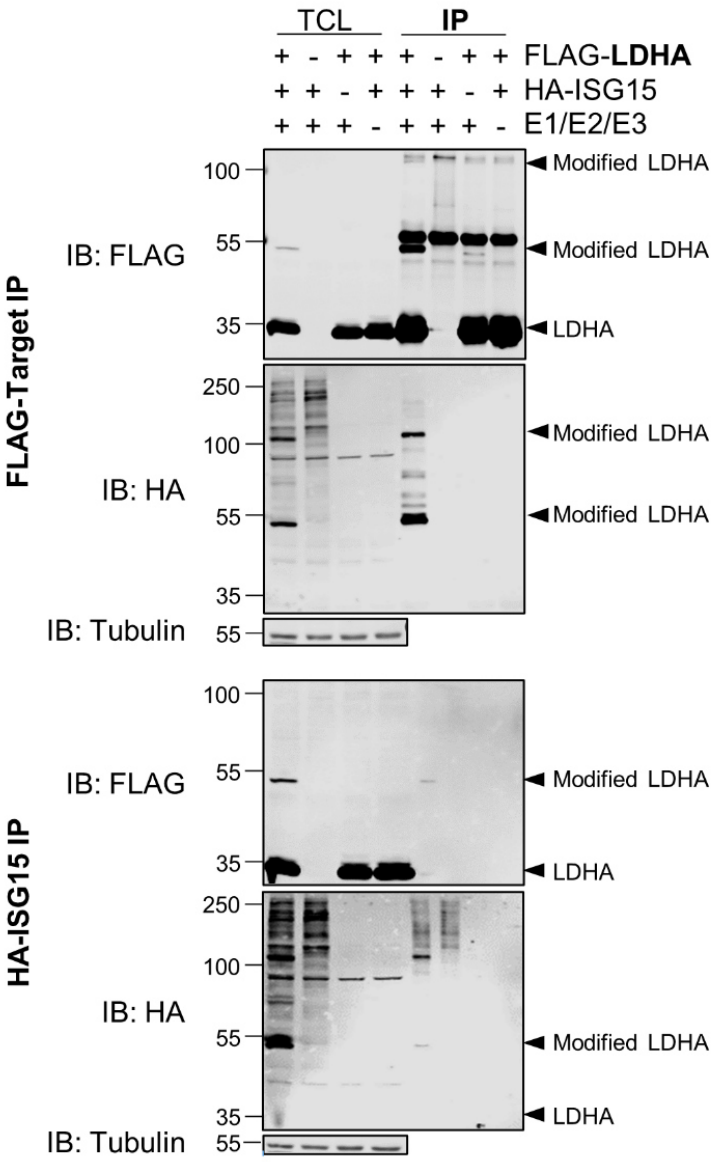

Figure 35: Target validation of lactate dehydrogenase.
HeLa cells were transfected with FLAG-tagged LDHA and a four-plasmid combination (HA-ISG15, Ube1L, Ube2L6, Herc5). FLAG-tagged target and HA-tagged ISG15 were enriched by FLAG- and HA-immunoprecipitation, respectively. LDHA modification was assessed by western blot. Antibodies against FLAG, HA, and Tubulin were used. A representative of n=3 experiments is depicted.

5.4.3.7 Validation of MDH1 as ISGylation target

The malate dehydrogenase has two isoforms, MDH1 and 2. MDH2 is located to the mitochondria where it participates in the citric acid cycle by catalyzing the conversion of malate to oxaloacetate. MDH1 on the other hand is located to the cytoplasm where it plays a role in the malate-aspartate shuttle ensuring that malate can pass across the mitochondrial membrane to be used in the citric acid cycle. In this study, the cytoplasmatic MDH1 was identified as bona fide ISGylation target (Tab. S5 and S9), which was sought to be confirmed *in vitro*.

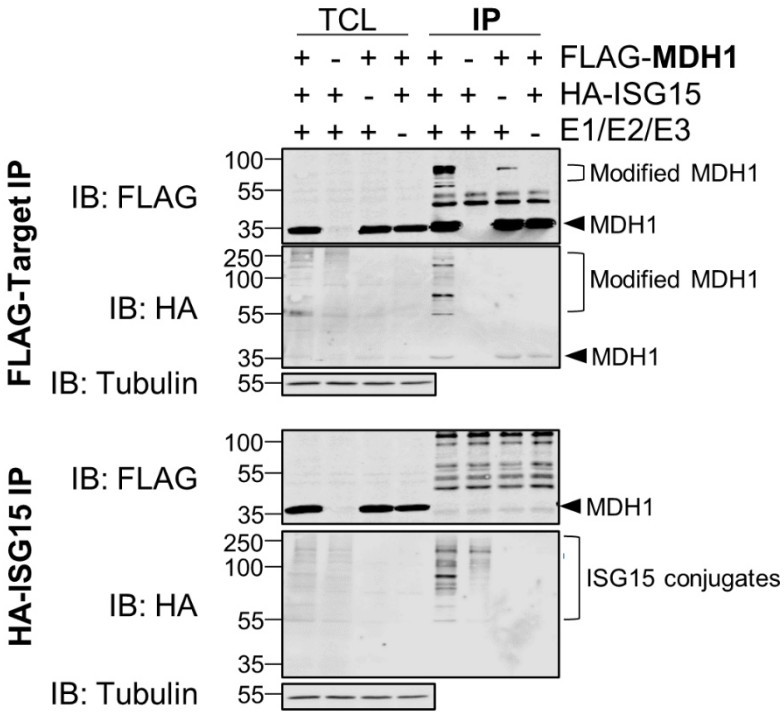

Figure 36: Target validation of Malate dehydrogenase 1.
HeLa cells were transfected with FLAG-tagged MDH1 and a four-plasmid combination (HA-ISG15, Ube1L, Ube2L6, Herc5). FLAG-tagged target and HA-tagged ISG15 were enriched by FLAG- and HA-immunoprecipitation, respectively. MDH1 modification was assessed by western blot. Antibodies against FLAG, HA, and Tubulin were used. A representative of n=3 experiments is depicted.

The FLAG-immunoprecipitation enriched two higher molecular weight modifications of MDH1, one of which can also be seen in the control lacking HA-ISG15 albeit to a lesser extent (Fig. 36, upper panel, lane 5 and 7). This could once again be endogenous ISG15 or another modification type, as discussed above. The HA-immunoblot confirmed the modification bands to be ISGylated and revealed another ISGylation band at approx. 130 kDa, which was not found in the FLAG-immunoblot, indicating a potential coprecipitation of an ISGylated high molecular weight interaction partner of MDH1 (Fig. 36, upper panel, lane 5). The HA-immunoprecipitation did not show any specific signals in the FLAG-immunoblot, however, the ISGylation pattern of the HA-immunoblot showed the same distinct modification band already detected in the FLAG-immunoprecipitation (Fig. 36, lower panel, lane 5). Thus, MDH1 was confirmed to be a target of ISGylation.

5.4.3.8 Validation of ECH1 as ISGylation target

ECH1 is located to the mitochondria where it isomerizes 3-trans, 5-cis-dienoyl-CoA to 2-trans, 4-trans-dienoyl-CoA as part of the auxiliary steps of the fatty acid β-oxidation pathway ensuring the successful processing of unsaturated fatty acids. As a mitochondrial protein, ECH1 possesses a mitochondrial transit sequence of approximately 3.5 kDa which is cleaved off in the mature protein, resulting in two bands on the FLAG-immunoblot (Fig. 37, upper panel); one band corresponding to the mature protein at ~35 kDa and another band

slightly above corresponding to the unprocessed version containing the transit sequence. While the mature protein is predominant in the total cell lysate, both bands are highly enriched in the FLAG-immunoprecipitation (Fig. 37, upper panel, lane 5-8).

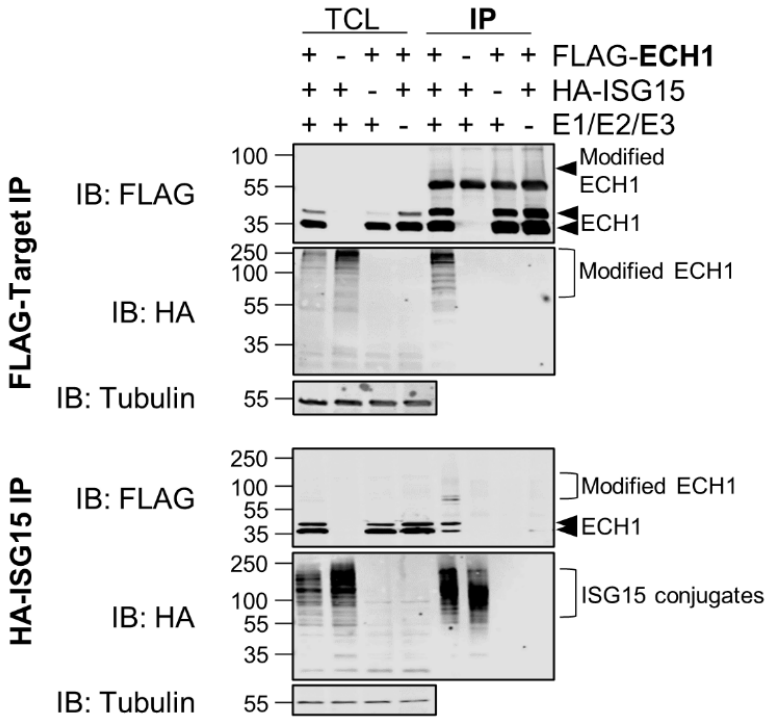

Figure 37: Target validation of delta(3,5)-delta(2,4)-dienoyl-CoA isomerase.
HeLa cells were transfected with FLAG-tagged ECH1 and a four-plasmid combination (HA-ISG15, Ube1L, Ube2L6, Herc5). FLAG-tagged target and HA-tagged ISG15 were enriched by FLAG- and HA-immunoprecipitation, respectively. ECH1 modification was assessed by western blot. Antibodies against FLAG, HA, and Tubulin were used. A representative of n=3 experiments is depicted.

The FLAG-immunoprecipitation further enriched a higher molecular weight modification of ECH1 (Fig. 37, upper panel, lane 5 and 7). The HA-immunoblot confirmed the modification bands to be ISGylated and revealed other ISGylation bands at higher molecular weight (Fig. 37, upper panel, lane 5). The HA-immunoprecipitation further showed specific signals for the mature and immature versions of ECH1 in the FLAG-immunoblot, as well as higher molecular weight bands (Fig. 37, lower panel, lane 5). The ISGylation pattern of the HA-immunoblot did not show any specific signals (Fig. 37, lower panel, lane 5). This confirms ECH1 as target of ISGylation.

5.4.3.9 Validation of XDH as ISGylation target

XDH catalyzes two reactions in the purine degradation pathway: the oxidation of hypoxanthine to xanthine and further to uric acid. This study detected a CVB3-dependent upregulation of XDH on the proteomic level (Fig. 11) as well as two putative ISGylation sites (Tab. S5 and S9). HA-immunoprecipitation of ISG15 did not reveal a relevant XDH-coimmunoprecipitation, as XDH appears to bind to the HA magnetic beads (Fig. 38, lower

panel, lane 5-8) and the enriched ISGylation pattern does not differ between the conditions with and without XDH (Fig. 38, lower panel, lane 5-6). However, this does not exclude XDH as target for covalent modification with ISG15, as explained above (section 5.4.3.1). Concordantly, two slight modification bands can be observed in the FLAG-immunoprecipitation overlapping with the signal in the HA-immunoblot (Fig. 38, upper panel, lane 5). Thus, XDH as target of ISGylation was validated *in vitro*.

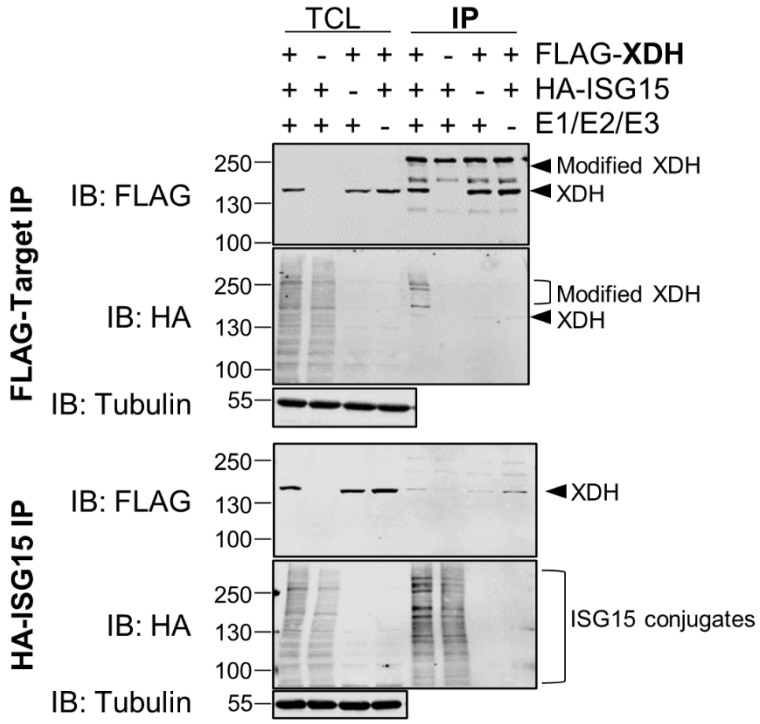

Figure 38: Target validation of Xanthine dehydrogenase.
HeLa cells were transfected with FLAG-tagged XDH and a four-plasmid combination (HA-ISG15, Ube1L, Ube2L6, Herc5). FLAG-tagged target and HA-tagged ISG15 were enriched by FLAG- and HA-immunoprecipitation, respectively. XDH modification was assessed by western blot. Antibodies against FLAG, HA, and Tubulin were used. A representative of n=3 experiments is depicted.

5.4.4 Investigation of identified ISGylation sites of LDH, HK2, and PFK

To investigate whether mutation of the modification sites determined in section 5.3 change the ISGylation pattern observed on the western blot, mutagenesis PCR was performed on LDH, HK2, and PFK (Tab. 6).

Tab. 6: ISGylation site mutagenesis. Identified ISGylation sites on HK2, LDH, and PFK were subjected to site-directed mutagenesis. Modified K residues were mutated to R, rendering them unsuitable for ISGylation.

Target	ISGylation site	Site mutation
LDH	K59	K59R
HK2	K419	K419R
PFK	K372 & K727	K372R & K727R

First, expression levels of the mutants compared to the wildtype enzymes were analyzed to confirm equal expression levels. As seen in Fig. 39 A-C, all generated mutants showed the same expression levels as the wildtype enzymes.

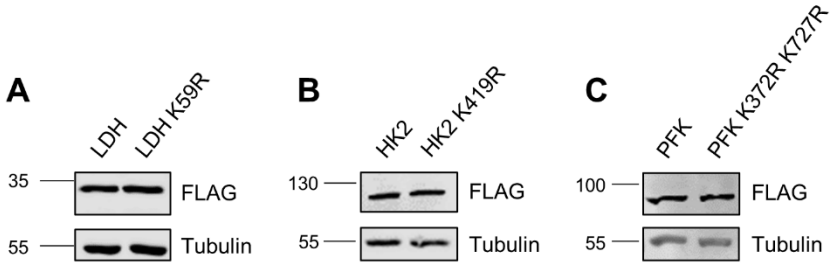

Figure 39: K to R mutation of identified ISGylation sites does not change enzyme expression pattern.
(A-C) K to R ISGylation site mutants were generated using site-directed mutagenesis of LDH K59 (A), HK2 K419 (B), and PFK K372 and K727 (C). Equal expression was validated by transfection into HeLa cells with subsequent western Blot analysis. Antibodies against FLAG and Tubulin were used.

Next, the generated mutants were cotransfected into HeLa cells together with HA-tagged ISG15 and the ISGylation machinery, as described in section 5.4.3.

Immunoprecipitation of FLAG-tagged target and subsequent western blot analysis was used to analyse ISGylation patterns of wildtype and mutated targets. K to R mutation of the identified ISGylation sites did not change the ISGylation pattern of either LDH (Fig. 40 A), HK2 (Fig. 40 B) or PFK (Fig. 40 D) as seen on the immunoblot analyses. However, this *in vitro* system only suggests that the ISGylation-potential is not limited to specific K residues. This is supported by a lack of an ISGylation motif (Radoshevich et al. 2015; Zhang et al. 2019), indicating that any surface-oriented K residue can be modified. The experimental setup employed here allows no conclusions about whether *in vivo* ISGylation at the identified sites could have an effect on protein function.

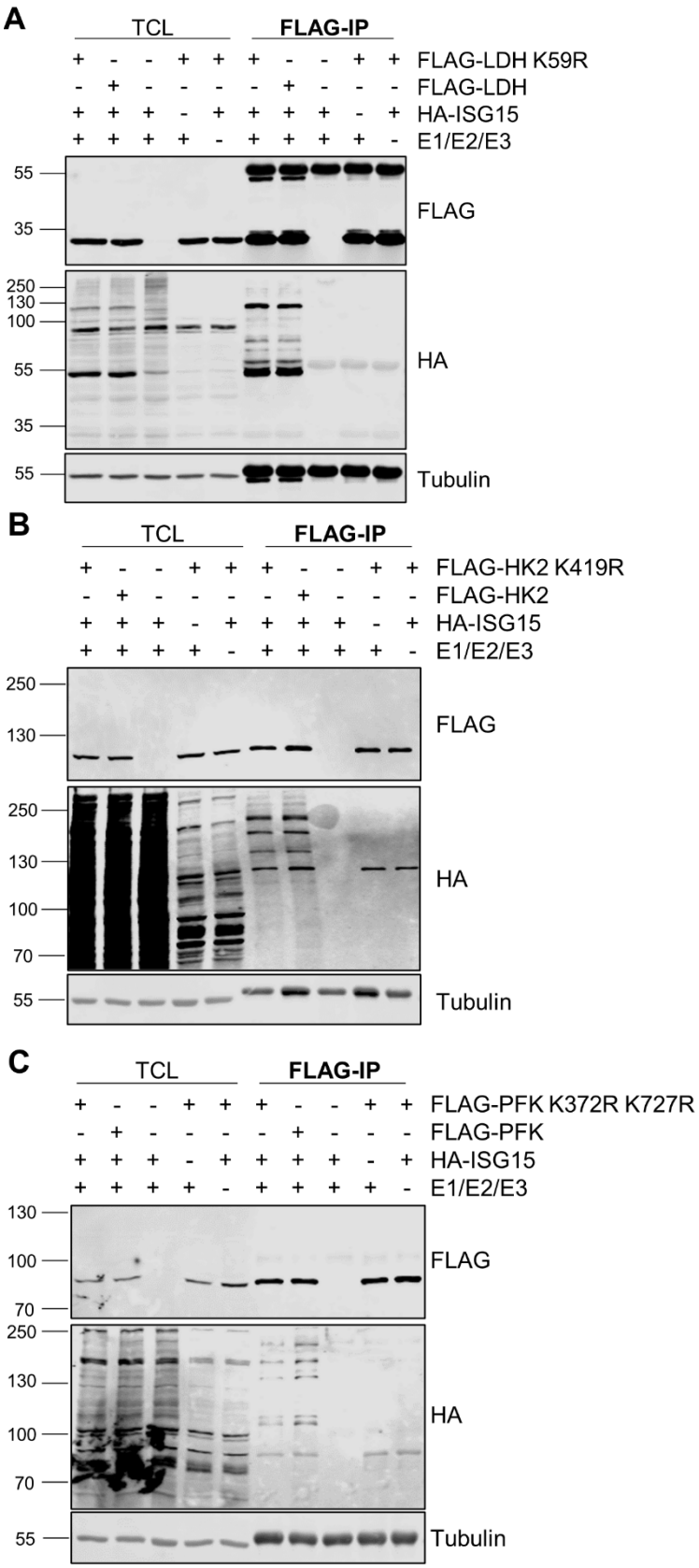

Figure 40: Analysis of K to R mutation on ISGylation pattern of glycolytic enzymes. Site mutants of LDH K59 **(A)**, HK2 K419 **(B)**, and PFK K372 and K727 **(C)** and their respective wildtypes were cotransfected wildtype and K/R site mutants together with HA-ISG15 and the ISGylation machinery. ISGylation pattern analysis was achieved by western blot. Antibodies against FLAG, HA, and Tubulin were used. A representative of n=3 experiments each is depicted.

5.4.5 Influence of ISGylation on metabolic target protein function

ISGylation has previously been observed to modify target protein function, depending on the location of the ISGylated K residue within the protein. As detailed in section 2.3.2, ISGylation of Nedd4 and PKR inhibits and activates the target proteins, respectively (Okumura et al. 2008; Okumura et al. 2013). Moreover, ISGylation has recently been shown to inhibit LDH activity, as well as downregulating glycolysis in primary adipocytes (Yan et al. 2021).

5.4.5.1 Impact of ISGylation on HK2 and PFK enzyme function

To assess the influence of ISGylation on HK2 and PFK, enzyme specific activity assays were performed subsequent to enrichment of the targets by FLAG-immunoprecipitation. Cell lysates of HeLa ISG15ko (Kespohl et al. 2020) cells were cotransfected with HA-tagged ISG15, FLAG-tagged HK2 or PFK, and the ISGylation machinery to avoid ISGylation by endogenous ISG15. Enzyme cotransfection with GFP instead of ISG15 served as baseline measurement.

As seen in Fig. 41, HK2 (Fig. 41 A) and PFK (Fig. 41 B) activity was negatively influenced by ISGylation. In the case of HK2, ISGylation decreased the enzyme's activity by approximately 50%, while K to R mutation of the identified ISGylation site (Tab. 6) resulted in a rescue of activity back to baseline levels. While the activity of ISGylated PFK significantly decreased as well, mutation of the two identified ISGylated residues K372 and K727 was unable to rescue activity levels (Fig. 41 B).

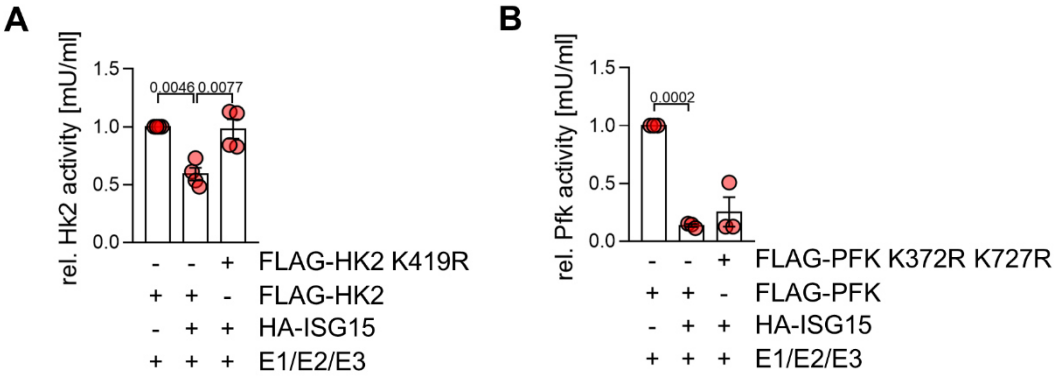

Figure 41: Impact of ISGylation on HK2 and PFK enzymatic activity.
(A-B) ISG15ko HeLa cells were cotransfected with wildtype or K/R site mutants of HK2 (n=4) (A) and PFK (n=3) (B) together with ISG15 and the ISGylation machinery. The enzymes were enriched by FLAG-IP and their function was analysed based on colorimetric measurement of substrate turnover. Measured activities were calculated back to expression levels and depicted relative to wildtype enzymatic function. One- and two-sample *t*-tests were performed to calculate *p*-values.

As shown in the co-immunoprecipitation studies (Fig. 40), this *in vitro* overexpression setup does not lead to specific residue modification. Thus, it is likely that other surface-oriented K residues are ISGylated as well. In the case of PFK, this appears to result in ISGylation of a

residue in proximity to an active site or substrate binding domain and thus reduced enzymatic activity. As K327 and K727 are not within any functional domains, mutation of these residues does not rescue PFK activity. HK2 K419 on the other hand is located close to glucose-6-phosphate and ATP binding domains. Thus, K419R-mediated abrogration of ISGylation rescues HK2 activity independent of other potential residues that would be modified in this setup.
Together with the already published negative effect of ISGylation on LDH activity (Yan et al. 2021), these data could point towards a negative effect of ISGylation on glycolysis.

5.4.5.2 Impact of ISG15 on glycolysis in primary cardiomyocytes

To gain insight into the influence of ISG15 on glycolytic function in a cellular environment, glycolytic rates were analyzed in primary cardiomyocytes using Seahorse metabolic measurement. Primary cardiomyocytes were cultured in low glucose medium prior to measurement, resulting in a low initial glycolytic rate.
Similar to the mitochondrial oxidative phosphorylation stress test (Fig. 14), during measurement in the Seahorse XFe96 analyzer, cells are sequentially exposed to glucose, rotenone/myxothiazol, and FCCP/monensin (Fig. 42). Notably, total ECAR levels are not completely proportional to glycolytic levels, as mitochondrial CO_2 production contributes to extracellular acidification along with other factors. As CO_2 production is proportional to oxygen consumption, CO_2 production as calculated by OCR levels is subtracted from total ECAR readings to calculate the proton efflux rate (PER). Together with the buffer factor of the assay solution, this allows for calculation of the proton efflux during glycolysis. Thus, the PER is a more precise reflection of glycolysis than ECAR (Mookerjee and Brand 2015).
First, injection of glucose provides an oversaturation of glycolytic substrate, which leads to a rapid increase in glycolysis and thus PER levels (Fig. 42). Rotenone and myxothiazol inhibit complex I and III of the respiratory chain, respectively and their injection results in shut-down of mitochondrial respiration. Consequently, glycolytic levels are increased further to cover the cellular ATP demand. Nonetheless, the protein gradient established prior to inhibition of complex I and III could result in remaining ATP production by the ATP synthase. Furthermore, other cellular ATPases, such as Na^+/K^+-ATPases are still able to contribute to cellular ATP production. Thus, to calculate the true maximal glycolytic capacity of the cells, FCCP and monensin are injected to the wells, which then dissolve the mitochondrial membrane potential and inhibit other cellular ATPases, respectively. This results in glycolysis as the sole ATP production pathway, leading to maximal PER levels (Fig. 42, (Mookerjee and Brand 2015)). Based on the resulting measurements and including specific parameters, i.e., buffer factor of the assay medium and well volume, basal and maximal

cellular glycolytic rates are determined. Additionally, the glycolytic reserve and the cellular ATP coverage by glycolysis can be calculated.

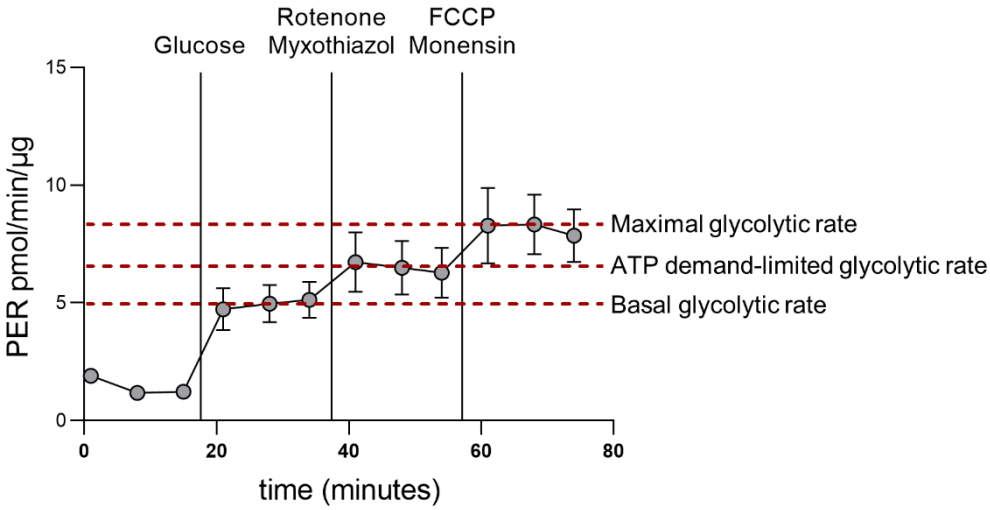

Figure 42: Seahorse measurement and injection strategy of glycolysis stress test.
Proton Efflux Rate (PER) over time normalized to the protein content of wildtype cardiomyocytes is displayed. After three measurement cycles under basal conditions, the indicated substrates/inhibitors are injected causing changes in ECAR levels. These changes then allow for calculation of different parameters: basal and maximal glycolysis, glycolytic reserve, and cellular ATP demand covered by glycolysis.

Wildtype and ISG15$^{-/-}$ primary cardiomyocytes were infected with CVB3 at an MOI of 1 prior to measurement of glycolytic function (Fig. 43). In contrast to mitochondrial respiration as determined by OCR (Fig. 15), CVB3 infection did not lead to increased glycolysis in wildtype primary cardiomyocytes, as determined by PER calculations (Fig. 43 A). Additionally, ISG15$^{-/-}$ primary cardiomyocytes displayed a tendency towards higher glycolytic levels, already during baseline conditions (Fig. 43 A). When infected with CVB3, ISG15$^{-/-}$ cells appear to slightly increase their glycolytic levels in comparison to wildtype control conditions (Fig. 43 A). These findings are mirrored in the ATP-demand limited glycolytic rates (Fig. 43 B), where ISG15$^{-/-}$ cells showed a tendency toward higher cellular ATP demand covered by glycolysis in all conditions. The maximum glycolytic capacity on the other hand appeared similar in control conditions (Fig. 43 C). During CVB3 infection, ISG15$^{-/-}$ cells again displayed a tendency toward higher maximal glycolytic levels than wildtype (Fig. 43 C), while glycolytic reserve capacities remained unchanged between genotypes and employed conditions. (Fig. 43 D).

During CVB3 infection, not all cells in the heart will be infected directly. Instead, the cytokine and chemokine signaling establishes an antiviral state. To mimic this cardiac antiviral state, wildtype and ISG15$^{-/-}$ primary cardiomyocytes were stimulated with IFNβ for 24 h prior to Seahorse analysis (Fig. 43). Reflecting the results of the CVB3 infected cells, IFNβ stimulation did not increase glycolytic rates in wildtype cardiomyocytes yet induced a slight increase in glycolytic levels in ISG15$^{-/-}$ cells (Fig. 43 A). The same result was observed when

calculating the coverage of the cellular ATP demand by glycolysis induced by IFNβ (Fig. 43 B). Here, the maximal glycolytic capacity in both, wildtype and ISG15$^{-/-}$ cells was slightly elevated (Fig. 43 C), while the glycolytic reserve capacities showed slightly higher levels in wildtype than in ISG15$^{-/-}$ cardiomyocytes (Fig. 43 D), indicating that under IFNβ stimulation, ISGylation does not impair the cellular capacity to upregulate glycolytic levels. In summary, these data indicate that ISG15 might negatively regulate glycolysis, as ISG15$^{-/-}$ cardiomyocytes displayed continuously higher levels than wildtype cells.

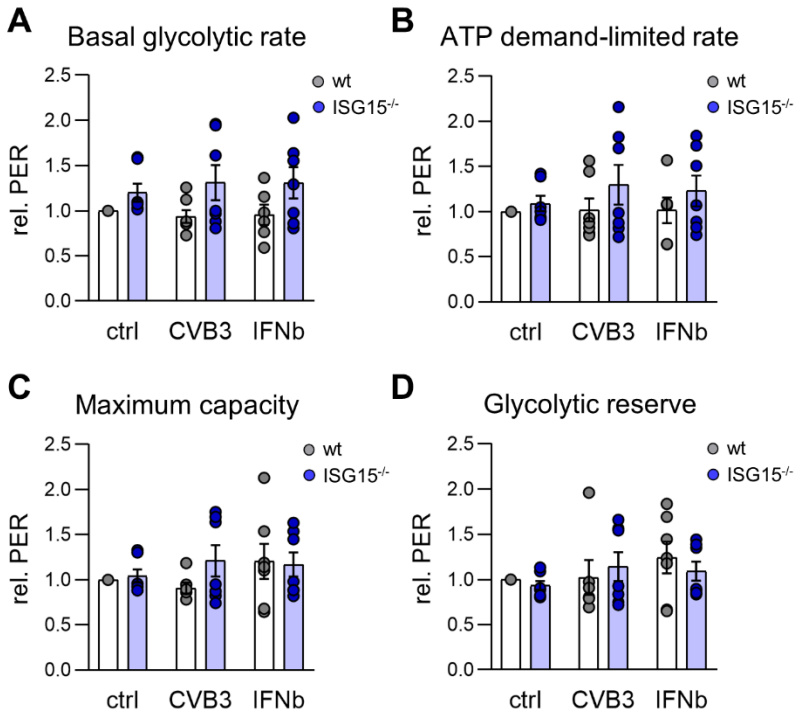

Figure 43: Measurement of glycolytic rates in primary cardiomyocytes.
Primary cardiomyocytes of wildtype (wt) and ISG15$^{-/-}$ mice were infected with CVB3 at an MOI of 1 for 6 h or treated with 100 U/ml murine IFNβ prior to analysis in a Seahorse XF Analyzer. **(A-D)** Calculated parameters based on PER per µg protein: **(A)** basal glycolytic rate, **(B)** cellular ATP demand covered by glycolysis, **(C)** maximal glycolytic capacity, and **(D)** glycolytic reserve. A collection of n=7 experiments is depicted.

6 Discussion

Over the last decade, ISG15 has been put into focus of several immunologic reactions. As part of the innate immunity, it has been proven protective against a plethora of infections (Perng and Lenschow 2018) with its modes of action manifold, depending on cellular localization and whether it operates as free or conjugated effector protein. In CVB3 infection, ISG15 alleviates viral load and viral myocarditis through direct antiviral function in its role as ubiquitin-like modifier (Rahnefeld et al. 2014). Hence, stabilizing ISGylation by inhibition of the deISGylating function of USP18 leads to increased resistance to CVB3 (Kespohl et al. 2020). Furthermore, ISG15 has been implicated in metabolic function, as it was reported to shield mitochondria from mitophagy and to maintain mitochondrial oxidative function in several cell types (Baldanta et al. 2017; Alcala et al. 2020). In CVB3 infection, ISG15 has been shown to be involved in the reprogramming of the central liver metabolism, reacting to infection-induced alterations in energy demand with increasing mitochondrial respiration (Kespohl et al. 2020). To elucidate the cellular pathways and functions influenced by ISG15 and ISGylation, this study identified the *in vivo* cardiac proteome, ISGylome, and ubiquitylome in CVB3 infection. The effects of ISGylation on other ISGs were addressed *in vitro* and cardiac respiratory function was investigated in dependence of ISG15/ISGylation *in vitro* and *in vivo*. As several glycolytic target proteins were identified over the course of infection, the impact of ISG15 on glycolytic function was also investigated.

6.1 ISG15 does not influence the cardiac proteome during Coxsackievirus B3 infection.

Mass spectrometry (MS) based proteomic analyses have been a key factor in the detection of thousands of proteins from small biological samples. This technique allows the study of broad-spectrum variations in protein abundance in response to chemical or environmental changes. Especially in the field of immunology, proteomic analyses have come to represent an essential method to investigate the influence of various pathogens on the host, as it can also provide insight into protein activity and stability by detecting post-translational modifications, i.e., phosphorylation. Moreover, temporal profiles of the host-cellular proteome can be elucidated, leading not only to a deeper understanding on how pathogens manipulate protein expression and signaling pathways but also providing potential therapeutic targets (Weekes et al. 2014). Additionally, specific interactions between proteins can be analysed, thus giving insight into viral evasion techniques. For instance, a proteomic screen revealed the interaction of the HIV-1 protein Vpx and the host cellular antiviral protein

SAMHD1. In this manner, Vpx induces SAMHD1 proteasomal degradation, thus preventing SAMHD1-mediated inhibition of HIV-1 infection (Hrecka et al. 2011).

In CVB3 infection, MS analysis of infected human cells revealed differential regulation of proteins involved in gene expression, as well as cellular structure, allowing a glimpse at the cellular responses to and the mechanism of infection (Rassmann et al. 2006). However, the insights gained in this study are limited as the utilized immortalized cell line does not represent the natural tissue composition and thus cannot model a reaction to the complex interaction of different cell types as well as soluble mediators. For a more detailed molecular understanding of the interplay between host and virus, murine models of CVB3 infections represent an excellent tool, since CVB3 induces a comparable pathology in humans and mice (Pankuweit and Klingel 2013). The herein performed cardiac LC-MS/MS analysis of CVB3-infected C57Bl/6 mice reveals a strong upregulation of the innate immune response, represented by proteins like IFIT1/2/3, SAMHD1, STAT1, and ISG15 (Fig. 11 C). A systematic GO enrichment analysis of heatmap-based protein clusters (Fig. 11 D) confirms that proteins upregulated during CVB3 infection belong to the innate immune system, the cytokine response, and the defense response to virus (Fig. 13 A). These results are in accordance with a smaller scale proteome analysis of CVB3-infected murine cardiac tissue, which found that significantly regulated proteins are involved in innate immunity and metabolism (Hammer et al. 2010). Concordantly, downregulated proteins in CVB3 infection are part of metabolic pathways, such as the TCA cycle, FA β-oxidation and the mitochondrial respiratory chain (Fig. 13 B). This also complements the results of a transcriptomic study showing that CVB3-induced myocarditis correlates with decreased transcription of genes related to energy metabolism (Remels et al. 2018).

Protection against severe CVB3 pathology is in part conferred by ISG15, a downstream effector protein of IFNβ, which is among the most upregulated proteins in infection (Fig. 11 C). Its expression and covalent modification of a range of target proteins is induced in several tissues as early as 1.5 days after CVB3 infection (Kespohl et al. 2020) and has been shown to interfere directly with viral replication, suppressing viral titers in human cardiomyocytes (Rahnefeld et al. 2014). Furthermore, inactivation of the deISGylating function of USP18 by mutation of the catalytic C61 residue to A (Ketscher et al. 2015) results in decreased viral replication and the amelioration of cardiac virus titers (Kespohl et al. 2020). To investigate whether the susceptibility and resistance to CVB3 infection of $ISG15^{-/-}$ (Osiak et al. 2005) and $USP18^{C61A/C61A}$ mice, respectively, was due to changes in protein expression levels, their cardiac proteomes were analyzed as well (Fig. 11). Comparison of protein expression between the genotypes revealed no significant differences between the genotypes, apart from the mitochondrial NAD(P) transhydrogenase

(NNT) (Fig. 12). NNT expression is an indicator for a different breeding background of the mice. The C57BL/6 subtype J is known to contain a deletion in the *Nnt* gene, while subtype N expresses NNT normally (Mekada et al. 2009; Simon et al. 2013). During the generation of the ISG15$^{-/-}$ mice, N and J subtypes were likely both used for breeding, as some but not all of the ISG15$^{-/-}$ mice express NNT, resulting in its significant regulation. Since NNT plays an important role in the mitochondrial redox functions (Ronchi et al. 2013), ISG15$^{+/+}$ and ISG15$^{-/-}$ littermates (Rahnefeld et al. 2014) were subsequently used for metabolic analyses to ensure the same genetic background. As no other proteins are significantly regulated between the genotypes, the induction of the cardiac antiviral proteome appears not to be impaired in mice lacking ISG15. This indicates that the previously observed ISG15/ISGylation-mediated protection against detrimental effects of CVB3 infection (Rahnefeld et al. 2014; Kespohl et al. 2020) is conferred through alterations in protein stability and function.

6.2 ISGylation upregulates mitochondrial respiration in CVB3 infection.

As discussed above, two dominant effects of CVB3 infection are the induction of antiviral proteins as well as changes in the cellular metabolism. Transcriptomic analyses of heart biopsies from patients as well as mice showed a downregulation of genes involved in metabolism (Remels et al. 2018), which was supported by the herein generated proteome data also pointing toward a downregulation of metabolic proteins (Fig. 11 D). However, a study of cardiac mitochondria showed that enhanced resistance to CVB3-induced myocarditis in mice was linked to increased CI and CIII activity of the respiratory chain (Ebermann et al. 2012). This could indicate that maintenance of mitochondrial ATP production during CVB3 infection counteracts the development of myocarditis. Interestingly, a lack of ISG15 and ISGylation has been described to result in decreased oxidative phosphorylation levels in VACV infection (Baldanta et al. 2017) which was also observed in pancreatic cancer stem cells, together with increased mitophagy (Alcala et al. 2020). In CVB3 infection, lack of ISG15 caused a premature downregulation of proteins involved in FA oxidation as evidenced by proteome analysis of the liver (Kespohl et al. 2020). GO analysis of heatmap-based clusters revealed a decrease in proteins connected to fatty acid oxidation and oxidative phosphorylation on day 8 of CVB3 infection (Kespohl et al. 2020). In contrast to wildtype controls, in ISG15$^{-/-}$ hepatic tissue this downregulation was already observed on day 3 post-infection (Kespohl et al. 2020). Furthermore, proteins associated with the GO-term “carbohydrate catabolic process” were decreased in abundance on day 3 post-infection in wildtype and ISG15$^{-/-}$ liver tissue, while on day 8, this process was upregulated again only in wildtype (Kespohl et al. 2020). Additionally, proteome-based kinetic modeling of hepatic metabolism (Hepatokin1) revealed a greater capacity for

gluconeogenesis in wildtype tissue. Together with decreased glucose levels in the serum, this could point toward ISG15-regulated glucose-production in response to infection-induced hypoglycemia (Kespohl et al. 2020). This hypothesis is supported by significantly increased levels of oxidative phosphorylation in wildtype but not ISG15$^{-/-}$ liver biopsies on day 3 of infection, which could be a way to supply ATP needed for gluconeogenesis (Kespohl et al. 2020). The ECAR measurements showed the same tendencies as the OCR results yet remained non-significant. This could reflect increased glycolysis, which would stand in contrast to the metabolic modeling. However, ECAR is not solely determined by glycolysis, as CO_2 production directly related to O_2 consumption also contributes to acidification of the detection medium (Mookerjee and Brand 2015). Thus, it would be of interest to determine glycolytic flux within hepatocytes in dependence of ISG15.

Here, changes in cellular respiration of primary cardiomyocytes upon infection were investigated, as CVB3 is a cardiotropic virus. Infection induced a significant increase in basal oxygen consumption in primary cardiomyocytes as compared to uninfected control conditions, showing that infection leads to a higher energy demand which is met by an increase in cellular respiration (Fig. 15). ISG15$^{-/-}$ cells on the other hand showed only a slight and non-significant increase in oxygen consumption upon CVB3 infection. Compared to wildtype levels, infected ISG15$^{-/-}$ primary cardiomyocytes exhibit significantly lower oxidative phosphorylation levels, in line with previous findings (Baldanta et al. 2017; Alcala et al. 2020; Kespohl et al. 2020). Moreover, this lack of increase in the oxygen consumption rate in ISG15$^{-/-}$ cardiomyocytes was corroborated by a decrease in MTDR influx into mitochondria (Fig. 16). MTDR is a small fluorescent dye, that accumulates in mitochondria by traversing the membrane in a membrane potential-dependent manner (Xiao et al. 2016). Thus, a reduced MTDR signal is indicative of a reduced mitochondrial membrane potential (Lugli et al. 2005). The mitochondrial membrane potential is mainly generated by the respiratory chain. Even though other factors, such as ion channels and ROS production, influence the proton-motive force as well (Zorova et al. 2018), reduced MTDR accumulation could point toward a decrease in proton-pump activity in oxidative phosphorylation.

Other reports found that cells lacking ISG15 displayed impaired mitochondrial integrity (Baldanta et al. 2017; Alcala et al. 2020). In contrast, this study did not observe that the change in respiratory chain function in ISG15-deficient cells was accompanied by alterations in mitochondrial morphology (Fig. 16 D). However, this might be due to the relatively short time frame in which the cells were analysed. Prolonged infection-induced impairment of the membrane potential would lead to mitochondrial fission and mitophagy (Lazarou et al. 2015). Thus, longer infection time points and more detailed microscopy

techniques, such as electron microscopy, would present elegant methods to further investigate this effect under CVB3 infection conditions.

Additionally, mitochondria could be enriched from cells or organs by differential centrifugation to investigate their proteomic composition in dependence of ISG15. This could provide deeper insight into the ISG15-mediated influence on oxidative phosphorylation. While several mitochondrial proteins were found to be ISGylated, no direct modification of respiratory chain complexes by ISG15 is known to date (Tab. S5 and S9, (Baldanta et al. 2017; Zhang et al. 2019)). As the herein observed changes in oxidative phosphorylation did not differentiate between free and conjugated ISG15, OCR levels of Ube1L$^{-/-}$ cardiomyocytes would be an interesting experimental addition.

Nonetheless, these data suggest that an increase in mitochondrial respiration and thus cellular ATP production is not only crucial to meet the infection-induced energy demand and eventual virus clearance but is also ISG15-dependent.

Of note, it is important to consider the cellular origin and developmental stage. As primary cardiomyocytes grow within a hypoxic environment in the embryo, their primary source of energy is glycolysis (Malandraki-Miller et al. 2018). This quickly changes after birth, where a shift towards β-oxidation as primary energy source is observable (Schwarzer and Doenst 2016). Moreover, culture of primary cells does not account for systemic effectors, i.e., altered substrate availability, which influence the cardiac metabolic state. Thus, it was essential to investigate whether the increase in mitochondrial respiration was conserved in the post-natal heart tissue. Small cardiac biopsies were taken from mice on day 3 of CVB3 infection and cardiac oxygen consumption was analysed by Seahorse metabolic measurement. Concordant to the results from primary cardiomyocytes, a significant increase in oxygen consumption was found in wildtype mice, while ISG15$^{-/-}$ cardiac oxygen consumption rates remained unchanged (Fig. 17). This further points towards an importance of increased oxidative phosphorylation to efficiently combat viral infection. Importantly, analysis of ISGylation-deficient Ube1L$^{-/-}$ cardiac tissue showed the same result as ISG15$^{-/-}$ tissue biopsies, suggesting that the increase in oxygen consumption rate is ISGylation-dependent (Fig. 17).

Previously, reduced CVB3 titers were correlated to increased CI and CIII activity (Ebermann et al. 2012). Together with the results presented here, this indicates that ISGylation-mediated protection against CVB3 infection might at least partly be conferred by increasing the mitochondrial respiratory activity, as ISGylation-deficient mice exhibit both, increased cardiac CVB3 titers (Kespohl et al. 2020) and decreased oxidative phosphorylation (Fig. 17).

6.3 Elucidation of the cardiac ISGylome and Ubiquitylome in CVB3 infection.

Since the resistance against CVB3 appears to be connected to mitochondrial metabolism, and both are dependent on ISGylation (Rahnefeld et al. 2014; Kespohl et al. 2020), an LC-MS/MS based approach was employed to identify the cardiac ISG15 target proteins at different timepoints of CVB3 infection. Until recently, ISGylome analyses were performed *in vitro* by co-immunoprecipitation of ISG15 and its modified target proteins with subsequent detection by mass spectrometry (Zhao et al. 2005). Another approach by stable isotope labelling coupled to LC-MS/MS analysis was able to identify 30 ISG15 targets in *L. monocytogenes* infection *in vitro* (Radoshevich et al. 2015). Yet, neither of these techniques identifies the location of ISG15-modified lysine (K) residues within targets (Giannakopoulos et al. 2005; Zhao et al. 2005; Takeuchi et al. 2006; Radoshevich et al. 2015). To identify both, targets and modification site, an *in vivo* ISGylome analysis model was developed (Zhang et al. 2019). Here, GG-modified proteins were analyzed *in vivo* on day 0, 3, and 8 of CVB3 infection (Fig. 18 C and D, Tab. S5 and S9). Of note, the experimental setup does not control for neddylation, as Nedd8 C-terminal LRGG motif is indistinguishable from that of ISG15 or ubiquitin. However, no influence of ISG15/ISGylation-deficiency on neddylation is known and neddylation-derived GG-remnants are likely misidentified as ubiquitination, not ISGylation. Moreover, ISGylation-enriched USP18$^{C61A/C61A}$ mice serve as control for potentially altered neddylation in ISG15$^{-/-}$ mice (Thery et al. 2021).

A systematic GO enrichment analysis of ubiquitinated proteins in infection shows that they belong to the IFNβ-response, metabolic proteins, and proteins involved in cardiac muscle maintenance and contraction. Since ubiquitination has broad cellular function, it is difficult to deduce the fate of the herein identified targets of ubiquitination. The most commonly known role of ubiquitination is targeting proteins for degradation (Grabbe et al. 2011). Ubiquitination-mediated degradation of metabolic proteins could complement their observed downregulation in infection on the level of the proteome (Fig. 13). At 8 days post infection, during acute viral myocarditis (Rahnefeld et al. 2014), more proteins related to cardiac health GO terms are enriched in the ubiquitination cluster, i.e., TITIN (Tab. S9), which could be representative of a worsening state of cardiac health (Kotter et al. 2016). However, several other functions of ubiquitination are known, such as induction of inflammatory processes and the adaptive immune response (Popovic et al. 2014) or the regulation of endocytosis and signaling (Mukhopadhyay and Riezman 2007). Without more detailed analysis regarding the fate of specific ubiquitinated proteins in infection, no definitive conclusions can be drawn about the role of ubiquitination in CVB3 infection.

GO analysis of ISGylated proteins shows that in the early stages of infection, proteins involved in the localization to early endosomes, metabolic processes and immunologic defense response are highly enriched. Targets of ISGylation are commonly modified cotranslationally (Durfee et al. 2010). Thus, it is not surprising to find proteins associated with the innate immune and defense response to virus (Fig. 19) to be enriched in the ISGylation cluster. As these proteins are highly upregulated, especially in the early phase of infection, they are ideal targets for ISGylation. Indeed, IFIT1 and IFIT3, as well as OAS3 and STAT1 have all been previously reported to be modified (Malakhov et al. 2003; Zhao et al. 2005; Zhang et al. 2019). Similarly, cotranslational modification most likely leads to ISGylation of Moesin and Ezrin, part of the GO term “localization to early endosomes”, on day 3 post-infection (Fig. 19 A), as structural maintenance proteins have been shown to be upregulated in the acute phase of CVB3 infection (Hammer et al. 2010). In fact, Moesin was upregulated in infection in the herein presented analysis, while Ezrin levels remain at a constant high level at all timepoints of analysis (Tab. S1).

Interestingly, the putative ISGylation targets that are part of the host defense response to viral infection (Fig. 19 A) include ISG15 itself. However, it cannot be distinguished whether the identified GG remnant stems from self-ISGylation or ubiquitination since no frame of reference is created in the employed model. Nontheless, the possibility of ubiquitination or self-ISGylation of ISG15 has been described previously (Fan et al. 2015; Zhang et al. 2019). To investigate self-ISGylation potential, overexpression of ISG15 and the machinery with subsequent excision and MS-based analysis of a 30 kDa modification band would not lead to the desired results, as many endogenous cellular proteins that are ~15 kDa in size could also be modified by ISG15. Thus, a cell-free *in vitro* approach combining recombinant ISG15 and ISGylation machinery would be the most comprehensive method. However, recombinant expression of the E3 ligase remains yet to be achieved.

Even though the herein investigated samples of different infection timepoints were not measured at the same time, 30 GG-modification sites were found to overlap, 8 of which change cluster (Tab. 5). Most cluster changes are from ISGylation to ubiquitination, suggesting that ISGylation has the capacity to modify ubiquitination sites and thus change the fate of the target protein. This is further substantiated by the fact, that most ISGylation sites identified on both days have been previously reported to be ubiquitination (Tab. S5 and S9). This is most likely the case for proteins where expression is ubiquitous and not tied to specific stimuli, such as metabolic enzymes. On the other hand, many herein identified ISGylation sites on proteins of the immune system, previously reported to be stemming from ubiquitin, were characterized by a proteomic screen using the PTMScan® Ubiquitin Remnant Motif (K-ε-GG) kit (Guo 2009) or a GG-lysine specific antibody (Wagner

et al. 2012) for enrichment. Neither of these studies controlled for ISGylation, thus the GG remnants could have in fact be stemming from ISGylation.

Despite extensive screening for ISG15 substrates in the past, this study identified 12 novel ISGylation targets (Tab. 4). Additionally, 62 novel ISGylation sites are reported here (Tab. S13). Concordant to Zhang et al., no ISGylation motif became apparent based on the secondary amino acid structure surrounding the identified sites (Zhang et al. 2019). However, it would be of great interest to employ structural modeling of ISGylated proteins to analyze whether the tertiary structure reveals indications for ISG15-conjugation, such as binding grooves or hydrophobic patches.

6.3.1 ISGylation of CVB3 proteins.

As ISGylation mainly occurs cotranslationally, direct modification of several pathogenic proteins which are highly expressed during infection has been shown. For instance, HPV capsid protein L1 (Durfee et al. 2010), Influenza A NS1 (Zhao et al. 2010), as well as Influenza B nucleoprotein (Zhao et al. 2016) have been reported to be ISGylated. In contrast, while *L. monocytogenes* infection is counteracted by ISGylation, no bacterial proteins have been found to be ISGylated *in vivo* (Zhang et al. 2019). Of the CVB3 proteins, the protease 2A has been shown to be modified by ISG15 leading to decreased 2A cleavage activity (Rahnefeld et al. 2014). Here, no coxsackieviral targets were identified *in vivo* (Fig. 18 C and D), suggesting that the focus of antiviral function of ISGylation is to promote host-cellular immunity rather than directly modify virus proteins. On the other hand, CVB3 proteins are not highly abundant within cardiac tissue, as none were detected on the proteomic level (Tab. S1). Thus, more detailed analysis into the interaction and modification of CVB3 proteins with ISG15 is warranted.

6.3.2 ISGylation stabilizes IFIT1 and IFIT3 expression.

This study identified several ISGs as targets of ISG15 in CVB3 infection that play a crucial role in the cellular antiviral response, such as STAT1, IFIT1, IFIT3, and OAS3 (Fig. 18 C and D). STAT1 was previously identified to be covalently modified by ISG15 *in vitro* (Malakhov et al. 2003) and *in vivo* (Zhang et al. 2019), although the function of STAT1-ISGylation remains to be elucidated.

IFIT1/2/3 are among the highest upregulated proteins during CVB3 infection (Szalay et al. 2006; Kimura et al. 2019; Kespohl et al. 2020) and play a role in the IFNβ-mediated antiviral activity against CVB3, as infection of IFIT1/2/3$^{-/-}$ cardiomyocytes leads to significantly higher viral replication levels than of wildtype controls (Kimura et al. 2019). However, *in vivo* experiments revealed contradictory function of IFIT proteins. IFIT1/2/3$^{-/-}$ mice suffered from enhanced viral load in the heart and liver as early as day 1 of CVB3 infection but exhibited

significantly less viral titers in the pancreas and liver at day 7 post-infection. Nonetheless, IFIT1/2/3 were required to restrict virus-induced myocarditis (Kimura et al. 2019). This inconsistent observation might be explained by the different immune-modulatory functions of the IFIT family members. IFIT1 was reported to have negative feedback function on antiviral signaling by disrupting the interaction of MAVS, TBK1, and mediator of IRF3 activation (MITA) (Li et al. 2009). In contrast, IFIT3 is known to act as a bridge of MAVS and TBK1, enhancing the IRF3-mediated antiviral gene expression (Liu et al. 2011). Furthermore, IFIT2 was shown to induce the mitochondrial apoptosis pathway which was counteracted by IFIT3 (Stawowczyk et al. 2011). To evaluate the influence of IFIT family members on CVB3 infection, either conditional IFIT1/2/3 triple knockout in specific organs or single knockout mouse strains (i.e., IFIT1$^{-/-}$, IFIT2$^{-/-}$, and IFIT3$^{-/-}$ mice) could provide a more comprehensive understanding of the antiviral action.

Interestingly, while the proteomic analysis of CVB3 infected heart tissue revealed a significant upregulation of IFIT1/2/3 even 8 days post-infection (Fig. 11 C), only IFIT1 and IFIT3 have been identified as targets of ISGylation here (Tab. S5 and S9) as well as in *L. monocytogenes* infection (Zhang et al. 2019). Although human IFIT2 has been reported to be ISGylated in IFNβ-stimulated HeLa cells (Zhao et al. 2005), the lack of *in vivo* evidence from mouse models could suggest a specific physiological effect for ISGylation of murine IFIT1/3 proteins, which is corroborated by the fact that the herein identified modification site K89 on murine IFIT1 is not conserved in human IFIT1. Moreover, low sequence identities of murine and human IFIT orthologues could result in differences in the functional consequences of ISGylation (Fensterl and Sen 2015). On the other hand, both, human IFIT1 and IFIT3, are ISGylation targets as shown in HeLa cells (Fig. 21, (Zhao et al. 2005)) and the detected IFIT3 ISGylation sites K119 and K189 are conserved in the human orthologue. Furthermore, additional IFIT K residues have been identified to be ISG15-target sites in *L. monocytogenes* infection in liver tissue (Zhang et al. 2019). This identification of different sites is likely caused by slight differences during tissue-processing and the mass spectrometric analysis. Nevertheless, investigation whether different residues are targeted specifically in viral and bacterial infection could provide important insight into the mechanism of action of ISGylation, especially as no clear ISGylation motif is apparent to date.

Remarkably, *Ifit1/3* mRNA was significantly increased in ISG15$^{-/-}$ mice at day 3 post CVB3 infection as compared to wildtype mice (Fig. 22 A), which was not reflected on the protein levels as evidenced by proteome analysis (Fig. 12). While ISG15 is known to accelerate gene transcription by influencing replication forks (Raso et al. 2020), its impact on protein expression warrants further investigation. In cell culture, IFNβ stimulation also led to increased levels of *IFIT1/3* mRNA in ISG15ko cells as compared to wildtype

control (Fig. 23 A). Since ISG15 negatively regulates the type I IFN signaling cascade (Zhang et al. 2015), higher levels of ISG mRNA are to be expected in ISG15-deficient cells. However, this did not translate to increased IFIT1/3 protein levels in ISG15ko cells. To avoid effects of ISG15 on IFNβ-mediated gene transcription, the influence of ISG15 on *IFIT1/3* mRNA were confirmed in an IFNβ-independent overexpression approach, which also showed increased mRNA levels in ISG15-deficient cells (Fig. 24 A). In contrast, ISGylation increased IFNβ-induced IFIT1/3 protein abundance (Fig. 23 B). This was not due to reduced IFIT1/3 degradation, as cycloheximide treatment did not alter protein levels between ISG15ko wildtype HeLa cells (Fig. 25 A and B). Moreover, rescue of ISG15 expression also rescued IFIT1/3 protein levels in ISG15ko cells, yet this rescue was not observed when unconjugable ISG15-LRAA was transfected (Fig. 26). The pulldown of FLAG-tagged ISG15 further revealed a co-precipitation of higher molecular weight bands (Fig. 21 A). Since the IFIT proteins are known to homodimerize as well as forming hetero-oligomeric complexes (Stawowczyk et al. 2011), this could indicate that ISGylation is necessary for formation of these complexes in addition to positively regulating IFIT1/3 protein expression (Kespohl et al. 2020).

Another antiviral protein, OAS3, was found to be ISGylated on day 3 of CVB3 infection (Fig. 18). In addition to modification of K858 found in this study, K1079 and K1084 were previously reported as target residues (Zhang et al. 2019). As with the IFIT orthologues, OAS3 sequence identity between human and mouse is low, at approximately 67%. Nonetheless, human OAS3 was confirmed to be covalently modified by ISG15 in an *in vitro* approach (Fig. 21). All identified sites are located to the OAS domain 3, which is only part of OAS3 and not OAS1 or 2. This could be the reason other OAS family members have not been found to be ISGylated in this study, although OAS1a has been identified as ISG15 target previously (Zhang et al. 2019; Yan et al. 2021). Unlike IFIT1/3, ISG15 does not influence OAS3 protein expression and did not affect OAS3 degradation either (Fig. 25 C). As neither OAS1, OAS2, nor OAS3 were detected on the proteomic level (Tab. S1) and are thus not highly abundant, it is unlikely that OAS3 is a key antiviral molecule in CVB3 infection. Indeed, knockdown as well as overexpression of OAS3 did not influence CVB3 replication *in vitro* (Fig. 27). Thus, the importance of OAS3 in CVB3 infection appears to be negligible. Nonetheless, the putative ISGylation site K858 is located close to ATP and cofactor binding sites, suggesting a functional influence of ISG15. Even though OAS3 appears to not play a role in CVB3 infection, an analysis of the influence of ISGylation on OAS3 function could be of interest in other viral infection models, such as VACV, Influenza, Chikungunya or Dengue virus infection (Brehin et al. 2009; Lin et al. 2009; Li et al. 2016).

In summary, ISGylation appears to exert a stabilizing effect on the expression of IFIT1, IFIT3, but not OAS3, without influencing their degradation. These varying results highlight the versatile function of ISGylation and underline the importance of separate analyses of each identified target protein.

6.4 ISGylation impairs glycolytic enzyme function.

Apart from innate immune proteins, ISG15 also modifies cellular metabolism, which has been reported in various cell types, such as bone marrow derived macrophages (BMDM) (Baldanta et al. 2017), primary adipocytes (Yan et al. 2021), and pancreatic cancer stem cells (CSC) (Alcala et al. 2020). Furthermore, ISG15 was linked to the central liver metabolism *in vivo*, increasing oxidative capacity and influencing glucose homeostasis in CVB3 infection (Kespohl et al. 2020). The ISGylome analysis revealed an enrichment in metabolic targets in both, the early stage of CVB3 infection and during acute myocarditis (Fig. 18 And Fig. 28). Notably, almost all enzymes of glycolysis were found to be modified, which could be an indicator for a functional influence of ISGylation on this pathway. To ensure that the GG-remnants found on these targets were not misidentified, ISGylation was verified by *in vitro* co-immunoprecipitation (Fig. 30 – Fig. 38). In contrast to the IFIT and OAS3 orthologues (section 6.3.2), glycolytic enzymes are highly conserved across species, which indicates that any influence of ISGylation on enzymatic stability or function is conserved as well.

K to R mutation of the identified modification sites of LDH, HK2, and PFK showed no difference in ISGylation pattern (Fig. 40), suggesting that K residues can be modified interchangeably and further supporting the lack of a distinct ISGylation motif. However, this does not exclude potential functional implications that ISGylation of specific residues might have. For instance, LDH K59 and HK2 K419 are both located in close proximity to binding sites of NAD^+ and G-1-P, respectively. While K372 of PFK is surface-oriented and not close to active sites, K727 is located next to the binding site of the allosteric activator of PFK, fructose 2,6-bisphosphate (F-2,6-BP). ISGylation of these sites could therefore impact the enzymatic activity of these proteins. Indeed, ISGylation was recently reported to inhibit LDH activity (Yan et al. 2021). Thus, the question whether ISGylation alters HK2 and PFK activity was addressed next. As seen in the validation experiments, only a small subset of a target is modified by ISG15 (Fig. 30 and Fig. 32). To ensure measurable effects of ISGylation, enzymes were enriched by FLAG-immunoprecipitation prior to activity measurement.

Strikingly, an inhibitory effect of ISGylation was observed for the activity of HK2, as well as PFK (Fig. 41) as was shown for LDH (Yan et al. 2021). Together, this suggests a downregulating effect of ISGylation on glycolysis.

For LDH, Yan et al. identified K57 as the ISGylated residue. In contrast, the ISGylome analysis identified K59 to be modified (Tab. S9). K57 and K59 are only two amino acids apart and proteomic sample preparation involves tryptic protein cleavage after K and R residues which could lead to inaccurate site identification. Furthermore, mutating LDH K59 to R did not lead to altered ISGylation pattern detected by western blot (Fig. 40 A). Potentially, both residues are ISGylated interchangeably with the same effect on LDH activity as they are part of and close to the NAD binding site spanning from aa29-57. Indeed, K57R mutation lead to a rescue of ISGylation-mediated restriction in LDH activity (Yan et al. 2021).

Remarkably, replacement of the identified ISGylation site of HK2 K419 by R also resulted in complete restoration of HK2 activity (Fig. 41 A). This could indicate that ISGylation blocks access to either the G-6-P binding region spanning aa413-415, or the ATP binding site at aa425-426, or both.

Activity measurement of the PFK K372R K727R double mutant on the other hand did not rescue enzymatic activity (Fig. 41 B). As described above, neither of these sites are close to the active center of the enzyme. Since the ISGylation pattern of the mutants did not change, it is likely that another K residue close to the active site is ISGylated in this *in vitro* approach. However, this does not allow conclusions about the effect of ISGylation on PFK *in vivo*. As K727 is located close to the binding site the allosteric activator of PFK, blocking the activation of PFK by ISGylation of K727 could have inhibitory function that cannot be analysed by the experimental setup employed here. Aside from mutating K residues closer to PFK substrate binding sites to test whether this rescues its activity or whether ISGylation of the here identified target sites have allosteric effects, it would be of interest to also investigate the influence of ISGylation on the remaining glycolytic enzymes and targets from other metabolic pathways.

In summary, ISGylation impairs the enzymatic activity of two glycolytic enzymes investigated here, suggesting an inhibitory effect of ISGylation on glycolytic function.

6.5 ISGylation potentially restricts glycolysis.

Corresponding to the herein observed inhibitory effect of ISGylation on HK2 and PFK function (Fig. 41), an ISGylation-dependent increase in glycolysis was reported in ISG15$^{-/-}$ primary adipocytes.(Yan et al. 2021). Thus, to investigate the impact of glycolytic enzyme ISGylation on the cellular glycolytic rate in the heart, wildtype and ISG15$^{-/-}$ primary cardiomyocytes were infected with CVB3 and analysed by Seahorse metabolic measurement. In line with the reduced HK2, PFK, and LDH enzymatic activity (Fig. 41, (Yan et al. 2021)) upon ISGylation, wildtype cells exhibit a tendency towards lower glycolytic levels than ISG15-deficient cells already in steady state conditions (Fig. 43). CVB3 infection

slightly increases glycolytic levels in ISG15$^{-/-}$ but not wildtype cardiomyocytes, suggesting an ISG15-mediated regulatory effect (Fig. 43 A). Moreover, ISG15$^{-/-}$ cells treated with IFNβ slightly increase their glycolytic rates as well (Fig. 43). This could indicate that the regulatory effect of ISG15 is mediated by ISGylation. However, as the measurements in primary cells resulted in highly variable results, it remains impossible to draw definitive conclusions from this experiment. Nonetheless, analysis of glycolytic levels in infected and IFNβ-treated Ube1L$^{-/-}$ cardiomyocytes would be a valuable addition to elucidate a potential ISGylation-mediated mechanism of glycolytic regulation.

CVB3 infection results in decreased blood glucose levels *in vivo*, leading to lower substrate availability for glycolysis. While this hypoglycemic state was already present in uninfected ISG15$^{-/-}$ mice, it was exacerbated in CVB3 infection, demonstrating a role of ISG15 in glucose homeostasis (Kespohl et al. 2020). The herein obtained results point towards restricted glycolytic activity in wildtype cardiomyocytes that is lost in ISG15-deficient cells (Fig. 43 A). The hypoglycemic state *in vivo* was modeled by culturing the primary cells in low glucose medium. Together, these findings could indicate that ISG15-mediated glucose homeostasis is at least partly achieved by preventing excessive glycolysis, which in turn might contribute to the control of virus replication. The cellular ATP demand covered by glycolysis after inhibition of the respiratory chain (Fig. 43 B) indicates a higher cellular energy demand in ISG15$^{-/-}$ cardiomyocytes, which correlates with decreased O_2-linked ATP production (Fig. 15). As the mitochondrial ATP production is more efficient than the glycolytic one (Berg 2012), this could indicate an involvement of ISG15 in the induction and maintenance of efficient cellular energy production in response to infection. This is corroborated by a study of infection-induced changes in the cardiac metabolome in wildtype and ISG15$^{-/-}$ mice, which shows a lower ATP/AMP ratio in ISG15$^{-/-}$ tissue on day 3 of CVB3 infection (unpublished data of the Beling group).

IFNβ stimulation has been described to increase glucose uptake mediated by PI3K/Akt signaling (Burke et al. 2014) and thus resulted in higher glucose uptake accompanied by decreased oxidative phosphorylation in T cells and macrophages (Pantel et al. 2014; Hedl et al. 2016). In contrast, murine DCs exhibited an IFNβ-mediated increase in oxidative phosphorylation, not glycolysis (Wu et al. 2016). Thus, the effect of IFNβ on metabolic function might be cell-type specific (Wu et al. 2016). It is unclear whether an IFNβ-mediated increase in glucose uptake capacity is intensified by a lack of ISG15. Higher intracellular glucose levels in ISG15$^{-/-}$ cells paired with a lack of glycolytic enzyme activity restriction could account for increased glycolysis. However, in this study, the primary cardiomyocytes were cultured in low-glucose medium prior to stimulation and infection. Thus, the effect of ISG15 on glycolytic function was analysed independent of an IFNβ-mediated increase in glucose uptake over time. Analysis of glucose uptake under IFNβ stimulation in

ISG15$^{-/-}$ cardiomyocytes would be an interesting addition to the results presented here. Furthermore, mitochondrial and glycolytic capacities of ISGylation-enriched USP18$^{C61A/C61A}$ mice would provide valuable insights into the ISGylation-mediated control of metabolic function.

Of note, many viruses upregulate cellular glucose-carbon flux to redirect the metabolic intermediates towards nucleotide and amino acid biosynthesis (Yu et al. 2011; Sanchez and Lagunoff 2015). Preventing this infection-mediated increase in an ISGylation-dependent manner could be a mechanism to restrict viral replication in directly infected cells. On the other hand, fatty acid catabolism produces more ATP than glucose metabolism (Berg 2012). ISG15/ISGylation appear to be crucial for upregulation of oxidative phosphorylation-mediated ATP production (Fig. 15 and 17) and might be responsible for the restriction of cardiomyocyte glycolytic levels (Fig. 43). In this manner, ISG15/ISGylation could ensure efficient energy production needed to counteract CVB3 infection.

6.6 Conclusion and outlook

This study first identified the *in vivo* cardiac proteome, ISGylome, and ubiquitylome in CVB3 infection, significantly advancing the understanding of the ISG15-mediated antiviral response. The herein performed ISGylome analysis confirms antiviral proteins as targets of ISGylation, as well as revealing a striking enrichment of glycolytic enzymes modified by ISG15, especially during acute myocarditis. Together, these results highlight a dual role of ISGylation in CVB3 infection: to support the cellular antiviral state by enhancing expression of ISGs as well as controlling cardiac metabolism. During infection, proteins of the innate immune system are upregulated as a first line of defense. This development of a cardiac antiviral proteome is independent of ISG15 and ISGylation. However, *in vitro* experiments show that expression of specific ISGs, namely IFIT1 and IFIT3, is stabilized by ISGylation. Even though this stabilization did not lead to significant differences in protein abundances *in vivo*, it could have an impact on the protein function or related pathways. Future studies should investigate the effect of ISGylation on other ISGs with regard to the functional implication as well as the stabilizing effect in a spatio-temporal approach. Furthermore, the herein demonstrated ISGylation-mediated increase in respiratory activity under infection-induced high energy demand could point towards ISG15 being imperative for mitochondrial integrity in CVB3 infection. Indeed, other studies have observed increased mitophagy in cells lacking ISG15 (Baldanta et al. 2017; Alcala et al. 2020). A diminished mitochondrial membrane potential of CVB3-infected ISG15-deficient primary cardiomyocytes presented here points towards a similar effect.

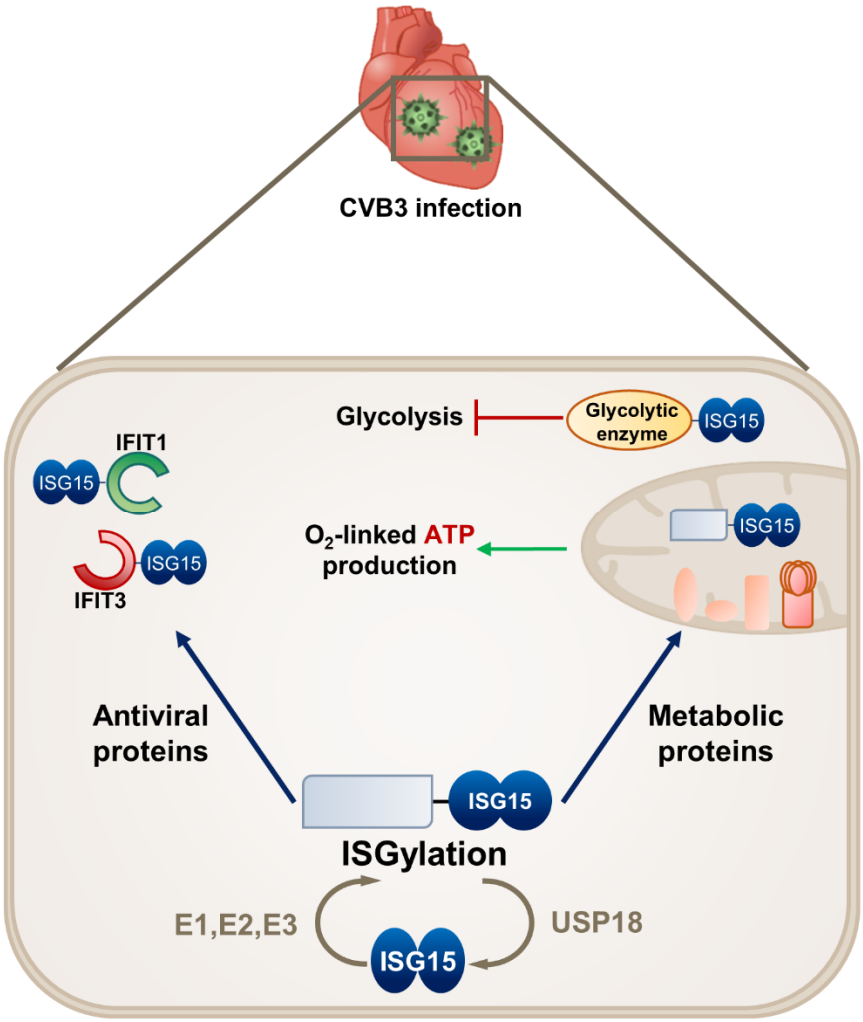

Figure 44: Graphical summary
CVB3 infection of the heart results in induction of an antiviral state by upregulated expression of immunity-related proteins, including the small ubiquitin-like modifier ISG15. In an E1/E2/E3 enzyme cycle, ISG15 covalently modifies a range of substrate proteins thereby counteracting CVB3-induced myocarditis. This so-called ISGylation important to enhance cellular expression levels of antiviral effector proteins IFIT1 and IFIT3. Additionally, ISGylation mediates cellular energy production to ensure efficient ATP-supply in infection. ISG15 and ISGylation are crucial to upregulate oxidative phosphorylation-mediated ATP production while preventing increased glycolytic activity, likely through inhibition of several glycolytic enzymes.

Concordant with a study on the influence of ISG15 on adipocyte thermogenicity (Yan et al. 2021), *in vitro* activity assays of isolated ISGylated HK2 and PFK show a significant downregulation of enzymatic substrate turnover. Moreover, analysis of the glycolytic capacity of primary cardiomyocytes showed elevated glycolytic levels in ISG15$^{-/-}$ cells in basal conditions, CVB3 infection, and IFNβ stimulation, suggesting that ISG15 suppresses glycolytic activity. Together, the metabolic investigations show that ISG15/ISGylation-deficiency results in increased glycolytic levels accompanied with decreased oxidative phosphorylation. As ISG15-deficiency is associated with increased viral load (Rahnefeld et al. 2014; Kespohl et al. 2020), this could be a way to ensure efficient energy production necessary to mount the antiviral defense. It would be of interest to investigate the *in vivo*

effect of ISG15 on metabolic function over longer infection periods. Additionally, a more detailed picture of the metabolic effector function ISG15 plays in the heart could be achieved by investigation of ISG15 in diet-induced cardiac inflammation. Altogether, this will greatly advance the insight in the impact of the ISG15 system on metabolism in inflammation.

7 References

Abbas YM, Laudenbach BT, Martinez-Montero S, Cencic R, Habjan M, Pichlmair A, Damha MJ, Pelletier J, Nagar B. 2017. Structure of human IFIT1 with capped RNA reveals adaptable mRNA binding and mechanisms for sensing N1 and N2 ribose 2'-O methylations. *Proc Natl Acad Sci U S A* **114**: E2106-E2115.

Abbas YM, Pichlmair A, Gorna MW, Superti-Furga G, Nagar B. 2013. Structural basis for viral 5'-PPP-RNA recognition by human IFIT proteins. *Nature* **494**: 60-64.

Abel ED. 2004. Glucose transport in the heart. *Front Biosci* **9**: 201-215.

Ablasser A, Hornung V. 2011. Where, in antiviral defense, does IFIT1 fit? *Nat Immunol* **12**: 588-590.

Alcala S, Sancho P, Martinelli P, Navarro D, Pedrero C, Martin-Hijano L, Valle S, Earl J, Rodriguez-Serrano M, Ruiz-Canas L et al. 2020. ISG15 and ISGylation is required for pancreatic cancer stem cell mitophagy and metabolic plasticity. *Nat Commun* **11**: 2682.

Althof N, Goetzke CC, Kespohl M, Voss K, Heuser A, Pinkert S, Kaya Z, Klingel K, Beling A. 2018. The immunoproteasome-specific inhibitor ONX 0914 reverses susceptibility to acute viral myocarditis. *EMBO molecular medicine*.

Althof N, Harkins S, Kemball CC, Flynn CT, Alirezaei M, Whitton JL. 2014. In vivo ablation of type I interferon receptor from cardiomyocytes delays coxsackieviral clearance and accelerates myocardial disease. *J Virol* **88**: 5087-5099.

Anderson DR, Wilson JE, Carthy CM, Yang D, Kandolf R, McManus BM. 1996. Direct interactions of coxsackievirus B3 with immune cells in the splenic compartment of mice susceptible or resistant to myocarditis. *J Virol* **70**: 4632-4645.

Antonsson A, Payne E, Hengst K, McMillan NA. 2006. The human papillomavirus type 16 E7 protein binds human interferon regulatory factor-9 via a novel PEST domain required for transformation. *Journal of interferon & cytokine research : the official journal of the International Society for Interferon and Cytokine Research* **26**: 455-461.

Arimoto KI, Lochte S, Stoner SA, Burkart C, Zhang Y, Miyauchi S, Wilmes S, Fan JB, Heinisch JJ, Li Z et al. 2017. STAT2 is an essential adaptor in USP18-mediated suppression of type I interferon signaling. *Nature structural & molecular biology* **24**: 279-289.

Ashburner M, Ball CA, Blake JA, Botstein D, Butler H, Cherry JM, Davis AP, Dolinski K, Dwight SS, Eppig JT et al. 2000. Gene ontology: tool for the unification of biology. The Gene Ontology Consortium. *Nat Genet* **25**: 25-29.

Ashley CL, Abendroth A, McSharry BP, Slobedman B. 2019. Interferon-Independent Innate Responses to Cytomegalovirus. *Front Immunol* **10**: 2751.

Bajaj R, Sinclair HC, Patel K, Low B, Pericao A, Manisty C, Guttmann O, Zemrak F, Miller O, Longhi P et al. 2021. Delayed-onset myocarditis following COVID-19. *Lancet Respir Med*.

Baldanta S, Fernandez-Escobar M, Acin-Perez R, Albert M, Camafeita E, Jorge I, Vazquez J, Enriquez JA, Guerra S. 2017. ISG15 governs mitochondrial function in macrophages following vaccinia virus infection. *PLoS pathogens* **13**: e1006651.

Bansal M. 2020. Cardiovascular disease and COVID-19. *Diabetes Metab Syndr* **14**: 247-250.

Barbalat R, Ewald SE, Mouchess ML, Barton GM. 2011. Nucleic acid recognition by the innate immune system. *Annu Rev Immunol* **29**: 185-214.

Basters A, Geurink PP, Rocker A, Witting KF, Tadayon R, Hess S, Semrau MS, Storici P, Ovaa H, Knobeloch KP et al. 2017. Structural basis of the specificity of USP18 toward ISG15. *Nature structural & molecular biology* **24**: 270-278.

Bedard KM, Semler BL. 2004. Regulation of picornavirus gene expression. *Microbes Infect* **6**: 702-713.

Beling A, Kespohl M. 2018. Proteasomal Protein Degradation: Adaptation of Cellular Proteolysis With Impact on Virus-and Cytokine-Mediated Damage of Heart Tissue During Myocarditis. *Front Immunol* **9**: 2620.

Belmont PJ, Chen WJ, San Pedro MN, Thuerauf DJ, Gellings Lowe N, Gude N, Hilton B, Wolkowicz R, Sussman MA, Glembotski CC. 2010. Roles for endoplasmic reticulum-associated degradation and the novel endoplasmic reticulum stress response gene Derlin-3 in the ischemic heart. *Circ Res* **106**: 307-316.

Berg JMTJLSL. 2012. *Biochemistry*. W.H. Freeman, Basingstoke.

Bertrand L, Horman S, Beauloye C, Vanoverschelde JL. 2008. Insulin signalling in the heart. *Cardiovasc Res* **79**: 238-248.

Bhattacharya S, Qian J, Tzimas C, Baker DP, Koumenis C, Diehl JA, Fuchs SY. 2011. Role of p38 protein kinase in the ligand-independent ubiquitination and down-regulation of the IFNAR1 chain of type I interferon receptor. *The Journal of biological chemistry* **286**: 22069-22076.

Bianco C, Mohr I. 2017. Restriction of Human Cytomegalovirus Replication by ISG15, a Host Effector Regulated by cGAS-STING Double-Stranded-DNA Sensing. *J Virol* **91**.

Bock CT, Klingel K, Kandolf R. 2010. Human parvovirus B19-associated myocarditis. *N Engl J Med* **362**: 1248-1249.

Bogunovic D, Byun M, Durfee LA, Abhyankar A, Sanal O, Mansouri D, Salem S, Radovanovic I, Grant AV, Adimi P et al. 2012. Mycobacterial disease and impaired IFN-gamma immunity in humans with inherited ISG15 deficiency. *Science* **337**: 1684-1688.

Brehin AC, Casademont I, Frenkiel MP, Julier C, Sakuntabhai A, Despres P. 2009. The large form of human 2',5'-Oligoadenylate Synthetase (OAS3) exerts antiviral effect against Chikungunya virus. *Virology* **384**: 216-222.

Brown DI, Willis MS, Berthiaume JM. 2016. Chapter 11 - Influence of Ischemia-Reperfusion Injury on Cardiac Metabolism. in *The Scientist's Guide to Cardiac Metabolism* (eds. M Schwarzer, T Doenst), pp. 155-167. Academic Press, Boston.

Burke JD, Platanias LC, Fish EN. 2014. Beta interferon regulation of glucose metabolism is PI3K/Akt dependent and important for antiviral activity against coxsackievirus B3. *J Virol* **88**: 3485-3495.

Campanella M, de Jong AS, Lanke KW, Melchers WJ, Willems PH, Pinton P, Rizzuto R, van Kuppeveld FJ. 2004. The coxsackievirus 2B protein suppresses apoptotic host cell responses by manipulating intracellular Ca2+ homeostasis. *The Journal of biological chemistry* **279**: 18440-18450.

Cao T, Liccardo D, LaCanna R, Zhang X, Lu R, Finck BN, Leigh T, Chen X, Drosatos K, Tian Y. 2019. Fatty Acid Oxidation Promotes Cardiomyocyte Proliferation Rate but Does Not Change Cardiomyocyte Number in Infant Mice. *Front Cell Dev Biol* **7**: 42.

Capobianchi MR, Uleri E, Caglioti C, Dolei A. 2015. Type I IFN family members: similarity, differences and interaction. *Cytokine & growth factor reviews* **26**: 103-111.

Catic A, Fiebiger E, Korbel GA, Blom D, Galardy PJ, Ploegh HL. 2007. Screen for ISG15-crossreactive deubiquitinases. *PLoS One* **2**: e679.

Chatham JC. 2002. Lactate -- the forgotten fuel! *J Physiol* **542**: 333.

Chebath J, Benech P, Hovanessian A, Galabru J, Revel M. 1987. Four different forms of interferon-induced 2',5'-oligo(A) synthetase identified by immunoblotting in human cells. *The Journal of biological chemistry* **262**: 3852-3857.

Cheung PK, Yuan J, Zhang HM, Chau D, Yanagawa B, Suarez A, McManus B, Yang D. 2005. Specific interactions of mouse organ proteins with the 5'untranslated region of coxsackievirus B3: potential determinants of viral tissue tropism. *J Med Virol* **77**: 414-424.

Chua B, Siehl DL, Morgan HE. 1979. Effect of leucine and metabolites of branched chain amino acids on protein turnover in heart. *The Journal of biological chemistry* **254**: 8358-8362.

Cox J, Mann M. 2012. 1D and 2D annotation enrichment: a statistical method integrating quantitative proteomics with complementary high-throughput data. *BMC Bioinformatics* **13 Suppl 16**: S12.

Coyne CB, Bozym R, Morosky SA, Hanna SL, Mukherjee A, Tudor M, Kim KS, Cherry S. 2011. Comparative RNAi screening reveals host factors involved in enterovirus infection of polarized endothelial monolayers. *Cell Host Microbe* **9**: 70-82.

D'Cunha J, Ramanujam S, Wagner RJ, Witt PL, Knight E, Jr., Borden EC. 1996. In vitro and in vivo secretion of human ISG15, an IFN-induced immunomodulatory cytokine. *J Immunol* **157**: 4100-4108.

Dao CT, Zhang DE. 2005. ISG15: a ubiquitin-like enigma. *Front Biosci* **10**: 2701-2722.

Das DK, Engelman RM, Rousou JA, Breyer RH. 1987. Aerobic vs anaerobic metabolism during ischemia in heart muscle. *Ann Chir Gynaecol* **76**: 68-76.

Dastur A, Beaudenon S, Kelley M, Krug RM, Huibregtse JM. 2006. Herc5, an interferon-induced HECT E3 enzyme, is required for conjugation of ISG15 in human cells. *The Journal of biological chemistry* **281**: 4334-4338.

Dauber B, Wolff T. 2009. Activation of the Antiviral Kinase PKR and Viral Countermeasures. *Viruses* **1**: 523-544.

Dauphinee SM, Richer E, Eva MM, McIntosh F, Paquet M, Dangoor D, Burkart C, Zhang DE, Gruenheid S, Gros P et al. 2014. Contribution of increased ISG15, ISGylation and deregulated type I IFN signaling in Usp18 mutant mice during the course of bacterial infections. *Genes Immun* **15**: 282-292.

Decroly E, Ferron F, Lescar J, Canard B. 2011. Conventional and unconventional mechanisms for capping viral mRNA. *Nature reviews Microbiology* **10**: 51-65.

Dennert R, Crijns HJ, Heymans S. 2008. Acute viral myocarditis. *Eur Heart J* **29**: 2073-2082.

Dewald O, Sharma S, Adrogue J, Salazar R, Duerr GD, Crapo JD, Entman ML, Taegtmeyer H. 2005. Downregulation of peroxisome proliferator-activated receptor-alpha gene expression in a mouse model of ischemic cardiomyopathy is dependent on reactive oxygen species and prevents lipotoxicity. *Circulation* **112**: 407-415.

Dittmann M, Hoffmann HH, Scull MA, Gilmore RH, Bell KL, Ciancanelli M, Wilson SJ, Crotta S, Yu Y, Flatley B et al. 2015. A serpin shapes the extracellular environment to prevent influenza A virus maturation. *Cell* **160**: 631-643.

Divakaruni AS, Brand MD. 2011. The regulation and physiology of mitochondrial proton leak. *Physiology (Bethesda)* **26**: 192-205.

Dong C, Gao N, Ross BX, Yu FX. 2017. ISG15 in Host Defense Against Candida albicans Infection in a Mouse Model of Fungal Keratitis. *Investigative ophthalmology & visual science* **58**: 2948-2958.

Dos Santos PF, Van Weyenbergh J, Delgobo M, Oliveira Patricio D, Ferguson BJ, Guabiraba R, Dierckx T, Menezes SM, Bafica A, Mansur DS. 2018. ISG15-Induced IL-10 Is a Novel Anti-Inflammatory Myeloid Axis Disrupted during Active Tuberculosis. *J Immunol*.

Du Y, Duan T, Feng Y, Liu Q, Lin M, Cui J, Wang RF. 2018. LRRC25 inhibits type I IFN signaling by targeting ISG15-associated RIG-I for autophagic degradation. *The EMBO journal* **37**: 351-366.

Durbin JE, Fernandez-Sesma A, Lee CK, Rao TD, Frey AB, Moran TM, Vukmanovic S, Garcia-Sastre A, Levy DE. 2000. Type I IFN modulates innate and specific antiviral immunity. *J Immunol* **164**: 4220-4228.

Durfee LA, Lyon N, Seo K, Huibregtse JM. 2010. The ISG15 conjugation system broadly targets newly synthesized proteins: implications for the antiviral function of ISG15. *Molecular cell* **38**: 722-732.

Dzimianski JV, Scholte FEM, Bergeron E, Pegan SD. 2019a. ISG15: It's Complicated. *J Mol Biol*.

Dzimianski JV, Scholte FEM, Williams IL, Langley C, Freitas BT, Spengler JR, Bergeron E, Pegan SD. 2019b. Determining the molecular drivers of species-specific interferon-stimulated gene product 15 interactions with nairovirus ovarian tumor domain proteases. *PLoS One* **14**: e0226415.

Ebermann L, Wika S, Klumpe I, Hammer E, Klingel K, Lassner D, Volker U, Erben U, Zeichhardt H, Schultheiss HP et al. 2012. The mitochondrial respiratory chain has a critical role in the antiviral process in Coxsackievirus B3-induced myocarditis. *Lab Invest* **92**: 125-134.

Eduardo-Correia B, Martinez-Romero C, Garcia-Sastre A, Guerra S. 2014. ISG15 is counteracted by vaccinia virus E3 protein and controls the proinflammatory response against viral infection. *J Virol* **88**: 2312-2318.

Escher F, Pietsch H, Aleshcheva G, Bock T, Baumeier C, Elsaesser A, Wenzel P, Hamm C, Westenfeld R, Schultheiss M et al. 2020. Detection of viral SARS-CoV-2 genomes and histopathological changes in endomyocardial biopsies. *ESC Heart Fail* **7**: 2440-2447.

Fajardo VM, Feng I, Chen BY, Perez-Ramirez CA, Shi B, Clark P, Tian R, Lien CL, Pellegrini M, Christofk H et al. 2021. GLUT1 overexpression enhances glucose metabolism and promotes neonatal heart regeneration. *Sci Rep* **11**: 8669.

Fan JB, Arimoto K, Motamedchaboki K, Yan M, Wolf DA, Zhang DE. 2015. Identification and characterization of a novel ISG15-ubiquitin mixed chain and its role in regulating protein homeostasis. *Sci Rep* **5**: 12704.

Farrell PJ, Broeze RJ, Lengyel P. 1979. Accumulation of an mRNA and protein in interferon-treated Ehrlich ascites tumour cells. *Nature* **279**: 523-525.

Faxon DP, Creager MA, Smith SC, Jr., Pasternak RC, Olin JW, Bettmann MA, Criqui MH, Milani RV, Loscalzo J, Kaufman JA et al. 2004. Atherosclerotic Vascular Disease Conference: Executive summary: Atherosclerotic Vascular Disease Conference proceeding for healthcare professionals from a special writing group of the American Heart Association. *Circulation* **109**: 2595-2604.

Felker GM, Mann DL. 2020. *Heart failure : a companion to Braunwald's heart disease*.

Feng Q, Langereis MA, Lork M, Nguyen M, Hato SV, Lanke K, Emdad L, Bhoopathi P, Fisher PB, Lloyd RE et al. 2014. Enterovirus 2Apro targets MDA5 and MAVS in infected cells. *J Virol* **88**: 3369-3378.

Feng Y, Zhang Y, Xiao H. 2018. AMPK and cardiac remodelling. *Sci China Life Sci* **61**: 14-23.

Fensterl V, Sen GC. 2015. Interferon-induced Ifit proteins: their role in viral pathogenesis. *J Virol* **89**: 2462-2468.

Flanegan JB, Petterson RF, Ambros V, Hewlett NJ, Baltimore D. 1977. Covalent linkage of a protein to a defined nucleotide sequence at the 5'-terminus of virion and replicative intermediate RNAs of poliovirus. *Proc Natl Acad Sci U S A* **74**: 961-965.

Fleith RC, Mears HV, Leong XY, Sanford TJ, Emmott E, Graham SC, Mansur DS, Sweeney TR. 2018. IFIT3 and IFIT2/3 promote IFIT1-mediated translation inhibition by enhancing binding to non-self RNA. *Nucleic Acids Res* **46**: 5269-5285.

Flynn CT, Kimura T, Frimpong-Boateng K, Harkins S, Whitton JL. 2017. Immunological and pathological consequences of coxsackievirus RNA persistence in the heart. *Virology* **512**: 104-112.

Francisco E, Suthar M, Gale M, Jr., Rosenfeld AB, Racaniello VR. 2019. Cell-type specificity and functional redundancy of RIG-I-like receptors in innate immune sensing of Coxsackievirus B3 and encephalomyocarditis virus. *Virology* **528**: 7-18.

Fuchs FD, Whelton PK. 2020. High Blood Pressure and Cardiovascular Disease. *Hypertension* **75**: 285-292.

Fuchs SY. 2013. Hope and fear for interferon: the receptor-centric outlook on the future of interferon therapy. *Journal of interferon & cytokine research : the official journal of the International Society for Interferon and Cytokine Research* **33**: 211-225.

Garmaroudi FS, Marchant D, Hendry R, Luo H, Yang D, Ye X, Shi J, McManus BM. 2015. Coxsackievirus B3 replication and pathogenesis. *Future Microbiol* **10**: 629-653.

Georgiadi A, Boekschoten MV, Muller M, Kersten S. 2012. Detailed transcriptomics analysis of the effect of dietary fatty acids on gene expression in the heart. *Physiol Genomics* **44**: 352-361.

Giannakopoulos NV, Arutyunova E, Lai C, Lenschow DJ, Haas AL, Virgin HW. 2009. ISG15 Arg151 and the ISG15-conjugating enzyme UbE1L are important for innate immune control of Sindbis virus. *J Virol* **83**: 1602-1610.

Giannakopoulos NV, Luo JK, Papov V, Zou W, Lenschow DJ, Jacobs BS, Borden EC, Li J, Virgin HW, Zhang DE. 2005. Proteomic identification of proteins conjugated to ISG15 in mouse and human cells. *Biochemical and biophysical research communications* **336**: 496-506.

Grabbe C, Husnjak K, Dikic I. 2011. The spatial and temporal organization of ubiquitin networks. *Nat Rev Mol Cell Biol* **12**: 295-307.

Graham N, Huang GN. 2021. Endocrine Influence on Cardiac Metabolism in Development and Regeneration. *Endocrinology* **162**.

Grandvaux N, Servant MJ, tenOever B, Sen GC, Balachandran S, Barber GN, Lin R, Hiscott J. 2002. Transcriptional profiling of interferon regulatory factor 3 target genes: direct involvement in the regulation of interferon-stimulated genes. *J Virol* **76**: 5532-5539.

Guo A. 2009. Phosphosite CST Curation Set CST Curation Set: 8159; Biosample/Treatment: tissue, spleen/untreated; Disease: -; SILAC: -; Specificities of Antibodies Used to Purify Peptides prior to LCMS: Ub(K-e-GG) Antibodies Used to Purify Peptides prior to LCMS: Ubiquitin (D4A7A10) XP(R) Rabbit mAb Cat#: 3925, PTMScan(R) Ubiquitin Branch Motif (K-e-GG) Immunoaffinity Beads Cat#: 1990.

Guo J, Peters KL, Sen GC. 2000. Induction of the human protein P56 by interferon, double-stranded RNA, or virus infection. *Virology* **267**: 209-219.

Gusho E, Baskar D, Banerjee S. 2020. New advances in our understanding of the "unique" RNase L in host pathogen interaction and immune signaling. *Cytokine* **133**: 153847.

Haas AL, Ahrens P, Bright PM, Ankel H. 1987. Interferon induces a 15-kilodalton protein exhibiting marked homology to ubiquitin. *The Journal of biological chemistry* **262**: 11315-11323.

Habjan M, Hubel P, Lacerda L, Benda C, Holze C, Eberl CH, Mann A, Kindler E, Gil-Cruz C, Ziebuhr J et al. 2013. Sequestration by IFIT1 impairs translation of 2'O-unmethylated capped RNA. *PLoS pathogens* **9**: e1003663.

Hammer E, Phong TQ, Steil L, Klingel K, Salazar MG, Bernhardt J, Kandolf R, Kroemer HK, Felix SB, Volker U. 2010. Viral myocarditis induced by Coxsackievirus B3 in A.BY/SnJ mice: analysis of changes in the myocardial proteome. *Proteomics* **10**: 1802-1818.

Han JQ, Townsend HL, Jha BK, Paranjape JM, Silverman RH, Barton DJ. 2007. A phylogenetically conserved RNA structure in the poliovirus open reading frame inhibits the antiviral endoribonuclease RNase L. *J Virol* **81**: 5561-5572.

Hare NJ, Chan B, Chan E, Kaufman KL, Britton WJ, Saunders BM. 2015. Microparticles released from Mycobacterium tuberculosis-infected human macrophages contain increased levels of the type I interferon inducible proteins including ISG15. *Proteomics* **15**: 3020-3029.

Harvala H, Kalimo H, Bergelson J, Stanway G, Hyypia T. 2005. Tissue tropism of recombinant coxsackieviruses in an adult mouse model. *J Gen Virol* **86**: 1897-1907.

Hedl M, Yan J, Abraham C. 2016. IRF5 and IRF5 Disease-Risk Variants Increase Glycolysis and Human M1 Macrophage Polarization by Regulating Proximal Signaling and Akt2 Activation. *Cell Rep* **16**: 2442-2455.

Herzum M, Ruppert V, Kuytz B, Jomaa H, Nakamura I, Maisch B. 1994. Coxsackievirus B3 infection leads to cell death of cardiac myocytes. *J Mol Cell Cardiol* **26**: 907-913.

Hrecka K, Hao C, Gierszewska M, Swanson SK, Kesik-Brodacka M, Srivastava S, Florens L, Washburn MP, Skowronski J. 2011. Vpx relieves inhibition of HIV-1 infection of macrophages mediated by the SAMHD1 protein. *Nature* **474**: 658-661.

Hsu NY, Ilnytska O, Belov G, Santiana M, Chen YH, Takvorian PM, Pau C, van der Schaar H, Kaushik-Basu N, Balla T et al. 2010. Viral reorganization of the secretory pathway generates distinct organelles for RNA replication. *Cell* **141**: 799-811.

Hsu YL, Shi SF, Wu WL, Ho LJ, Lai JH. 2013. Protective roles of interferon-induced protein with tetratricopeptide repeats 3 (IFIT3) in dengue virus infection of human lung epithelial cells. *PLoS One* **8**: e79518.

Huhn MH, McCartney SA, Lind K, Svedin E, Colonna M, Flodstrom-Tullberg M. 2010. Melanoma differentiation-associated protein-5 (MDA-5) limits early viral replication but is not essential for the induction of type 1 interferons after Coxsackievirus infection. *Virology* **401**: 42-48.

Ikeda F, Dikic I. 2008. Atypical ubiquitin chains: new molecular signals. 'Protein Modifications: Beyond the Usual Suspects' review series. *EMBO reports* **9**: 536-542.

Ivashkiv LB, Donlin LT. 2014. Regulation of type I interferon responses. *Nat Rev Immunol* **14**: 36-49.

Iwasaki A, Medzhitov R. 2004. Toll-like receptor control of the adaptive immune responses. *Nat Immunol* **5**: 987-995.

Jakel S, Kuckelkorn U, Szalay G, Plotz M, Textoris-Taube K, Opitz E, Klingel K, Stevanovic S, Kandolf R, Kotsch K et al. 2009. Differential interferon responses enhance viral epitope generation by myocardial immunoproteasomes in murine enterovirus myocarditis. *Am J Pathol* **175**: 510-518.

Jang SK, Krausslich HG, Nicklin MJ, Duke GM, Palmenberg AC, Wimmer E. 1988. A segment of the 5' nontranslated region of encephalomyocarditis virus RNA directs internal entry of ribosomes during in vitro translation. *J Virol* **62**: 2636-2643.

Jiang Z, Su C, Zheng C. 2016. Herpes Simplex Virus 1 Tegument Protein UL41 Counteracts IFIT3 Antiviral Innate Immunity. *J Virol* **90**: 11056-11061.

Justesen J, Hartmann R, Kjeldgaard NO. 2000. Gene structure and function of the 2'-5'-oligoadenylate synthetase family. *Cell Mol Life Sci* **57**: 1593-1612.

Kaimoto S, Hoshino A, Ariyoshi M, Okawa Y, Tateishi S, Ono K, Uchihashi M, Fukai K, Iwai-Kanai E, Matoba S. 2017. Activation of PPAR-alpha in the early stage of heart failure maintained myocardial function and energetics in pressure-overload heart failure. *Am J Physiol Heart Circ Physiol* **312**: H305-H313.

Kalogeris T, Baines CP, Krenz M, Korthuis RJ. 2012. Cell biology of ischemia/reperfusion injury. *Int Rev Cell Mol Biol* **298**: 229-317.

Kang D, Jiang H, Wu Q, Pestka S, Fisher PB. 2001. Cloning and characterization of human ubiquitin-processing protease-43 from terminally differentiated human melanoma cells using a rapid subtraction hybridization protocol RaSH. *Gene* **267**: 233-242.

Kang DC, Gopalkrishnan RV, Lin L, Randolph A, Valerie K, Pestka S, Fisher PB. 2004. Expression analysis and genomic characterization of human melanoma differentiation associated gene-5, mda-5: a novel type I interferon-responsive apoptosis-inducing gene. *Oncogene* **23**: 1789-1800.

Kawai T, Akira S. 2006. Innate immune recognition of viral infection. *Nat Immunol* **7**: 131-137.

Kawai T, Akira S. 2008. Toll-like receptor and RIG-I-like receptor signaling. *Ann N Y Acad Sci* **1143**: 1-20.

Kemball CC, Alirezaei M, Flynn CT, Wood MR, Harkins S, Kiosses WB, Whitton JL. 2010. Coxsackievirus infection induces autophagy-like vesicles and megaphagosomes in pancreatic acinar cells in vivo. *J Virol* **84**: 12110-12124.

Kespohl M, Bredow C, Klingel K, Voss M, Paeschke A, Zickler M, Poller W, Kaya Z, Eckstein J, Fechner H et al. 2020. Protein modification with ISG15 blocks coxsackievirus pathology by antiviral and metabolic reprogramming. *Sci Adv* **6**: eaay1109.

Ketscher L, Basters A, Prinz M, Knobeloch KP. 2012. mHERC6 is the essential ISG15 E3 ligase in the murine system. *Biochemical and biophysical research communications* **417**: 135-140.

Ketscher L, Hannss R, Morales DJ, Basters A, Guerra S, Goldmann T, Hausmann A, Prinz M, Naumann R, Pekosz A et al. 2015. Selective inactivation of USP18 isopeptidase activity in vivo enhances ISG15 conjugation and viral resistance. *Proc Natl Acad Sci U S A* **112**: 1577-1582.

Kim KI, Giannakopoulos NV, Virgin HW, Zhang DE. 2004. Interferon-inducible ubiquitin E2, Ubc8, is a conjugating enzyme for protein ISGylation. *Mol Cell Biol* **24**: 9592-9600.

Kim KI, Malakhova OA, Hoebe K, Yan M, Beutler B, Zhang DE. 2005. Enhanced antibacterial potential in UBP43-deficient mice against Salmonella typhimurium infection by up-regulating type I IFN signaling. *J Immunol* **175**: 847-854.

Kim KI, Yan M, Malakhova O, Luo JK, Shen MF, Zou W, de la Torre JC, Zhang DE. 2006. Ube1L and protein ISGylation are not essential for alpha/beta interferon signaling. *Mol Cell Biol* **26**: 472-479.

Kim KI, Zhang DE. 2003. ISG15, not just another ubiquitin-like protein. *Biochemical and biophysical research communications* **307**: 431-434.

Kim MJ, Hwang SY, Imaizumi T, Yoo JY. 2008. Negative feedback regulation of RIG-I-mediated antiviral signaling by interferon-induced ISG15 conjugation. *J Virol* **82**: 1474-1483.

Kim YJ, Kim ET, Kim YE, Lee MK, Kwon KM, Kim KI, Stamminger T, Ahn JH. 2016. Consecutive Inhibition of ISG15 Expression and ISGylation by Cytomegalovirus Regulators. *PLoS pathogens* **12**: e1005850.

Kimmey JM, Campbell JA, Weiss LA, Monte KJ, Lenschow DJ, Stallings CL. 2017. The impact of ISGylation during Mycobacterium tuberculosis infection in mice. *Microbes Infect* **19**: 249-258.

Kimura T, Flynn CT, Alirezaei M, Sen GC, Whitton JL. 2019. Biphasic and cardiomyocyte-specific IFIT activity protects cardiomyocytes from enteroviral infection. *PLoS pathogens* **15**: e1007674.

Kimura T, Katoh H, Kayama H, Saiga H, Okuyama M, Okamoto T, Umemoto E, Matsuura Y, Yamamoto M, Takeda K. 2013. Ifit1 inhibits Japanese encephalitis virus replication through binding to 5' capped 2'-O unmethylated RNA. *J Virol* **87**: 9997-10003.

Kindermann I, Kindermann M, Kandolf R, Klingel K, Bultmann B, Muller T, Lindinger A, Bohm M. 2008. Predictors of outcome in patients with suspected myocarditis. *Circulation* **118**: 639-648.

Kitagawa Y, Yamaguchi M, Kohno M, Sakai M, Itoh M, Gotoh B. 2020. Respirovirus C protein inhibits activation of type I interferon receptor-associated kinases to block JAK-STAT signaling. *FEBS letters* **594**: 864-877.

Klingel K, Hohenadl C, Canu A, Albrecht M, Seemann M, Mall G, Kandolf R. 1992. Ongoing enterovirus-induced myocarditis is associated with persistent heart muscle infection: quantitative analysis of virus replication, tissue damage, and inflammation. *Proc Natl Acad Sci U S A* **89**: 314-318.

Knight E, Jr., Cordova B. 1991. IFN-induced 15-kDa protein is released from human lymphocytes and monocytes. *J Immunol* **146**: 2280-2284.

Knight E, Jr., Fahey D, Cordova B, Hillman M, Kutny R, Reich N, Blomstrom D. 1988. A 15-kDa interferon-induced protein is derived by COOH-terminal processing of a 17-kDa precursor. *The Journal of biological chemistry* **263**: 4520-4522.

Knobeloch KP, Utermohlen O, Kisser A, Prinz M, Horak I. 2005. Reexamination of the role of ubiquitin-like modifier ISG15 in the phenotype of UBP43-deficient mice. *Mol Cell Biol* **25**: 11030-11034.

Kochs G, Janzen C, Hohenberg H, Haller O. 2002. Antivirally active MxA protein sequesters La Crosse virus nucleocapsid protein into perinuclear complexes. *Proc Natl Acad Sci U S A* **99**: 3153-3158.

Kolwicz SC, Jr., Purohit S, Tian R. 2013. Cardiac metabolism and its interactions with contraction, growth, and survival of cardiomyocytes. *Circ Res* **113**: 603-616.

Kotter S, Kazmierowska M, Andresen C, Bottermann K, Grandoch M, Gorressen S, Heinen A, Moll JM, Scheller J, Godecke A et al. 2016. Titin-Based Cardiac Myocyte Stiffening Contributes to Early Adaptive Ventricular Remodeling After Myocardial Infarction. *Circ Res* **119**: 1017-1029.

Kramarz B, Lovering RC. 2019. Gene Ontology: A Resource for Analysis and Interpretation of Alzheimer's Disease Data. in *Alzheimer's Disease* (ed. T Wisniewski), Brisbane (AU).

Kretschmer S, Lee-Kirsch MA. 2017. Type I interferon-mediated autoinflammation and autoimmunity. *Current opinion in immunology* **49**: 96-102.

Kristiansen H, Gad HH, Eskildsen-Larsen S, Despres P, Hartmann R. 2011. The oligoadenylate synthetase family: an ancient protein family with multiple antiviral activities. *Journal of interferon & cytokine research : the official journal of the International Society for Interferon and Cytokine Research* **31**: 41-47.

Kuang Z, Seo EJ, Leis J. 2011. Mechanism of inhibition of retrovirus release from cells by interferon-induced gene ISG15. *J Virol* **85**: 7153-7161.

Kubli DA, Gustafsson AB. 2014. Cardiomyocyte health: adapting to metabolic changes through autophagy. *Trends Endocrinol Metab* **25**: 156-164.

Kuhl U, Pauschinger M, Seeberg B, Lassner D, Noutsias M, Poller W, Schultheiss HP. 2005. Viral persistence in the myocardium is associated with progressive cardiac dysfunction. *Circulation* **112**: 1965-1970.

Kumar P, Sweeney TR, Skabkin MA, Skabkina OV, Hellen CU, Pestova TV. 2014. Inhibition of translation by IFIT family members is determined by their ability to interact selectively with the 5'-terminal regions of cap0-, cap1- and 5'ppp- mRNAs. *Nucleic Acids Res* **42**: 3228-3245.

Kumthip K, Chusri P, Jilg N, Zhao L, Fusco DN, Zhao H, Goto K, Cheng D, Schaefer EA, Zhang L et al. 2012. Hepatitis C virus NS5A disrupts STAT1 phosphorylation and suppresses type I interferon signaling. *J Virol* **86**: 8581-8591.

Laflamme MA, Murry CE. 2011. Heart regeneration. *Nature* **473**: 326-335.

Lazarou M, Sliter DA, Kane LA, Sarraf SA, Wang C, Burman JL, Sideris DP, Fogel AI, Youle RJ. 2015. The ubiquitin kinase PINK1 recruits autophagy receptors to induce mitophagy. *Nature* **524**: 309-314.

Lee-Kirsch MA. 2017. The Type I Interferonopathies. *Annu Rev Med* **68**: 297-315.

Lenschow DJ, Giannakopoulos NV, Gunn LJ, Johnston C, O'Guin AK, Schmidt RE, Levine B, Virgin HWt. 2005. Identification of interferon-stimulated gene 15 as an antiviral molecule during Sindbis virus infection in vivo. *J Virol* **79**: 13974-13983.

Lenschow DJ, Lai C, Frias-Staheli N, Giannakopoulos NV, Lutz A, Wolff T, Osiak A, Levine B, Schmidt RE, Garcia-Sastre A et al. 2007. IFN-stimulated gene 15 functions as a critical antiviral molecule against influenza, herpes, and Sindbis viruses. *Proc Natl Acad Sci U S A* **104**: 1371-1376.

Li Y, Banerjee S, Wang Y, Goldstein SA, Dong B, Gaughan C, Silverman RH, Weiss SR. 2016. Activation of RNase L is dependent on OAS3 expression during infection with diverse human viruses. *Proc Natl Acad Sci U S A* **113**: 2241-2246.

Li Y, Li C, Xue P, Zhong B, Mao AP, Ran Y, Chen H, Wang YY, Yang F, Shu HB. 2009. ISG56 is a negative-feedback regulator of virus-triggered signaling and cellular antiviral response. *Proc Natl Acad Sci U S A* **106**: 7945-7950.

Lin RJ, Chang BL, Yu HP, Liao CL, Lin YL. 2006. Blocking of interferon-induced Jak-Stat signaling by Japanese encephalitis virus NS5 through a protein tyrosine phosphatase-mediated mechanism. *J Virol* **80**: 5908-5918.

Lin RJ, Yu HP, Chang BL, Tang WC, Liao CL, Lin YL. 2009. Distinct antiviral roles for human 2',5'-oligoadenylate synthetase family members against dengue virus infection. *J Immunol* **183**: 8035-8043.

Lindner HA, Fotouhi-Ardakani N, Lytvyn V, Lachance P, Sulea T, Menard R. 2005. The papain-like protease from the severe acute respiratory syndrome coronavirus is a deubiquitinating enzyme. *J Virol* **79**: 15199-15208.

Liu G, Lee JH, Parker ZM, Acharya D, Chiang JJ, van Gent M, Riedl W, Davis-Gardner ME, Wies E, Chiang C et al. 2021. ISG15-dependent activation of the sensor MDA5 is antagonized by the SARS-CoV-2 papain-like protease to evade host innate immunity. *Nat Microbiol* **6**: 467-478.

Liu S, Jiang M, Wang W, Liu W, Song X, Ma Z, Zhang S, Liu L, Liu Y, Cao X. 2018. Nuclear RNF2 inhibits interferon function by promoting K33-linked STAT1 disassociation from DNA. *Nat Immunol* **19**: 41-52.

Liu SY, Aliyari R, Chikere K, Li G, Marsden MD, Smith JK, Pernet O, Guo H, Nusbaum R, Zack JA et al. 2013. Interferon-inducible cholesterol-25-hydroxylase broadly inhibits viral entry by production of 25-hydroxycholesterol. *Immunity* **38**: 92-105.

Liu XY, Chen W, Wei B, Shan YF, Wang C. 2011. IFN-induced TPR protein IFIT3 potentiates antiviral signaling by bridging MAVS and TBK1. *J Immunol* **187**: 2559-2568.

Lloyd RE, Jense HG, Ehrenfeld E. 1987. Restriction of translation of capped mRNA in vitro as a model for poliovirus-induced inhibition of host cell protein synthesis: relationship to p220 cleavage. *J Virol* **61**: 2480-2488.

Loeb KR, Haas AL. 1992. The interferon-inducible 15-kDa ubiquitin homolog conjugates to intracellular proteins. *The Journal of biological chemistry* **267**: 7806-7813.

Lu J, Yi L, Zhao J, Yu J, Chen Y, Lin MC, Kung HF, He ML. 2012. Enterovirus 71 disrupts interferon signaling by reducing the level of interferon receptor 1. *J Virol* **86**: 3767-3776.

Lu L, Wei L, Peng G, Mu Y, Wu K, Kang L, Yan X, Zhu Y, Wu J. 2008. NS3 protein of hepatitis C virus regulates cyclooxygenase-2 expression through multiple signaling pathways. *Virology* **371**: 61-70.

Lugli E, Troiano L, Ferraresi R, Roat E, Prada N, Nasi M, Pinti M, Cooper EL, Cossarizza A. 2005. Characterization of cells with different mitochondrial membrane potential during apoptosis. *Cytometry A* **68**: 28-35.

Luptak I, Yan J, Cui L, Jain M, Liao R, Tian R. 2007. Long-term effects of increased glucose entry on mouse hearts during normal aging and ischemic stress. *Circulation* **116**: 901-909.

Magnani JW, Dec GW. 2006. Myocarditis: current trends in diagnosis and treatment. *Circulation* **113**: 876-890.

Mahrholdt H, Goedecke C, Wagner A, Meinhardt G, Athanasiadis A, Vogelsberg H, Fritz P, Klingel K, Kandolf R, Sechtem U. 2004. Cardiovascular magnetic resonance assessment of human myocarditis: a comparison to histology and molecular pathology. *Circulation* **109**: 1250-1258.

Maisch B. 2019. Cardio-Immunology of Myocarditis: Focus on Immune Mechanisms and Treatment Options. *Front Cardiovasc Med* **6**: 48.

Malakhov MP, Kim KI, Malakhova OA, Jacobs BS, Borden EC, Zhang DE. 2003. High-throughput immunoblotting. Ubiquitiin-like protein ISG15 modifies key regulators of signal transduction. *The Journal of biological chemistry* **278**: 16608-16613.

Malakhov MP, Malakhova OA, Kim KI, Ritchie KJ, Zhang DE. 2002. UBP43 (USP18) specifically removes ISG15 from conjugated proteins. *The Journal of biological chemistry* **277**: 9976-9981.

Malakhova OA, Kim KI, Luo JK, Zou W, Kumar KG, Fuchs SY, Shuai K, Zhang DE. 2006. UBP43 is a novel regulator of interferon signaling independent of its ISG15 isopeptidase activity. *The EMBO journal* **25**: 2358-2367.

Malakhova OA, Yan M, Malakhov MP, Yuan Y, Ritchie KJ, Kim KI, Peterson LF, Shuai K, Zhang DE. 2003. Protein ISGylation modulates the JAK-STAT signaling pathway. *Genes & development* **17**: 455-460.

Malakhova OA, Zhang DE. 2008. ISG15 inhibits Nedd4 ubiquitin E3 activity and enhances the innate antiviral response. *The Journal of biological chemistry* **283**: 8783-8787.

Malandraki-Miller S, Lopez CA, Al-Siddiqi H, Carr CA. 2018. Changing Metabolism in Differentiating Cardiac Progenitor Cells-Can Stem Cells Become Metabolically Flexible Cardiomyocytes? *Front Cardiovasc Med* **5**: 119.

Malathi K, Dong B, Gale M, Jr., Silverman RH. 2007. Small self-RNA generated by RNase L amplifies antiviral innate immunity. *Nature* **448**: 816-819.

Martindale JJ, Fernandez R, Thuerauf D, Whittaker R, Gude N, Sussman MA, Glembotski CC. 2006. Endoplasmic reticulum stress gene induction and protection from ischemia/reperfusion

injury in the hearts of transgenic mice with a tamoxifen-regulated form of ATF6. *Circ Res* **98**: 1186-1193.
McClure TD, Young ME, Taegtmeyer H, Ning XH, Buroker NE, Lopez-Guisa J, Portman MA. 2005. Thyroid hormone interacts with PPARalpha and PGC-1 during mitochondrial maturation in sheep heart. *Am J Physiol Heart Circ Physiol* **289**: H2258-2264.
McManus BM, Chow LH, Wilson JE, Anderson DR, Gulizia JM, Gauntt CJ, Klingel KE, Beisel KW, Kandolf R. 1993. Direct myocardial injury by enterovirus: a central role in the evolution of murine myocarditis. *Clinical immunology and immunopathology* **68**: 159-169.
Meijer AJ, Lorin S, Blommaart EF, Codogno P. 2015. Regulation of autophagy by amino acids and MTOR-dependent signal transduction. *Amino Acids* **47**: 2037-2063.
Mekada K, Abe K, Murakami A, Nakamura S, Nakata H, Moriwaki K, Obata Y, Yoshiki A. 2009. Genetic differences among C57BL/6 substrains. *Exp Anim* **58**: 141-149.
Memet S, Besancon F, Bourgeade MF, Thang MN. 1991. Direct induction of interferon-gamma- and interferon-alpha/beta-inducible genes by double-stranded RNA. *J Interferon Res* **11**: 131-141.
Meurs EF, Watanabe Y, Kadereit S, Barber GN, Katze MG, Chong K, Williams BR, Hovanessian AG. 1992. Constitutive expression of human double-stranded RNA-activated p68 kinase in murine cells mediates phosphorylation of eukaryotic initiation factor 2 and partial resistance to encephalomyocarditis virus growth. *J Virol* **66**: 5805-5814.
Meuwissen ME, Schot R, Buta S, Oudesluijs G, Tinschert S, Speer SD, Li Z, van Unen L, Heijsman D, Goldmann T et al. 2016. Human USP18 deficiency underlies type 1 interferonopathy leading to severe pseudo-TORCH syndrome. *J Exp Med* **213**: 1163-1174.
Mi H, Muruganujan A, Casagrande JT, Thomas PD. 2013. Large-scale gene function analysis with the PANTHER classification system. *Nat Protoc* **8**: 1551-1566.
Mielech AM, Kilianski A, Baez-Santos YM, Mesecar AD, Baker SC. 2014. MERS-CoV papain-like protease has deISGylating and deubiquitinating activities. *Virology* **450-451**: 64-70.
Milstone AM, Petrella J, Sanchez MD, Mahmud M, Whitbeck JC, Bergelson JM. 2005. Interaction with coxsackievirus and adenovirus receptor, but not with decay-accelerating factor (DAF), induces A-particle formation in a DAF-binding coxsackievirus B3 isolate. *J Virol* **79**: 655-660.
Minakawa M, Sone T, Takeuchi T, Yokosawa H. 2008. Regulation of the nuclear factor (NF)-kappaB pathway by ISGylation. *Biol Pharm Bull* **31**: 2223-2227.
Minamino T, Komuro I, Kitakaze M. 2010. Endoplasmic reticulum stress as a therapeutic target in cardiovascular disease. *Circ Res* **107**: 1071-1082.
Mohamud Y, Shi J, Qu J, Poon T, Xue YC, Deng H, Zhang J, Luo H. 2018. Enteroviral Infection Inhibits Autophagic Flux via Disruption of the SNARE Complex to Enhance Viral Replication. *Cell Rep* **22**: 3292-3303.
Mookerjee SA, Brand MD. 2015. Measurement and Analysis of Extracellular Acid Production to Determine Glycolytic Rate. *J Vis Exp*: e53464.
Morales DJ, Monte K, Sun L, Struckhoff JJ, Agapov E, Holtzman MJ, Stappenbeck TS, Lenschow DJ. 2015. Novel mode of ISG15-mediated protection against influenza A virus and Sendai virus in mice. *J Virol* **89**: 337-349.
Mot AI, Liddell JR, White AR, Crouch PJ. 2016. Circumventing the Crabtree Effect: A method to induce lactate consumption and increase oxidative phosphorylation in cell culture. *Int J Biochem Cell Biol* **79**: 128-138.
Mukhopadhyay D, Riezman H. 2007. Proteasome-independent functions of ubiquitin in endocytosis and signaling. *Science* **315**: 201-205.
Munoz-Jordan JL, Laurent-Rolle M, Ashour J, Martinez-Sobrido L, Ashok M, Lipkin WI, Garcia-Sastre A. 2005. Inhibition of alpha/beta interferon signaling by the NS4B protein of flaviviruses. *J Virol* **79**: 8004-8013.
Murphy K. 2018. *JANEWAY IMMUNOLOGIE*. SPRINGER, [Place of publication not identified].

Nakasato N, Ikeda K, Urano T, Horie-Inoue K, Takeda S, Inoue S. 2006. A ubiquitin E3 ligase Efp is up-regulated by interferons and conjugated with ISG15. *Biochemical and biophysical research communications* **351**: 540-546.

Nakashima H, Nguyen T, Goins WF, Chiocca EA. 2015. Interferon-stimulated gene 15 (ISG15) and ISG15-linked proteins can associate with members of the selective autophagic process, histone deacetylase 6 (HDAC6) and SQSTM1/p62. *The Journal of biological chemistry* **290**: 1485-1495.

Napolitano A, van der Veen AG, Bunyan M, Borg A, Frith D, Howell S, Kjaer S, Beling A, Snijders AP, Knobeloch KP et al. 2018. Cysteine-Reactive Free ISG15 Generates IL-1beta-Producing CD8alpha(+) Dendritic Cells at the Site of Infection. *J Immunol* **201**: 604-614.

Narasimhan J, Wang M, Fu Z, Klein JM, Haas AL, Kim JJ. 2005. Crystal structure of the interferon-induced ubiquitin-like protein ISG15. *The Journal of biological chemistry* **280**: 27356-27365.

Neely JR, Liedtke AJ, Whitmer JT, Rovetto MJ. 1975. Relationship between coronary flow and adenosine triphosphate production from glycolysis and oxidative metabolism. *Recent Adv Stud Cardiac Struct Metab* **8**: 301-321.

Negishi H, Osawa T, Ogami K, Ouyang X, Sakaguchi S, Koshiba R, Yanai H, Seko Y, Shitara H, Bishop K et al. 2008. A critical link between Toll-like receptor 3 and type II interferon signaling pathways in antiviral innate immunity. *Proc Natl Acad Sci U S A* **105**: 20446-20451.

Neil SJ, Zang T, Bieniasz PD. 2008. Tetherin inhibits retrovirus release and is antagonized by HIV-1 Vpu. *Nature* **451**: 425-430.

Neishabouri SH, Hutson SM, Davoodi J. 2015. Chronic activation of mTOR complex 1 by branched chain amino acids and organ hypertrophy. *Amino Acids* **47**: 1167-1182.

Newgard CB. 2012. Interplay between lipids and branched-chain amino acids in development of insulin resistance. *Cell Metab* **15**: 606-614.

Ni G, Konno H, Barber GN. 2017. Ubiquitination of STING at lysine 224 controls IRF3 activation. *Sci Immunol* **2**.

Nickel A, Kohlhaas M, Maack C. 2014. Mitochondrial reactive oxygen species production and elimination. *J Mol Cell Cardiol* **73**: 26-33.

O'Carroll IP, Rein A. 2016. Viral Nucleic Acids. in *Encyclopedia of Cell Biology* (eds. RA Bradshaw, PD Stahl), pp. 517-524. Academic Press, Waltham.

Okumura A, Lu G, Pitha-Rowe I, Pitha PM. 2006. Innate antiviral response targets HIV-1 release by the induction of ubiquitin-like protein ISG15. *Proc Natl Acad Sci U S A* **103**: 1440-1445.

Okumura A, Pitha PM, Harty RN. 2008. ISG15 inhibits Ebola VP40 VLP budding in an L-domain-dependent manner by blocking Nedd4 ligase activity. *Proc Natl Acad Sci U S A* **105**: 3974-3979.

Okumura F, Okumura AJ, Uematsu K, Hatakeyama S, Zhang DE, Kamura T. 2013. Activation of double-stranded RNA-activated protein kinase (PKR) by interferon-stimulated gene 15 (ISG15) modification down-regulates protein translation. *The Journal of biological chemistry* **288**: 2839-2847.

Okumura F, Zou W, Zhang DE. 2007. ISG15 modification of the eIF4E cognate 4EHP enhances cap structure-binding activity of 4EHP. *Genes & development* **21**: 255-260.

Opitz E, Koch A, Klingel K, Schmidt F, Prokop S, Rahnefeld A, Sauter M, Heppner FL, Volker U, Kandolf R et al. 2011. Impairment of immunoproteasome function by beta5i/LMP7 subunit deficiency results in severe enterovirus myocarditis. *PLoS pathogens* **7**: e1002233.

Osiak A, Utermohlen O, Niendorf S, Horak I, Knobeloch KP. 2005. ISG15, an interferon-stimulated ubiquitin-like protein, is not essential for STAT1 signaling and responses against vesicular stomatitis and lymphocytic choriomeningitis virus. *Mol Cell Biol* **25**: 6338-6345.

Pankuweit S, Klingel K. 2013. Viral myocarditis: from experimental models to molecular diagnosis in patients. *Heart Fail Rev* **18**: 683-702.

Pantel A, Teixeira A, Haddad E, Wood EG, Steinman RM, Longhi MP. 2014. Direct type I IFN but not MDA5/TLR3 activation of dendritic cells is required for maturation and metabolic shift to glycolysis after poly IC stimulation. *PLoS Biol* **12**: e1001759.

Park JH, Yang SW, Park JM, Ka SH, Kim JH, Kong YY, Jeon YJ, Seol JH, Chung CH. 2016. Positive feedback regulation of p53 transactivity by DNA damage-induced ISG15 modification. *Nat Commun* **7**: 12513.

Pavlovic J, Zurcher T, Haller O, Staeheli P. 1990. Resistance to influenza virus and vesicular stomatitis virus conferred by expression of human MxA protein. *J Virol* **64**: 3370-3375.

Pei R, Qin B, Zhang X, Zhu W, Kemper T, Ma Z, Trippler M, Schlaak J, Chen X, Lu M. 2014. Interferon-induced proteins with tetratricopeptide repeats 1 and 2 are cellular factors that limit hepatitis B virus replication. *J Innate Immun* **6**: 182-191.

Pelletier J, Kaplan G, Racaniello VR, Sonenberg N. 1988. Cap-independent translation of poliovirus mRNA is conferred by sequence elements within the 5' noncoding region. *Mol Cell Biol* **8**: 1103-1112.

Perng YC, Lenschow DJ. 2018. ISG15 in antiviral immunity and beyond. *Nature reviews Microbiology* **16**: 423-439.

Pichlmair A, Lassnig C, Eberle CA, Gorna MW, Baumann CL, Burkard TR, Burckstummer T, Stefanovic A, Krieger S, Bennett KL et al. 2011. IFIT1 is an antiviral protein that recognizes 5'-triphosphate RNA. *Nat Immunol* **12**: 624-630.

Piganis RA, De Weerd NA, Gould JA, Schindler CW, Mansell A, Nicholson SE, Hertzog PJ. 2011. Suppressor of cytokine signaling (SOCS) 1 inhibits type I interferon (IFN) signaling via the interferon alpha receptor (IFNAR1)-associated tyrosine kinase Tyk2. *The Journal of biological chemistry* **286**: 33811-33818.

Pincetic A, Kuang Z, Seo EJ, Leis J. 2010. The interferon-induced gene ISG15 blocks retrovirus release from cells late in the budding process. *J Virol* **84**: 4725-4736.

Pingale KD, Kanade GD, Karpe YA. 2019. Hepatitis E virus polymerase binds to IFIT1 to protect the viral RNA from IFIT1-mediated translation inhibition. *J Gen Virol* **100**: 471-483.

Pinto AK, Williams GD, Szretter KJ, White JP, Proenca-Modena JL, Liu G, Olejnik J, Brien JD, Ebihara H, Muhlberger E et al. 2015. Human and Murine IFIT1 Proteins Do Not Restrict Infection of Negative-Sense RNA Viruses of the Orthomyxoviridae, Bunyaviridae, and Filoviridae Families. *J Virol* **89**: 9465-9476.

Popovic D, Vucic D, Dikic I. 2014. Ubiquitination in disease pathogenesis and treatment. *Nature medicine* **20**: 1242-1253.

Portbury AL, Ronnebaum SM, Zungu M, Patterson C, Willis MS. 2012. Back to your heart: ubiquitin proteasome system-regulated signal transduction. *J Mol Cell Cardiol* **52**: 526-537.

Potter JL, Narasimhan J, Mende-Mueller L, Haas AL. 1999. Precursor processing of pro-ISG15/UCRP, an interferon-beta-induced ubiquitin-like protein. *The Journal of biological chemistry* **274**: 25061-25068.

Pyper SR, Viswakarma N, Yu S, Reddy JK. 2010. PPARalpha: energy combustion, hypolipidemia, inflammation and cancer. *Nucl Recept Signal* **8**: e002.

Radoshevich L, Impens F, Ribet D, Quereda JJ, Nam Tham T, Nahori MA, Bierne H, Dussurget O, Pizarro-Cerda J, Knobeloch KP et al. 2015. ISG15 counteracts Listeria monocytogenes infection. *eLife* **4**.

Rahnefeld A, Klingel K, Schuermann A, Diny NL, Althof N, Lindner A, Bleienheuft P, Savvatis K, Respondek D, Opitz E et al. 2014. Ubiquitin-like protein ISG15 (interferon-stimulated gene of 15 kDa) in host defense against heart failure in a mouse model of virus-induced cardiomyopathy. *Circulation* **130**: 1589-1600.

Raso MC, Djoric N, Walser F, Hess S, Schmid FM, Burger S, Knobeloch KP, Penengo L. 2020. Interferon-stimulated gene 15 accelerates replication fork progression inducing chromosomal breakage. *J Cell Biol* **219**.

Rassmann A, Henke A, Zobawa M, Carlsohn M, Saluz HP, Grabley S, Lottspeich F, Munder T. 2006. Proteome alterations in human host cells infected with coxsackievirus B3. *J Gen Virol* **87**: 2631-2638.

Raychoudhuri A, Shrivastava S, Steele R, Kim H, Ray R, Ray RB. 2011. ISG56 and IFITM1 proteins inhibit hepatitis C virus replication. *J Virol* **85**: 12881-12889.

Reczek CR, Chandel NS. 2015. ROS-dependent signal transduction. *Curr Opin Cell Biol* **33**: 8-13.

Reich N, Evans B, Levy D, Fahey D, Knight E, Jr., Darnell JE, Jr. 1987. Interferon-induced transcription of a gene encoding a 15-kDa protein depends on an upstream enhancer element. *Proc Natl Acad Sci U S A* **84**: 6394-6398.

Remels AHV, Derks WJA, Cillero-Pastor B, Verhees KJP, Kelders MC, Heggermont W, Carai P, Summer G, Ellis SR, de Theije CC et al. 2018. NF-kappaB-mediated metabolic remodelling in the inflamed heart in acute viral myocarditis. *Biochim Biophys Acta Mol Basis Dis* **1864**: 2579-2589.

Ritchie KJ, Malakhov MP, Hetherington CJ, Zhou L, Little MT, Malakhova OA, Sipe JC, Orkin SH, Zhang DE. 2002. Dysregulation of protein modification by ISG15 results in brain cell injury. *Genes & development* **16**: 2207-2212.

Ritterhoff J, Tian R. 2017. Metabolism in cardiomyopathy: every substrate matters. *Cardiovasc Res* **113**: 411-421.

Robinson SM, Tsueng G, Sin J, Mangale V, Rahawi S, McIntyre LL, Williams W, Kha N, Cruz C, Hancock BM et al. 2014. Coxsackievirus B exits the host cell in shed microvesicles displaying autophagosomal markers. *PLoS pathogens* **10**: e1004045.

Rodriguez B, Trayanova N, Noble D. 2006. Modeling cardiac ischemia. *Ann N Y Acad Sci* **1080**: 395-414.

Rodriguez JE, Liao JY, He J, Schisler JC, Newgard CB, Drujan D, Glass DJ, Frederick CB, Yoder BC, Lalush DS et al. 2015. The ubiquitin ligase MuRF1 regulates PPARalpha activity in the heart by enhancing nuclear export via monoubiquitination. *Mol Cell Endocrinol* **413**: 36-48.

Rodriguez KR, Bruns AM, Horvath CM. 2014. MDA5 and LGP2: accomplices and antagonists of antiviral signal transduction. *J Virol* **88**: 8194-8200.

Ronchi JA, Figueira TR, Ravagnani FG, Oliveira HC, Vercesi AE, Castilho RF. 2013. A spontaneous mutation in the nicotinamide nucleotide transhydrogenase gene of C57BL/6J mice results in mitochondrial redox abnormalities. *Free Radic Biol Med* **63**: 446-456.

Ronnebaum SM, Patterson C, Schisler JC. 2014. Minireview: hey U(PS): metabolic and proteolytic homeostasis linked via AMPK and the ubiquitin proteasome system. *Mol Endocrinol* **28**: 1602-1615.

Rothenfusser S, Goutagny N, DiPerna G, Gong M, Monks BG, Schoenemeyer A, Yamamoto M, Akira S, Fitzgerald KA. 2005. The RNA helicase Lgp2 inhibits TLR-independent sensing of viral replication by retinoic acid-inducible gene-I. *J Immunol* **175**: 5260-5268.

Rudolph JD, Cox J. 2019. A Network Module for the Perseus Software for Computational Proteomics Facilitates Proteome Interaction Graph Analysis. *J Proteome Res* **18**: 2052-2064.

Rui L. 2014. Energy metabolism in the liver. *Compr Physiol* **4**: 177-197.

Russell RC, Yuan HX, Guan KL. 2014. Autophagy regulation by nutrient signaling. *Cell Res* **24**: 42-57.

Rut W, Lv Z, Zmudzinski M, Patchett S, Nayak D, Snipas SJ, El Oualid F, Huang TT, Bekes M, Drag M et al. 2020. Activity profiling and crystal structures of inhibitor-bound SARS-CoV-2 papain-like protease: A framework for anti-COVID-19 drug design. *Sci Adv* **6**.

Sadler AJ, Williams BR. 2008. Interferon-inducible antiviral effectors. *Nat Rev Immunol* **8**: 559-568.

Sag CM, Santos CX, Shah AM. 2014. Redox regulation of cardiac hypertrophy. *J Mol Cell Cardiol* **73**: 103-111.

Saitoh T, Tun-Kyi A, Ryo A, Yamamoto M, Finn G, Fujita T, Akira S, Yamamoto N, Lu KP, Yamaoka S. 2006. Negative regulation of interferon-regulatory factor 3-dependent innate antiviral response by the prolyl isomerase Pin1. *Nat Immunol* **7**: 598-605.

Sanchez-Aparicio MT, Feinman LJ, Garcia-Sastre A, Shaw ML. 2018. Paramyxovirus V Proteins Interact with the RIG-I/TRIM25 Regulatory Complex and Inhibit RIG-I Signaling. *J Virol* **92**.
Sanchez EL, Lagunoff M. 2015. Viral activation of cellular metabolism. *Virology* **479-480**: 609-618.
Sarkar SN, Ghosh A, Wang HW, Sung SS, Sen GC. 1999. The nature of the catalytic domain of 2'-5'-oligoadenylate synthetases. *The Journal of biological chemistry* **274**: 25535-25542.
Sato M, Hata N, Asagiri M, Nakaya T, Taniguchi T, Tanaka N. 1998. Positive feedback regulation of type I IFN genes by the IFN-inducible transcription factor IRF-7. *FEBS letters* **441**: 106-110.
Satoh T, Kato H, Kumagai Y, Yoneyama M, Sato S, Matsushita K, Tsujimura T, Fujita T, Akira S, Takeuchi O. 2010. LGP2 is a positive regulator of RIG-I- and MDA5-mediated antiviral responses. *Proc Natl Acad Sci U S A* **107**: 1512-1517.
Schisler JC, Rubel CE, Zhang C, Lockyer P, Cyr DM, Patterson C. 2013. CHIP protects against cardiac pressure overload through regulation of AMPK. *J Clin Invest* **123**: 3588-3599.
Schneider-Schaulies S, Schneider-Schaulies J, Schuster A, Bayer M, Pavlovic J, ter Meulen V. 1994. Cell type-specific MxA-mediated inhibition of measles virus transcription in human brain cells. *J Virol* **68**: 6910-6917.
Schultheiss HP, Kuhl U, Cooper LT. 2011. The management of myocarditis. *Eur Heart J* **32**: 2616-2625.
Schwarzer M, Doenst T. 2016. *The scientist's guide to cardiac metabolism*.
Selinka HC, Wolde A, Sauter M, Kandolf R, Klingel K. 2004. Virus-receptor interactions of coxsackie B viruses and their putative influence on cardiotropism. *Med Microbiol Immunol* **193**: 127-131.
Sen S, Kundu BK, Wu HC, Hashmi SS, Guthrie P, Locke LW, Roy RJ, Matherne GP, Berr SS, Terwelp M et al. 2013. Glucose regulation of load-induced mTOR signaling and ER stress in mammalian heart. *J Am Heart Assoc* **2**: e004796.
Sesti-Costa R, Francozo MCS, Silva GK, Proenca-Modena JL, Silva JS. 2017. TLR3 is required for survival following Coxsackievirus B3 infection by driving T lymphocyte activation and polarization: The role of dendritic cells. *PLoS One* **12**: e0185819.
Shao D, Tian R. 2015. Glucose Transporters in Cardiac Metabolism and Hypertrophy. *Compr Physiol* **6**: 331-351.
Sharma N, Okere IC, Duda MK, Chess DJ, O'Shea KM, Stanley WC. 2007. Potential impact of carbohydrate and fat intake on pathological left ventricular hypertrophy. *Cardiovasc Res* **73**: 257-268.
Shi HX, Yang K, Liu X, Liu XY, Wei B, Shan YF, Zhu LH, Wang C. 2010. Positive regulation of interferon regulatory factor 3 activation by Herc5 via ISG15 modification. *Mol Cell Biol* **30**: 2424-2436.
Shin D, Mukherjee R, Grewe D, Bojkova D, Baek K, Bhattacharya A, Schulz L, Widera M, Mehdipour AR, Tascher G et al. 2020. Papain-like protease regulates SARS-CoV-2 viral spread and innate immunity. *Nature* **587**: 657-662.
Siddiqui MA, Malathi K. 2012. RNase L induces autophagy via c-Jun N-terminal kinase and double-stranded RNA-dependent protein kinase signaling pathways. *The Journal of biological chemistry* **287**: 43651-43664.
Silverman RH. 2007. Viral encounters with 2',5'-oligoadenylate synthetase and RNase L during the interferon antiviral response. *J Virol* **81**: 12720-12729.
Silverman RH, Skehel JJ, James TC, Wreschner DH, Kerr IM. 1983. rRNA cleavage as an index of ppp(A2'p)nA activity in interferon-treated encephalomyocarditis virus-infected cells. *J Virol* **46**: 1051-1055.
Simon MM, Greenaway S, White JK, Fuchs H, Gailus-Durner V, Wells S, Sorg T, Wong K, Bedu E, Cartwright EJ et al. 2013. A comparative phenotypic and genomic analysis of C57BL/6J and C57BL/6N mouse strains. *Genome Biol* **14**: R82.
Southworth R, Davey KA, Warley A, Garlick PB. 2007. A reevaluation of the roles of hexokinase I and II in the heart. *Am J Physiol Heart Circ Physiol* **292**: H378-386.

Speer SD, Li Z, Buta S, Payelle-Brogard B, Qian L, Vigant F, Rubino E, Gardner TJ, Wedeking T, Hermann M et al. 2016. ISG15 deficiency and increased viral resistance in humans but not mice. *Nat Commun* **7**: 11496.

Stanley WC, Recchia FA, Lopaschuk GD. 2005. Myocardial substrate metabolism in the normal and failing heart. *Physiol Rev* **85**: 1093-1129.

Stawowczyk M, Van Scoy S, Kumar KP, Reich NC. 2011. The interferon stimulated gene 54 promotes apoptosis. *The Journal of biological chemistry* **286**: 7257-7266.

Sun H, Olson KC, Gao C, Prosdocimo DA, Zhou M, Wang Z, Jeyaraj D, Youn JY, Ren S, Liu Y et al. 2016a. Catabolic Defect of Branched-Chain Amino Acids Promotes Heart Failure. *Circulation* **133**: 2038-2049.

Sun L, Wang X, Zhou Y, Zhou RH, Ho WZ, Li JL. 2016b. Exosomes contribute to the transmission of anti-HIV activity from TLR3-activated brain microvascular endothelial cells to macrophages. *Antiviral Res* **134**: 167-171.

Sun L, Wu J, Du F, Chen X, Chen ZJ. 2013. Cyclic GMP-AMP synthase is a cytosolic DNA sensor that activates the type I interferon pathway. *Science* **339**: 786-791.

Sun L, Xing Y, Chen X, Zheng Y, Yang Y, Nichols DB, Clementz MA, Banach BS, Li K, Baker SC et al. 2012. Coronavirus papain-like proteases negatively regulate antiviral innate immune response through disruption of STING-mediated signaling. *PLoS One* **7**: e30802.

Swaim CD, Canadeo LA, Monte KJ, Khanna S, Lenschow DJ, Huibregtse JM. 2020. Modulation of Extracellular ISG15 Signaling by Pathogens and Viral Effector Proteins. *Cell Rep* **31**: 107772.

Swaim CD, Scott AF, Canadeo LA, Huibregtse JM. 2017. Extracellular ISG15 Signals Cytokine Secretion through the LFA-1 Integrin Receptor. *Molecular cell* **68**: 581-590 e585.

Swatek KN, Aumayr M, Pruneda JN, Visser LJ, Berryman S, Kueck AF, Geurink PP, Ovaa H, van Kuppeveld FJM, Tuthill TJ et al. 2018. Irreversible inactivation of ISG15 by a viral leader protease enables alternative infection detection strategies. *Proc Natl Acad Sci U S A* **115**: 2371-2376.

Szalay G, Meiners S, Voigt A, Lauber J, Spieth C, Speer N, Sauter M, Kuckelkorn U, Zell A, Klingel K et al. 2006. Ongoing coxsackievirus myocarditis is associated with increased formation and activity of myocardial immunoproteasomes. *Am J Pathol* **168**: 1542-1552.

Szretter KJ, Daniels BP, Cho H, Gainey MD, Yokoyama WM, Gale M, Jr., Virgin HW, Klein RS, Sen GC, Diamond MS. 2012. 2'-O methylation of the viral mRNA cap by West Nile virus evades ifit1-dependent and -independent mechanisms of host restriction in vivo. *PLoS pathogens* **8**: e1002698.

Takeuchi T, Inoue S, Yokosawa H. 2006. Identification and Herc5-mediated ISGylation of novel target proteins. *Biochemical and biophysical research communications* **348**: 473-477.

Takeuchi T, Iwahara S, Saeki Y, Sasajima H, Yokosawa H. 2005. Link between the ubiquitin conjugation system and the ISG15 conjugation system: ISG15 conjugation to the UbcH6 ubiquitin E2 enzyme. *J Biochem* **138**: 711-719.

Tang Y, Zhong G, Zhu L, Liu X, Shan Y, Feng H, Bu Z, Chen H, Wang C. 2010. Herc5 attenuates influenza A virus by catalyzing ISGylation of viral NS1 protein. *J Immunol* **184**: 5777-5790.

Terai K, Hiramoto Y, Masaki M, Sugiyama S, Kuroda T, Hori M, Kawase I, Hirota H. 2005. AMP-activated protein kinase protects cardiomyocytes against hypoxic injury through attenuation of endoplasmic reticulum stress. *Mol Cell Biol* **25**: 9554-9575.

Terenzi F, Hui DJ, Merrick WC, Sen GC. 2006. Distinct induction patterns and functions of two closely related interferon-inducible human genes, ISG54 and ISG56. *The Journal of biological chemistry* **281**: 34064-34071.

The Gene Ontology C. 2017. Expansion of the Gene Ontology knowledgebase and resources. *Nucleic Acids Res* **45**: D331-D338.

The Gene Ontology C. 2019. The Gene Ontology Resource: 20 years and still GOing strong. *Nucleic Acids Res* **47**: D330-D338.

Thery F, Eggermont D, Impens F. 2021. Proteomics Mapping of the ISGylation Landscape in Innate Immunity. *Front Immunol* **12**: 720765.

Tokarz S, Berset C, La Rue J, Friedman K, Nakayama K, Nakayama K, Zhang DE, Lanker S. 2004. The ISG15 isopeptidase UBP43 is regulated by proteolysis via the SCFSkp2 ubiquitin ligase. *The Journal of biological chemistry* **279**: 46424-46430.

Toko H, Takahashi H, Kayama Y, Okada S, Minamino T, Terasaki F, Kitaura Y, Komuro I. 2010. ATF6 is important under both pathological and physiological states in the heart. *J Mol Cell Cardiol* **49**: 113-120.

Triantafilou K, Orthopoulos G, Vakakis E, Ahmed MA, Golenbock DT, Lepper PM, Triantafilou M. 2005. Human cardiac inflammatory responses triggered by Coxsackie B viruses are mainly Toll-like receptor (TLR) 8-dependent. *Cell Microbiol* **7**: 1117-1126.

Tyanova S, Temu T, Cox J. 2016a. The MaxQuant computational platform for mass spectrometry-based shotgun proteomics. *Nat Protoc* **11**: 2301-2319.

Tyanova S, Temu T, Sinitcyn P, Carlson A, Hein MY, Geiger T, Mann M, Cox J. 2016b. The Perseus computational platform for comprehensive analysis of (prote)omics data. *Nat Methods* **13**: 731-740.

van der Veen AG, Ploegh HL. 2012. Ubiquitin-like proteins. *Annu Rev Biochem* **81**: 323-357.

van Kuppeveld FJ, Hoenderop JG, Smeets RL, Willems PH, Dijkman HB, Galama JM, Melchers WJ. 1997. Coxsackievirus protein 2B modifies endoplasmic reticulum membrane and plasma membrane permeability and facilitates virus release. *The EMBO journal* **16**: 3519-3532.

Versteeg GA, Hale BG, van Boheemen S, Wolff T, Lenschow DJ, Garcia-Sastre A. 2010. Species-specific antagonism of host ISGylation by the influenza B virus NS1 protein. *J Virol* **84**: 5423-5430.

Vuillier F, Li Z, Commere PH, Dynesen LT, Pellegrini S. 2019. USP18 and ISG15 coordinately impact on SKP2 and cell cycle progression. *Sci Rep* **9**: 4066.

Wagner SA, Beli P, Weinert BT, Scholz C, Kelstrup CD, Young C, Nielsen ML, Olsen JV, Brakebusch C, Choudhary C. 2012. Proteomic analyses reveal divergent ubiquitylation site patterns in murine tissues. *Mol Cell Proteomics* **11**: 1578-1585.

Wang B, Li Y, Wang H, Zhao J, Zhao Y, Liu Z, Ma H. 2019. FOXO3a is stabilized by USP18-mediated de-ISGylation and inhibits TGF-beta1-induced fibronectin expression. *J Investig Med*.

Wang JP, Cerny A, Asher DR, Kurt-Jones EA, Bronson RT, Finberg RW. 2010a. MDA5 and MAVS mediate type I interferon responses to coxsackie B virus. *J Virol* **84**: 254-260.

Wang Q, Donthi RV, Wang J, Lange AJ, Watson LJ, Jones SP, Epstein PN. 2008. Cardiac phosphatase-deficient 6-phosphofructo-2-kinase/fructose-2,6-bisphosphatase increases glycolysis, hypertrophy, and myocyte resistance to hypoxia. *Am J Physiol Heart Circ Physiol* **294**: H2889-2897.

Wang X, Hinson ER, Cresswell P. 2007. The interferon-inducible protein viperin inhibits influenza virus release by perturbing lipid rafts. *Cell Host Microbe* **2**: 96-105.

Wang Z, Ying Z, Bosy-Westphal A, Zhang J, Schautz B, Later W, Heymsfield SB, Muller MJ. 2010b. Specific metabolic rates of major organs and tissues across adulthood: evaluation by mechanistic model of resting energy expenditure. *Am J Clin Nutr* **92**: 1369-1377.

Warr MR, Binnewies M, Flach J, Reynaud D, Garg T, Malhotra R, Debnath J, Passegue E. 2013. FOXO3A directs a protective autophagy program in haematopoietic stem cells. *Nature* **494**: 323-327.

Wathelet M, Moutschen S, Defilippi P, Cravador A, Collet M, Huez G, Content J. 1986. Molecular cloning, full-length sequence and preliminary characterization of a 56-kDa protein induced by human interferons. *Eur J Biochem* **155**: 11-17.

Weekes MP, Tomasec P, Huttlin EL, Fielding CA, Nusinow D, Stanton RJ, Wang ECY, Aicheler R, Murrell I, Wilkinson GWG et al. 2014. Quantitative temporal viromics: an approach to investigate host-pathogen interaction. *Cell* **157**: 1460-1472.

Wenzel P, Kopp S, Gobel S, Jansen T, Geyer M, Hahn F, Kreitner KF, Escher F, Schultheiss HP, Munzel T. 2020. Evidence of SARS-CoV-2 mRNA in endomyocardial biopsies of patients with clinically suspected myocarditis tested negative for COVID-19 in nasopharyngeal swab. *Cardiovasc Res* **116**: 1661-1663.

Werneke SW, Schilte C, Rohatgi A, Monte KJ, Michault A, Arenzana-Seisdedos F, Vanlandingham DL, Higgs S, Fontanet A, Albert ML et al. 2011. ISG15 is critical in the control of Chikungunya virus infection independent of UbE1L mediated conjugation. *PLoS pathogens* **7**: e1002322.

Werner C, Doenst T, Schwarzer M. 2016. Chapter 4 - Metabolic Pathways and Cycles. in *The Scientist's Guide to Cardiac Metabolism* (eds. M Schwarzer, T Doenst), pp. 39-55. Academic Press, Boston.

Werner M, Purta E, Kaminska KH, Cymerman IA, Campbell DA, Mittra B, Zamudio JR, Sturm NR, Jaworski J, Bujnicki JM. 2011. 2'-O-ribose methylation of cap2 in human: function and evolution in a horizontally mobile family. *Nucleic Acids Res* **39**: 4756-4768.

Why HJ, Meany BT, Richardson PJ, Olsen EG, Bowles NE, Cunningham L, Freeke CA, Archard LC. 1994. Clinical and prognostic significance of detection of enteroviral RNA in the myocardium of patients with myocarditis or dilated cardiomyopathy. *Circulation* **89**: 2582-2589.

Wilkins C, Gale M, Jr. 2010. Recognition of viruses by cytoplasmic sensors. *Current opinion in immunology* **22**: 41-47.

Wong J, Zhang J, Si X, Gao G, Mao I, McManus BM, Luo H. 2008. Autophagosome supports coxsackievirus B3 replication in host cells. *J Virol* **82**: 9143-9153.

Wong JJ, Pung YF, Sze NS, Chin KC. 2006. HERC5 is an IFN-induced HECT-type E3 protein ligase that mediates type I IFN-induced ISGylation of protein targets. *Proc Natl Acad Sci U S A* **103**: 10735-10740.

Woodruff JF. 1980. Viral myocarditis. A review. *Am J Pathol* **101**: 425-484.

Wreschner DH, James TC, Silverman RH, Kerr IM. 1981. Ribosomal RNA cleavage, nuclease activation and 2-5A(ppp(A2'p)nA) in interferon-treated cells. *Nucleic Acids Res* **9**: 1571-1581.

Wu D, Sanin DE, Everts B, Chen Q, Qiu J, Buck MD, Patterson A, Smith AM, Chang CH, Liu Z et al. 2016. Type 1 Interferons Induce Changes in Core Metabolism that Are Critical for Immune Function. *Immunity* **44**: 1325-1336.

Xia C, Anderson P, Hahm B. 2018. Viral dedication to vigorous destruction of interferon receptors. *Virology* **522**: 19-26.

Xiao B, Deng X, Zhou W, Tan EK. 2016. Flow Cytometry-Based Assessment of Mitophagy Using MitoTracker. *Front Cell Neurosci* **10**: 76.

Xu D, Zhang T, Xiao J, Zhu K, Wei R, Wu Z, Meng H, Li Y, Yuan J. 2015. Modification of BECN1 by ISG15 plays a crucial role in autophagy regulation by type I IFN/interferon. *Autophagy* **11**: 617-628.

Xu J, Nie HG, Zhang XD, Tian Y, Yu B. 2011. Down-regulated energy metabolism genes associated with mitochondria oxidative phosphorylation and fatty acid metabolism in viral cardiomyopathy mouse heart. *Mol Biol Rep* **38**: 4007-4013.

Yan S, Kumari M, Xiao H, Jacobs C, Kochumon S, Jedrychowski M, Chouchani E, Ahmad R, Rosen ED. 2021. IRF3 reduces adipose thermogenesis via ISG15-mediated reprogramming of glycolysis. *J Clin Invest*.

Yanagawa B, McManus B, Hollander Z, Luo H, Ng R, Yang D. 2003. From gene expression profiles to biological validation in enteroviral heart disease. *Exp Clin Cardiol* **8**: 125-130.

Yasukawa H, Misawa H, Sakamoto H, Masuhara M, Sasaki A, Wakioka T, Ohtsuka S, Imaizumi T, Matsuda T, Ihle JN et al. 1999. The JAK-binding protein JAB inhibits Janus tyrosine kinase activity through binding in the activation loop. *The EMBO journal* **18**: 1309-1320.

Ye Y, Akutsu M, Reyes-Turcu F, Enchev RI, Wilkinson KD, Komander D. 2011. Polyubiquitin binding and cross-reactivity in the USP domain deubiquitinase USP21. *EMBO reports* **12**: 350-357.

Yellon DM, Hausenloy DJ. 2007. Myocardial reperfusion injury. *N Engl J Med* **357**: 1121-1135.
Young DF, Andrejeva J, Li X, Inesta-Vaquera F, Dong C, Cowling VH, Goodbourn S, Randall RE. 2016. Human IFIT1 Inhibits mRNA Translation of Rubulaviruses but Not Other Members of the Paramyxoviridae Family. *J Virol* **90**: 9446-9456.
Young LH, Renfu Y, Russell R, Hu X, Caplan M, Ren J, Shulman GI, Sinusas AJ. 1997. Low-flow ischemia leads to translocation of canine heart GLUT-4 and GLUT-1 glucose transporters to the sarcolemma in vivo. *Circulation* **95**: 415-422.
Yu Y, Clippinger AJ, Alwine JC. 2011. Viral effects on metabolism: changes in glucose and glutamine utilization during human cytomegalovirus infection. *Trends Microbiol* **19**: 360-367.
Yuan W, Krug RM. 2001. Influenza B virus NS1 protein inhibits conjugation of the interferon (IFN)-induced ubiquitin-like ISG15 protein. *The EMBO journal* **20**: 362-371.
Yue TL, Bao W, Jucker BM, Gu JL, Romanic AM, Brown PJ, Cui J, Thudium DT, Boyce R, Burns-Kurtis CL et al. 2003. Activation of peroxisome proliferator-activated receptor-alpha protects the heart from ischemia/reperfusion injury. *Circulation* **108**: 2393-2399.
Zaheer RS, Wiehler S, Hudy MH, Traves SL, Pelikan JB, Leigh R, Proud D. 2014. Human rhinovirus-induced ISG15 selectively modulates epithelial antiviral immunity. *Mucosal Immunol* **7**: 1127-1138.
Zhang X, Bogunovic D, Payelle-Brogard B, Francois-Newton V, Speer SD, Yuan C, Volpi S, Li Z, Sanal O, Mansouri D et al. 2015. Human intracellular ISG15 prevents interferon-alpha/beta over-amplification and auto-inflammation. *Nature* **517**: 89-93.
Zhang Y, Thery F, Wu NC, Luhmann EK, Dussurget O, Foecke M, Bredow C, Jimenez-Fernandez D, Leandro K, Beling A et al. 2019. The in vivo ISGylome links ISG15 to metabolic pathways and autophagy upon Listeria monocytogenes infection. *Nat Commun* **10**: 5383.
Zhao C, Beaudenon SL, Kelley ML, Waddell MB, Yuan W, Schulman BA, Huibregtse JM, Krug RM. 2004. The UbcH8 ubiquitin E2 enzyme is also the E2 enzyme for ISG15, an IFN-alpha/beta-induced ubiquitin-like protein. *Proc Natl Acad Sci U S A* **101**: 7578-7582.
Zhao C, Denison C, Huibregtse JM, Gygi S, Krug RM. 2005. Human ISG15 conjugation targets both IFN-induced and constitutively expressed proteins functioning in diverse cellular pathways. *Proc Natl Acad Sci U S A* **102**: 10200-10205.
Zhao C, Hsiang TY, Kuo RL, Krug RM. 2010. ISG15 conjugation system targets the viral NS1 protein in influenza A virus-infected cells. *Proc Natl Acad Sci U S A* **107**: 2253-2258.
Zhao C, Sridharan H, Chen R, Baker DP, Wang S, Krug RM. 2016. Influenza B virus non-structural protein 1 counteracts ISG15 antiviral activity by sequestering ISGylated viral proteins. *Nat Commun* **7**: 12754.
Zheng H, Qian J, Baker DP, Fuchs SY. 2011a. Tyrosine phosphorylation of protein kinase D2 mediates ligand-inducible elimination of the Type 1 interferon receptor. *The Journal of biological chemistry* **286**: 35733-35741.
Zheng H, Qian J, Varghese B, Baker DP, Fuchs S. 2011b. Ligand-stimulated downregulation of the alpha interferon receptor: role of protein kinase D2. *Mol Cell Biol* **31**: 710-720.
Zorova LD, Popkov VA, Plotnikov EY, Silachev DN, Pevzner IB, Jankauskas SS, Babenko VA, Zorov SD, Balakireva AV, Juhaszova M et al. 2018. Mitochondrial membrane potential. *Anal Biochem* **552**: 50-59.
Zou W, Zhang DE. 2006. The interferon-inducible ubiquitin-protein isopeptide ligase (E3) EFP also functions as an ISG15 E3 ligase. *The Journal of biological chemistry* **281**: 3989-3994.

8 Publication Summary

Voss M, Kleinau G, Gimber N, Janek K, **Bredow C**, Thery F, Impens F, Schmoranzer J, Scheerer P, Kloetzel PM et al. 2022. A cytosolic disulfide bridge-supported dimerization is crucial for stability and cellular distribution of Coxsackievirus B3 protein 3A. *The FEBS journal*.

Thery F, Martina L, Asselman C, Zhang Y, Vessely M, Repo H, Sedeyn K, Moschonas GD, **Bredow C**, Teo QW et al. 2021. Ring finger protein 213 assembles into a sensor for ISGylated proteins with antimicrobial activity. *Nat Commun* **12**: 5772.

Voss M, Braun V, **Bredow C**, Kloetzel PM, Beling A. 2021. Coxsackievirus B3 Exploits the Ubiquitin-Proteasome System to Facilitate Viral Replication. *Viruses* **13**.

Kespohl M, **Bredow C**, Klingel K, Voss M, Paeschke A, Zickler M, Poller W, Kaya Z, Eckstein J, Fechner H et al. 2020. Protein modification with ISG15 blocks coxsackievirus pathology by antiviral and metabolic reprogramming. *Sci Adv* **6**: eaay1109.

Zhang Y, Thery F, Wu NC, Luhmann EK, Dussurget O, Foecke M, **Bredow C**, Jimenez-Fernandez D, Leandro K, Beling A et al. 2019. The in vivo ISGylome links ISG15 to metabolic pathways and autophagy upon Listeria monocytogenes infection. *Nat Commun* **10**: 5383.

Benn A, **Bredow C**, Casanova I, Vukicevic S, Knaus P. 2016. VE-cadherin facilitates BMP-induced endothelial cell permeability and signaling. *J Cell Sci* **129**: 206-218.

9 List of abbreviations

1,3-BPG	1,3-bisphosphoglycerate
2-5A	2'-5'oligoadenylates
25HC	25-hydroxycholesterol
3-PG	3-phosphoglycerate
4EHP	eIF4E-homologous protein
aa	Amino acids
ACO	Aconitase
AGS	Aicardi-Goutières syndrome
ALDO	Aldolase
AMPK	AMP activated protein kinase
AP	Activator protein
ATP	Adenosine triphosphate
BCA	Bicinchoninic acid
BCAA	Branched chain amino acids
BCATm	Branched-chain aminotransferase
BECN1	Beclin-1
BMDM	Bone marrow derived macrophages
bp	Base pair
BSA	Bovine serum albumin
CAR	Coxsackie and adenoviral receptor
cGAS	Cyclic GMP-AMP synthase
CH25H	Cholesterol-25-hydroxylase
CHIP	HSC70-interacting protein
CI	Complex I
CII	Complex II
CIII	Complex III
CIV	Complex IV
CMV	Cytomegalovirus
CoA	Coenzyme A
CoV	Coronavirus
CPT	Carnitine-palmitoyl transferase
CSY	Citrate synthase
CV	Complex V
CVB3	Coxsackievirus B3
CVD	Cardiovascular disease
DAF	Co-receptor decay accelarating factor
DAMP	Damage-associated molecular pattern
DC	Dendritic cell
DHAP	Dihydroxyacetone phosphate
DMEM	Dulbecco's Modified Eagle's Medium
ds	Double-stranded
DTT	Dithiothreitol
DUB	Deubiquitination
ECAR	Extracellular acidification rate
ECH1	Delta(3,5)-delta(2,4)-dienoyl-coa isomerase
EFP	Estrogen-responsive finger protein
eIF4E	Eukaryotic translation initiation factor 4E
EMCV	Encephalomyocarditis Virus
ENO	Enolase
ER	Endoplasmic Reticulum
ESCRT	Endosomal sorting complex

ETC	Electron transport chain
EV71	Enterovirus 71
F-1,6-BP	Fructose-1,6-bisphosphate
F-6-P	Fructose-6-phosphate
FA	Fatty acid
FABP	FA binding protein
FCCP	Carbonyl cyanide-p-trifluoromethoxyphenylhydrazone
FMDV	Foot and Mouth Disease Virus
FOX	Forkhead Box
FUM	Fumarase
G-3-P	Glyceraldehyde-3-phosphate
G-6-P	Glucose-6-phosphate
GAPDH	Glyceraldehyde-3-phosphate dehydrogenase
GAS	Gamma-activated sequence
GFP	Green fluorescent protein
GG	Double-glycine
GLUT	Glucose transporter
GMK	Green Monkey Kidney
GO	Gene ontology
GPI	Glucose-6-phosphate isomerase
H&E	Hematoxylin and eosin
HBV	Hepatitis B Virus
HCV	Hepatitis C Virus
HDAC6	Histone deacetylase 6
HEV	Hepatitis E Virus
HHARI	Human homolog of Drosophila ariadne
HIV	Human immunodeficiency virus
HK	Hexokinase
HPRT	hypoxanthine guanine phosphoribosyltransferase
HPV	Human papillomavirus
HRV	Human rhinovirus
HSV	Herpes Simplex Virus
I/R	Ischemia/reperfusion
IB	Immunoblot
IBB	ISG15-binding boxes
ICC	Image cross correlation
ICS	Image correlation spectroscopy
IDH	Isocitrate dehydrogenase
IFIT	Interferon Induced Protein with Tetratricopeptide Repeats
IFN	Interferon
IFNAR	IFN activated receptor
IFNGR	IFNγ-receptor
IIGP	Interferon-inducible gtpase
IL	Interleukin
IP	Immunoprecipitation
IRES	Internal ribosomal entry site
IRF	Interferon regulatory factor
ISG15	Interferon Stimulated Gene of 15 kda
ISGF3	IFN-stimulated gene factor 3
ISRE	IFN-stimulated response elements
JAK1	Janus kinase 1
JEV	Japanese Encephalitis Virus
LACV	La Crosse Virus

LC-MS/MS	Liquid chromatography-tandem MS
LC-MS/MS	Liquid chromatography-tandem mass spectrometry
LDH	Lactate dehydrogenase
LFA-1	Lymphocyte function-associated antigen-1
LGP2	Laboratory of genetics and physiology 2
LKB1	Liver kinase B1
LPS	Lipopolysaccharide
LRRC25	Leucine Rich Repeat Containing protein 25
MAVS	Mitochondrial antiviral signaling protein
MDA5	Melanoma differentiation-associated 5
MDH	Malate dehydrogenase
MEF	Mouse embryonic fibroblast
MERS	Middle eastern respiratory syndrome
MeV	Measles Virus
MITA	Mediator of IRF3 activation
MTDR	Mitotracker® Deep Red
mTOR	Mechanistic target of rapamycin
mTORC1	Mechanistic target of rapamycin complex 1
MuRF1	Muscle ring finger-1
Mx	Myxovirus-resistance protein
MyD88	Myeloid differentiation primary response 88
NAD	Nicotinamide adenine dinucleotide
Nedd	Neural precursor cell expressed, developmentally down-regulated
NF-κB	Nuclear factor κb
NNT	NAD(P) transhydrogenase
NP	Nucleoproteins
NS1	Influenza virus non-structural protein 1
OAA	Oxaloacetate
OAS	Oligoadenylate synthase
OCR	Oxygen consumption rate
OD	Optical density
ORF	Open reading frame
OTU	Ovarian Tumor Domains
PAGE	Polyacrylamide gel electrophoresis
PAMP	Pathogen-associated molecular pattern
PBS	Phosphate buffered saline
PCA	Principal component analysis
PEI	Polyethylenimine
PEP	Phosphoenolpyruvate
PFK	Phosphofructokinase
PGC	Peroxisome proliferator-activated receptor-gamma coactivator
PGI	Phosphoglucose isomerase
PGK	Phosphoglycerate kinase
PGM	Phosphoglucomutase
Pin1	Peptidylpropyl isomerase 1
PK	Pyruvate kinase
PKR	Protein kinase R
PLpro	Papain-like protease
PPARα	Peroxisome proliferator-activated receptor alpha
PRR	Pattern recognition receptor
PYG	Glycogen phosphorylase
Q	Ubiquinone

QH_2	Ubiquinol
RIG	Retinoic acid inducible gene
RLR	Retinoic acid inducible gene-I like receptor
RNA	Ribonucleic acid
RNaseL	Ribonuclease L
RNF	E3 ligase ring finger protein
ROS	Reactive oxygen species
RT	Room temperature
SARS	Severe acute respiratory syndrome
SCS	Succinyl-CoA synthethase
SDH	Succinate dehydrogenase
SDS	Sodium dodecyl sulfate
SEM	Standard error of the mean
SERPIN E1	Plasminogen activator inhibitor-1
SH2	Src homology 2
SKP2	S-phase kinase associated protein 2
SOCS	Suppressor of cytokine signaling
ss	Single-stranded
STAT	Signal transducer and activator of transcription
STING	Stimulator of interferon genes
SucCoA	Succinyl-CoA
TAG	Triacylglycerol
TBK1	TANK Binding Kinase 1
TCA	Tricarboxylic acid
TCL	Total cell lysates
TG	Triglyceride
TH	Thyroid hormones
TLR	Toll-like receptor
TNF	Tumor necrosis factor
TRAF6	TNF receptor associated factor 6
TRIF	TIR domain-containing adaptor–inducing interferon β
TYK2	Tyrosine kinase 2
UBA7	Ubiquitin-like modifier-activating enzyme 7
Ube1L	Ubiquitin-activating enzyme 1L
Ube2L6	Ubituitin / ISG15-conjugating enzyme E2 L6
UBL	Ubiquitin-like modifier
UPR	Unfolded protein response
UPS	Ubiquitin proteasome system
USP	Ubiquitin specific protease
Viperin	Virus inhibitory protein, endoplasmic reticulum-associated, IFN-inducible
VSV	vesicular stomatitis virus
WIPI2	WD Repeat Domain, Phosphoinositide Interacting 2
XDH	Xanthine dehydrogenase/oxidase
α-KG	α-ketoglutarate
αKGDH	α-ketoglutarate dehydrogenase

10 List of figures

11 Anhang

Tab. S1: Shotgun Proteomics

Tab. S2: Proteom GO Analysis Biological Process

Tab. S3: Proteom GO Analysis Molecular Function

Tab. S4: Proteom GO Analysis Cellular Component

Tab. S5: GG-IP Day 3

Tab. S6: GG-IP Day 3 GO Analysis Biological Process

Tab. S7: GG-IP Day 3 GO Analysis Molecular Function

Tab. S8: GG-IP Day 3 GO Analysis Cellular Component

Tab. S9: GG-IP Day 8

Tab. S10: GG-IP Day 8 GO Analysis Biological Process

Tab. S11: GG-IP Day 8 GO Analysis Molecular Function

Tab. S12: GG-IP Day 8 GO Analysis Cellular Component

Tab. S13: ISGylation Site Comparison with Literature

Tab. S14: Shotgun Volcano Plot Fig 13

Please see the zip file for the supplemental tables.